THE BIOGEOCHEMISTRY OF METHANE ISOTOPOLOGUES IN MARINE AND LACUSTRINE SEDIMENTS

by

Ellen Lalk

B.S., Washington University in St Louis, 2017

Submitted to the Department of Earth, Atmosphere and Planetary Sciences
in partial fulfillment of the requirements for the degree of

DOCTOR OF PHILOSOPHY IN GEOCHEMISTRY

At the MASSACHUSSETTS INSTITUTE OF TECHNOLOGY
And the WOODS HOLE OCEANOGRAPHIC INSTITUTION

FEBRUARY 2023

Authored by: Ellen Lalk
Department of Earth, Atmosphere and Planetary Sciences, MIT
Marine Chemistry and Geochemistry Department, WHOI
MIT/WHOI Joint Program in Oceanography/Applied Ocean Science and Engineering
December 12, 2022

Certified by: Prof. Shuhei Ono
Thesis Supervisor
MIT

Accepted by: Prof. Ed Boyle
Chair, Joint Committee for Chemical Oceanography
MIT/WHOI

THE BIOGEOCHEMISTRY OF METHANE ISOTOPOLOGUES IN MARINE AND LACUSTRINE SEDIMENTS

Ellen Lalk

Submitted to the Joint Program in Oceanography/Applied Ocean Science and Engineering,
Massachusetts Institute of Technology & Woods Hole Oceanographic Institution
On December 12, 2022 in partial fulfillment of the requirements for the degree of
Doctor of Philosophy in the field of Geochemistry

Abstract

Methane is a globally significant greenhouse gas, energy resource, and it is a product and reactant of microbial metabolisms. Multiple sources and sinks of methane can be challenging to distinguish from each other, thus complicating the understanding of methane budgets and the effects of microbes on mediating Earth's carbon cycle. The relative abundances of methane isotopologues (e.g., $^{12}CH_4$, $^{13}CH_4$, $^{12}CH_3D$, and $^{13}CH_3D$) record process-based information about the formation conditions, transport, and fate of methane, and in select environments can serve as a temperature proxy. This geochemical tool is herein applied to methane from marine and lacustrine sediments to test assumptions about prevailing mechanisms of its formation and consumption in these settings.

This thesis describes 1) three studies about biogeochemical insights gained by quantifying the relative abundance of clumped methane isotopologue, $^{13}CH_3D$, in samples from marine and lacustrine sediments, and 2) one foray into method development to improve the quantification of methane in these environments. Chapter 2 presents a global survey of marine gas hydrates where isotope-based temperatures are used to assess whether linkages between methane sources and seepage-associated seafloor features match putative geologic models. Chapter 3 describes two kilometer-scale profiles of methane isotopologues from marine sediments, where the relationship between expected sediment temperature and isotope-based temperature is used to evaluate the temperature limit of microbial processing and abiotic re-equilibration mechanisms. Chapter 4 reports the largest set of methane isotopologue data from ebullition in a single lake basin, which is used to gauge the relative importance of aerobic and anaerobic methane oxidation in the study site and recommend a general sampling strategy to constrain methane source signatures in similar lake settings. Chapter 5 explains the development of a method to quantify the *in situ* concentration of methane based on ratios of dissolved gases, and its comparison to four other methane quantification methods for surface sediments from marine cold seeps. The findings from this research contribute to ongoing efforts to understand the sedimentary carbon cycle and microbial activity in remote environments.

THESIS SUPERVISOR: Shuhei Ono
TITLE: Full Professor, MIT

Contents

List of Figures

List of Tables

A

Acknowledgements

There is no way to do justice to the many people who have supported my growth as a scientist and the development of this thesis, but I will try my best.

I want to start by thanking my advisor Shuhei Ono, for opening his lab to me and sharing his creative outlook on geochemistry and practical engineering expertise. Truly, I could never have imagined I would learn or care so much about how different valves function. His breadth of curiosity (both scientific and other), make the lab a special place and I hope to emulate his courage to tackle new ideas as I continue to grow as a scientist.

I also want to thank my thesis committee members Jeff Seewald, Verena Heuer, and Art Spivack for their input on my projects and investment in my growth. I could always count on this group for kind and honest feedback about my ideas, opportunities, and career path. Additionally, conversations with these individuals always resulted in newfound enthusiasm for science and my work, even through difficult roadblocks including the pandemic-related destruction of some intended work. I have felt very lucky to have them on my team.

Thank you to Roger Summons for chairing my defense and offering thoughts on this thesis, as well as welcoming me to various lab meetings, dinners, and classes. I will miss strolling through this lab on the way to and from the Ono lab. I also wish to thank Julie Huber for chairing my thesis proposal defense, and feedback during the early stages of this work.

I would like to acknowledge all my collaborators for their contributions to the work presented in this dissertation; thanks to Thomas Pape, Danielle Gruen, Norbert Kaul, Jen Karolewski, Gerhard Bohrmann, Jeff Seewald, Taras Bryndzia, Verena Heuer, Amber Velez, Art Spivack, and David T. Wang. The scientists (Casey Hubert's and Todd Ventura's groups) and crew on the 2021 *Atlantic Condor* expedition are thanked for facilitating the collection of samples used in this thesis and teaching me a lot about sea-going fieldwork (including supplying my very naïve self with seasickness medication, before it was too late). I want to additionally thank Amber Velez for her trust in me as a research advisor—it was a great honor.

Many members of the MIT Hardcore Stable Isotope Laboratory have contributed their time and ideas to the work presented in this thesis. I am grateful for Jeemin Rhim, my sister in lab (and life), who patiently trained me to use all our analytical equipment, listened to every practice talk, and has been a source of kind and sound advice for the rawest forms of my ideas. Our many adventures near and far are dear to me. I would also like to thank Patrick Beaudry, Eric Ryberg, Jeehyun Yang, Gareth Izon, Yenny Gonzalez Ramos, Ben Uveges, Jian Gong, Mihkel Pajusalu, Jiayang Sun, Amber Velez, and Vanessa Sun for their support and friendship both in and out of the lab.

I have been lucky to be surrounded by many wonderful and engaging people in the E25-6th floor community. Thank you to Angel Mojarro, Diana Dumit, Fatima Husain, Michaela Fendrock, Christopher Kinsley, James Hall, Matt Baldes, Jimmy Bramante, and Lubna Shawar for being extremely reliable sources of trouble-shooting assistance, advice navigating the

department, and perhaps most importantly—a laugh. I would also like to thank the 6th floor faculty (Ed Boyle, Tanja Bosak, David McGee, Roger Summons, and Shuhei Ono) and administrators (Melody Abedinejad, Erin Chen, and Liz Washburn) for their roles in fostering an alcove of an enjoyable work community.

The E25 administrators are also thanked for the many innumerable ways they made this work possible and easier every day. I want to thank the staff of the MIT Joint Program Office (Kris Kipp and Tricia Nesti), EAPS HQ (Allison Provaire, Dave Wright, Madelyn Musick, Maggie Cedarstrom), EAPS Education Office (Brandon Milardo, Megan Jordan, Julia Hollingsworth, Ann Greany-Williams), and the WHOI APO (Meg Tivey, Delia Oppo, Ann Tarrant, Lea Fraser, Christine Charette, Meredith Bittrich, and Julia Westwater).

A special thanks to my JP chemistry cohort (Tyler Tamasi, Kalina Grabb, Becca Chmiel, Riss Kellogg, Ben Granzow, Jay Li, and Jess Dabrowski) who have supported each other through classes, generals, and everything that came next. The JP Sunfish cohort (Kevin Doherty, Jing He, Alia Hidayat, Lauren Dykman, Emman Codillo, Adrian Garcia, Fiona Clerc, Michaela Fendrock, Drew Hirzel, and Nastasia Winey) are also thanked for their support in the forms of ice cream runs and generously hosting me on the cape. My MIT EAPS cohort (Angel Mojarro, Meghana Ranganathan, Julia Wilcots, Craig Martin, Jonathan Lin, Zahra Essack, Kasturi Shah, Ali Ramadhan) has also been a frequent source of support (and commissary, when needed)—Mystery Science Box 3000 was never good, but we had a good time.

There are many people in the MIT EAPS and WHOI communities to thank for dedicating lots of their time and energy in the pursuit of making these communities more inclusive places to work. This includes members of TIDE, ESAC, WiXII, the DEI-C and WHOI and MIT URGE pods. Additional thanks are owed to the most collaborative team I have ever been a part of (Meghana Ranganathan, Lyssa Freese, Mara Freilich, Julia Wilcots, Margaret Duffy, and Rohini Shivamoggi), for setting the bar as high as it belongs.

I have had two major strokes of luck for officemates in the form of Kelsey Moore and Emilie Skoog. Kelsey is thanked for her unwavering support and advice, as well as her willingness (enthusiasm) to partake in a healthy dose of shenanigans; our 6th Floor "Handprint Microbiome Madness" was one of the highlights of my graduate career. Emilie Skoog was physically by my side for an incredible amount of the writing of this thesis, which made the process significantly more enjoyable. She has also, on occasion, jumped in a freezing lake for me—just out of support. I won the lottery with roommates/colleagues Meghana Ranganathan and Fiona Clerc. Meghana's can-do attitude and positive impact on her personal, scientific, and other professional communities has always served as a great source of inspiration for me. Fiona's unbounded creativity and willingness to try new things (including questionable bouldering moves) kept things fun, even through the uncertain days of early pandemic lockdown.

Finally, I thank my family: my parents and sister—none of this would be possible without your support and enthusiasm, and my partner Kyle, who believes in me so much that I have no choice but to buy into it. Thank you.

Financial acknowledgement

The works described in this thesis was made possible by grants to my advisor from sources including the National Science Foundation (EAR-1852946 to S.O.), U.S. Science Support Program Office associated with the International Ocean Discovery program (OCE-14-50528 to D.T.W and S.O.), the Deep Carbon Observatory Deep Life Community Grant (to S.O.), MISTI Japan, and the mTerra Catalyst Fund (to S.O. and E.L). From 2017-2018 I was funded by the MIT Presidential Fellowship, and from 2018-2020 I was funded as a fellow through the MIT Energy Initiative. The collection of samples from the Scotian Slope was funded by the WHOI Ocean Ventures Fund (to E.L.). The Montrym Fund for student climate research (to E.L) funded the sampling of Upper Mystic Lake. My participation in the 2018 ECORD Summer School was funded by the U.S. Science Support Program Office, and the MIT GSC Conference fund providing funding for my participation in the AGU 2021 Fall Meeting and Goldschmidt 2022.

Chapter 1

Introduction

1.1 METHANE AND THE GLOBAL CARBON CYCLE

Methane, CH_4, is the most abundant alkane on Earth and an important component of the global carbon cycle. In the atmosphere, methane is a potent greenhouse gas, with 28 times the warming potential of CO_2 over a 100-year timescale (Myhre et al., 2013). In sediments, the creation of methane fuels microbial life, as it is the byproduct of the final step of microbially-mediated anerobic degradation of organic matter. In deep sediments, methane can also be produced by the heating of larger organic molecules, contributing to energy reservoirs.

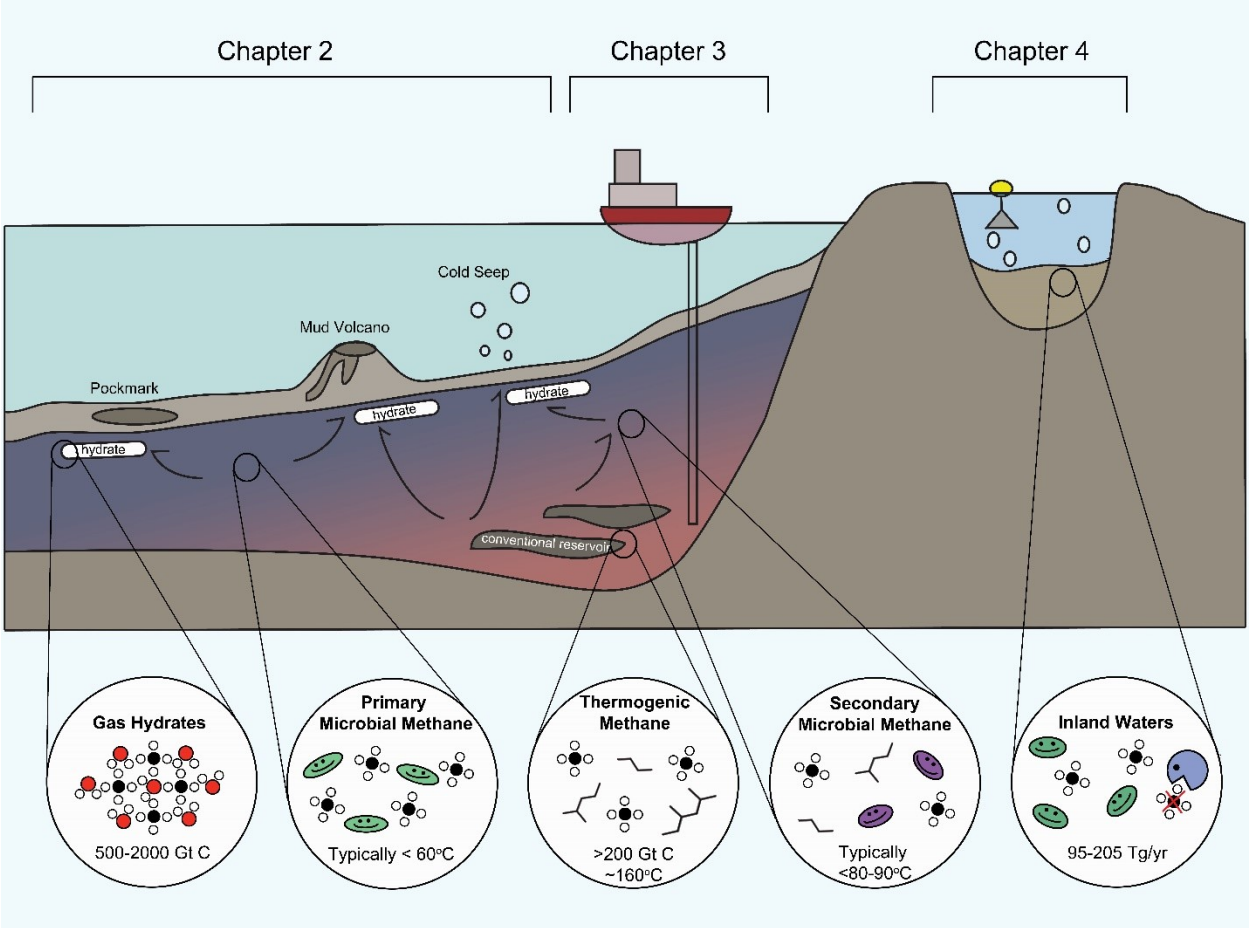

Figure 1.1: Relevant sources and reservoirs of methane in marine and lacustrine sedimentary environments for the scope of this thesis.

Figure 1.1 summarizes relevant sources and reservoirs of methane in marine and lacustrine (i.e., lake) sediments. Earth's largest reservoir of methane resides in ocean sediments (500-10,000 Gt CH_4), typically along continental margins (Bruhwiler et al., 2018; Kvenvolden et al., 2002; Milkov et al., 2004). The upper hundreds of meters of coastal marine sediments store

large volumes of methane (500-2,000 Gt CH_4) in the crystal lattices of ice-like gas hydrates (e.g., Pinero et al., 2013). Marine sedimentary methane can enter the deep ocean via seepage, which forms cold seeps, pockmarks, and mud volcanoes at the seafloor.

In marine sediments, temperature is deeply intertwined with mechanisms of methane production. In relatively shallow sediments and low temperatures (typically < 60°C), methane forms as a byproduct of microbially mediated organic matter degradation (e.g., Rice and Claypool, 1981). Additionally, microbial biodegradation of oil has been considered a prominent source of methane production at temperatures up to 80 to 90°C (e.g., Head et al., 2003; Wilhelms et al., 2001). Methane can also form from the heating of large organic molecules at temperatures as low as 60°C, although peak thermogenic methane generation typically occurs at ca. 160°C (Hunt, 1996). While different production mechanisms are predominant in different temperature ranges, these temperatures do not necessarily reflect the absolute limits at which these processes can occur, and further, these methane production processes often co-occur in marine sediments.

The largest surface source of methane is from the sediments of wetlands and inland waters (95 to 205 Tg/yr) (Saunois et al., 2020). Methane formed in lakebeds can diffuse into the water column where it is mostly consumed by aerobic methanotrophy, an important biofilter that regulated the global methane budget. Alternatively, if methane concentrations are greater than saturation, methane can form bubbles and quickly rise through the water column to the atmosphere (i.e., ebullition).

Characterizing methane is important to assess the sources of accumulations and contributes to understanding the ecosystems in which microbes actively metabolize organic matter and mediate biogeochemical cycles.

1.2 METHANE ISOTOPOLOGUES

"Isotopologues" are compounds that have the same chemical structure, but differ in the isotopes of one or more atoms. The four most abundant isotopologues of methane are $^{12}CH_4$, $^{13}CH_4$, $^{12}CH_3D$, and $^{13}CH_3D$.

All isotopologue measurements presented in this thesis are made using a Tunable Infrared Laser Direct Absorption Spectroscopy (TILDAS) instrument at MIT (Ono et al., 2014). Other techniques used for methane clumped isotopologue measurements includes isotope ratio mass

spectrometry for Δ_{18}, which is the combined abundance of $^{13}CH_3D$ and $^{12}CH_2D_2$ (Stolper et al., 2014a). Additionally, a double-focusing large-radius isotope ratio mass spectrometry instrument (the Nu Instruments Panorama) has been developed to resolve $^{13}CH_3D$ and $^{12}CH_2D_2$ (Young et al., 2016). One benefit of the Panorama instrument is that $^{12}CH_2D_2$ can be resolved using smaller sample sizes than what is required with laser spectroscopy (ca. 3 mL vs 20 mL CH_4 at lab temperature and pressure) (Gonzalez et al., 2019). Benefits of laser spectroscopy include the relatively shorter measurement time (ca. 2 hrs vs 24 hrs), and that the method is non-destructive to the methane samples.

The metric $\Delta^{13}CH_3D$ quantifies the deviation of isotopologue abundances from a random distribution among the four most abundant isotopologues.

$$\Delta^{13}CH_3D = \ln(Q)$$

Where Q is the reaction quotient from the isotopologue exchange reaction in **Figure 1.2**. $\Delta^{13}CH_3D$ is reported in permil units (‰), or parts per thousand.

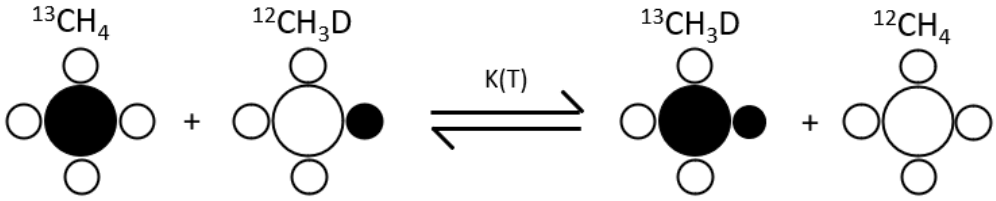

Figure 1.2: Exchange reaction between four isotopologues of methane.

The equilibrium constant (K) of this exchange reaction is dependent on temperature:

$$K(T) = \frac{[^{13}CH_3D][^{12}CH_4]}{[^{12}CH_3D][^{13}CH_4]}$$

Where T is in Kelvin. K approaches unity at high temperatures (>1000 K), but is higher at lower temperatures (e.g., K = 1.006 at 25ºC). The higher abundance of multiply substituted isotopologue, $^{13}CH_3D$ (**Figure 1.3**), comes from a disproportionate lowering of zero-point energy associated with the substitution of two or more heavy isotopes (e.g., Eiler et al., 2007).

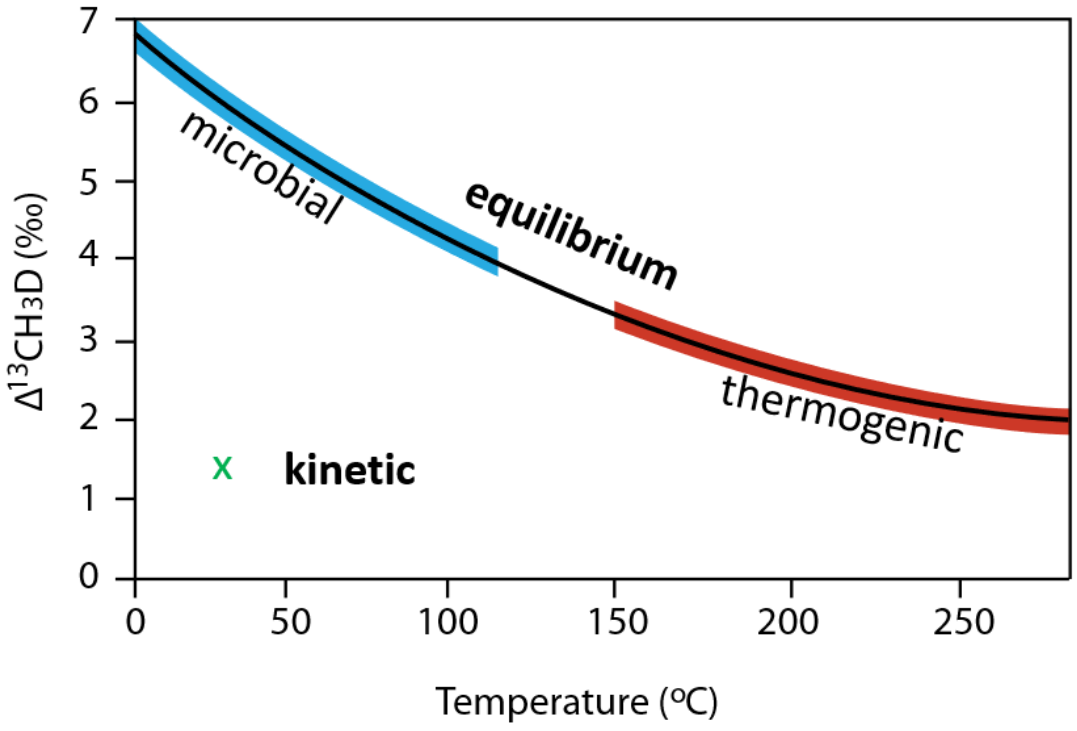

Figure 1.3: The relationship between environmental temperature (in °C) and measured values of $\Delta^{13}CH_3D$ in ‰.

When methane is equilibrated, Q = K. Thus, the temperature of methane equilibration can be precisely measured by quantifying the abundances of $^{12}CH_4$, $^{13}CH_4$, $^{12}CH_3D$, and $^{13}CH_3D$. Isotope-based temperatures are herein referred to as "apparent temperature" due to an inherent assumption about methane equilibrium in their application.

Methane samples from geologic environments demonstrate that this thermometer yields environmentally reasonable temperatures (Stolper et al., 2014a; Stolper et al., 2015; Wang et al., 2015; Young et al., 2017); while methane from lab studies and surface environments is characterized by kinetic isotope fractionations that arise during microbial methane generation (Douglas et al., 2020b, 2016; Gruen et al., 2018; Stolper et al., 2015; Wang et al., 2015; Young et al., 2017).

The mechanisms by which methane isotopologues equilibrate in natural environments is the subject of ongoing research. Proposed mechanisms fall into two broad categories of 1)

microbial and 2) abiotic isotope exchange. Microbially mediated bond reordering has been proposed to occur by the slow rate of microbial methanogenesis in marine sediments favoring higher rates of enzyme reversibility (e.g., Douglas et al., 2020; Wang et al., 2015) or by coupling with anaerobic methane oxidation (e.g., Ash et al., 2019; Giunta et al., 2019; Ono et al., 2021). Both hypotheses suggest that the enzyme, methyl coenzyme M reductase is an important biomolecule. For abiotic bond reordering, D/H exchange between methane and water has been proposed as the prevailing mechanism. This exchange mechanism is thought to be unable to equilibrate methane on geologically relevant timescales below ca. 150°C; however, rates of $^{13}CH_3D/^{12}CH_4$ equilibration are uncharacterized below this temperature. Abiotic bond reordering at temperatures as low as 65°C has been proposed to occur in hydrothermal settings and mediated by mineral catalysis (e.g., Labidi et al., 2020), but this hypothesized process is lacking an exchange mechanism.

1.3 PREVIEW OF THESIS CONTENT

This thesis contributes 1) three studies and one appendix quantifying the natural abundance of methane isotopologues from marine and lacustrine sediments to test assumptions about prevailing mechanisms of methane formation and consumption, and 2) one method development study aimed to improve the quantification of methane in these environments.

Chapter 2 presents a global survey of the abundance of $^{13}CH_3D$ in marine gas hydrate specimen from 11 of the world's most prominent hydrate-bearing regions. We document the link between methane isotopologue-based temperature estimates and key submarine gas hydrate seepage features for the first time. The results from gas hydrates associated with cold seeps, pockmarks, and oil-seeps validate previous models about their geologic driving forces, while methane from mud volcanoes comes from at least two different sources, depending on the tectonic environment.

Chapter 3 reports two novel kilometer-scale profiles of methane isotopologues from marine sediments, representing the transition between microbial and thermal methanogenic zones. Methane isotopologues do not follow two-component mixing between microbial and thermal sources, but rather indicate microbially catalyzed re-equilibration along geothermal gradients up to temperature of 100^{+14}_{-15}°C. This signal may be preserved up until the rate of abiotic exchange becomes comparable to the rate of temperature increase, around 150°C. These

results suggest that methane isotopologue characterization represents a means to trace the upper-temperature limits of microbial activity in hydrocarbon-rich marine sedimentary environments.

Chapter 4 applies the characterization of $^{13}CH_3D$ abundance to ebullition from the sediments of a mid-latitude lake. We produce the largest set of freshwater $\Delta^{13}CH_3D$ values in a single lake basin, which is used to develop a sampling strategy to constrain lake source signatures. The results show that clumped methane isotopologues may yield a means to isotopically differentiate aerobic and anerobic methane oxidation in freshwater environments, but the large variation in $\Delta^{13}CH_3D$ values from a single lake points to the challenge of constraining the total source signal from freshwater lakes.

Chapter 5 documents the development of a method to extract and quantify dissolved gases in sediment porewaters to determine *in situ* methane concentration from gas-rich sediments. This method is tested using surface sediments from hydrocarbon seeps, and results are compared to those from four other methods of methane quantification. The results show that volumes of gas components match predictions from air-equilibrated water (N_2 and Ar) and standard headspace analysis (CH_4), but dissolved gases in porewater experience additional alteration between void gas formation and sample processing. The functionality of this method is additionally limited by unreliable accounting of air-contamination, as O_2 reacts quickly in reduced sediment.

Appendix A provides details on initial efforts to characterize methane isotopologue abundances from the 1.2 km of sediment core collected during IODP expedition 370.

Prior to the start of this thesis, no work had been published on clumped methane isotopologue values of marine gas hydrates (the topic of **chapter 2**), and no work had been published on clumped methane isotopologue values through deep profiles of marine sediment (the topic of **chapter 3** and **appendix A**). Additionally, while measurements from freshwater lakes have been published (Douglas et al., 2020; Douglas et al., 2016; Wang et al., 2015), there was previously no in-depth survey of methane isotopologue variation within a single lake system (the topic of **chapter 4**). Thus, the contents of this thesis fill several large information gaps in the use of clumped methane isotopologues as a biogeochemical tracer.

1.4 REFERENCES

Bruhwiler, L., Michalak, Anna, M., Birdsey, R., Fischer, J.B., Houghton, R.A., Huntzinger, D.N., Miller, J.B., 2018. Overview of the Global Carbon Cycle, in: Cavallaro, N., Shrestha, G., Birdsey, R., Mayes, M.A., Najjar, R.G., Reed, S.C., Romero-Lankao, P., Zhu, Z. (Eds.), Second State of the Carbon Cycle Report (SOCCR2): A Sustained Assessment Report. U.S. Global Change Research Program, Washington, D.C., pp. 1–29.

Douglas, P.M.J., Gonzalez Moguel, R., Walter Anthony, K.M., Wik, M., Crill, P.M., Dawson, K.S., Smith, D.A., Yanay, E., Lloyd, M.K., Stolper, D.A., Eiler, J.M., Sessions, A.L., 2020. Clumped isotopes link older carbon substrates with slower rates of methanogenesis in northern lakes. Geophys. Res. Lett. 47, e2019GL086756. https://doi.org/10.1029/2019GL086756

Douglas, P.M.J., Stolper, D.A., Smith, D.A., Walter Anthony, K.M., Paull, C.K., Dallimore, S., Wik, M., Crill, P.M., Winterdahl, M., Eiler, J.M., Sessions, A.L., 2016. Diverse origins of Arctic and Subarctic methane point source emissions identified with multiply-substituted isotopologues. Geochim. Cosmochim. Acta 188, 163–188. https://doi.org/10.1016/j.gca.2016.05.031

Eiler, J.M., 2007. "Clumped-isotope" geochemistry-- The study of naturally occuring, multiply-substituted isotopologues. Earth Planet. Sci. Lett. 262, 309–327.

Gruen, D.S., Wang, D.T., Könneke, M., Topçuoğlu, B.D., Stewart, L.C., Goldhammer, T., Hinrichs, K.U., Ono, S., 2018. Experimental investigation on the controls of clumped isotopologue and hydrogen isotope ratios in microbial methane. Geochim. Cosmochim. Acta 237, 339–356. https://doi.org/10.1016/j.gca.2018.06.029

Head, I.M., Jones, D.M., Larter, S.R., 2003. Biological activity in the deep subsurface and the origin of heavy oil. Nature 426, 344–352. https://doi.org/10.1038/nature02134

Hunt, J., 1996. Petroleum Geochemistry and Geology, second. ed. New York.

Kvenvolden, K.A., 2002. Methane hydrate in the global organic carbon cycle. Terra Nov. 14, 302–306. https://doi.org/10.1046/j.1365-3121.2002.00414.x

Labidi, J., Young, E.D., Giunta, T., Kohl, I.E., Seewald, J., Tang, H., Lilley, M.D., Früh-Green, G.L., 2020. Methane thermometry in deep-sea hydrothermal systems: Evidence for re-ordering of doubly-substituted isotopologues during fluid cooling. Geochim. Cosmochim. Acta 288, 248–261. https://doi.org/10.1016/j.gca.2020.08.013

Milkov, A. V., 2004. Global estimates of hydrate-bound gas in marine sediments: How much is really out there? Earth-Science Rev. 66, 183–197. https://doi.org/10.1016/j.earscirev.2003.11.002

Ono, S., Wang, D.T., Gruen, D.S., Sherwood Lollar, B., Zahniser, M.S., McManus, B.J., Nelson, D.D., 2014. Measurement of a doubly substituted methane isotopologue, $^{13}CH_3D$, by tunable infrared laser direct absorption spectroscopy. Anal. Chem. 86, 6487–6494. https://doi.org/10.1021/ac5010579

Piñero, E., Marquardt, M., Hensen, C., Haeckel, M., Wallmann, K., 2013. Estimation of the

global inventory of methane hydrates in marine sediments using transfer functions. Biogeosciences 10, 959–975. https://doi.org/10.5194/bg-10-959-2013

Rice, D., Claypool, G., 1981. Generation, Accumulation, and Resource Potential of Biogenic Gas. Am. Assoc. Pet. Geol. Bull. 65. https://doi.org/10.1306/2F919765-16CE-11D7-8645000102C1865D

Saunois, M., Stavert, A.R., Poulter, B., Bousquet, P., Canadell, J.G., Jackson, R.B., Raymond, P.A., Dlugokencky, E.J., Houweling, S., Patra, P.K., Ciais, P., Arora, V.K., Bastviken, D., Bergamaschi, P., Blake, D.R., Brailsford, G., Bruhwiler, L., Carlson, K.M., Carrol, M., Castaldi, S., Chandra, N., Crevoisier, C., Crill, P.M., Covey, K., Curry, C.L., Etiope, G., Frankenberg, C., Gedney, N., Hegglin, M.I., Höglund-Isaksson, L., Hugelius, G., Ishizawa, M., Ito, A., Janssens-Maenhout, G., Jensen, K.M., Joos, F., Kleinen, T., Krummel, P.B., Langenfelds, R.L., Laruelle, G.G., Liu, L., Machida, T., Maksyutov, S., McDonald, K.C., McNorton, J., Miller, P.A., Melton, J.R., Morino, I., Müller, J., Murguia-Flores, F., Naik, V., Niwa, Y., Noce, S., O'Doherty, S., Parker, R.J., Peng, C., Peng, S., Peters, G.P., Prigent, C., Prinn, R., Ramonet, M., Regnier, P., Riley, W.J., Rosentreter, J.A., Segers, A., Simpson, I.J., Shi, H., Smith, S.J., Steele, L.P., Thornton, B.F., Tian, H., Tohjima, Y., Tubiello, F.N., Tsuruta, A., Viovy, N., Voulgarakis, A., Weber, T.S., van Weele, M., van der Werf, G.R., Weiss, R.F., Worthy, D., Wunch, D., Yin, Y., Yoshida, Y., Zhang, W., Zhang, Z., Zhao, Y., Zheng, B., Zhu, Q., Zhu, Q., Zhuang, Q., 2020. The Global Methane Budget 2000--2017. Earth Syst. Sci. Data 12, 1561–1623. https://doi.org/10.5194/essd-12-1561-2020

Stolper, D.A., Lawson, M., Davis, C.L., Ferreira, A.A., Santos Neto, E. V., Ellis, G.S., Lewan, M.D., Martini, A.M., Tang, Y., Schoell, M., Sessions, A.L., Eiler, J.M., 2014. Formation temperatures of thermogenic and biogenic methane. Science (80-.). 344, 1500–1503. https://doi.org/10.1126/science.1254509

Stolper, D.A., Martini, A.M., Clog, M., Douglas, P.M., Shusta, S.S., Valentine, D.L., Sessions, A.L., Eiler, J.M., 2015. Distinguishing and understanding thermogenic and biogenic sources of methane using multiply substituted isotopologues. Geochim. Cosmochim. Acta 161, 219–247. https://doi.org/10.1016/j.gca.2015.04.015

Wang, D.T., Gruen, D.S., Sherwood Lollar, B., Hinrichs, K.U., Stewart, L.C., Holden, J.F., Hristov, A.N., Pohlman, J.W., Morrill, P.L., Könneke, M., Delwiche, K.B., Reeves, E.P., Sutcliffe, C.N., Ritter, D.J., Seewald, J.S., McIntosh, J.C., Hemond, H.F., Kubo, M.D., Cardace, D., Hoehler, T.M., Ono, S., 2015. Nonequilibrium clumped isotope signals in microbial methane. Science (80-.). 348, 428–431. https://doi.org/10.1126/science.aaa4326

Wilhelms, A., Larter, S.R., Head, I., Farrimond, P., Di-Primio, R., Zwach, C., 2001. Biodegradation of oil in uplifted basins prevented by deep-burial sterilization. Nature 411, 1034–1037.

Young, E.D., Kohl, I.E., Lollar, B.S., Etiope, G., Rumble, D., Li, S., Haghnegahdar, M.A., Schauble, E.A., McCain, K.A., Foustoukos, D.I., Sutclife, C., Warr, O., Ballentine, C.J., Onstott, T.C., Hosgormez, H., Neubeck, A., Marques, J.M., Pérez-Rodríguez, I., Rowe, A.R., LaRowe, D.E., Magnabosco, C., Yeung, L.Y., Ash, J.L., Bryndzia, L.T., 2017. The relative abundances of resolved $^{12}CH_2D_2$ and $^{13}CH_3D$ and mechanisms controlling isotopic bond ordering in abiotic and biotic methane gases. Geochim. Cosmochim. Acta 203, 235–

264. https://doi.org/10.1016/j.gca.2016.12.041

Young, E.D., Rumble, D., Freedman, P., Mills, M., 2016. A large-radius high-mass-resolution multiple-collector isotope ratio mass spectrometer for analysis of rare isotopologues of O_2, N_2, CH_4 and other gases. Int. J. Mass Spectrom. 401, 1–10. https://doi.org/10.1016/j.ijms.2016.01.006

Chapter 2

Clumped methane isotopologue-based temperature estimates for sources of methane in marine gas hydrates and associated vent gases

ABSTRACT

Gas hydrates stored in the continental margins of the world's oceans represent the largest global reservoir of methane. Determining the source and history of methane from gas hydrate deposits informs the viability of sites as energy resources, and potential hazards from hydrate dissociation or intense methane degassing from ocean warming. Stable isotope ratios of methane ($^{13}C/^{12}C$, D/H) and the molecular ratio of methane over ethane plus propane (C_1/C_{2+3}) have traditionally been applied to infer methane sources, but often yield ambiguous results when two or more sources are mixed, or when compositions are altered by physical (e.g., diffusion) or microbial (e.g., methanotrophy) processes.

We measured the abundance of clumped methane isotopologue ($^{13}CH_3D$) alongside $^{13}C/^{12}C$ and D/H of methane, and C_1/C_{2+3} for 46 submarine gas hydrate specimens and associated vent gases from 11 regions of the world's oceans. These samples are associated with different seafloor seepage features (oil seeps, pockmarks, mud volcanoes, and other cold seeps). The average apparent equilibration temperatures of methane calculated from the $\Delta^{13}CH_3D$ (the excess abundance of $^{13}CH_3D$ relative to the stochastic distribution) geothermometer increase from cold seeps (15 to 65 ℃) and pockmarks (36 to 54 ℃) to oil-associated gas hydrates (48 to 120 ℃). These apparent temperatures are consistent with, or a few tens of degrees higher than, the temperature expected for putative microbial methane sources. Apparent methane generation depths were derived for cold seep, pockmark, and oil seep methane from isotopologue-based temperatures and the local geothermal gradients. Estimated methane generation depths ranged from 0.2 to 5.3 kmbsf, and are largely consistent with source rock information, and other chemical geothermometers based on clay mineralogy and fluid chemistry (e.g., Cl, B, and Li concentrations).

Methane associated with mud volcanoes yielded a wide range of apparent temperatures (15 to 313℃). Gas hydrates from mud volcanoes the Kumano Basin and Mediterranean Sea yielded $\delta^{13}C\text{-}CH_4$ values from -36.9 to -51.0‰, typical for thermogenic sources. $\Delta^{13}CH_3D$ values (3.8 to 6.0‰) from these sites, however, are consistent with prevailing microbial sources. These mud volcanoes are located at active convergent plate margins, where hydrogen may be supplied from basement rocks, and fuel methanogenesis to the point of substrate depletion. In contrast, gas hydrate from mud volcanoes located on km-thick sediments in tectonically less active or passive settings (Black Sea, North Atlantic) yielded microbial-like $\delta^{13}C\text{-}CH_4$ and C_1/C_{2+3} values, and low $\Delta^{13}CH_3D$ values (1.6 to 3.3‰), which may be due to kinetic isotope effects. Additionally, using samples from two sites, we found that $\Delta^{13}CH_3D$ values of hydrate-bound gas and vent gas agree within measurement error. This study is the first to document the link

between methane isotopologue-based temperature estimates and key submarine gas hydrate seepage features, and validate previous models about their geologic driving forces.

A version of this chapter has been published as:

Lalk, E., Pape, T., Gruen, D.S., Kaul, N., Karolewski, J.S., Bohrmann, G. & Ono, S. 2022. Clumped methane isotopologue-based temperature estimates for sources of methane in marine gas hydrates and associated vent gases. Geochim. Cosmochim. Acta 327, 276-297. doi.org/10.1016/j.gca.2022.04.013

2.1 INTRODUCTION

Submarine gas hydrates are one of Earth's largest reservoirs of methane (ca. 550 Gt C), an energy resource and potent greenhouse gas (Piñero et al., 2013; Saunois et al., 2020). Gas hydrates are found close to the seafloor, in anoxic sediments of continental margins. They are stable over a limited range of low-temperature and intermediate-pressure conditions (the gas hydrate stability zone) when pore water is saturated with methane (Dickens and Quinby-Hunt, 1997). These narrow stability conditions can make gas hydrate susceptible to perturbations in temperature (e.g., warming bottom seawater) and hydrostatic pressure (e.g., sea level change) associated with global climate change (Paull et al., 1996; Kennett et al., 2003; Krey et al., 2009; Biastoch et al., 2011). Release of methane from hydrates has been hypothesized as a possible cause of abrupt climate change, relevant both in the present day and during the Paleocene-Eocene Thermal Maximum (Dickens, 2011; Whiteman et al., 2013). Understanding the process(es) and environment of methane generation may yield information that would help assess the productivity of the source, capacity of the reservoir, and the probability of hazards, including the risk of hydrate dissociation and intense methane degassing due to ocean warming.

Gas hydrates may contain light hydrocarbons from microbial, thermogenic, or a mixture of these sources. In marine sedimentary environments, methane and other light hydrocarbons can be produced by thermal breakdown of large organic molecules or microbial methanogenesis via organic matter decomposition. Thermal methanogenesis typically occurs at high temperatures (peak generation ≈ 160 °C) and greater than ca. 5 kilometers sediment depth (e.g., Seewald, 2003; Stolper et al., 2014), but onset may occur at temperatures as low as 60 to 120 °C (Hunt 1996). Primary microbial methane production from the reduction of CO_2 by H_2 or disproportionation of acetate, occurs at lower temperatures (typically below 60 °C) and generally less than 2 km below seafloor (kmbsf) (e.g., Inagaki et al., 2015). Secondary microbial methane production via the biodegradation of oil can proceed at temperatures higher than typical primary microbial methanogenesis (up to 80 °C) (Wilhelms et al., 2001; Head et al., 2003). Additionally, methane can be formed abiotically during water-rock reactions of seafloor basement rocks, although this is considered to be a minor contribution to the marine sedimentary methane pool (e.g., Klein et al., 2019; McDermott et al., 2015).

The carbon ($^{13}C/^{12}C$) and hydrogen (D/H) stable isotope ratios and the ratio of methane to ethane and propane (C_1/C_{2+3}), are often applied to infer the source of methane (e.g., Bernard et al., 1976; Whiticar, 1999; Milkov and Etiope, 2018). However, source identification can be obscured by overlaps in geochemical fields. Typical microbial methane has $\delta^{13}C\text{-}CH_4$ values less than -50‰, but thermogenic methane may have $\delta^{13}C\text{-}CH_4$ values from -70 to -20‰ (**Figure 3**). Similarly, microbial gas is expected to have C_1/C_{2+3} values greater than 100, but microbial gas produced by oil biodegradation (termed 'secondary microbial gas') may have C_1/C_{2+3} values less than 10. Thermogenic gas is expected to have C_1/C_{2+3} values less than 100, but late maturity thermogenic gas has been observed with C_1/C_{2+3} values over 1000 (**Figure 3**). Nevertheless, the application of these geochemical proxies to hydrate samples has shown that gas hydrates are largely archives of microbially produced methane (Milkov, 2005; Bohrmann and Torres, 2006; You et al., 2019).

Several microbial and physical processes can fractionate the isotopic composition of methane and relative alkane composition of gas, obscuring source identification. In anoxic sediments, dissolved methane can be oxidized by consortia of bacteria and archaea, in a process known as anaerobic oxidation of methane (AOM) (Barnes and Goldberg, 1976; Reeburgh, 1976). Laboratory culture studies showed AOM may leave the methane pool enriched in ^{13}C, D, and $^{13}CH_3D$ (e.g., Holler et al., 2009; Ono et al., 2021). However, inference from natural settings suggests that AOM may promote isotope exchange, leaving residual methane with equilibrium isotopologue compositions (e.g., Yoshinaga et al., 2014; Ash et al., 2019; Giunta et al., 2019; Young et al., 2019; Zhang et al., 2021). Additionally, methane produced from oil biodegradation ('secondary microbial methane') is relatively enriched in ^{13}C compared to methane from primary methanogenesis (Valentine et al., 2004; Milkov and Dzou, 2007). Physical processes, including diffusion and migration, can fractionate isotope and gas compositions and has explained compositions of natural gas that do not follow simple mixing trends in $\delta^{13}C$ and C_1/C_{2+3} diagrams (Prinzhofer and Pernaton, 1997). Diffusion fractionation of isotopes and relative chemical composition of alkanes is expected to occur as a function of mass, such that lighter isotopes and lighter alkanes are transported more quickly than their heavy counterparts. Thus, it is expected that the values of $^{13}C\text{-}CH_4$ and $D\text{-}CH_4$ for a diffused gas are depleted relative to its source, while C_1/C_{2+3} is relatively enriched (Prinzhofer and Pernaton, 1997; Zhang and Krooss, 2001).

Clumped methane isotopologue analysis is a technique developed in the 2010s in which the abundances of isotopologues of methane ($^{12}CH_4$, $^{13}CH_4$, $^{12}CH_3D$, $^{13}CH_3D$, and $^{12}CH_2D_2$) are quantified relative to that expected for a random distribution of isotopes among methane molecules (Ono et al., 2014; Stolper et al., 2014; Young et al., 2017; Gonzalez et al., 2019). This measurement can reveal information about methane formation and alteration processes, and the temperature at which methane formed can be inferred assuming the methane is in thermodynamic equilibrium and has not re-equilibrated since its formation.

Clumped isotopologue analysis has previously been applied to hydrate-bound methane from Hydrate Ridge on the Cascadia Margin, Kumano Basin mud volcano #5, as well as five sites from the Japan Sea (Wang et al., 2015; Ijiri et al., 2018b; Zhang et al., 2021). Samples from Hydrate Ridge and the Kumano forearc basin yielded apparent temperatures from the clumped methane geothermometer of ca. 10 to 40 ℃, consistent with a relatively shallow microbial source. Samples from the Japan Sea presented apparent temperatures ranging from 15 to 170 ℃, which were used to constrain the proportions of microbial and thermogenic methane sources, assuming microbial methane is equilibrated at near-seafloor temperatures by AOM (Zhang et. al., 2021). Several hydrate deposits with ambiguous geochemical signatures have been documented (e.g., Graves et al., 2017; Pape et al., 2020); therefore, apparent temperature from clumped isotopologue analysis has the potential to constrain the origin and geochemical history of hydrate deposits.

The apparent temperature of equilibrium can be a useful geothermometer if methane was generated under isotopologue equilibrium or equilibrated later, not by kinetically controlled processes. Laboratory experiments yield disequilibrium signatures for microbial generation (e.g., Stolper et al., 2015; Wang et al., 2015; Douglas et al., 2016; Gruen et al., 2018) as well as thermal and abiotic generation (e.g., Shaui et al., 2018; Dong et al., 2021). Methane in marine sedimentary basins often shows carbon and hydrogen isotope equilibrium between CO_2 and H_2O, respectively (e.g., Meister et al., 2019; Pape et al., 2021; Turner et al. 2021). Similarly, environmentally reasonable temperatures have been observed for both thermogenic and microbial methane found in marine sedimentary basins (Stolper et al., 2014; Wang et al., 2015; Douglas et al., 2017; Stolper et al., 2017; Ash et al., 2019; Giunta et al., 2019; Douglas et al., 2020b; Thiagarajan et al., 2020). Microbial methane is expected to produce near-equilibrium

methane under energy-limitation (Valentine et al., 2004; Ono et al., 2022), and abiotic catalysis may be geologically fast enough to equilibrate methane for high maturity thermogenic gas. Measurements of natural samples, however, showed that kinetic fractionation dominates the methane isotopologue signature of surface reservoirs, including wetlands, freshwater bodies, and rudiments (e.g., Wang et al., 2015). Further, kinetic methane isotopologue signals were observed for low maturity thermogenic gases, whereas high maturity thermogenic gases tend to show equilibrium signals. (Xie et al., 2021). Measurements of $^{12}CH_2D_2$, in addition to $^{13}CH_3D$, can be used to assess whether methane is internally equilibrated, or carries a kinetic (disequilibrium) signal, although mixing of methane sources may complicate the interpretations (e.g., Zhang et al., 2021; Giunta et al., 2021). Whether methane isotopologues indicate the temperature of generation or post-generation equilibration is currently debated (e.g., Okumura et al., 2016; Turner et al., 2021).

The presence of gas hydrates in near seafloor sediments is often associated with methane-rich fluid seepage (e.g., You et al., 2019). Submarine gas hydrates can be categorized by their fluid and gas chemistry or venting structure morphology. Physical seafloor expressions include pockmarks, mud volcanoes, and other cold seeps. Cold seeps are widely distributed on the seafloor along continental margins (e.g., Suess, 2014), and are the primary conduit for methane transport from the lithosphere to the hydrosphere. Seepage often occurs over fissures in the seafloor caused by tectonic activity, but can also occur along passive continental margins. Authigenic carbonate formation resulting from AOM can alter seafloor topography over time at these sites (Bohrmann et al., 1998). Cold seeps are a unique biome, harboring complex primary and secondary microbial communities where anaerobic methanotrophs play the role of primary producers (Orphan et al., 2002; Levin, 2005). Pockmarks are (sub-) circular seafloor depressions that are usually related to intense focused migration of fluids with typically limited number of emission sites. They can be caused by sediment removal, high gas flux in a confined seafloor area, and often coalescence of several smaller pockmarks (e.g., King and MacLean, 1970; Sahling et al., 2008; Davy et al., 2010; Sultan et al., 2014; Wenau et al., 2017). Pockmarks occasionally reach hundreds of meters in diameters (called giant pockmarks). Mud volcanoes are geologic features formed from localized outflow of sediments and warm fluids that have been mobilized from depth (Milkov, 2000; Dimitrov, 2002; Kopf, 2002; Kaul et al., 2006). Some mud volcanoes are rooted as deeply as several kilometers within the sediment column, where

thermogenic methane may be produced. Most mud volcanoes are located in compressional forearc basins (Kopf, 2002; Milkov, 2004).

Some methane seepages are associated with oil. Oil seeps are sites where natural gaseous and liquid hydrocarbons escape from oil-bearing deposits. Oil is thought to form in sediments at temperatures of ca. 100-150 ºC, thus oil associated hydrates are expected to be connected to a deeper, higher temperature environment, and reflect a prevailing thermogenic source (Hunt, 1996). Secondary methane formation from microbial oil biodegradation can occur at temperatures as high as 80 ºC (Wilhelms et al., 2001; Head et al., 2003), which can be incorporated into the gas hydrate reservoir within the hydrate stability zone.

In this study, we analyzed isotopologue ($\Delta^{13}CH_3D$, $\delta^{13}C$-CH_4, δD-CH_4) and hydrocarbon (C_1/C_{2+3}) compositions for 46 submarine gas hydrates and associated vent gases from 11 regions of the world's oceans to investigate origins of methane bound in hydrates and present in associated vent gas from different types of hydrocarbon seepage. We used clumped methane isotopologue geothermometry to add temperature ranges to the different geologic processes that result in submarine gas hydrate deposits and compare them to previous models for seepage driving forces and methane origin. These data were also used to resolve origins of light hydrocarbons for sites that were previously considered ambiguous. Apparent temperatures from clumped isotopologue data, along with site specific geothermal gradients were used to estimate the depth at which methane was formed. The estimated source depth was compared with information from source rock biomarkers and chemical geothermometers based on clay mineralogy and fluid chemistry to assess the depth of hydrocarbon generation.

1.3 MATERIALS AND METHODS

Submarine gas hydrate samples and associated vent gases were collected from the Cascadia Margin, the Gulf of Mexico, the North Atlantic, the Mediterranean Sea, the Gulf of Guinea, the Congo Fan, the Black Sea, the Makran Accretionary Prism (south of Pakistan) and the Kumano Basin (**Figure 1**). Hydrate-bound gas was collected using the MARUM-MeBo (Freudenthal and Wefer, 2013) drill rig and gravity corers. Vent gases were collected using the Gas Bubble Samplers (Pape et al., 2010a). One sedimentary gas from Venere mud volcano in the Mediterranean Sea was collected using the Dynamic Autoclave Piston Corer (Pape et al., 2010a).

There were 20 samples from 11 cold seep sites, 5 samples from 5 pockmark sites, 9 samples from 4 oil-associated sites, and 12 samples from 8 mud volcanoes (**Table 2.1**).

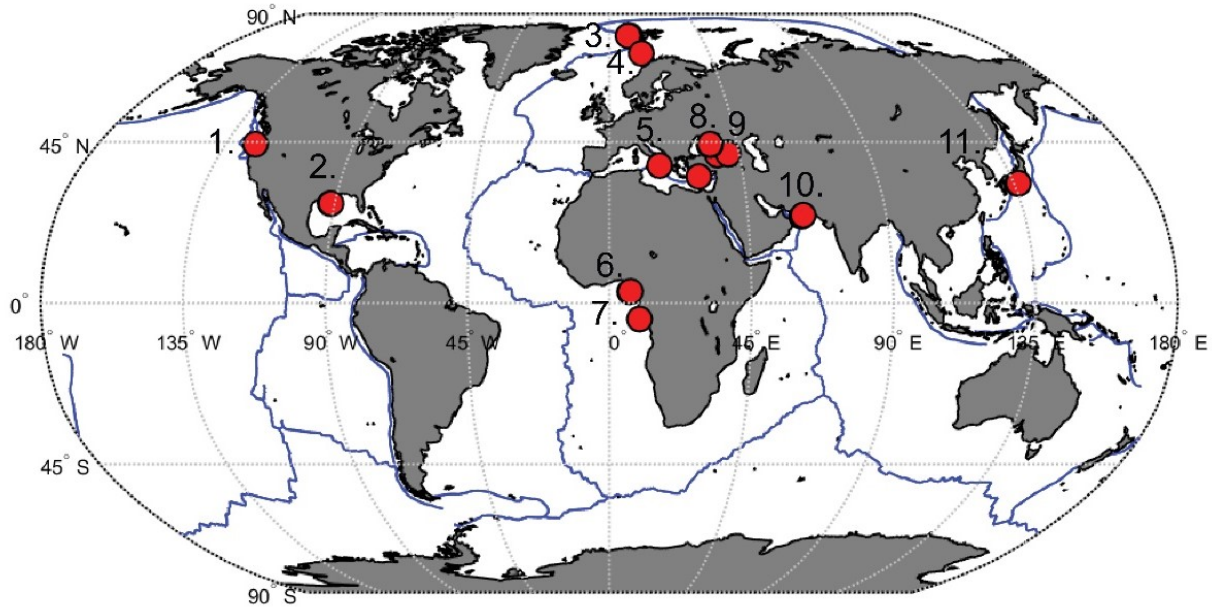

1. Cascadia Margin
2. Gulf of Mexico
3. North Atlantic, W. of Spitsbergen
4. North Atlantic, Barents Sea
5. Mediterranean Sea
6. West of Africa, Gulf of Guinea
7. West of Africa, Congo Fan
8. Northern Black Sea
9. Eastern Black Sea
10. South of Pakistan
11. Kumano Basin

Figure 2.1: Sample site locations. Continental plate boundaries are shown in dark blue.

2.1 Site descriptions

Cascadia Margin: Cascadia Margin is a convergent boundary between the Juan de Fuca and North American plates in the northeast Pacific Ocean. Hydrate Ridge is a morphological high, located at ca. 750 to 900 m water depth, and a site of extensive hydrate deposits underlain by free-gas containing sediments (e.g., Suess et al., 1999).

Gulf of Mexico: Bush Hill is a hydrate mound located in the northern Gulf of Mexico at ca. 570 m water depth, and characterized by oil and gas seepage. This site is approximately 500 m wide and 40 m high, with fluid migrating along two antithetic faults from depth (MacDonald et al., 1994; Vardaro et al., 2006). Hydrate and vent gas at this site has a thermogenic source tied to hydrocarbons from Jurassic-aged source rocks and stored in the Jolliet reservoir at ca. 1.7 to 3.1 kmbsf (Sassen et al., 2001).

North Atlantic W. of Spitsbergen: The West Spitsbergen continental margin is formed of glacial sediments from the advance and retreat of the Svalbard-Barents Sea ice sheet overlying marine sediments. Samples from this region are vent gases. Area 1 is at a water depth of ca. 90 m, Area 2 is at a water depth of ca. 240 m, and Area 3 is at a water depth of ca. 400 m (Sahling et al., 2014).

North Atlantic Barents Sea: The continental slope of the Barents Sea has a 6 km thick sediment column of largely glacial marine sediments. Håkon Mosby mud volcano is about 1 km^2 in area, and located at ca. 1250 m water depth (Kaul et al., 2006; Pape et al., 2011a). Unlike most other mud volcanoes, the Håkon Mosby mud volcano is not associated with plate subduction or salt tectonics. Formation of over-pressurized fluids may coincide with past submarine landslides and fluids are expected to rise from 2 to 3 km through a central conduit (Vogt et al., 1997).

Mediterranean Sea: The Calabrian accretionary prism in the central Mediterranean Sea is formed from the subduction of the African plate below the Eurasian plate. Over 50 mud volcanoes have been identified in this region. Venere mud volcano is located at a water depth of 1600 m and is a site of active gas emissions (Loher et al., 2018). The Anaximander Mountains in the eastern Mediterranean Sea is host to Thessaloniki mud volcano, at 1260 m water depth. The Anaximander Mountains are situated at the junction of the African Plate with the Aegean and Anatolian microplates, causing complex deformation (ten Veen et al., 2004).

West of Africa Gulf of Guinea: A pockmark field is located on the passive continental margin west of Africa, which is slowly deforming by gravity tectonism from sediment loading and seaward progradation (Damuth, 1994; Cohen and McClay, 1996). The pockmark field lies at water depths between 1140 and 1200 m (Sultan et al., 2014).

West of Africa Congo Fan: The western African passive continental margin in the Congo Basin is a known methane-rich seep area with pockmarks occurring from the shelf to deep basins. This region is characterized by 2 to 3 km of terrigenous sediment overlaying Cretaceous shales and large accumulations of evaporites, forming compressional structures and faulting (György Marton et al., 2000). Pockmarks included in this study are located at water depths around 3100 m.

Northern Black Sea: The Sorokin Trough, in the northern Black Sea off the Crimean Peninsula, is considered a foredeep basin characterized by diapirs formed from compressive deformation of the Shatsky Ridge and Tetyaev Rise (Krastel et al., 2003; Sheremet et al., 2016). Over-pressurized fluids from this compressive environment and associated faults form the mud volcanoes observed in this region. These mud volcanoes are located at water depths of ca. 2050 m (Sahling et al., 2009). The Kerch seep area is located northeast of the Sorokin Trough at a water depth of ca. 900 m (Römer et al., 2012).

Eastern Black Sea: The eastern Black Sea on the continental slope off Georgia is characterized by a system of ridges formed by active compressional deformation (Meredith and Egan, 2002). Oil-associated hydrate sites in this locality include Pechori Mound, Iberia Mound, and Colkheti Seep, located at water depths of ca. 850 to 1500 m (Pape et al., 2011a; Reitz et al., 2011; Körber et al., 2014; Pape et al., 2021). Sources of thermogenic methane in this region may include the clay-rich Maikop Group, which is dated to the late Oligocene to early Miocene, and considered one of the most significant hydrocarbon source rocks in this region of the Black Sea (Robinson et al., 1996) and/or the Middle Eocene Kuma Formation (e.g., Boote et al., 2018; Sachsenhofer et al., 2018; Vincent and Kaye, 2018).

South of Pakistan: The Makran Accretionary prism, south of Pakistan is a convergent plate boundary between Arabian and Eurasian plates, overlain with 6 to7 km thick sediments (White, 1983). Samples are from cold seep sites at water depths of ca. 1000 m (Römer et al., 2012; Fischer et al., 2013).

Kumano Basin: The Kumano forearc basin within the Nankai accretionary wedge is an active convergent plate boundary where the Philippine Sea plate subducts under the Eurasian plate. Mud volcanoes within this basin lay on the forearc basin sediments, but extruding fluids may

come from the sediments in the underlying accretionary prism or basement (Ijiri et al., 2018b). Mud volcanoes in this study are located at water depths 1800-2000 m (Pape et. al., 2014).

2.2 Methods

2.2.1 Gas Chromatographic Analysis

The molecular compositions of light hydrocarbons (C_1/C_{2+3}) were taken from previous studies when available (Sahling et al., 2008; Sahling et al., 2009; Pape et al., 2011b; Pape et al., 2011a; Reitz et al., 2011; Römer et al., 2012; Fischer et al., 2013; Körber et al., 2014; Pape et al., 2014; Sahling et al., 2014; Sultan et al., 2014; Wei et al., 2015), or otherwise analyzed by gas chromatography (GC) at MIT, using a flame ionization detector to quantify C_1-C_3 hydrocarbon gases. The GC was equipped with a 10 feet long column packed with HayeSep-Q (VICI), and operated at a temperature of 90°C, where helium served as the carrier gas. Duplicate measurements were made for each sample and calibrated by reference gas mixtures (SCOTTY®).

2.2.2 Clumped Isotopologue Analysis

The abundances of four isotopologues of methane ($^{12}CH_4$, $^{13}CH_4$, $^{12}CH_3D$, and $^{13}CH_3D$) were quantified using a Tunable Infrared Laser Direct Absorption Spectroscopy (TILDAS) instrument (Ono et al., 2014). Methane gas was first purified from hydrate and seep gas subsamples using an automated preparative GC system, previously described by Wang et al., 2015. For most analyses, between 6 and 12 mL STP of methane was used. Measurements made using TILDAS give the abundances of the four methane isotopologues relative to a reference gas. Each measurement run consists of 7 to 9 acquisition cycles (one sample-standard pair).

In order to determine the value of $\Delta^{13}CH_3D$ of a sample relative to the stochastic distribution, the $\Delta^{13}CH_3D$ value of the reference gas (commercially sourced methane, "AL1", from Airgas) is required. Calibration of the reference gas was achieved by heating AL1 in flame-sealed glass tubes in the presence of a platinum catalyst between 150°C and 400°C, as described by Ono et al. (2014). Stable isotope ratios of carbon and hydrogen ($\delta^{13}C$-CH_4 and δD-CH_4) are reported using standard delta notation against Vienna Pee Dee Belemnite (VPDB) and Vienna Standard Mean Ocean Water (VSMOW) for the ratios $^{13}C/^{12}C$ and D/H, respectively.

$$\delta^{13}C = \frac{\left(\frac{^{13}C}{^{12}C}\right)_{sample}}{\left(\frac{^{13}C}{^{12}C}\right)_{VPDB}} - 1 \qquad (1) \qquad \delta D = \frac{\left(\frac{D}{H}\right)_{sample}}{\left(\frac{D}{H}\right)_{VSMOW}} - 1 \qquad (2.2)$$

These values are reported in per mil (‰) units. The isotope scale was calibrated by the measurements of IAEA reference standards NGS-1 and NGS-3 (Wang et al., 2015).

The values of $\delta^{13}C$-CH_4 and δD-CH_4 in this study have been derived from the measurements of isotopologue absorptions. Ratios of isotopologues are transposable with ratios of isotopes such that $^{13}C/^{12}C$ is sufficiently equivalent to $[^{13}CH_4/^{12}CH_4]$ and D/H is sufficiently equivalent to ¼ $[^{12}CH_3D/^{12}CH_4]$. $\delta^{13}C$-CH_3 values determined by TILDAS in this study are similar to those determined on the same samples using isotope mass spectrometers in previous studies.

Methane isotopologue thermometry for doubly substituted isotopologue, $^{13}CH_3D$, is based on the following isotopologue exchange reaction:

$$^{13}CH_4 + {}^{12}CH_3D \leftrightarrow {}^{13}CH_3D + {}^{12}CH_4 \qquad (2.3)$$

$\Delta^{13}CH_3D$ is reported in per mil (‰) units, and represents the deviation of multiply substituted isotopologue $^{13}CH_3D$ abundance from that of the stochastic distribution, such that:

$$\Delta^{13}CH_3D = \ln\frac{[^{13}CH_3D][^{12}CH_4]}{[^{13}CH_4][^{12}CH_3D]} \qquad (2.4)$$

The equilibrium constant, *K*, for Eq. 3, is primarily a function of temperature, and apparent temperature of equilibrium in Kelvin can be derived from $\Delta^{13}CH_3D$ values as:

$$\Delta^{13}CH_3D\ (T) = (-0.1101)\left(\frac{1000}{T}\right)^3 + (1.0415)\left(\frac{1000}{T}\right)^2 - (0.5223)\left(\frac{1000}{T}\right) \qquad (2.5)$$

Calculated temperatures are herein referred to as 'apparent temperatures' (T_{13D}) because of an inherent assumption of equilibrium in the application of the geothermometer (Bigeleisen and Mayer, 1947; Urey, 1947). The temperature dependence for the value of $\Delta^{13}CH_3D$ (**Equation 2.5**) yields slightly different results from recent experimental calibration by Eldridge and colleagues (Webb and Miller, 2014; Wang et al., 2015; Liu and Liu, 2016; Eldridge et al., 2019). This will affect both the reported $\Delta^{13}CH_3D$ values and apparent temperatures (T_{13D}), but calibration uncertainty for $\Delta^{13}CH_3D$ values is less than the 95% confidence interval of our measurements (<0.1‰ vs ca. 0.2‰) and is not expected to significantly alter our results. Both

approaches yield T_{13D} consistent within 1.5-4.0 °C, where the calibration using **Equation 2.5** results in slightly higher apparent temperatures (T_{13D}).

2.2.3 Calculation of Geothermal Gradients

Background geothermal gradients for sites are estimated from the International Heatflow Comission Global Heat Flow Database (Fuchs et al., 2021). We extracted geothermal gradient data for a 25 km radius around sample sites, then filtered out measurements taken on hotspots. For the Kumano Basin, North Atlantic, West of Spitsbergen, and Bush Hill, insufficient data was available from the heat flow database, so datasets from other sources (Labails et al., 2007; Hamamoto et al., 2012; Riedel et al., 2018) were used. The median and standard error of the median were calculated to estimate the representative background geothermal gradient. The derived geothermal gradients and their errors are shown in **Table 2.S1**, and extracted geothermal gradient data can be found in **Table 2.S2**. We are aware of uncertainty in using linear depth extrapolation of geothermal gradients from near-surface sediments; we apply this approach in the absence of more precise temperature data from deep sediments at study sites.

2.3 RESULTS

Results from isotopologue analyses and C_1/C_{2+3} values are summarized in **Table 2.1**. Samples from proximal sites cluster together as expected for gases from the same source. At sites where vent gases and hydrate-bound gases were measured in close proximity (e.g., Helgoland mud volcano and Batumi seep area), isotopologue and hydrocarbon compositions are similar. At these sites, the difference between $\Delta^{13}CH_3D$ values of hydrate-bound and vent gases is 0.18‰ and 0.11‰, respectively, which is within analytical error.

Samples analyzed in this survey yielded $\Delta^{13}CH_3D$ values between 1.5 and 6.0‰, corresponding to apparent temperatures (T_{13D}) from 300 °C to 15 °C (**Figure 2.2**). Methane samples associated with pockmark and cold seep features have $\Delta^{13}CH_3D$ values greater than 4.5‰ (T_{13D} < 80 °C). Methane samples associated with oil seepage generally have lower $\Delta^{13}CH_3D$ values than samples from cold seeps and pockmarks, between 3.5 to 5.1‰ (T_{13D} ca. 50 °C to 120 °C). Methane from mud volcanoes spans the full range of $\Delta^{13}CH_3D$ values measured in this survey from 1.5 and 6.0‰ (T_{13D} ca. 10 °C to 315 °C) (**Figure 2.2**).

Region	Sample ID	Site	Gas Type	Feature	C_1/C_{2+}	$\delta^{13}C$ (‰)	95% CI	δD (‰)	95% CI	$\Delta^{13}CH_3D$ (‰)	95% CI	T_{13D} (°C)	+ (°C)	- (°C)
Cascadia Marg	SO148-1	Hydrate Ridge	hydrated	CS	2231*	-67.94	0.03	-189.19	0.04	5.92	0.2	18	6	6
	SO148-2	Hydrate Ridge	hydrated	CS	2786*	-67.66	0.15	-190.11	0.12	5.44	0.53	34	19	17
Gulf of Mexi	SO174-1	Bush Hill	hydrated	OA	7.79*	-45.48	0.05	-194.05	0.05	3.6	0.26	115	16	14
	SO174-2	Bush Hill	hydrated	OA	7.10*	-45.44	0.04	-193.87	0.09	3.56	0.16	118	10	9
North Atlantic, West of Spitsbergen	16807-2	Area 1	vent	CS	6,363	-42.94	0.06	-182.93	0.06	3.32	0.26	132	18	16
	16823-2	Area 2	vent	CS	7,497	-55.08	0.11	-186.57	0.05	5.76	0.31	23	10	10
	16823-5	Area 2	vent	CS	7,418	-55.02	0.05	-186.98	0.15	5.91	0.4	19	13	12
	16833-2	Area 3	vent	CS	7,748	-53.01	0.11	-186.07	0.08	5.9	0.33	19	11	10
	16833-3	Area 3	vent	CS	8,385	-56.85	0.05	-186.28	0.06	6.03	0.12	15	4	4
	16848-2	Area 4	vent	CS	9,028	-55.7	0.05	-187.44	0.06	5.8	0.31	22	10	10
North Atlantic, Barents	PS70-94-1	Haakon Mosby MV	hydrated	MV	4,563*	-63.61	0.59	-219.62	0.13	1.88	0.59	264	98	65
	PS70-110-1	Haakon Mosby MV	hydrated	MV	5,082*	-63.77	0.11	-221.83	0.15	1.55	0.65	313	151	88
Mediterranean Sea	17908-1	Thessalonkiki MV	hydrated	MV	2772*	-50.94	0.07	-169.56	0.16	5.33	0.67	38	26	22
	19224-3	Venere MV Flare 1	vent	MV	1843	-48.06	0.08	-180.2	0.14	6.04	0.59	15	19	17
	19240-2	Venere MV Flare 5	vent	MV	1175	-47.24	0.08	-180.49	0.1	5.84	0.42	21	14	13
	19251-1	Venere MV western summit	sedimentary	MV	111	-38.86	0.05	-145.47	0.1	4.78	0.35	59	15	14
West of Afric	16022-1	Pockmark A	hydrated	PM	8,443	-51.97	0.07	-176	0.1	4.9	0.09	54	4	3
	16016-1	Pockmark C1	hydrated	PM	6,467	-53.39	0.06	-176.06	0.1	5.37	0.53	36	20	17
West of Africa, Congo	13114-3	Hydrate Hole	hydrated	PM	1,988	-71.36	0.07	-180.72	0.18	5.3	0.23	39	8	8
	13115-1	Baboon Hole	hydrated	PM	1,638	-71.08	0.02	-183.88	0.21	5.05	0.34	48	13	12
	13118-1	Worm Hole	hydrated	PM	1,419	-71.72	0.06	-183.24	0.22	4.9	0.47	54	19	17
Northern Black Sea	11913	Vodyanitskii MV	hydrated	MV	2,018	-61.14	0.07	-209.48	0.05	2.74	0.12	174	10	10
	15525-1	Helgoland MV	hydrated	MV	3,054	-62.47	0.08	-213.61	0.07	3.27	0.28	136	19	17
	14339-3	Helgoland MV	vent	MV	2,257	-61.64	0.05	-212.39	0.06	3.09	0.31	148	23	20
	15518	Kerch Flare	hydrated	CS	2,498	-69.88	0.06	-245.44	0.04	4.69	0.12	62	5	5
Eastern Black Sea	15260	Batumi seep area	hydrated	CS	4,178	-52.35	0.09	-207.45	0.18	4.97	0.18	51	7	7
	11907	Batumi seep area	vent	CS	5,383	-52.85	0.06	-209.63	0.18	4.86	0.13	55	5	5
	11921-1	Batumi seep area	vent	CS	4,631	-52.5	0.06	-209.1	0.16	4.93	0.38	53	16	14
	11971	Colkheti Seep	hydrated	OA	32	-48.8	0.08	-196.08	0.08	4.64	0.24	64	10	10
	11938	Iberia Mound	hydrated	OA	2,090	-48.12	0.04	-214.21	0.19	4.99	0.3	50	12	11
	15268-1	Ordu ridge patch#02	hydrated	CS	3,131	-71.22	0.04	-219.57	0.11	5.48	0.26	33	9	9
	15503-1	Ordu ridge patch#03	hydrated	CS	2,816	-71.37	0.02	-216.72	0.04	4.91	0.13	53	5	5
	15505	Ordu ridge patch#05	hydrated	CS	2,335	-70.58	0.02	-214.01	0.01	5.29	0.08	39	3	3
	15507	Ordu ridge patch#07	hydrated	CS	3,258	-70.67	0.03	-219.61	0.02	5.2	0.09	42	3	3
	15227-3	Pechori Mound-1/23cm	hydrated	OA	n.det.	-48.08	0.15	-208.57	0.22	5.06	0.97	48	42	33
	15227-3	Pechori Mound-1cm	hydrated	OA	87	-48.57	0.09	-211.22	0.2	4.76	0.25	59	10	10
	15227-3	Pechori Mound-5cm	hydrated	OA	310	-48.52	0.09	-212.7	0.18	4.83	0.39	57	16	15
	15227-3	Pechori Mound-7cm	hydrated	OA	694	-51.24	0.02	-212.18	0.13	3.52	0.49	120	32	27
	15227-3	Pechori Mound-9cm	hydrated	OA	914	-49.04	0.06	-211.13	0.02	4.21	0.21	83	10	10
	15244-2	Poti Seep	hydrated	CS	4,153	-54.37	0.14	-209.48	0.06	4.83	0.38	57	16	14
South of Pakistan	12303	Nascent Ridge	hydrated	CS	6,463	-67.17	0.02	-186.68	0.11	5.11	0.37	46	14	13
	12316-3	Flare 2	hydrated	CS	3,632	-70.1	0.03	-194.26	0.05	4.62	0.15	65	6	6
	12316-4	Flare 2	hydrated	CS	6,173	-70.31	0.03	-191.06	0.04	5.11	0.08	46	3	3
Kumano Basin, South of	16716-2	MV10	hydrated	MV	65	-36.9	0.06	-147.67	0.06	3.78	0.25	105	14	13
	16736-2	MV4	hydrated	MV	59	-38.34	0.06	-189.19	0.06	5.36	0.12	37	4	4
	16772	MV2	hydrated	MV	173	-38.88	0.11	-160.72	0.06	4.98	0.32	51	13	12

Table 2.1: Gas geochemistry data. $\delta^{13}C$-CH_4 is in reference to V-PDB, δD-CH_4 is in reference to V-SMOW, *indicates C_1/C_{2+3} values are from this study. Other hydrocarbon ratios are from previous studies (Sahling et al., 2008; Sahling et al., 2009; Pape et al., 2011b; Pape et al., 2011a; Reitz et al., 2011; Römer et al., 2012; Fischer et al., 2013; Körber et al., 2014; Pape et al., 2014; Sahling et al., 2014; Sultan et al., 2014; Wei et al., 2015). All isotope measurements were made

at MIT. CI refers to Confidence Interval. Feature abbreviations are: CS- Cold Seep, PM- Pockmark, OA- Oil-Associated, MV- Mud Volcano.

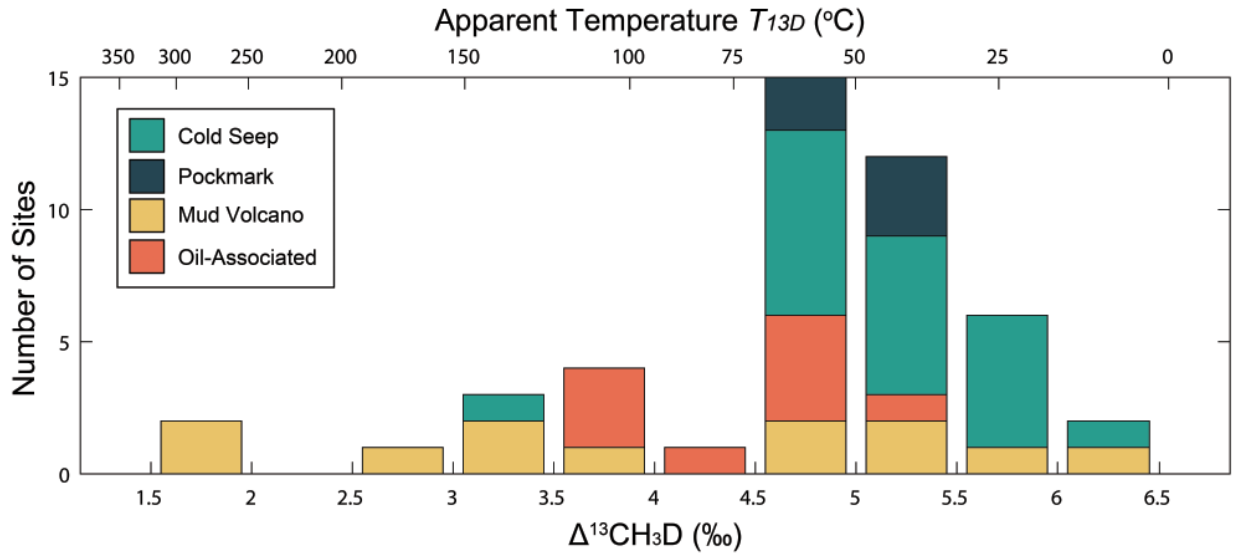

Figure 2.2: Distribution of $\Delta^{13}CH_3D$ values and respective apparent temperatures (T_{13D}) for methane associated with pockmarks, oil seeps, mud volcanoes, and other cold seeps.

2.3.1 Origin of hydrocarbons

Apparent temperature (T_{13D}) calculated from $\Delta^{13}CH_3D$ supports methane origin attribution as predicted by $\delta^{13}C\text{-}CH_4$, $\delta D\text{-}CH_4$, and C_1/C_{2+3} for methane samples from cold seeps, pockmarks, and oil-associated sites, but not mud volcanoes. For a microbial source, the expected range is temperatures below ca. 80 °C, and for a thermogenic source, the expected range is temperatures above ca. 100°C (Hunt, 1996; Wilhelms et al., 2001). Methane from oil-associated sites is expected to bridge these ranges, as contribution from a thermogenic source may be inferred by the presence of oil, and contribution from a microbial source may occur via methane generation during oil biodegradation. Source attributions based on $\delta^{13}C\text{-}CH_4$, $\delta D\text{-}CH_4$, and C_1/C_{2+3} values are summarized for each category of seafloor feature (**Figure 2.3**).

2.3.1.1 Cold Seeps

Across global locations of cold seep sites, results from methane isotopologue analyses support a prevailing shallow microbial methane source. Within this survey, samples classified as

cold seeps have C_1/C_{2+3} values greater than 1000 and $\delta^{13}C\text{-}CH_4$ values less than -50‰, which is consistent with a dominantly microbial source of methane (**Figure 2.3B**, e.g., Milkov and Etiope, 2018). The values of $\delta^{13}C\text{-}CH_4$ generally form two clusters at -70‰ (these include samples from the eastern Black Sea, northern Black Sea, Cascadia Margin, and Makran Accretionary Prism south of Pakistan) and -50‰ (these include the samples from the North Atlantic, West of Spitsbergen, and the eastern Black Sea), with one outlier from the West of Spitsbergen that has $\delta^{13}C\text{-}CH_4$ = -43‰ (**Table 2.1**, **Figure 2.3**).

Values of $\Delta^{13}CH_3D$ for cold seep samples were greater than 4.5‰ (T_{13D} < ca. 80 °C), with the exception of one site from west of Spitsbergen, where the value of $\Delta^{13}CH_3D$ = 3.32±0.26‰, and apparent temperatures $T_{13D} = 132^{+18/-16}$ °C. Approximately two thirds of sites have T_{13D} less than ca. 50°C (**Figure 2.2**). The isotopologue data, thus, strongly support mostly microbial origin for methane in cold seeps, consistent with the high (>1000) C_1/C_{2+3} values.

2.3.1.2 Pockmarks

Samples from pockmarks are geochemically similar to the cold seep samples, and indicate a predominately microbial hydrocarbon source (**Figure 2.3)**. All pockmark samples have C_1/C_{2+3} values greater than 1000, which is consistent with a microbial source of methane. Similar to cold seeps, the values of $\delta^{13}C\text{-}CH_4$ generally form two clusters at -70‰ and -50‰. Values of $\Delta^{13}CH_3D$ for pockmark samples are greater than 4.5‰ (T_{13D} < ca. 80 °C), supporting strong contribution from a microbial source.

2.3.1.3 Oil-associated sites

Samples from oil-associated sites have $\delta^{13}C\text{-}CH_4$ and $\delta D\text{-}CH_4$ values that are typical of low maturity thermogenic hydrocarbons (**Figure 2.3**) (Whiticar, 1999). The C_1/C_{2+3} values of these samples range from 7 to 1000, which encompasses values that are expected from mixing of microbial and thermogenic hydrocarbons. Methane formed during oil generation would be expected to have a thermogenic source with a higher temperature of peak catagenesis. Microbial methane from the biodegradation of oil can result in relatively high $\delta^{13}C\text{-}CH_4$ with respect to typical microbially produced methane, due to substrate (e.g., CO_2) limitation (e.g., Milkov and Dzou, 2007). The $\Delta^{13}CH_3D$ values of oil-associated samples are lower than those from cold

seeps and pockmarks, ranging from 3.5 to 5.1‰, which corresponds to T_{13D} of 50 to 120 °C (**Figure 2.2**).

2.3.1.4 Mud Volcanoes

Samples from mud volcanoes fall into two geochemical groups across the four measured parameters (C_1/C_{2+3}, $\delta^{13}C\text{-}CH_4$, $\delta D\text{-}CH_4$, and $\Delta^{13}CH_3D$). There were no mud volcanoes in this study that yielded methane that is consistent with either a microbial or thermogenic source across all four geochemical parameters (**Figure 2.3**). The first group, which includes samples from the northern Black Sea and the Håkon Mosby mud volcano in the North Atlantic, is defined by a microbial-like C_1/C_{2+3}, $\delta^{13}C\text{-}CH_4$, and $\delta D\text{-}CH_4$. The values of $\Delta^{13}CH_3D$ from these sites, however, are low (ca. <3.5‰, T_{13D} >150 °C). The second group of mud volcanoes includes sites in the Kumano Basin and Mediterranean Sea. These mud volcanoes have ambiguous or thermogenic-like C_1/C_{2+3}, $\delta^{13}C\text{-}CH_4$, and $\delta D\text{-}CH_4$, but high $\Delta^{13}CH_3D$ values (>4.7‰) that are consistent with a shallow microbial source.

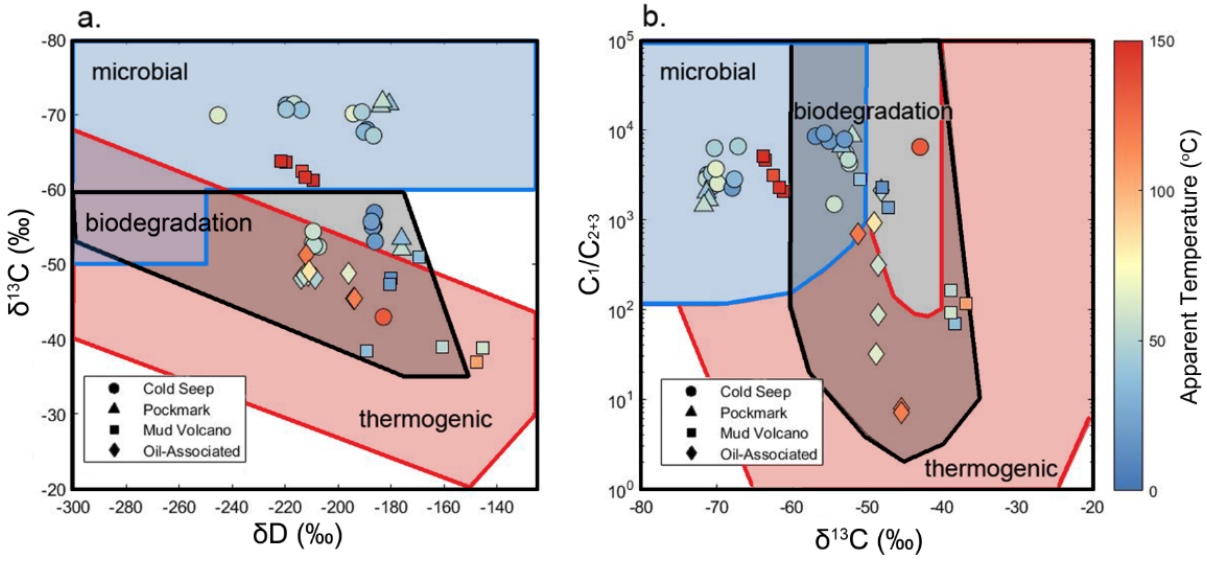

Figure 2.3: Diagrams for methane source. (a) "Whiticar-Schoell plot" showing $\delta^{13}C$ values of methane vs δD values of methane, modified from Milkov and Etiope (2018). (b) "Bernard plot" modified from (Milkov and Etiope, 2018) showing $\delta^{13}C$ values of methane vs C_1/C_{2+3}. Clumped methane temperature shown using color, where apparent temperatures (T_{13D}) less than 50°C are in blue, and apparent temperatures (T_{13D}) greater than 100°C are in red.

2.4 DISCUSSION

2.4.1 Deep microbial methanogenesis in marine sedimentary environments

Determining the history of formation and preservation of gas hydrates deposits is complicated by the various processes that can affect methane isotope compositions, including mixing of microbial and thermogenic methane formed at various temperatures, fractionation during microbial re-working, and migration. Hydrate formation effects on $\delta^{13}C\text{-}CH_4$, $\delta D\text{-}CH_4$, and C_1/C_{2+3} values are expected to be small. Isotope fractionation may occur between gas and hydrate phases by a few per-mille for δD, but not $\delta^{13}C$ (Hachikubo et al., 2007), and it has been theoretically and experimentally demonstrated that quasi-steady state hydrates in an open system approach the C_1/C_{2+3} values of the gas from which they were derived (Kondo et al., 2014). Some hydrate deposits may be fossil, and differently sourced than younger precipitates; hydrates in shallow sediments are often thought to be relatively young compared to their deeply-buried counterparts. Further, hydrates and associated vent gases are often assumed to share the same hydrocarbon source, which may not be true if hydrate deposits are fossil and seepage characteristics have changed. In this study, we measured both hydrate-bound and vent gas at Helgoland Mud Volcano and Batumi seep area in the Black Sea, and found that the clumped isotopologue compositions of these gases are within measurement error (**Table 2.1**). This similarity in isotopologue ratios supports the model that vent gas and near-surface gas hydrates share the same hydrocarbon source at the Helgoland Mud Volcano and the Batumi seep area, and that $\Delta^{13}CH_3D$ values are not fractionated between hydrate–bound and vent gases, beyond measurement error.

As a first order observation, clumped isotope-based temperatures ranging from 15 ℃ to 60 ℃ appear to correspond well with the temperature of microbial methane generation, which is the prevalent methane source at the studied pockmarks and cold seeps (**Figure 2.2**). This suggests that microbially produced methane in deep marine sediments largely reflects equilibrium processes, despite the kinetic fractionation that is often observed for laboratory cultures of methanogens (Stolper et al., 2015; Young et al., 2017; Gruen et al., 2018, Douglas et al., 2020; Shuai et al., 2021) or in some shallow marine sediments (Ash et al., 2019). However, interpretation for the origin of near-equilibrium clumped isotopologues signals in marine sedimentary microbial methane is debated. The two prevailing hypotheses used to explain near-

equilibrium microbial methane are 1) bond re-ordering exclusive to anaerobic oxidation of methane (AOM) (e.g., Ash et al., 2019; Giunta et al., 2019; Ono et al., 2021), and 2) slow methanogenesis, such that the steps of the reaction pathway are fully reversible (e.g., Stolper et al., 2015; Wang et al., 2015; Douglas et al., 2020; Shuai et al., 2021).

AOM by consortia of anaerobic methane-oxidizing archaea and sulfate reducing bacteria is an important methane removal process, and may contribute to the near-equilibrium isotopologue signals found in marine sediments (Knittel et al., 2005; Ash et al., 2019; Ono et al., 2021). Previous analysis of clumped methane isotopologues from gas hydrate samples interpreted near-equilibrium microbial signals as mixes of thermogenic methane, with microbial methane from shallow depths, equilibrated by AOM at bottom seawater temperature from 1 to 2 ℃ (Zhang et al., 2021). However, it is not conclusive whether AOM is required to produce near-equilibrium $\Delta^{13}CH_3D$ signals, and slow methanogenesis could contribute the clumped isotopic composition of microbial methane in subsurface environments (Okumura et al., 2016; Gruen et al., 2018; Jautzy et al., 2021). The sulfate-methane transition zone at sites with high levels of methane advection are expected to occur at shallow depths, as upward expulsion of fluids would make it unlikely for electron acceptors to penetrate deeply (e.g., Borowski et al., 1996). The depth of the AOM zones are as shallow as 10s of cm in the eastern Black Sea, Mediterranean Sea and Cascadia Margin and 1 to 3 m in the Kumano Basin (Treude et al., 2003; Pape et al., 2010b; Reitz et al., 2011; Ijiri et al., 2018b; Pape et al., 2021). Therefore, at hydrate-bearing sites, AOM in the sulfur-methane transition zone typically occurs above the top of gas hydrate bearing sediment (Treude et al., 2003; Bhatnagar et al., 2011), and is unlikely to re-order bonds of methane trapped in hydrate lattice. Further, AOM occurring in environments with relatively high sulfate concentrations is unlikely to produce equilibrium signals (e.g., Ono et al., 2021).

In contrast to the model that assumes AOM is required for near-equilibrium low (1 to 2 ℃) temperature methane isotopologue signals (e.g., Zhang et al., 2021), our $\Delta^{13}CH_3D$ data for gas hydrates are consistent with previous studies that suggest peaks of methane generation between ca. 30 to 60 ℃ (typically more than 500 m depth in marine sediments) (Hyndman and Davis, 1992; Weston and Joye, 2005; Burdige, 2011). When put in their geologic context, our data are best explained as methane isotopologues which continue to equilibrate to a few km below seafloor. Methyl co-enzyme M reductase (Mcr) catalyzes the last step of methanogenesis

and the first step of AOM, and has been shown to be reversible (Scheller et al., 2010; Thauer et al., 2019). In addition, several studies suggested that anaerobic methanotrophic archaea species (ANME), commonly found in symbiosis with sulfate reducers, are capable of both methanotrophy and methanogenesis (Orcutt et al., 2005; Lloyd et al., 2011; Kevorkian et al., 2021). Therefore, methane isotopologue equilibration can be catalyzed by ANME that operates methanogenesis but is unlikely to be by ANME operating AOM because of the general absence of sulfate below methane hydrate, from where the majority of methane is sourced (e.g., Wallmann et al., 2012; Davie and Buffet, 2003).

We hypothesize that the apparent clumped temperature reflects the temperature of enzyme-catalyzed re-equilibration and the process requires live methanogenic (or ANME) microbes because Mcr enzyme degrades within days after cell death (Kaneko et al., 2021). The model is consistent with previous studies that suggest peaks of methane generation between ca. 30 to 60 °C. Thus deeper microbial activity is a source for the relatively shallow gas hydrate reservoirs (e.g., Wallmann et al., 2012).

Methane is the terminal product of early diagenesis of organic matter, and produced via hydrolysis of organic matter in sediments, followed by fermentation of the hydrolysis products to CO_2 and H_2 by bacteria, and methanogenesis from CO_2 and H_2 by methanogenic archaea (e.g., Schink, 1997). The rate of methanogenesis is controlled by several factors, including: 1) the quantity and reactivity of organic matter, 2) the rate of hydrolysis and fermentation of organics, and 3) sterilization of microbes at depth and high temperatures. The quantity and the reactivity of organic matter decreases with increasing age and burial, because more reactive organic matter is preferentially remineralized during early diagenesis (e.g., Middelburg, 1989), or because sediment compaction limits access of organic material to microbes degrading organic matter (Rothman and Forney, 2007). In addition, incubation experiments for marine sediments have shown that the rate of methanogenesis is temperature dependent, with activation energy ranging from 50 to 200 kJ/mol, likely depending upon the nature and the maturity of organic matter (e.g., Burdige, 2011; Weston and Joye, 2005). Activation energy of 100 kJ/mol, for example, increases the rate of microbial methanogenesis by a factor of 60 when temperature increases from 10 to 40 °C. As a result, Burdige (2011) suggested activation energy of 200 kJ/mol, and a subsurface maximum of methanogenesis deeper than 500 mbsf. The two-dimensional model of

methanogenesis by Archer et al. (2012) used activation energy of 70 kJ/mol, and predicted the subsurface maximum, from 500 to 1000 mbsf for microbial methanogenesis in passive margin sediments. These depths are consistent with methane apparent temperatures (T_{13D}) from ca. 15 ℃ to 65 ℃ observed in methane from cold seep and pockmark associated gas hydrate reservoirs investigated in this study.

The upper limit of microbial methanogenesis is thought to be about 60 ℃ to 80 ℃ for marine sedimentary environments (Wilhelms et al., 2001; Inagaki et al., 2015); however, some measured apparent temperatures (T_{13D}) for gas hydrates, in particular, those associated with oil, are higher than 80°C (max 120 ℃) (**Table 2.1**, **Figure 2.2**). At greater depth, higher temperatures accelerate rates of protein denaturation, and when the required maintenance energy becomes higher than the rate of energy supply (i.e., the rate of supply of H_2 and CO_2 for methanogens), methanogens would die (Inagaki et al., 2015). Inagaki et al., (2015) showed active microbial methanogenesis in a coal bed down to 2 kmbsf with *in situ* temperature of <60 ℃. Methanogenesis at warmer temperatures may require a faster rate of supply of CO_2 and H_2, and this may be a reason why biodegradation of petroleum proceeds up to 80 ℃ (Wilhelms et al., 2001; Head et al., 2003). Relatively low C_1/C_{2+3} values for oil-associated hydrates (**Figure 2.3b**) suggest their apparent high temperatures may be due to contribution from thermogenic methane. Additionally, chemical-kinetic effects have been observed for early maturity thermogenic gases, sometimes associated with oil formation, and may contribute to the isotope composition of methane from oil seeps (Xie et al., 2021).

2.4.2 Multiple sources of methane in mud volcanoes

We found that methane samples from pockmarks, oil-associated, and other cold seep hydrate deposits yielded $\Delta^{13}CH_3D$ values consistent with source attribution by $\delta^{13}C$, δD, and C_1/C_{2+3} values (**Figure 2.4**). Data for mud volcanoes, however, do not match these conventional source attributions (**Figure 2.4**). In $\delta^{13}C$ vs. $\Delta^{13}CH_3D$ space, methane from a microbial source would have $\delta^{13}C$ values less than -50‰ and $\Delta^{13}CH_3D$ values greater than 4.3‰ ($T_{13D} \leq 80$ ℃), while methane from a thermogenic source would have a $\delta^{13}C$ value greater than -50‰ and a $\Delta^{13}CH_3D$ value less than 4.3‰. These boundaries are based on the $\delta^{13}C$ contours from other source attribution diagrams (e.g., Whiticar, 1999; Milkov and Etiope, 2018), and the upper temperature limit of secondary microbial methanogenesis (Wilhelms et al., 2001; Head et al.,

2003). Most methane associated with cold seep and pockmark sites plots in the top left quadrant of this space, consistent with a microbial source, and methane found in association with oil is also consistent in terms of $\Delta^{13}CH_3D$ and $\delta^{13}C$ values as having mixed microbial and thermogenic sources. Mixing between estimated microbial and thermogenic end-members show that oil-associated hydrates from the Gulf of Mexico may be 70 to 80% thermogenic in origin, while oil-associated hydrates from the Black Sea may be closer to 40 to 50% thermogenic in origin (**Figure 2.S1)**. Samples from mud volcanoes fall into two categories of discordant $\Delta^{13}CH_3D$ and $\delta^{13}C$ values, in the upper right and bottom left quadrants (**Figure 2.4**).

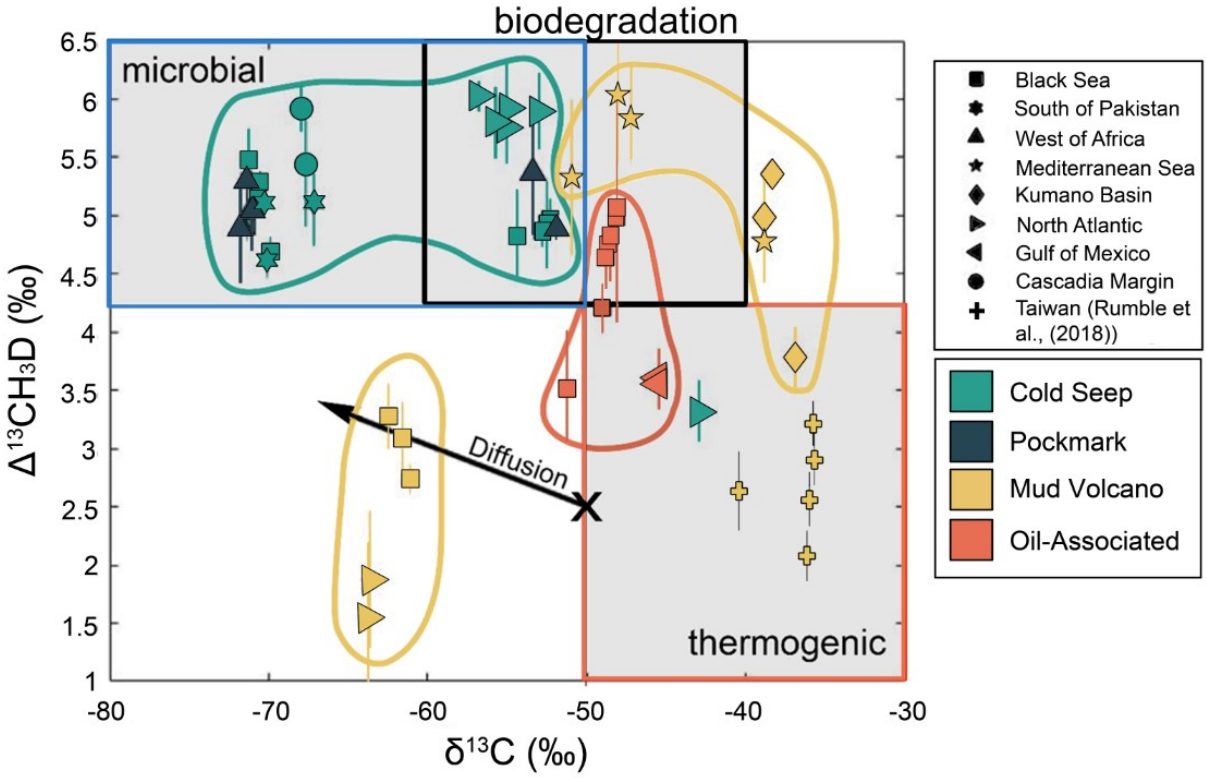

Figure 2.4: Relationship between $\Delta^{13}CH_3D$ and $\delta^{13}C$, categorized by site location (symbol shape) and defining site feature (color). Quadrants are delineated at $\Delta^{13}CH_3D$ = 4.3‰ (≃80°C) and $\delta^{13}C$-CH_4 = -50‰, and as low as -40‰ for biodegradation, based on $\delta^{13}C$ from other source attribution diagrams (e.g., Whiticar, 1999; Milkov and Etiope, 2018), and the upper limit of secondary microbial methanogenesis (Wilhelms et al., 2001; Head et al., 2003). Microbially produced hydrocarbons are expected to fall in the upper left quadrant, and thermogenic hydrocarbons are expected to fall in the lower right quadrant. The line with arrow in the lower left quadrant represents a fractionation scenario of a diffused thermogenic hydrocarbons with an initial composition of $\Delta^{13}CH_3D$ = 2.5‰ and $\delta^{13}C$ = -50‰.

The tectonic settings of the mud volcanoes may have important implications for chemistry of their deeply-sourced fluids and mechanism of methane production. The Kumano Basin mud volcanoes and the Mediterranean Sea mud volcanoes are both situated in proximity to subduction zones (**Figure 2.4**, upper right quadrant), while the Black Sea mud volcanoes and Håkon Mosby mud volcano, in the North Atlantic are situated in a thickly sedimented back-arc basin and a passive continental slope, respectively (**Figure 2.4**, lower left quadrant). Unlike methane from the submarine mud volcanoes in this study, methane emitted from a mud volcano positioned on an active fault in the subduction-accretion system onshore Taiwan has $\delta^{13}C\text{-}CH_4$ values (ca. –35.6 to –40.3‰) and $\Delta^{13}CH_3D$ values (2.1 to 3.2‰) expected for a putative deep thermogenic source (Rumble et al., 2018).

2.4.2.1 Origin of high $\delta^{13}C$ and high $\Delta^{13}CH_3D$ methane due to substrate depletion (CO_2) at mud volcanoes on convergent margins

At convergent margins, such as those associated with the Kumano Basin and Mediterranean Sea mud volcanoes, burial and dehydration of clay minerals can lead to formation and ascent of deeply-sourced fluid, which can transport mud, methane, and other volatiles to the surface (e.g., Hensen et al., 2004; Torres et al., 2004). Processes that lead to fluid expulsion include dewatering of sediments by compression from subduction, and dehydration of mineral-bound water at increasing temperatures and pressures (Kulm et al., 1986; Moore et al., 2011). Samples from the Western summit of Venere and Thessaloniki mud volcanoes in the Mediterranean Sea were found to have pore-water chloride that was depleted to 20% of seawater concentrations, used as evidence for clay dehydration (Pape et al., 2010b; Loher et al., 2018). Similarly, mud volcanoes from the Kumano Basin have been found to have chloride concentrations roughly half of seawater from deeply sourced clay dehydration (Ijiri et al., 2018a). In addition to low Cl concentrations, increased concentrations of boron and lithium are indicative of inputs of fluids from basaltic basement rocks (Kastner et al., 2014). In the Mediterranean Sea, pore-water boron and lithium concentrations exceed typical ranges (e.g., boron concentrations up to 13mM while typical concentrations are below 5mM) (Kopf and Deyhle, 2002; Klasek et al., 2019). The lithium isotopic composition of pore-waters from Kumano basin mud volcano #5 have further shown that some fluid originated from the serpentinized mantle wedge (Nishio et al., 2015).

High concentrations of H_2 have been observed at mud volcanoes located at convergent margins. At Kumano Basin mud volcano #5 *in situ* H_2 concentration is 28.1μM (at 61.5 mbsf from piston core sampled porewater) (Ijiri et al., 2018b), and at the serpentinite mud volcano South Chamorro Seamount in the Mariana Basin H_2 concentration is < 10μM (from CORK fluid) (Kawagucci et al., 2018), compared to typical submarine sediment values of < 0.1 μM (Lin et al., 2012). In these settings, H_2 can be produced by serpentinization, or through fault friction (Hirose et al., 2011; Nishio et al., 2015). In the Nankai trough, it is hypothesized that H_2 is supplied from water-rock reactions in the underlying basement rocks (Ijiri et al., 2018b).

Methane from mud volcanoes with thermogenic-like $\delta^{13}C\text{-}CH_4$ values (>-50‰), and microbial-like $\Delta^{13}CH_3D$ values (>4.3‰) may be explained either by 1) a microbial end-member produced by closed-system distillation in which low (<80 °C) temperature methanogenesis is fueled by deeply rooted fluids that carry H_2 from serpentinization reactions, or 2) isotopic re-setting of thermogenic methane upon ascent. Thermogenic-like $\delta^{13}C\text{-}CH_4$ values from microbially produced hydrocarbons have been observed in several ocean sediment sites including the Middle America Trench ($\delta^{13}C\text{-}CH_4$ up to -39.0‰), the Kumano Basin mud volcano #5 ($\delta^{13}C\text{-}CH_4$ ca. -38.0‰), and the Cascadia Margin ($\delta^{13}C\text{-}CH_4$ ca. -39.5‰) (Jenden and Kaplan, 1986; Pohlman et al., 2009; Pape, 2014; Ijiri et al., 2018b). Microbially produced methane with high $\delta^{13}C\text{-}CH_4$ values may occur from depletion of CO_2. During methanogenesis, ^{12}C-containing dissolved inorganic carbon (DIC) is preferentially consumed, leaving the remaining DIC pool increasingly enriched in ^{13}C. As the substrate gets depleted, the accumulated methane will become more enriched in ^{13}C (Whiticar, 1999). Gases from mud volcanoes located around Japan and Italy have been documented to have high $\delta^{13}C\text{-}CO_2$ (>5‰), supporting this model (Mazzini and Etiope, 2017). For example, values of $\delta^{13}C\text{-}CO_2$ from Kumano Basin mud volcano #5, which is in close proximity to other Kumano Basin mud volcanoes, range from 35 to 40‰ between 15 to 125 mbsf (Ijiri et al., 2018). These values are in contrast to CO_2 produced from thermogenic kerogen maturation in catagenesis, which has values of $\delta^{13}C\text{-}CO_2$ from -15 to -25‰ (Hunt, 1996; Jenden et al. 1993). CO_2 associated with microbial methanogenesis has $\delta^{13}C\text{-}CO_2$ >-3‰, and reflect residual CO_2 from microbial consumption through substrate utilization or secondary methanogenesis following oil biodegradation (Etiope et al., 2009). Microbial methane of this nature may mix with methane of thermogenic origins to produce the observed isotopic compositions.

Alternatively, methane with microbial-like $\delta^{13}C\text{-}CH_4$ values and thermogenic-like $\Delta^{13}CH_3D$ values may occur due to bond re-ordering of thermogenic methane that ascended to shallower depths and lower temperatures. Bond re-ordering has previously been suggested to account for apparent $^{12}CH_2D_2$ re-ordering without resolvable $^{13}CH_3D$ re-ordering, in marine hydrothermal vent fluids, down to 65°C (Labidi et al., 2020). Non-enzymatic bond re-ordering has additionally been suggested to explain relatively high (90 °C and 130 °C) apparent temperatures of microbial-like methane from cold seeps in the Sea of Marmara (Giunta et al., 2021). Re-equilibration rates following D/H exchange are expected to be slow at low temperatures (re-equilibration would take $>10^{10}$ years at temperatures <100 °C) (e.g., Wang et al., 2018), but rates for re-equilibration are unknown in natural environments. Enzymatic bond re-ordering from processes like AOM may also drive $\Delta^{13}CH_3D$ values towards cooler temperatures than those at which they formed (e.g., Young et al., 2019). Apparent temperatures observed for mud volcanoes with thermogenic-like methane studied herein are typically less than 60 °C, which are lower temperatures than other hypothesized cases of bond re-ordering. Given that these apparent temperatures are well within the temperature limit of microbial life in marine sedimentary environments (i.e., <80 °C), and that the rate of non-enzymatic equilibration is expected to be exceedingly slow at low temperatures, enzymatic bond re-ordering is more likely than non-enzymatic bond re-ordering to explain the observed isotopologue distributions. Observations of irregularly shaped mud chambers are widespread, and have the potential to create traps, including buried sub-chambers (e.g., Somoza et al., 2012; Xing et al., 2015) and "Christmas-tree" structures (e.g., Deville et al., 2006; Deville 2009), where bond re-ordering may occur. The interplay of old and fresh fluids from different phases of mud volcano activity (e.g., Mazzini and Etiope 2017) may lead to spatially and temporally complex intensities of microbial methane cycling. However, given the available data we cannot conclusively rule out closed-system distillation or bond re-ordering as the controlling mechanism for observed methane isotopologue compositions from mud volcanoes located at active convergent margins.

2.4.2.2 Origin of low $\delta^{13}C$ and low $\Delta^{13}CH_3D$ methane from kinetic fractionation at mud volcanoes in less active and passive tectonic environments

Isotopologue signals of methane from mud volcanoes with microbial-like $\delta^{13}C\text{-}CH_4$ (<-50‰), and thermogenic-like $\Delta^{13}CH_3D$ (<4.3‰) may be governed by kinetic isotopologue

fractionation, potentially by physical transport processes or during microbial methane production. Fluid mobilization at mud volcanoes in thickly sedimented, tectonically minor active, and passive margin settings, such as those in the Black Sea and the North Atlantic (Håkon Mosby), may be driven by mechanisms including sediment loading, differential compaction, overpressure, and facies changes (Suess, 2014). In mud volcanoes, advection is expected to be the dominant physical transport process responsible for the upward transport of chemicals from deeper sediment layers to the sediment-seafloor interface (e.g., Niemann and Boetius, 2010). Advection rate is difficult to measure directly, but fluid flow velocities for mud volcanoes in the Black Sea (Dvurechenski) and North Atlantic (Håkon Mosby) have been resolved as 8-25 and 40-600 cm yr^{-1}, respectively (de Beer et al., 2006; Kaul et al., 2006; Aloisi et al., 2004). However, transport associated with advection is not expected to yield significant isotopic fractionation. Transport of gases could result in fractionation due to diffusion or adsorption (the geochromatographic effect), in which the transported gas is depleted in heavy isotopologues and ethane and propane (Prinzhofer and Pernaton, 1997).

A slope of molecular diffusion for $\delta^{13}C\text{-}CH_4$ vs $\Delta^{13}CH_3D$ can be estimated using Graham's law as a Rayleigh process (e.g., Young et al., 2017). Molecular diffusion can be modeled with an inverse power-law function of Graham's law (Bourg and Sposito, 2008)

$$\alpha = \frac{^*D}{D} = \left(\frac{^*m}{m}\right)^{-\beta} \qquad (2.6)$$

where α is the fractionation factor, D is the diffusivity of isotopologues, and m is the molecular mass of isotopologues. The exponent, β, equals 0.5 for diffusion involving ideal gases, but the value of β is less than 0.25 for solute diffusion in water (Christensen et al., 2019). The exponent is solute dependent and is less than 0.05 for ions in solution, but larger for noble gases and uncharged molecules (Bourg and Sposito, 2008).

The expected trajectory of diffused methane, represented as different fractions of original gas remaining after Rayleigh fractionation for $\beta = 0.5$ is shown in **Figure 2.4**. Isotopic values of methane and molecular compositions of hydrocarbons from the Black Sea mud volcanoes can be reproduced by the diffusion of thermogenic hydrocarbons with $\delta^{13}C\text{-}CH_4$ = -50‰, $\delta D\text{-}CH_4$ = -200‰, C_1/C_{2+3} = 50, and $\Delta^{13}CH_3D$ = 2.5‰ (**Figure 2.S2**); diffusion produces a relatively large change in $\delta^{13}C\text{-}CH_4$ and $\delta D\text{-}CH_4$ values, but change in $\Delta^{13}CH_3D$ value is relatively minor. For

example, a 15‰ depletion in $\delta^{13}C\text{-}CH_4$ and $\delta D\text{-}CH_4$ is expected to be accompanied by a 0.75‰ enrichment in $\Delta^{13}CH_3D$. The hydrocarbons from the northern Black Sea are hypothesized to be derived from early oil-cracking processes and altered by secondary microbial methane from oil biodegradation. While an apparent temperature of T_{13D}~195°C, for a gas with a $\Delta^{13}CH_3D$ value of 2.5‰, is higher than the expected temperature windows for either early maturity thermogenic gas production or oil biodegradation, it has been observed that early maturity thermogenic gases are not always equilibrated (Xie et al., 2021). Therefore gas with a $\Delta^{13}CH_3D$ value of 2.5‰ does not require formation at 195°C. Alternatively, fractionation associated with microbial reactions could result in a gas with the hypothesized isotopic composition. Biomarker and isotopic evidence suggests that the mud volcanoes are supplied by upward transport of altered thermogenic fluid from a deep source, potentially the Lutetian-basal Priabonian Kuma Formation or the Oligocene-lower Miocene Maikop Series (Stadnitskaia et al., 2008; Boote et al., 2018). Further, $\delta^{13}C\text{-}CH_4$ and C_2/C_1 of gas from these mud volcanoes does not follow a simple mixing line; similar relationship between $\delta^{13}C\text{-}CH_4$ and C_2/C_1 values has previously been interpreted as the result from fractionation during leakage of a thermogenic fluid from a deep reservoir (Prinzhofer and Pernaton, 1997).

The relatively low $\Delta^{13}CH_3D$ (ca. 1.6 to 1.9‰; **Table 2.1**), yet microbial-like $\delta^{13}C\text{-}CH_4$ (–63.6 to –63.8‰) and C_1/C_{2+3} (>1000) of the two samples of hydrated hydrocarbons from the North Atlantic Håkon Mosby mud volcano are not well described by the fractionation of thermogenic gas, and can be explained by kinetic fractionation associated with microbial reactions. A diffused gas from depth would need to have an initial $\Delta^{13}CH_3D$ <1.0‰ and apparent temperature (T_{13D}) > 430 °C in order to reconcile the low observed $\Delta^{13}CH_3D$ values. This is significantly higher than expected sediment temperatures below the central conduit of ca. 185 °C (Eldholm et al., 1999). Microbial methane in disequilibrium has been previously observed in both natural and laboratory settings (Stolper et al., 2015; Wang et al., 2015; Young et al., 2017; Gruen et al., 2018; Ash et al., 2019; Douglas et al., 2020; Shuai et al., 2021). Additional studies have reported kinetic isotope effects associated with microbial and thermogenic methane, as well as clumped isotope disequilibrium in thermogenic methane in which apparent temperatures (T_{13D}) are higher than experimental or natural conditions (Douglas et al., 2017; Stolper et al., 2017; Shuai et al., 2018, Xie et al. 2021). The measurement of the methane isotopologue, $^{12}CH_2D_2$, has been used to assess whether samples of methane are in internal isotopic

equilibrium (e.g., Zhang et al., 2021), and, thus, can serve as a screen for whether or not the apparent temperature (T_{13D}) unambiguously reflects geological formation or re-equilibration temperature.

2.4.3 Apparent depths of methane production

Clumped isotopologue temperatures can be used to estimate the approximate depth of methane generation or last equilibration, once local geothermal gradients are established (See **Table 2.S1**); this value is herein called "apparent depth" because equilibration of methane isotopologues cannot always be demonstrated. The advantage of this approach is the calculation of apparent depths allows for comparison of hypothetical generation depths between seepage locations with different geothermal gradients. Conversely, if estimated generation depth differs from depths predicted by other geochemical proxies, kinetic control on methane generation could be identified. Apparent depths of methane formation, categorized by seafloor expression are shown in **Figure 2.5** and **Table 2.S1**. Methane from cold seeps and pockmarks typically have apparent depths less than 1.5 kmbsf, with the exception of samples Area 1 from the North Atlantic W. of Spitsbergen. Oil-associated methane has a much wider range of apparent depths from ca. 1.0 to 4.5 kmbsf. Apparent depths of methane from mud volcanoes ranges from ca. 0.5 to 5.5 kmbsf.

Where available, we compared the implications of methane source rocks and geothermometry based on clay mineralogy and fluid chemistry (Li, B, and Cl) to the apparent depths from clumped methane isotopologue thermometry, and overall found good agreement with estimated apparent depths. Limited geochemical proxies are available to assess the depth of hydrocarbon formation, but apparent temperatures (T_{13D}) from clumped methane isotopologue thermometry provide valuable information to evaluate source depths. For example, empirical relationships between clay minerals and temperature serves as the basis for several geothermometers, most notably smectite to illite transition which occurs between temperatures of ca. 70 to 110°C (Perry and Hower, 1972). Temperature induced mobilization of elements including lithium and boron can be applied to assess whether fluids have exceeded the temperature range of this transformation (Ishikawa and Nakamura, 1993). Other elemental concentrations in fluids can be applied as geothermometers including Li-Mg, Na-Li, and silica geothermometers (Kharaka and Mariner, 1989). For thermogenic hydrocarbons, biomarkers can

yield information about source rock strata. Further, the extent of isotopic fractionation between environmental water and hydrogen in methane can be applied to assess equilibration temperature (Horibe and Craig, 1995).

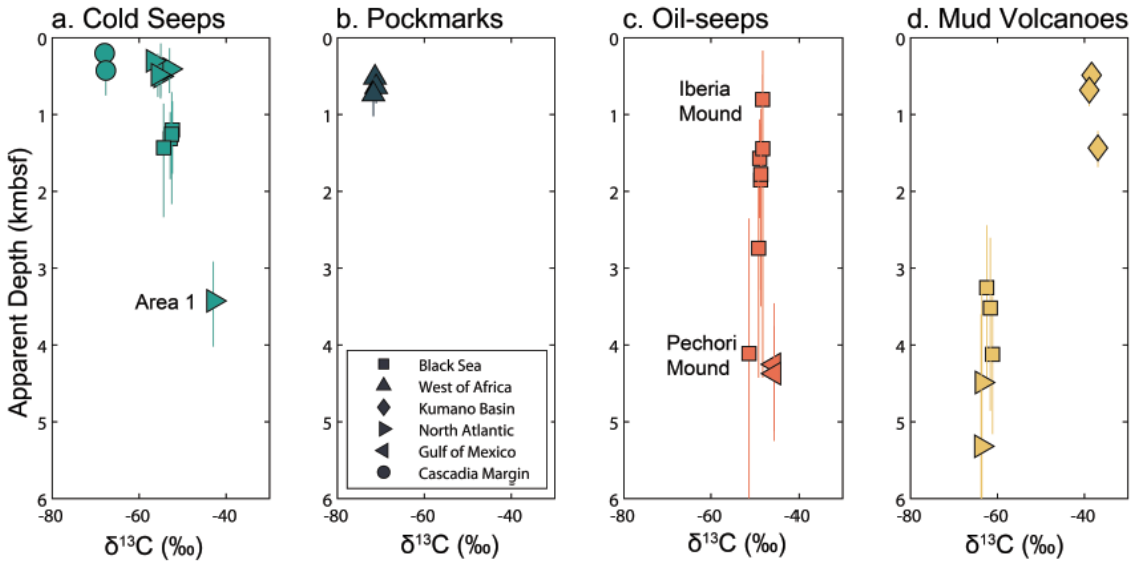

Figure 2.5: Apparent depths of methane generation or re-equilibration derived from $\Delta^{13}CH_3D$ values and background geothermal gradients (see **Table 2.S1**) vs $\delta^{13}C$ of methane. Error accounts for error in calibrated temperatures from the 95% confidence interval of $\Delta^{13}CH_3D$ measurements, as well as thermal gradient error. Thermal gradients used for this calculation and associated references can be found in **Table 2.S1**.

Methane from cold seep and pockmark sites have apparent depths that suggest methane generation typically occurs shallower than ca. 1.5 kmbsf (**Figure 2.5a, b**). Most mineral geothermometers and thermal maturity indicators apply to sediments and fluids that have experienced temperatures higher than ca. 60 °C, so data to corroborate estimated apparent depths for microbial methane sources is limited to the interpretation that sediments and fluids have remained below alteration temperatures. Apparent generation depths of methane from most cold seep and pockmark sites are consistent with methane production below temperatures associated with thermal alteration. Conversely, the apparent depth of methane formation from gas collected at site Area 1, West of Spitsbergen, is ca. 3.5 kmbsf. Previous studies on the West coast of Svalbard have suggested thermogenic methane production at ca. 2.0 kmbsf from Miocene-age source rock. This work is based on basin modeling and sediment studies of ODP sites 909 and 986, located ca. 270 and 146 km, respectively, from sites included in this study (Myhre et al.,

1995; Butt et al., 2000; Knies et al., 2018; Pape et al., 2020a). Thus, the apparent depth of methane from this site is inconsistent with what is typical for cold seep-derived methane and deeper than what has been inferred from previous studies. This observation implies that methane from this site may have experienced kinetic alteration (e.g., oxidation), or is derived from a higher temperature thermogenic source than previously thought.

Methane from oil-associated sites (**Figure 2.5c**) in the Black Sea (Pechori Mound, Iberia Mound, Colkheti Seep), have apparent formation depths that are consistent with information from mineral geothermometers and source rock biomarkers. Information from biomarkers (e.g., oleanane) suggests that oils at these sites come from the Eocene Kuma Formation and/or the Oligocene to Miocene-aged Maikop Group, prolific source rocks in the Black Sea. However, due to intense folding induced by tectonic compression, the local burial depth of source rocks remains largely unknown (Robinson et al., 1996; Reitz et al., 2011; Pape et al., 2021). Fluids from the Pechori Mound carry signals of clay alteration at temperatures between 60 and 110 °C and depths between 1.2 and 2.2 km, using Li-Mg, Na-Li and silica geothermometers (Reitz et al., 2011). Apparent depths of methane formation from these sites range from ca. 0.8 to 2.7 kmbsf, consistent with mineral geothermometers (Kutas et al., 1998). As C_1/C_{2+3} values and $\delta^{13}C$ values suggest contribution from thermogenic methane, near-equilibrium signals might have been produced during thermogenic generation of methane in these sites.

For methane from Bush Hill in the Gulf of Mexico, apparent depth is intermediate between the hypothesized reservoir depth (1.7 to 3.1 kmbsf) and source rock depth (6 to 10 kmbsf). Apparent depth estimations from clumped methane isotopologues are ca. 4.3 kmbsf (T_{13D} ~115 °C). This may represent some admixture of thermogenic methane with methane produced by oil biodegradation.

Apparent depths from mud volcanoes (**Figure 2.5d**) may in some cases yield information about the depths at which microbial methanogenesis occurs in mud volcano systems, but may be less meaningful for sites in which kinetic effects are suspected. Previous work on the Kumano Basin mud volcano #5 suggested biogenic methane production at 0.3 to 0.9 kmbsf, i.e., based on methane clumped isotopologue thermometry (Ijiri et al., 2018b). This is also observed at Kumano Basin mud volcanoes #2, and #4, in which methane has apparent depths ca. 0.5 and 0.7 kmbsf, respectively. Kumano Basin mud volcano #10 is expected to have a higher contribution

of thermogenic methane than mud volcano #5, with an apparent depth of methane formation at 1.4 kmbsf. At nearby IODP site C0009 high concentrations of methane were detected at ca. 1.2 kmbsf, correlated to high amounts of wood and lignite (Saffer et al., 2010).

Gas hydrate from mud volcanoes in the northern Black Sea and the North Atlantic yielded low $\Delta^{13}CH_3D$ (<1.9‰), characteristic of thermogenic methane. Their relatively low $\delta^{13}C\text{-}CH_4$ values (ca. -64‰), however, support microbial origin, suggesting methane isotopologues were not equilibrated, so apparent depth of methane formation should be regarded critically. Gas hydrate from the northern Black Sea mud volcanoes has been hypothesized to be partially derived from thermal cracking of organic matter in the Maikop Group, which is located below 3 kmbsf, (Stadnitskaia et al., 2008). This source is corroborated by apparent depths of methane from these features, ca. 3.5 kmbsf. The apparent depth of equilibration for gas hydrate at the North Atlantic Håkon Mosby mud volcano is ca. 4.5 to 5.3 kmbsf, which correlated to pre-glacial Middle Miocene to Late Pliocene-aged strata below the ca. 3.1 km thick glacial sediment column. Previous studies have suggested that considerable amounts of thermogenic methane may have formed in pre-glacial or interglacial sediments below the North Atlantic Håkon Mosby mud volcano (Lein et al., 1999; Berndt and Planke, 2006).

This calculation assumes methane isotopologue abundances reflect the temperature of generation or the temperature at which isotopologues were last equilibrated by microbial catalysis. Bond re-ordering of methane isotopologues was suggested to be a potentially important process at non-hydrate bearing cold seeps and marine sediments (Ash et al., 2019; Giunta et al., 2021). It is assumed that methane trapped in the lattice of a gas hydrate structure is unlikely to re-equilibrate; however, previous work has shown that isotope fractionation may occur between gas and hydrate phases by a few per-mille for δD, but not $\delta^{13}C$ (Hachikubo et al., 2007). Further, most gas hydrate samples included in this study were collected from the uppermost meters below seafloor, but the interface between free gas and the base of the gas hydrate stability zone may be situated several tens to hundreds of meters below seafloor. It is assumed that water deficiency or local heat prevent hydrate formation and facilitate migration of methane in the free gas phase through the gas hydrate stability zone. However, in dynamic systems, such as mud volcanoes, episodic formation and dissociation of hydrates may result in repeated trapping and release of hydrocarbons. Given the possible kinetic alteration, bond-re-ordering, or closed-system

distillation suspected for submarine mud volcano samples, the assumption of equilibrium, and thus the extrapolation to apparent depth of formation is uncertain.

2.5 SUMMARY

In this study, we applied clumped methane isotopologue geothermometry alongside isotope ratios of methane ($\delta^{13}C$, and δD) and hydrocarbon ratios (C_1/C_{2+3}) to test whether isotope-based temperatures are consistent with putative formation processes at different seepage morphologies. We assess 46 submarine gas hydrates and associated vent gases from 11 regions of the world's oceans from oil seeps, pockmarks, mud volcanoes, and other cold seeps. Our findings are summarized below.

1. Methane associated with cold seeps and pockmarks yielded $\Delta^{13}CH_3D$ values from 4.5 to 6.0‰, consistent with a microbial source of methane, produced between 15 and 65 °C. Methane from oil-associated gas hydrates yielded lower $\Delta^{13}CH_3D$ values, corresponding to secondary methane generation at higher temperature (50 to 120 °C). Methane associated with mud volcanoes yielded a range of $\Delta^{13}CH_3D$ values (1.5 to 6.0‰), suggesting their diverse origins.
2. We measure samples from two sites (Batumi seep area and Helgoland mud volcano, Black Sea) where both hydrate-bound gas and vent gas were collected. We find that $\Delta^{13}CH_3D$ values for the gases are within measurement error, suggesting that methane in hydrate and vent gas at these sites share the same origin.
3. The $\Delta^{13}CH_3D$ values and apparent temperatures (T_{13D}) of equilibration for methane associated with cold seeps, pockmarks, and oil-rich hydrates are consistent with conventional source attribution based on $\delta^{13}C$, δD and C_1/C_{2+3} values. In contrast, methane from mud volcanoes yields methane with dissonant source attributions from $\Delta^{13}CH_3D$ and $\delta^{13}C$ values, and fall into two geochemical groupings. We hypothesize that these differences are connected to the tectonic environments at which the mud volcanoes are situated.
4. We use methane isotopologue temperatures and local geothermal gradients to infer the apparent depth of methane generation. These apparent depths often corroborate available information from previous studies regarding methane source rocks based on biomarker studies, and geothermometry based on clay mineralogy and fluid chemistry (Li, B, and Cl).

2.6 ACKNOWLEDGMENTS

We thank Dr. Stefano Bernasconi, as well as Dr. Thomas Giunta, and two anonymous reviewers for constructive comments that significantly improved this work. This work was supported by the Deep Carbon Observatory through a Deep Life Community Grant (to S.O.), N. Braunsdorf and D. Smit of Shell PTI/EG (to S.O), and the German Research Foundation (DFG) through DFG-Research Center/Excellence Cluster 'The Ocean in the Earth System' (EXC 309 / FZT 15). D.S.G. was supported by a National Science Foundation Graduate Research Fellowship. E.L. was supported by the Presidential Graduate Fellowship at MIT. D.S.G and E.L. were also supported by MIT Energy Initiative Graduate Fellowships.

2.7 SUPPLEMENTARY INFORMATION

2.7.1 End-member mixing

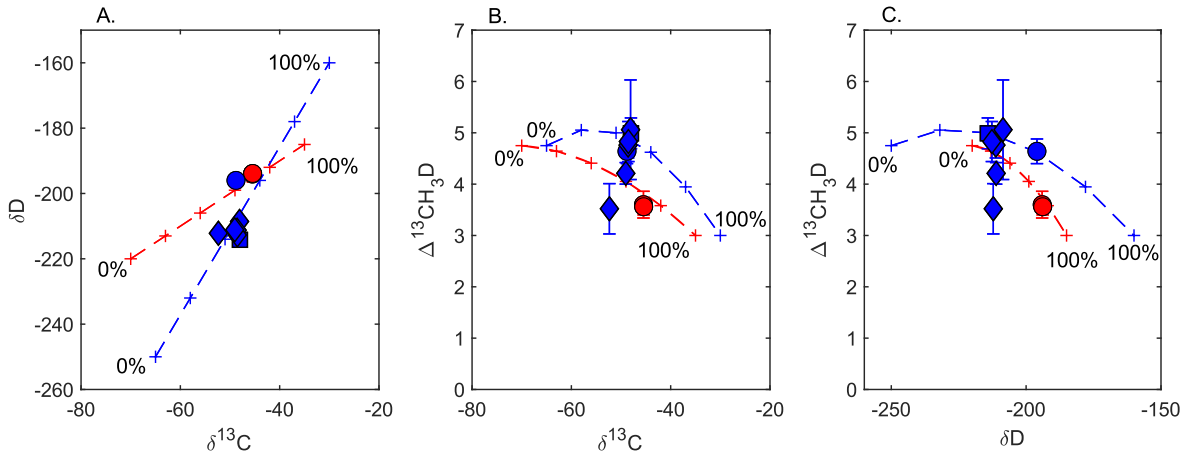

Figure 2.S1: Modeling results for end-member mixing scenarios for oil-associated hydrates in the Gulf of Mexico (red) and Black Sea (blue) in A) $\delta^{13}C$ vs δD, B) $\delta^{13}C$ vs $\Delta^{13}CH_3D$, and C) δD vs $\Delta^{13}CH_3D$ space. The thermogenic end-members are marked as 0% and the microbial end-members are marked as 100%.

We define the end-members for the Gulf of Mexico mixing scenario as: Microbial = [$\delta^{13}C$ = -70‰, δD =-220‰, $\Delta^{13}CH_3D$ = 4.75‰], Thermogenic = [$\delta^{13}C$ = -35‰, δD =-185‰, $\Delta^{13}CH_3D$ = 3.0‰]. We define the end-members for the Black Sea mixing scenario as: Microbial = [$\delta^{13}C$ = -65‰, δD =-250‰, $\Delta^{13}CH_3D$ = 4.75‰], Thermogenic = [$\delta^{13}C$ = -30‰, δD =-160‰, $\Delta^{13}CH_3D$ = 3.0‰]. A microbial end-member value for $\Delta^{13}CH_3D$ was chosen as 4.75‰ because the corresponding apparent temperature of 60°C is an approximate upper temperature limit of primary microbial methanogenesis. A thermogenic end-member value for $\Delta^{13}CH_3D$ was chosen as 3.0‰ because the corresponding apparent temperature of 150°C falls within the temperature range of peak oil generation. Using these end-members, oil-associated hydrates from the Gulf of Mexico may be 70 to 80% thermogenic in origin, while oil-associated hydrated from the Black Sea may be closer to 40 to 50% thermogenic in origin.

In cases where source gases have large (i.e., 10s ‰) differences in δD-CH_4 and $\delta^{13}C$-CH_4, mixing is non-linear due to the definition of $\Delta^{13}CH_3D$ in reference to the stochastic distribution of isotopologues, which is a non-linear function with respect to δD-CH_4 and $\delta^{13}C$-CH_4. Resultant $\Delta^{13}CH_3D$ can be either larger or smaller than what is predicted by conservative mixing. In the mixing scenarios we model for the two regions, the non-linear mixing effect

results in higher $\Delta^{13}CH_3D$ than what is predicted from conservative mixing. For the modeled Black Sea mixing scenario, $\Delta^{13}CH_3D$ values can be up to 1.0‰ higher than what is predicted from conservative mixing, and for the modeled Gulf of Mexico mixing scenario, $\Delta^{13}CH_3D$ values can be up to 0.4‰ higher than what is predicted from conservative mixing. This effect results in apparent temperatures (T_{13D}) of methane from oil-associated hydrates to be lower than what would be predicted by a conservative mixing. An implication of this is that apparent depth estimates for these samples may be under-estimates.

4.7.2 Diffusion of thermogenic gas

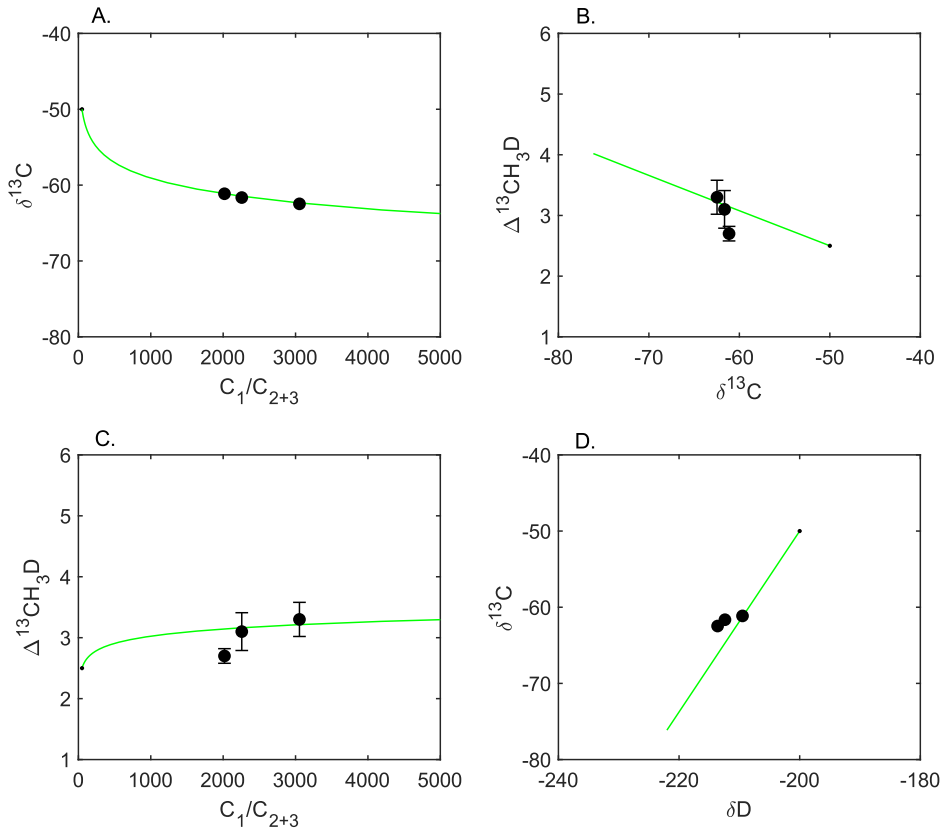

Figure 2.S2: Diffusion trajectory of a thermogenic gas with composition (C_1/C_{2+3} = 50, $\delta^{13}C$ = -50‰, δD= -200‰, $\Delta^{13}CH_3D$ = 2.5‰). **A** C_1/C_{2+3} vs $\delta^{13}C$, **B** $\delta^{13}C$ vs $\Delta^{13}CH_3D$, **C** C_1/C_{2+3} vs $\Delta^{13}CH_3D$ **D** δD vs $\delta^{13}C$. Data from Black Sea mud volcanoes is shown as black circles. Diffusivity of methane is set as $9.467*10^{-5}$ and ethane is set as $4.733*10^{-5}$ m^2/yr (Zhang and Kroos 2001).

2.7.3 Additional site information

Region	Sample ID	Site	Latitude	Longitude	Water temperature (°C)	Geothermal gradient (°C/km)	±	Water depth (m)	Apparent depth (km)	-	+	References
Eastern Black Sea	15260	Batumi seep area	41.95876	41.2924	9	35	7.3	850	1.2	0.41	0.41	Reitz et al., 2011
	11907	Batumi seep area	41.95876	41.2924	9	35	7.3	850	1.31	0.35	0.35	Reitz et al., 2011
	11921-1	Batumi seep area	41.95876	41.2924	9	35	7.3	850	1.26	0.67	0.61	Reitz et al., 2011
	11971	Colkheti Seep	41.9678	41.1033	9	39	10.4	1000	1.57	0.49	0.49	Reitz et al., 2011
	11938	Iberia Mound	41.879	41.1671	9	51	11.1	1000	0.8	0.45	0.43	Reitz et al., 2011
	15268-1	Ordu ridge patch#02	41.535	37.62889	9			1530				Bohrmann, 2011
	15503-1	Ordu ridge patch#03	41.535	37.62889	9			1530				Bohrmann, 2011
	15505	Ordu ridge patch#05	41.53528	37.62944	9			1530				Bohrmann, 2011
	15507	Ordu ridge patch#07	41.535	37.62944	9			1530				Bohrmann, 2011
	15227-3	Pechori Mound-1/23cm	41.9827	41.1257	9	27	8.7	1000	1.85	0.69	0.69	Reitz et al., 2011
	15227-3	Pechori Mound-1cm	41.9827	41.1257	9	27	8.7	1000	1.44	1.88	1.54	Reitz et al., 2011
	15227-3	Pechori Mound-5cm	41.9827	41.1257	9	27	8.7	1000	1.78	0.91	0.88	Reitz et al., 2011
	15227-3	Pechori Mound-7cm	41.9827	41.1257	9	27	8.7	1000	4.11	1.51	1.32	Reitz et al., 2011
	15227-3	Pechori Mound-9cm	41.9827	41.1257	9	27	8.7	1000	2.74	0.58	0.69	Reitz et al., 2011
	15244-2	Poti Seep	41.95833	41.30667	9	33.5	6.1	890	1.43	0.66	0.6	Klaucke et al., 2006
Northern Black Sea	11913	Vodyanitskii MV	44.285	35.03361	9.1	40	6.1	2065	4.12	0.4	0.4	Sahling et al., 2009
	15525-1	Helgoland MV	44.2875	35	9	39	6	2050	3.25	0.64	0.59	Bohrmann, 2011
	14339-3	Helgoland MV	44.2875	35	9	39	6	2050	3.52	0.74	0.67	Bohrmann, 2011
	15518	Kerch Flare	44.62167	35.7075	9			900				Bohrmann, 2011
Gulf of Guinea	16022-1	Pockmark_A	3.25	6.699	4.53			1140				Wei et al., 2015
	16016-1	Pockmark_C1	3.235	6.699	4.53			1189				Wei et al., 2015
Northern Congo Fan	13114-3	Hydrate Hole	-4.80111	9.9475	2.5	70.5	0.8	3110	0.52	0.12	0.12	Sahling et al., 2008
	13115-1	Baboon Hole	-4.94083	9.94417	2.5	71	2.5	3000	0.64	0.22	0.2	Sahling et al., 2008
	13118-1	Worm Hole	-4.75167	9.945	2.5	70	1	3110	0.74	0.29	0.26	Sahling et al., 2008
Kumano Basin, South of Japan	16716-2	MV10	33.53556	136.26889	2	71.8	2.3	1825	1.43	0.23	0.21	Hamamoto et al., 2012; Pape, 2014; Ijiri et al., 2018
	16736-2	MV4	33.66472	136.63389	2	71.8	2.3	1980	0.49	0.09	0.09	Hamamoto et al., 2012; Pape, 2014; Ijiri et al., 2018
	16772	MV2	33.68083	136.92194	2	71.8	2.3	2000	0.68	0.21	0.2	Hamamoto et al., 2012; Pape, 2014; Ijiri et al., 2018
Makran Accretionary	12303	Nascent Ridge										
	12316-3	Flare 2	24.83556	63.02889	5			1027				Römer et al., 2012
	12316-4	Flare 2	24.83556	63.02889	5			1027				Römer et al., 2012
North Atlantic-West of Spitsbergen	16807-2	Area 1	78.54733	10.23754	3.2	37.6	1.1	94	3.43	0.51	0.45	Sahling et al., 2014; Riedel et al., 2018
	16823-2	Area 2	78.65424	9.25755	4.1	37.6	1.1	242	0.5	0.3	0.3	Sahling et al., 2014; Riedel et al., 2018
	16823-5	Area 2	78.6542	9.43401	4.1	37.6	1.1	240	0.4	0.38	0.35	Sahling et al., 2014; Riedel et al., 2018
	16833-2	Area 3	78.62031	9.41099	3.7	37.6	1.1	382	0.41	0.32	0.3	Sahling et al., 2014; Riedel et al., 2018
	16833-3	Area 3	78.62017	9.4095	3.7	37.6	1.1	384	0.3	0.14	0.14	Sahling et al., 2014; Riedel et al., 2018
	16848-2	Area 4	78.55544	9.47597	3.9	37.6	1.1	387	0.48	0.3	0.3	Sahling et al., 2014; Riedel et al., 2018
North Atlantic-Håkon	PS70-94-1	Håkon Mosby MV	72.00139	14.71861	-0.8	59	3.7	1250	4.49	1.72	1.16	Pape et al., 2011
	PS70-110-1	Håkon Mosby MV	72.00139	14.71861	-0.8	59	3.7	1250	5.32	2.62	1.55	Pape et al., 2011
Gulf of Mexic	SO174-1	Bush Hill	27.78472	-91.501	7.75	25	1.7	570	4.25	0.71	0.63	Labails et al., 2007
	SO174-2	Bush Hill	27.78472	-91.501	7.75	25	1.7	570	4.37	0.47	0.43	Labails et al., 2007
Cascadia Margin	SO148-1	Hydrate Ridge	44.57139	-125.10222	3.7	71	5.4	887	0.2	0.16	0.16	Linke and Suess, 2001
	SO148-2	Hydrate Ridge	44.57139	-125.10222	3.7	71	5.4	777	0.43	0.34	0.32	Linke and Suess, 2001
Mediterranean Sea	17908-1	Thessaloniki MV	35.41806	30.25	14.01							Pape et al., 2010
	19224-3	Venere MV Flare 1	38.61667	17.185	13.8			1600				Loher et al., 2018
	19240-2	Venere MV Flare 5	38.58444	17.2	13.8			1600				Loher et al., 2018
	19251-1	Venere MV western summit	38.60111	17.18389	13.8			1600				Loher et al., 2018

Table 2.S1: Additional information for hydrate samples including site location, bottom water temperature, local geothermal gradient, and apparent depth of methane formation.

2.7.4 Thermal gradient determination

Table 2.S2: Data from International Heatflow Commission Global Heat Flow Database (Fuchs et al., 2021) used to calculate local geothermal gradients at sites. Geothermal gradients from hot spots or with the value '0' are excluded for not being representative of background sediment, and shown in red. The threshold for hotspots is temperature gradients greater than 130 K/km. The FID numbers refer to the International Geo Sample Numbers from the heat flow database.

		Distance from hydrate sample	Elevation	Thermal gradient	Latitude	Longitude
geotherm data within 50 km from Batumi Seep (lat: 41.958760, long: 41.292400; gradient: 35 (+/- 7.3) K/km)						
FID: 37217	site: A2-1470G	at 10.2 km	elevation: -906	20 K/km	lat:42.05	long:41.30
FID: 38558	site: 15	at 24.2 km	elevation: -1300	53 K/km	lat:41.95	long:41.00
FID: 38881	site: BS1470G	at 10.2 km	elevation: -906	51 K/km	lat:42.05	long:41.30
FID: 60945	site: Geol 1-5	at 10.3 km	elevation: -750	27 K/km	lat:42.03	long:41.37
FID: 60946	site: Geol 1-6	at 18.6 km	elevation: -750	25 K/km	lat:42.12	long:41.37
FID: 60947	site: Geol 1-7	at 24.2 km	elevation: -640	43 K/km	lat:42.15	long:41.43
geotherm data within 50 km from Colkheti Seep (lat: 41.967800, long: 41.103300; gradient: 39 (+/- 10.4) K/km)						
FID: 37217	site: A2-1470G	at 18.6 km	elevation: -906	20 K/km	lat:42.05	long:41.30
FID: 38558	site: 15	at 8.8 km	elevation: -1300	53 K/km	lat:41.95	long:41.00
FID: 38881	site: BS1470G	at 18.6 km	elevation: -906	51 K/km	lat:42.05	long:41.30
FID: 60945	site: Geol 1-5	at 23.0 km	elevation: -750	27 K/km	lat:42.03	long:41.37
geotherm data within 50 km from Iberia Mound (lat: 41.879000, long: 41.167100; gradient: 51 (+/- 11.1) K/km)						
FID: 37217	site: A2-1470G	at 22.0 km	elevation: -906	20 K/km	lat:42.05	long:41.30
FID: 38558	site: 15	at 15.9 km	elevation: -1300	53 K/km	lat:41.95	long:41.00
FID: 38559	site: 16	at 21.5 km	elevation: -1050	68 K/km	lat:41.70	long:41.27
FID: 38881	site: BS1470G	at 22.0 km	elevation: -906	51 K/km	lat:42.05	long:41.30
FID: 60945	site: Geol 1-5	at 23.8 km	elevation: -750	27 K/km	lat:42.03	long:41.37
geotherm data within 50 km from Ordu ridge patch#02 (lat: 41.535000, long: 37.628889; gradient: N/A)						
FID: 37219	site: A2-1476P	at 10.1 km	elevation: -1741	21 K/km	lat:41.62	long:37.68
FID: 38886	site: BS1476G	at 11.1 km	elevation: -1741	69 K/km	lat:41.63	long:37.65
geotherm data within 50 km from Ordu ridge patch#03 (lat: 41.535000, long: 37.628889; gradient: N/A)						
FID: 37219	site: A2-1476P	at 10.1 km	elevation: -1741	21 K/km	lat:41.62	long:37.68
FID: 38886	site: BS1476G	at 11.1 km	elevation: -1741	69 K/km	lat:41.63	long:37.65
geotherm data within 50 km from Ordu ridge patch#05 (lat: 41.535278, long: 37.629444; gradient: N/A)						
FID: 37219	site: A2-1476P	at 10.1 km	elevation: -1741	21 K/km	lat:41.62	long:37.68

FID: 38886	site: BS1476G	at 11.0 km	elevation: -1741	69 K/km	lat:41.63	long:37.65

geotherm data within 50 km from Ordu ridge patch#07 (lat: 41.535000, long: 37.629444; gradient: N/A)						
FID: 37219	site: A2-1476P	at 10.1 km	elevation: -1741	21 K/km	lat:41.62	long:37.68
FID: 38886	site: BS1476G	at 11.1 km	elevation: -1741	69 K/km	lat:41.63	long:37.65

geotherm data within 50 km from Pechori Mound (lat: 41.982700, long: 41.125700; gradient: 27 (+/- 8.7) K/km)						
FID: 37217	site: A2-1470G	at 16.2 km	elevation: -906	20 K/km	lat:42.05	long:41.30
FID: 38558	site: 15	at 11.0 km	elevation: -1300	53 K/km	lat:41.95	long:41.00
FID: 38881	site: BS1470G	at 16.2 km	elevation: -906	51 K/km	lat:42.05	long:41.30
FID: 60945	site: Geol 1-5	at 20.7 km	elevation: -750	27 K/km	lat:42.03	long:41.37
FID: 60946	site: Geol 1-6	at 24.9 km	elevation: -750	25 K/km	lat:42.12	long:41.37

geotherm data within 50 km from Poti Seep (lat: 41.958333, long: 41.306667; gradient: 33.5 (+/- 6.1) K/km)						
FID: 37217	site: A2-1470G	at 10.2 km	elevation: -906	20 K/km	lat:42.05	long:41.30
FID: 38881	site: BS1470G	at 10.2 km	elevation: -906	51 K/km	lat:42.05	long:41.30
FID: 60944	site: Geol 1-4	at 24.3 km	elevation: -720	40 K/km	lat:42.13	long:41.48
FID: 60945	site: Geol 1-5	at 9.7 km	elevation: -750	27 K/km	lat:42.03	long:41.37
FID: 60946	site: Geol 1-6	at 18.3 km	elevation: -750	25 K/km	lat:42.12	long:41.37
FID: 60947	site: Geol 1-7	at 23.7 km	elevation: -640	43 K/km	lat:42.15	long:41.43

geotherm data within 50 km from Vodyanitskii MV (lat: 44.285000, long: 35.033611; gradient: 40 (+/- 6.1) K/km)						
FID: 37213	site: A2-1433P	at 24.4 km	elevation: -2170	11 K/km	lat:44.07	long:35.00
FID: 37222	site: A2-1485G	at 22.6 km	elevation: -1758	25 K/km	lat:44.42	long:35.25
FID: 38893	site: BS1485G	at 22.6 km	elevation: -1758	37 K/km	lat:44.42	long:35.25
FID: 60662	site: 5661	at 4.1 km	elevation: -2055	305 K/km	lat:44.28	long:34.98
FID: 60675	site: 5660	at 5.3 km	elevation: -2047	68 K/km	lat:44.28	long:34.97
FID: 60690	site: 5616	at 10.5 km	elevation: -2038	70 K/km	lat:44.28	long:34.90
FID: 60726	site: 5615	at 20.2 km	elevation: -2020	53 K/km	lat:44.24	long:34.79
FID: 60728	site: 5627	at 21.3 km	elevation: -1900	44 K/km	lat:44.47	long:34.95
FID: 60738	site: 5626	at 17.1 km	elevation: -2015	43 K/km	lat:44.40	long:34.88
FID: 60754	site: 5625	at 16.8 km	elevation: -2052	40 K/km	lat:44.33	long:34.83
FID: 60773	site: 5617	at 14.3 km	elevation: -1818	38 K/km	lat:44.38	long:35.15
FID: 60787	site: 5616r	at 5.0 km	elevation: -2035	35 K/km	lat:44.33	long:35.03
FID: 60795	site: 5624	at 20.7 km	elevation: -2133	36 K/km	lat:44.24	long:34.78
FID: 60924	site: AVA 1957	at 22.8 km	elevation: -1919	70 K/km	lat:44.47	long:34.90

geotherm data within 50 km from Helgoland MV (lat: 44.287500, long: 35.000000; gradient: 39 (+/- 6) K/km)						
FID: 37213	site: A2-1433P	at 24.6 km	elevation: -2170	11 K/km	lat:44.07	long:35.00
FID: 37222	site: A2-1485G	at 24.5 km	elevation: -1758	25 K/km	lat:44.42	long:35.25
FID: 38893	site: BS1485G	at 24.5 km	elevation: -1758	37 K/km	lat:44.42	long:35.25
FID: 58026	site: G 8022	at 24.3 km	elevation: -1800	20 K/km	lat:44.50	long:34.91

FID: 60662	site: 5661	at 1.5 km	elevation: -2055	305 K/km	lat:44.28	long:34.98
FID: 60675	site: 5660	at 2.7 km	elevation: -2047	68 K/km	lat:44.28	long:34.97
FID: 60690	site: 5616	at 7.9 km	elevation: -2038	70 K/km	lat:44.28	long:34.90
FID: 60726	site: 5615	at 17.6 km	elevation: -2020	53 K/km	lat:44.24	long:34.79
FID: 60728	site: 5627	at 20.3 km	elevation: -1900	44 K/km	lat:44.47	long:34.95
FID: 60738	site: 5626	at 15.1 km	elevation: -2015	43 K/km	lat:44.40	long:34.88
FID: 60754	site: 5625	at 14.1 km	elevation: -2052	40 K/km	lat:44.33	long:34.83
FID: 60773	site: 5617	at 16.0 km	elevation: -1818	38 K/km	lat:44.38	long:35.15
FID: 60787	site: 5616r	at 5.2 km	elevation: -2035	35 K/km	lat:44.33	long:35.03
FID: 60795	site: 5624	at 18.2 km	elevation: -2133	36 K/km	lat:44.24	long:34.78
FID: 60924	site: AVA 1957	at 21.5 km	elevation: -1919	70 K/km	lat:44.47	long:34.90

geotherm data within 50 km from Kerch Flare (lat: 44.621667, long: 35.707500; gradient: N/A)

geotherm data within 50 km from Pockmark A (lat: 3.250000, long: 6.699000; gradient: N/A)

geotherm data within 50 km from Pockmark C1 (lat: 3.235000, long: 6.699000; gradient: N/A)

geotherm data within 50 km from Hydrate Hole (lat: -4.801111, long: 9.947500; gradient: 70.5 (+/- 0.8) K/km)

FID: 48445	site: GGH44	at 22.6 km	elevation: -3135	72 K/km	lat:-4.75	long:10.14
FID: 48452	site: GGH16	at 17.0 km	elevation: -3201	72 K/km	lat:-4.84	long:10.10
FID: 48475	site: GGH15	at 18.8 km	elevation: -3191	71 K/km	lat:-4.88	long:10.10
FID: 48481	site: GGH17	at 16.6 km	elevation: -3190	70 K/km	lat:-4.79	long:10.10
FID: 48486	site: GGH42	at 23.5 km	elevation: -3141	71 K/km	lat:-4.88	long:10.14
FID: 48496	site: GGH14	at 21.6 km	elevation: -3179	71 K/km	lat:-4.93	long:10.10
FID: 48501	site: GGH4	at 14.5 km	elevation: -3224	70 K/km	lat:-4.88	long:10.05
FID: 48541	site: GGH43	at 21.7 km	elevation: -3170	68 K/km	lat:-4.79	long:10.14
FID: 48543	site: GGH45	at 24.4 km	elevation: -3132	67 K/km	lat:-4.70	long:10.14
FID: 48609	site: GGH3	at 18.0 km	elevation: -3220	66 K/km	lat:-4.93	long:10.05

geotherm data within 50 km from Baboon Hole (lat: -4.940833, long: 9.944167; gradient: 71 (+/- 2.5) K/km)

FID: 48390	site: GGH39	at 23.7 km	elevation: -3090	78 K/km	lat:-5.02	long:10.14
FID: 48399	site: GGH40	at 22.4 km	elevation: -3083	77 K/km	lat:-4.97	long:10.14
FID: 48410	site: GGH41	at 22.1 km	elevation: -3105	75 K/km	lat:-4.93	long:10.14
FID: 48452	site: GGH16	at 20.5 km	elevation: -3201	72 K/km	lat:-4.84	long:10.10
FID: 48475	site: GGH15	at 18.1 km	elevation: -3191	71 K/km	lat:-4.88	long:10.10
FID: 48481	site: GGH17	at 23.8 km	elevation: -3190	70 K/km	lat:-4.79	long:10.10
FID: 48486	site: GGH42	at 23.0 km	elevation: -3141	71 K/km	lat:-4.88	long:10.14
FID: 48496	site: GGH14	at 17.0 km	elevation: -3179	71 K/km	lat:-4.93	long:10.10
FID: 48501	site: GGH4	at 13.4 km	elevation: -3224	70 K/km	lat:-4.88	long:10.05
FID: 48609	site: GGH3	at 11.8 km	elevation: -3220	66 K/km	lat:-4.93	long:10.05
FID: 48933	site: GGH13	at 19.0 km	elevation: -3178	57 K/km	lat:-5.02	long:10.10

FID: 48965	site: GGH12	at 21.8 km	elevation: -3164	56 K/km	lat:-5.07	long:10.10

geotherm data within 50 km from Worm Hole (lat: -4.751667, long: 9.945000; gradient: 70 (+/ 1) K/km)

FID: 48445	site: GGH44	at 22.0 km	elevation: -3135	72 K/km	lat:-4.75	long:10.14
FID: 48452	site: GGH16	at 19.3 km	elevation: -3201	72 K/km	lat:-4.84	long:10.10
FID: 48475	site: GGH15	at 22.2 km	elevation: -3191	71 K/km	lat:-4.88	long:10.10
FID: 48481	site: GGH17	at 17.3 km	elevation: -3190	70 K/km	lat:-4.79	long:10.10
FID: 48501	site: GGH4	at 18.6 km	elevation: -3224	70 K/km	lat:-4.88	long:10.05
FID: 48541	site: GGH43	at 22.4 km	elevation: -3170	68 K/km	lat:-4.79	long:10.14
FID: 48543	site: GGH45	at 22.7 km	elevation: -3132	67 K/km	lat:-4.70	long:10.14
FID: 48609	site: GGH3	at 22.7 km	elevation: -3220	66 K/km	lat:-4.93	long:10.05

geotherm data within 50 km from MV #10 (lat: 33.535556, long: 136.268889; gradient: N/A)

FID: 41384	site: RYOFU 81-6	at 17.1 km	elevation: -2060	115 K/km	lat:33.41	long:136.37
FID: 41385	site: RYOFU 81-7	at 10.4 km	elevation: -1930	105 K/km	lat:33.57	long:136.37
FID: 57792	site: NT-B	at 19.1 km	elevation: -2055	58 K/km	lat:33.42	long:136.42

geotherm data within 50 km from MV #4 (lat: 33.664722, long: 136.633889; gradient: N/A)

FID: 50900	site: null	at 17.3 km	elevation: -1999	0 K/km	lat:33.82	long:136.65
FID: 57795	site: NT-D	at 1.8 km	elevation: -2073	45 K/km	lat:33.65	long:136.64

geotherm data within 50 km from MV #2 (lat: 33.680833, long: 136.921944; gradient:N/A)

FID: 59977	site: GH97 307	at 22.1 km	elevation: -1990	0 K/km	lat:33.82	long:137.10

geotherm data within 50 km from Nascent Ridge (lat: N/A, long: N/A; gradient: N/A)

geotherm data within 50 km from Flare 2 (lat: 24.835556, long: 63.028889; gradient: N/A)

geotherm data within 50 km from Area 1 (lat: 78.547325, long: 10.237540; gradient: N/A)

geotherm data within 50 km from Area 2 (lat: 78.654236, long: 9.257554; gradient: N/A)

geotherm data within 50 km from Area 2 (lat: 78.654196, long: 9.434012; gradient: N/A)

geotherm data within 50 km from Area 3 (lat: 78.620308, long: 9.410987; gradient: N/A)

geotherm data within 50 km from Area 3 (lat: 78.620172, long: 9.409495; gradient: N/A)

geotherm data within 50 km from Area 4 (lat: 78.555436, long: 9.475971; gradient: N/A)

geotherm data within 50 km from Haakon Mosby MV (lat: 72.001389, long: 14.718611; gradient: 59 (+/- 3.7) K/km)

FID: 44407	site: PL96-5a 36 B-296	at 0.8 km	elevation: -1228	817 K/km	lat:72.01	long:14.73
FID: 44414	site: PL96-5b 36 B-507	at 0.7 km	elevation: -1228	637 K/km	lat:72.00	long:14.74
FID: 44447	site: HM95-20	at 0.8 km	elevation: -1260	314 K/km	lat:72.01	long:14.73
FID: 44470	site: PL96-7b 27 G-342	at 0.6 km	elevation: -1224	167 K/km	lat:72.01	long:14.71
FID: 44491	site: PL96-7a 27 G-230	at 0.5 km	elevation: -1224	141 K/km	lat:72.00	long:14.71
FID: 44525	site: 47 G	at 1.3 km	elevation: -1230	0 K/km	lat:72.00	long:14.68
FID: 44540	site: PL96-7c 36 B-496	at 1.0 km	elevation: -1233	108 K/km	lat:72.01	long:14.71
FID: 44679	site: PL96-5c 36B-784	at 1.0 km	elevation: -1249	68 K/km	lat:72.00	long:14.75
FID: 44693	site: HM95-22a	at 6.9 km	elevation: -1147	68 K/km	lat:71.98	long:14.91
FID: 44756	site: 108UB84	at 24.5 km	elevation: -1433	59 K/km	lat:72.00	long:14.01
FID: 44767	site: HM95-21	at 23.5 km	elevation: -1506	71 K/km	lat:71.94	long:14.07
FID: 44804	site: HM95-22c	at 4.5 km	elevation: -1215	56 K/km	lat:71.99	long:14.85
FID: 44817	site: PL96-5e 36 B-1320	at 1.6 km	elevation: -1218	51 K/km	lat:72.00	long:14.76
FID: 44828	site: HM95-22b	at 6.8 km	elevation: -1155	54 K/km	lat:71.98	long:14.91
FID: 45516	site: PL96-6d 36 B-376	at 0.5 km	elevation: -1233	0 K/km	lat:72.00	long:14.73
FID: 45517	site: PL96-6c 36 B-219	at 0.6 km	elevation: -1220	0 K/km	lat:72.01	long:14.72
FID: 45524	site: 85-95	at 0.9 km	elevation: -1257	0 K/km	lat:72.01	long:14.73
FID: 45530	site: PL96-6b 27 G-460	at 0.4 km	elevation: -1247	0 K/km	lat:72.00	long:14.72
FID: 45531	site: PL96-6a 27 G-186	at 0.8 km	elevation: -1223	0 K/km	lat:72.01	long:14.70
FID: 45533	site: 75-95	at 9.4 km	elevation: -1245	0 K/km	lat:71.92	long:14.77
FID: 45534	site: 73-95	at 6.4 km	elevation: -1380	0 K/km	lat:71.95	long:14.66
FID: 45545	site: 77-95	at 19.8 km	elevation: -1419	0 K/km	lat:71.85	long:14.42
FID: 45546	site: 74-95	at 8.4 km	elevation: -1314	0 K/km	lat:71.93	long:14.65
FID: 45568	site: 69-95	at 6.3 km	elevation: -1269	0 K/km	lat:72.04	long:14.58
FID: 45570	site: 68-95	at 6.3 km	elevation: -1161	0 K/km	lat:72.03	long:14.57
FID: 45572	site: 78-95	at 20.2 km	elevation: -1521	0 K/km	lat:71.90	long:14.23
FID: 45578	site: 72-95	at 0.8 km	elevation: -1255	0 K/km	lat:72.01	long:14.73

geotherm data within 50 km from Bush Hill (lat: 27.784722, long: -91.501000; gradient: N/A)

geotherm data within 50 km from Hydrate Ridge (lat: 44.571389, long: -125.102222; gradient: 71 (+/- 5.4) K/km)

FID: 37431	site: 2	at 7.6 km	elevation: -735	172 K/km	lat:44.63	long:-125.07
FID: 37432	site: 3	at 9.0 km	elevation: -768	148 K/km	lat:44.65	long:-125.14
FID: 37433	site: 4	at 6.2 km	elevation: -820	133 K/km	lat:44.62	long:-125.06
FID: 37434	site: 5	at 10.4 km	elevation: -900	156 K/km	lat:44.66	long:-125.14
FID: 37435	site: 6	at 6.5 km	elevation: -973	72 K/km	lat:44.62	long:-125.06
FID: 43263	site: AII112-1A	at 18.6 km	elevation: -2337	78 K/km	lat:44.68	long:-125.29
FID: 43264	site: AII112-1C	at 16.8 km	elevation: -2375	82 K/km	lat:44.66	long:-125.27
FID: 43265	site: AII112-1D	at 16.5 km	elevation: -2380	92 K/km	lat:44.66	long:-125.27
FID: 43266	site: AII112-1E	at 16.1 km	elevation: -2380	77 K/km	lat:44.66	long:-125.26
FID: 43267	site: AII112-1F	at 15.4 km	elevation: -2380	82 K/km	lat:44.66	long:-125.25

FID: 43268	site: AII112-3A	at 22.9 km	elevation: -2983	70 K/km	lat:44.66	long:-125.36
FID: 43269	site: AII112-3B	at 22.4 km	elevation: -2903	32 K/km	lat:44.66	long:-125.35
FID: 43270	site: AII112-3C	at 22.0 km	elevation: -2779	36 K/km	lat:44.66	long:-125.35
FID: 43271	site: AII112-3D	at 21.5 km	elevation: -2790	38 K/km	lat:44.66	long:-125.34
FID: 43272	site: AII112-3E	at 21.5 km	elevation: -2917	44 K/km	lat:44.65	long:-125.35
FID: 43308	site: AII112-C10	at 17.9 km	elevation: -2264	0 K/km	lat:44.67	long:-125.28
FID: 43631	site: W836-9A	at 16.0 km	elevation: -2254	68 K/km	lat:44.65	long:-125.27
FID: 43632	site: W836-9B	at 17.6 km	elevation: -2120	74 K/km	lat:44.65	long:-125.30
FID: 43633	site: W836-9C	at 17.5 km	elevation: -2124	77 K/km	lat:44.65	long:-125.30
FID: 43634	site: W836-9D	at 19.0 km	elevation: -2015	65 K/km	lat:44.65	long:-125.31
FID: 43635	site: W836-9E	at 19.0 km	elevation: -2015	55 K/km	lat:44.65	long:-125.32
FID: 43637	site: W836-9G	at 22.7 km	elevation: -2864	34 K/km	lat:44.65	long:-125.37
FID: 43640	site: W836-10A	at 9.2 km	elevation: -935	99 K/km	lat:44.65	long:-125.14
FID: 43641	site: W836-10B	at 8.9 km	elevation: -911	43 K/km	lat:44.65	long:-125.07
FID: 43642	site: W836-10C	at 9.2 km	elevation: -948	44 K/km	lat:44.65	long:-125.06
FID: 43643	site: W836-10D	at 11.2 km	elevation: -1008	83 K/km	lat:44.65	long:-125.02
FID: 43644	site: W836-10E	at 13.8 km	elevation: -820	81 K/km	lat:44.65	long:-124.97
FID: 43659	site: W836-RK24	at 19.9 km	elevation: -2420	0 K/km	lat:44.66	long:-125.32
FID: 43660	site: W836-RK26	at 20.9 km	elevation: -2795	0 K/km	lat:44.65	long:-125.34
FID: 43661	site: W836-RK27	at 19.9 km	elevation: -2623	0 K/km	lat:44.65	long:-125.33

geotherm data within 50 km from Thessalonkiki MV (lat 35.418056, long: 30.250000; gradient: N/A)

FID: 61078	site: CH61-54	at 15.3 km	elevation: -2017	38 K/km	lat:35.33	long:30.12

geotherm data within 50 km from Venere MV Flare 1 (lat: 38.616667, long: 17.185000; gradient: N/A)

geotherm data within 50 km from Venere MV Flare 5 (lat: 38.584444, long: 17.200000; gradient: N/A)

geotherm data within 50 km from Venere MV western summit (lat: 38.601111, long: 17.183889; gradient: N/A)

2.8 REFERENCES

Aloisi G., Drews M., Wallmann K., Bohrmann G. (2004) Fluid expulsion from the Dvurechenskii mud volcano (Black Sea) - Part I. Fluid sources and relevance to Li, B, Sr, I and dissolved inorganic nitrogen cycles. *Earth Planet Sci Lett* **225**: 347–363. doi.org/10.1016/j.epsl.2004.07.006

Archer D. E., Buffett B. A. and Mcguire P. C. (2012) A two-dimensional model of the passive coastal margin deep sedimentary carbon and methane cycles. *Biogeosciences* **9**, 2859–2878. doi.org/1-.5194/bg-9-2859-2012

Ash J. L., Egger M., Treude T., Kohl I., Cragg B., Parkes R. J., Slomp C. P., Lollar B. S. and Young E. D. (2019) Exchange catalysis during anaerobic methanotrophy revealed by $^{12}CH_2D_2$ and $^{13}CH_3D$ in methane. *Geochemical Perspect. Lett.* **10**, 26–30. doi.org/10.7185/geochemlet.1910

Barnes R. O. and Goldberg E. D. (1976) Methane production and consumption in anoxic marine sediments. *Geology* **4**, 297–300. doi.org/10.1130/0091-7613(1976)4<297:MPACIA>2.0.CO;2

Bernard B. B., Brooks J. M. and Sackett W. M. (1976) Natural gas seepage in the Gulf of Mexico. *Earth Planet. Sci. Lett.* **31**, 48–54. doi.org/10.1016/0012-821X(76)90095-9

Berndt C. and Planke S. (2006) The plumbing system of the Håkon Mosby Mud Volcano - New insights from high-resolution 3D seismic data. AAPG/GSTT Hedberg Conference "Mobile Shale Basins- Genesis, Evolution and Hydrocarbon Systems". Port of Spain, Trinidad and Tobago, June 5-7, 2006.

Berner, U., and Faber, E., (1996) Empirical carbon isotope/maturity relationships for gases from algal kerogens and terrigenous organic matter, based on dry, open-system pyrolysis. *Org. Geochem*. **24**, 947–955. doi.org/10.1016/S0146-6380(96)00090-3

Bhatnagar G., Chatterjee S., Chapman W. G., Dugan B., Dickens G. R. and Hirasaki G. J. (2011) Analytical theory relating the depth of the sulfate-methane transition to gas hydrate distribution and saturation. *Geochemistry, Geophys. Geosystems* **12**, 3, Q03003. doi.org/10.1029/2010gc003397

Biastoch A., Treude T., Rüpke L. H., Riebesell U., Roth C., Burwicz E. B., Park W., Latif M., Böning C. W., Madec G. and Wallmann K. (2011) Rising Arctic Ocean temperatures cause gas hydrate destabilization and ocean acidification. *Geophys. Res. Lett.* **38**, L08602. doi.org/10.1029/2011GL047222

Bigeleisen J. and Mayer M. G. (1947) Calculation of equilibrium constrants for isotopic exchange reactions. *J. Chem. Phys.* **15**, 261–267. doi.org/10.1063/1.1746492

Bohrmann G. (2011) Short Cruise Report RV Meteor Cruise M84/2, 26 February - 2 April 2011.

Bohrmann G., Greinert J., Suess E. and Torres M. (1998) Authigenic carbonates from the Cascadia subduction zone and their relation to gas hydrate stability. *Geology* **26**, 647–650. doi.org/10.1130/0091-7613(1998)026<0647:ACFTCS>2.3.CO;2

Bohrmann G. and Torres M. E. (2006) Gas hydrate in marine sediments. In *Marine*

Geochemistry (eds. H. Schulz and M. Zabel). pp. 481–512.

Boote D. R. D., Sachsenhofer R. F., Tari G. and Arbouille D. (2018) Petroleum provinces of the Paratethyan region. *J. Pet. Geol.* **41**, 247–297. doi.org/10.1111/jpg.12703

Borowski W. S., Paull C. K. and Ussler W. (1996) Marine pore-water sulfate profiles indicate in situ methane flux from underlying gas hydrate. *Geology* **24**, 655–658. doi/org10.1130/0091-7613(1996)024<0655:MPWSPI>2.3.CO;2

Bourg I. C. and Sposito G. (2008) Isotopic fractionation of noble gases by diffusion in liquid water: Molecular dynamics simulations and hydrologic applications. *Geochim. Cosmochim. Acta* **72**, 2237–2247. doi.org/10.1016/j.gca.2008.02.012

Burdige D. J. (2011) Temperature dependence of organic matter remineralization in deeply-buried marine sediments. *Earth Planet. Sci. Lett.* **311**, 396–410. doi.org/10.1016/j.epsl.2001.09.043

Butt F. A., Elverhøi A., Solheim A. and Forsberg C. F. (2000) Deciphering Late Cenozoic development of the western Svalbard Margin from ODP Site 986 results. *Mar. Geol.* **169**, 373–390. doi.org/10.1016/S0025-3227(00)00088-8

Christensen J. N., Hofmann A. E. and Depaolo D. J. (2019) Isotopic fractionation of potassium by diffusion in methanol. *ACS Omega* **4**, 9497–9501.doi.org/10.1021/acomega.9b00690

Cohen H. A. and McClay K. (1996) Sedimentation and shale tectonics of the northwestern Niger Delta front. *Mar. Pet. Geol.* **13**, 313–328. doi.org/10.1016/0264-8172(95)00067-4

Damuth J. E. (1994) Neogene gravity tectonics and depositional processes on the deep Niger Delta continental margin. *Mar. Pet. Geol.* **11**, 320–346. doi.org/10.1016/0264-8172(94)90053-1

Davie, M.K., and Buffett, B.A. (2003) Sources of methane for marine gas hydrate: inferences from a comparison of observations and numerical models. *Earth Planet Sci Lett*. **206**, 51–63. doi.org/10.1016/S0012-821X(02)01064-6

Davy B., Pecher I., Wood R., Carter L. and Gohl K. (2010) Gas escape features off New Zealand: Evidence of massive release of methane from hydrates. *Geophys. Res. Lett.* **37**, L21309. doi.org/10.1029/2010gl045184

de Beer D., Sauter E., Niemann H., Kaul N., Foucher J.P., Witte U., Schlüter M., Boetius A. (2006) In situ fluxes and zonation of microbial activity in surface sedi- ments of the Hakon Mosby Mud Volcano. *Limnol Oceanogr* **51**(3): 1315–1331. doi.org/10.4319/lo.2006.51.3.1315

Deville, E., Guerlais, S.H., Callec, Y., Griboulard, R., Huyghe, P., Lallemant, S., Mascle, A., Noble, M., Schmitz, J. (2006) Liquefied vs stratified sediment mobilization processes: Insight from the South of the Barbados accretionary prism. *Tectonophysics* **428**, 33–47. doi.org/10.1016/j.tecto.2006.08.011

Deville, E. (2009) Mud volcano systems, in: Lewis, N., Moretti, A. (Eds.), Volcanoes: Formation, Eruptions and Modeling. Nova Science Publishers, Inc., 1–31.

Dickens G. R. (2011) Down the Rabbit Hole: Toward appropriate discussion of methane release from gas hydrate systems during the Paleocene-Eocene thermal maximum and other past hyperthermal events. *Clim. Past* **7**, 831–846. doi.org/10.5194/cp-7-831-2011

Dickens G. R. and Quinby-Hunt M. S. (1997) Methane hydrate stability in pore water: A simple theoretical approach for geophysical applications. *J. Geophys. Res. Solid Earth* **102**, 773–783. doi.org/10.1029/96JB02941

Dimitrov L. I. (2002) Mud volcanoes—the most important pathway for degassing deeply buried sediments. *Earth-Science Rev.* **59**, 49–76. doi.org/10.1016/S0012-8252(02)00069-7

Dong, G., Xie, H., Formolo, M., Lawson, M., Sessions, A., Eiler, J. (2021) Clumped isotope effects of thermogenic methane formation: Insights from pyrolysis of hydrocarbons. *Geochim. Cosmochim. Acta* **303**, 159–183. doi.org/10.1016/j.gca.2021.03.009

Douglas P. M. J., Gonzalez Moguel R., Walter Anthony K. M., Wik M., Crill P. M., Dawson K. S., Smith D. A., Yanay E., Lloyd M. K., Stolper D. A., Eiler J. M. and Sessions A. L. (2020a) Clumped isotopes link older carbon substrates with slower rates of methanogenesis in northern lakes. *Geophys. Res. Lett.* **47**, e2019GL086756. doi.org/10.1029/2019GL086756

Douglas P. M. J., Stolper D. A., Eiler J. M., Sessions A. L., Lawson M., Shuai Y., Bishop A., Podlaha O. G., Ferreira A. A., Santos Neto E. V., Niemann M., Steen A. S., Huang L., Chimiak L., Valentine D. L., Fiebig J., Luhmann A. J., Seyfried W. E., Etiope G., Schoell M., Inskeep W. P., Moran J. J. and Kitchen N. (2017) Methane clumped isotopes: Progress and potential for a new isotopic tracer. *Org. Geochem.* **113**, 262–282. doi.org/10.1016/j.orggeochem.2017.07.016

Eldholm O., Sundvor E., Vogt P. R., Hjelstuen B. O., Crane K., Nilsen A. K. and Gladczenko T. P. (1999) SW Barents Sea continental margin heat flow and Hakon Mosby Mud Volcano. *Geo-Marine Lett.* **19**, 29–37. doi.org/10.1007/s003670050090

Eldridge D. L., Korol R., Lloyd M. K., Turner A. C., Webb M. A., Miller T. F. and Stolper D. A. (2019) Comparison of experimental vs theoretical abundances of $^{13}CH_3D$ and $^{12}CH_2D_2$ for isotopically equilibrated systems from 1 to 500 °C. *ACS Earth Sp. Chem.* **3**, 2747–2764. doi.org/10.1021/acsearthspacechem.9b00244

Etiope G., Feyzullayev A., Milkov A. V., Waseda A., Mizobe K. and Sun C. H. (2009) Evidence of subsurface anaerobic biodegradation of hydrocarbons and potential secondary methanogenesis in terrestrial mud volcanoes. *Mar. Pet. Geol.* **26**, 1692–1703. doi.org/10.1016/j.marpetgeo.2008.12.002

Fischer D., Mogollón J. M., Strasser M., Pape T., Bohrmann G., Fekete N., Spiess V. and Kasten S. (2013) Subduction zone earthquake as potential trigger of submarine hydrocarbon seepage. *Nat. Geosci.* **6**, 647–651. doi.org/10.1038/ngeo1886

Freudenthal T. and Wefer G. (2013) Drilling cores on the sea floor with the remote-controlled sea floor drilling rig MeBo. *Geosci. Instrumentation, Methods Data Syst.* **2**, 329–337. doi.org/10.5194/gi-2-329-2013

Fuchs, S., Norden, B. (2021) International Heat Flow Commission: The Global Heat Flow Database: Release 2021. GFZ Data Services

Giunta T., Labidi J., Kohl I. E., Ruffine L., Donval J. P., Géli L., Çağatay M. N., Lu H. and Young E. D. (2021) Evidence for methane isotopic bond re-ordering in gas reservoirs sourcing cold seeps from the Sea of Marmara. *Earth Planet. Sci. Lett.* **553**, 116619. doi.org/10.1016/j.epsl.2020.116619

Giunta T., Young E. D., Warr O., Kohl I., Ash J. L., Martini A., Mundle S. O. C., Rumble D., Pérez-Rodríguez I., Wasley M., LaRowe D. E., Gilbert A. and Sherwood Lollar B. (2019) Methane sources and sinks in continental sedimentary systems: New insights from paired clumped isotopologues $^{13}CH_3D$ and $^{12}CH_2D_2$. *Geochim. Cosmochim. Acta* **245**, 327–351. doi.org/10.1016/j.gca.2018.10.030

Gonzalez Y., Nelson D. D., Shorter J. H., Mcmanus J. B., Formolo M. J., Wang D. T., Western C. M. and Ono S. (2019) Precise measurements of $^{12}CH_2D_2$ by tunable infrared laser direct absorption spectroscopy. *Anal. Chem.* **91**, 14967–14974.doi.org/10.1021/acs.analchem.9b03412

Graves C. A., James R. H., Sapart C. J., Stott A. W., Wright I. C., Berndt C., Westbrook G. K. and Connelly D. P. (2017) Methane in shallow subsurface sediments at the landward limit of the gas hydrate stability zone offshore western Svalbard. *Geochim. Cosmochim. Acta* **198**, 419–438. doi.org/10.1016/j.gca.2016.11.015

Gruen D. S., Wang D. T., Könneke M., Topçuoğlu B. D., Stewart L. C., Goldhammer T., Hinrichs K. U. and Ono S. (2018) Experimental investigation on the controls of clumped isotopologue and hydrogen isotope ratios in microbial methane. *Geochim. Cosmochim. Acta* **237**, 339–356. doi.org/10.1016/j.gca.2018.06.029

György Marton L., Tari G. C. and Lehmann C. T. (2000) Evolution of the Angolan passive margin, West Africa, with emphasis on post-salt structural styles. *Washingt. DC Am. Geophys. Union Geophys. Monogr. Ser.* **115**, 129–149. doi.org/10.1029/GM115p0129

Hachikubo A., Kosaka T., Kida M., Krylov A., Sakagami H., Minami H., Takahashi N. and Shoji H. (2007) Isotopic fractionation of methane and ethane hydrates between gas and hydrate phases. *Geophys. Res. Lett.* **34**, L21502. doi.org/10.1029/2007GL030557

Hamamoto H., Yamano M., Goto S., Kinoshita M., Fujino K. and Wang K. (2012) Heat flow distribution and thermal structure of the Nankai subduction zone off the Kii Peninsula. *Geochemistry, Geophys. Geosystems* **12**, Q0AD20. doi.org/10.1029/2011GC00362

Head I. M., Jones D. M. and Larter S. R. (2003) Biological activity in the deep subsurface and the origin of heavy oil. *Nature* **426**, 344–352. doi.org/10.1038/nature02134

Hensen C., Wallmann K., Schmidt M., Ranero C. R. and Suess E. (2004) Fluid expulsion related to mud extrusion off Costa Rica - A window to the subducting slab. *Geology* **32**, 201–204. doi.org/10.1130/g20119.1

Hirose T., Kawagucci S. and Suzuki K. (2011) Mechanoradical H_2 generation during simulated faulting: Implications for an earthquake-driven subsurface biosphere. *Geophys. Res. Lett.* **38**, L17303. doi.org/10.1029/2011GL048850

Holler T., Wegener G., Knittel K., Boetius A., Brunner B., Kuypers M. M. M. and Widdel F. (2009) Substantial $^{13}C/^{12}C$ and D/H fractionation during anaerobic oxidation of methane by

marine consortia enriched in vitro. *Environ. Microbiol. Rep.* **1**, 370–376. doi.org/10.1111/j.1758-2229.2009.00074.x

Horibe Y. and Craig H. (1995) D/H fractionation in the system methane-hydrogen-water. *Geochim. Cosmochim. Acta* **59**, 5209–5217. doi.org/10.1016.0016-7037(95)00391-6

Hunt J. (1996) *Petroleum Geochemistry and Geology*. second. ed. W. Freeman, New York.

Hyndman R. D. and Davis E. E. (1992) A mechanism for the formation of methane hydrate and seafloor bottom-simulating reflectors by vertical fluid expulsion. *J. Geophys. Res.* **97**, 7025-7041. doi.org/10.1029/91jb03061

Ijiri A., Iijima K., Tsunogai U., Ashi J. and Inagaki F. (2018a) Clay mineral suites in submarine mud volcanoes in the Kumano Forearc Basin, Nankai Trough: Constraints on the origin of mud volcano sediments. *Geosciences* **8**, 220. doi.org/10.3390/geosciences8060220

Ijiri A., Inagaki F., Kubo Y., Adhikari R. R., Hattori S., Hoshino T., Imanchi H., Kawagucci S., Morono Y., Ohtomo Y., Ono S., Sakai S., Takai K., Toki T., Wang D. T., Toshinaga M. Y., Arnold G. L., Ashi J., Case D. H., Feseker T., Hinrichs K.-U., Ikegawa Y., Ikehara M., Kallmeyer J., Kumagai H., Lever M. A., Morita S., Makamura K., Nakamura Y., Nishizawa M., Orphan V. J., Roy H., Schmidt F., Tani A., Tanikawa M., Terada T., Tomaru H., Tsuji T., Tsunogai U., Yamaguchi Y. T. and Yoshida N. (2018b) Deep-biosphere methane production stimulated by geofluids in the Nankai accretionary complex. *Sci. Adv.* **4**, eaao4631. doi.org/ 10.1126/sciadv.aao4631

Inagaki F., Hinrichs K.-U., Kubo Y., Bowles M. W., Heuer V. B., Hong W.-L., Hoshino T., Ijiri A., Imachi H., Ito M., Kaneko M., Lever M. A., Lin Y.-S., Methe B. A., Morita S., Morono Y., Tanikawa W., Bihan M., Bowden S. A., Elvert M., Glombitza C., Gross D., Harrington G. J., Hori T., Li K., Limmer D., Liu C.-H., Murayama M., Ohkouchi N., Ono S., Park Y.-S., Phillips S. C., Prieto-Mollar X., Purkey M., Riedinger N., Sanada Y., Sauvage J., Snyder G., Susilawati R., Takano Y., Tasumi E., Terada T., Tomaru H., Trembath-Reichert E., Wang D. T. and Yamada Y. (2015) Exploring deep microbial life in coal-bearing sediment down to 2.5 km below the ocean floor. *Science.* **349**, 420–424. doi.org/10.1126/science.aaa6882

Ishikawa T. and Nakamura E. (1993) Boron isotope systematics of marine sediments. *Earth Planet. Sci. Lett.* **117**, 567–580. doi.org/10.1016/0012-821X(93)90103-G

Jautzy J. J., Douglas P. M. J., Xie H., Eiler J. M. and Clark I. D. (2021) CH_4 isotopic ordering records ultra-slow hydrocarbon biodegradation in the deep subsurface. *Earth Planet. Sci. Lett.* **562**, 116841. doi.org/10.1016/j.epsl.2021.116841

Jenden P. D. and Kaplan I. R. (1986) Comparison of microbial* gases from the Middle America Trench and Scripps Submarine Canyon: implications for the origin of natural gas. *Appl. Geochemistry* **1**, 631–646. doi.org/10.1016.0883-2927(86)90085-5

Jenden P. D., Kaplan I. R., Hilton D. R. and Craig H. (1993) Abiogenic hydrocarbons and mantle helium in oil and gas fields. *United States Geol. Surv. Prof. Pap. (United States)*.

Kastner M., Solomon E. A., Harris R. N. and Torres M. E. (2014) Fluid origins, thermal regimes, and fluid and solute fluxes in the forearc of subduction zones. *Developments in Marine*

Geology 7. 671–733. doi.org/10.1016/B978-0-444-62617-2.00022-0

Kaul N., Foucher J. P. and Heesemann M. (2006) Estimating mud expulsion rates from temperature measurements on Håkon Mosby Mud Volcano, SW Barents Sea. *Mar. Geol.* **229**, 1–14. doi.org/10.1016/j.margeo.2006.02.004

Kawagucci S., Miyazaki J., Morono Y., Seewald J. S., Wheat C. G. and Takai K. (2018) Cool, alkaline serpentinite formation fluid regime with scarce microbial habitability and possible abiotic synthesis beneath the South Chamorro Seamount. *Prog. Earth Planet. Sci.* **5**, 1-20. doi.org/10.1186/s40645-018-0232-3

Kennett J. P., Cannariato K. G., Hendy I. L. and Behl R. J. (2003) Methane hydrates in quaternary climate change: The clathrate gun hypothesis. In *Methane Hydrates in Quatarnary Climate Change: The Clathrate Gun Hypothesis* (eds. J. P. Kennett, K. G. Cannariato, I. L. Hendy, and R. J. Behl). Wiley Online Library. pp. 1–9.

Kevorkian R. T., Callahan S., Winstead R. and Lloyd K. G. (2021) ANME-1 archaea may drive methane accumulation and removal in estuarine sediments. *Environ. Microbiol. Rep.* **13**, 185–194. doi.org/10.1111/1758-2229.12926

Kharaka Y. K. and Mariner R. H. (1989) Chemical geothermometers and their application to formation waters from sedimentary basins. In *Thermal History of Sedimentary Basins* (eds. N. D. Naeser and T. H. McCulloh). Springer New York, New York, NY. pp. 99–117.

King L. H. and MacLean B. (1970) Pockmarks on the Scotian Shelf. *Bull. Geol. Soc. Am.* **81**, 3141–3148. doi.org/10.1130/0016-7606(1970)81[3141:POTSS]2.0.CO;2

Klasek S. A., Torres M. E., Loher M., Bohrmann G., Pape T. and Colwell F. S. (2019) Deep-sourced fluids from a convergent margin host distinct subseafloor microbial communities that change upon mud flow expulsion. *Front. Microbiol.* **10**, 1–17. doi.org/10.3389/fmicb.2019.01436

Klaucke I., Sahling H., Weinrebe W., Blinova V., Bürk D., Lursmanashvili N. and Bohrmann G. (2006) Acoustic investigation of cold seeps offshore Georgia, eastern Black Sea. *Mar. Geol.* **231**, 51–67. doi.org/10.1016/j.margeo.2006.05.011

Klein F., Grozeva N. G. and Seewald J. S. (2019) Abiotic methane synthesis and serpentinization in olivine-hosted fluid inclusions. *Proc. Natl. Acad. Sci. U. S. A.* **116**, 17666–17672. doi.org/10.1073/pnas.1907871116

Knies J., Daszinnies M., Plaza-Faverola A., Chand S., Sylta Ø., Bünz S., Johnson J. E., Mattingsdal R. and Mienert J. (2018) Modelling persistent methane seepage offshore western Svalbard since early Pleistocene. *Mar. Pet. Geol.* **91**, 800–811. doi.org/10.1016/j.marpetgeo.2018.01.020

Knittel K., Lösekann T., Boetius A., Kort R. and Amann R. (2005) Diversity and distribution of methanotrophic archaea at cold seeps diversity and distribution of methanotrophic archaea at cold seeps. *Appl. Environ. Microbiol.* **71**, 467–479. doi.org/10.1016/j.marpetgeo.2018.01.020

Kondo W., Ohtsuka K., Ohmura R., Takeya S. and Mori Y. H. (2014) Clathrate-hydrate formation from a hydrocarbon gas mixture: Compositional evolution of formed hydrate

during an isobaric semi-batch hydrate-forming operation. *Appl. Energy* **113**, 864–871. doi.org/10.1016/j.apenergy.2013.08.033

Kopf A. and Deyhle A. (2002) Back to the roots: Boron geochemistry of mud volcanoes and its implications for mobilization depth and global B cycling. *Chem. Geol.* **192**, 195–210. doi.org/10.1016/S0009-2541(02)00221-8

Kopf A. J. (2002) Significance of mud volcanism. *Rev. Geophys.* **40**, 2–52. doi.org/10.1029/2000RG000093

Körber J. H., Sahling H., Pape T., dos Santos Ferreira C., MacDonald I. and Bohrmann G. (2014) Natural oil seepage at Kobuleti Ridge, eastern Black Sea. *Mar. Pet. Geol.* **50**, 68–82. doi.org/10.1016/j.marpetgeo.2013.11.007

Krastel S., Spiess V., Ivanov M., Weinrebe W., Bohrmann G., Shashkin P. and Heidersdorf F. (2003) Acoustic investigations of mud volcanoes in the Sorokin Trough , Black Sea. *Geo-Mar. Lett.* **23**, 230–238. doi.org/10.1007/s00367-003-0143-0

Krey V., Canadell J. G., Nakicenovic N., Abe Y., Andruleit H., Archer D., Grubler A., Hamilton N. T. M., Johnson A., Kostov V., Lamarque J. F., Langhorne N., Nisbet E. G., O'Neill B., Riahi K., Riedel M., Wang W. and Yakushev V. (2009) Gas hydrates: entrance to a methane age or climate threat? *Environ. Res. Lett.* **4**, 034007. doi.org/10.1088/1748-9326/4/3/034007

Kulm L. D., Suess E., Moore J. C., Carson B., Lewis B. T., Ritger S. D., Kadko D. C., Thornburg T. M., Embley R. W., Rugh W. D., Massoth G. J., Langseth M. G., Cochrane G. R. and Scamman R. L. (1986) Oregon subduction zone: venting, fauna, and carbonates. *Science* **231**, 561–566. doi.org/10.1126/science.231.4738.561

Kutas R. I., Kobolev V. P. and Tsvyashchenko V. A. (1998) Heat flow and geothermal model of the Black Sea depression. *Tectonophysics* **291**, 91–100. doi.org/10.1016/S0040-1951(98)00033-X

Labails C., Géli L., Sultan N., Novosel I. and Winters W. J. (2007) Thermal measurements from the Gulf of Mexico Continental Slope: Results from the PAGE Cruise. 2016-09-29. edx.netl.doe.gov/dataset/thermal-measurements-from-the-gulf=of-mexico-continental-slope-results-from-the-page-cruise

Labidi, J., Young, E.D., Giunta, T., Kohl, I.E., Seewald, J., Tang, H., Lilley, M.D., and Früh-Green, G.L. (2020). Methane thermometry in deep-sea hydrothermal systems: Evidence for re-ordering of doubly-substituted isotopologues during fluid cooling. *Geochim. Cosmochim. Acta* **288**, 248–261. doi.org/10.1016/j.gca.2020.08.013

Lein A., Vogt P., Crane K., Egorov A., and Ivanov M. (1999) Chemical and isotopic evidence for the nature of the fluid in CH_4-containing sediments of the Hakon Mosby Mud Volcano. *Geo-Marine Lett.* **19**, 76–83. doi.org/10.1007/s003670050095

Levin L. A. (2005) Ecology of cold seep sediments: interactions of fauna with flow, chemistry and microbes. In *Oceanography and marine biology* CRC Press. pp. 11–56.

Lin, Y.S., Heuer, V.B., Goldhammer, T., Kellermann, M.Y., Zabel, M., and Hinrichs, K.U. (2012). Towards constraining H_2 concentration in subseafloor sediment: A proposal for

combined analysis by two distinct approaches. *Geochim. Cosmochim. Acta* **77**, 186–201. doi.org/10.1016/j.gca.2011.11.008

Linke P. and Suess E. (2001) R/V Sonne Cruise Report SO148: Tecflux-11-2000, TECtonically-induced material FLuxes, Victoria-Victoria-Victoria, July 20 - August 15, 2000. *GEOMAR-Report* **098**, 10.3289/geomar_rep_98_2001.

Liu Q. and Liu Y. (2016) Clumped-isotope signatures at equilibrium of CH_4, NH_3, H_2O, H_2S and SO_2. *Geochim. Cosmochim. Acta* **175**, 252–270. doi.org/10.1016/j.gca.2015.11.040

Lloyd K. G., Alperin M. J. and Teske A. (2011) Environmental evidence for net methane production and oxidation in putative ANaerobic MEthanotrophic (ANME) archaea. *Environ. Microbiol.* **13**, 2548–2564. doi.org/10.1111/j.1462-2920.2011.02526.x

Loher M., Pape T., Marcon Y., Römer M., Wintersteller P., Praeg D., Torres M., Sahling H. and Bohrmann G. (2018) Mud extrusion and ring-fault gas seepage - Upward branching fluid discharge at a deep-sea mud volcano. *Sci. Rep.* **8**, 6275. doi.org/10.1038/s41598-018-24689-1

MacDonald I. R., Guinasso Jr N. L., Sassen R., Brooks J. M., Lee L. and Scott K. T. (1994) Gas hydrate that breaches the seafloor on the continental slope of the Gulf of Mexico. *Geology* **22**, 699–702. doi.org/10.1130/0091-7613(1994)022<0699:ghtbts>2.3.co;2

Mazzini A. and Etiope G. (2017) Mud volcanism: An updated review. *Earth-Science Rev.* **168**, 81–112. doi.org/10.1016/j.earscirev.2017.03.001.

McDermott J. M., Seewald J. S., German C. R. and Sylva S. P. (2015) Pathways for abiotic organic synthesis at submarine hydrothermal fields. *Proc. Natl. Acad. Sci. U. S. A.* **112**, 7668–7672. doi.org/10.1073/pnas.1506295112

Meister, P., and Reyes, C. (2019). The carbon-isotope record of the sub-seafloor biosphere. *Geosci*. **9**, 1–25. doi.org/10.3390/geosciences9120507

Meredith D. J. and Egan S. S. (2002) The geological and geodynamic evolution of the eastern Black Sea basin: insights from 2-D and 3-D tectonic modelling. *Tectonophysics* **350**, 157–179. doi.org/10.1016/S0040-1951(02)00121-X

Middelburg J. J. (1989) A simple rate model for organic matter decomposition in marine sediments. *Geochim. Cosmochim. Acta* **53**, 1577–1581. doi.org/10.1016/0016-7037(89)90239-1

Milkov A. V. (2004) Global estimates of hydrate-bound gas in marine sediments: How much is really out there? *Earth-Science Rev.* **66**, 183–197. doi.org/10.1016/j.earscirev.2003.11.002

Milkov A. V. (2005) Molecular and stable isotope compositions of natural gas hydrates: A revised global dataset and basic interpretations in the context of geological settings. *Org. Geochem.* **36**, 681–702. doi.org/10.1016/j.orggeochem.2005.01.010

Milkov A. V. (2000) Worldwide distribution of submarine mud volcanoes and associated gas hydrates. *Mar. Geol.* **167**, 29–42. doi.org/10.1016/S00025-3227(00)00022-0

Milkov A. V. and Dzou L. (2007) Geochemical evidence of secondary microbial methane from

very slight biodegradation of undersaturated oils in a deep hot reservoir. *Geology* **35**, 455–458. doi.org/10.1130/g23557a.1

Milkov A. V. and Etiope G. (2018) Revised genetic diagrams for natural gases based on a global dataset of >20,000 samples. *Org. Geochem.* **125**, 109–120. doi.org/10.1016/j.orggeochem.2018.09.002

Moore G. F., Saffer D., Studer M. and Costa Pisani P. (2011) Structural restoration of thrusts at the toe of the Nankai Trough accretionary prism off Shikoku Island, Japan: Implications for dewatering processes. *Geochemistry, Geophys. Geosystems* **12**. Q0AD12. doi.org/10.1029/2010GC003453

Myhre A. M., Thiede J. and Firth J. V (1995) North Atlantic-Arctic Gateway Sites 907-913. *Proc. Ocean Drill. Progr.* **151**.

Niemann, H., and Boetius, A. (2010). Mud Volcanoes, in: Timmis, K.N. (Ed.), Handbook of Hydrocarbon and Lipid Microbiology. Springer-Verlag Berlin Heidelberg, pp. 206–213. doi.org/10.1007/978-3-642-00810-8_3

Nishio Y., Ijiri A., Toki T., Morono Y., Tanimizu M., Nagaishi K. and Inagaki F. (2015) Origins of lithium in submarine mud volcano fluid in the Nankai accretionary wedge. *Earth Planet. Sci. Lett.* **414**, 144–155. doi.org/10.1016/j.epsl.2015.01.018

Okumura T., Kawagucci S., Saito Y., Matsui Y., Takai K. and Imachi H. (2016) Hydrogen and carbon isotope systematics in hydrogenotrophic methanogenesis under H_2-limited and H_2-enriched conditions: implications for the origin of methane and its isotopic diagnosis. *Prog. Earth Planet. Sci.* **3**, 2–15. doi.org/10.1186/s40645-016-0088-3

Ono S., Rhim J. H., Gruen D. S., Taubner H., Kölling M. and Wegener G. (2021) Clumped isotopologue fractionation by microbial cultures performing the anaerobic oxidation of methane. *Geochim. Cosmochim. Acta* **293**, 70–85. doi.org/10.1016/j.gca.2020.10.015

Ono S., Wang D. T., Gruen D. S., Sherwood Lollar B., Zahniser M. S., McManus B. J. and Nelson D. D. (2014) Measurement of a doubly substituted methane isotopologue, $^{13}CH_3D$, by tunable infrared laser direct absorption spectroscopy. *Anal. Chem.* **86**, 6487–6494. doi.org/10.1021/ac5010579

Orcutt B., Boetius A., Elvert M., Samarkin V. and Joye S. B. (2005) Molecular biogeochemistry of sulfate reduction, methanogenesis and the anaerobic oxidation of methane at Gulf of Mexico cold seeps. *Geochim. Cosmochim. Acta* **69**, 4267–4281. doi.org/10.1016/j.gca.2005.04.012

Orphan V. J., House C. H., Hinrichs K.-U., McKeegan K. D. and DeLong E. F. (2002) Multiple archaeal groups mediate methane oxidation in anoxic cold seep sediments. *Proc. Natl. Acad. Sci.* **99**, 7663–7668. doi.org/10.1073/pnas.072210299

Pape T., Bahr A., Klapp S. A., Abegg F. and Bohrmann G. (2011a) High-intensity gas seepage causes rafting of shallow gas hydrates in the southeastern Black Sea. *Earth Planet. Sci. Lett.* **307**, 35–46. doi.org/10.1016/j.epsl.2011.04.030

Pape T., Bahr A., Rethemeyer J., Kessler J. D., Sahling H., Hinrichs K. U., Klapp S. A., Reeburgh W. S. and Bohrmann G. (2010a) Molecular and isotopic partitioning of low-

molecular-weight hydrocarbons during migration and gas hydrate precipitation in deposits of a high-flux seepage site. *Chem. Geol.* **269**, 350–363. doi.org/10.1016/j.chemgeo.2009.10.009

Pape T., Blumenberg M., Reitz A., Scheeder G., Schmidt M., Haeckel M., Blinova V. N., Ivanov M. K., Sahling H., Wallmann K. and Bohrmann G. (2021) Oil and gas seepage offshore Georgia (Black Sea) – Geochemical evidences for a paleogene-neogene hydrocarbon source rock. *Mar. Pet. Geol.* **128**, 104995. doi.org/10.1016/j.marpetgeo.2021.104995

Pape T., Bünz S., Hong W. L., Torres M. E., Riedel M., Panieri G., Lepland A., Hsu C. W., Wintersteller P., Wallmann K., Schmidt C., Yao H. and Bohrmann G. (2020a) Origin and transformation of light hydrocarbons ascending at an active pockmark on Vestnesa Ridge, Arctic Ocean. *J. Geophys. Res. Solid Earth* **125**, e2018JB016679. doi.org/10.1029/2018JB016679

Pape T., Feseker T., Kasten S., Fischer D. and Bohrmann G. (2011b) Distribution and abundance of gas hydrates in near-surface deposits of the Håkon Mosby Mud Volcano, SW Barents Sea. *Geochemistry, Geophys. Geosystems* **12**, 1–22. doi.org/10.1029/2011gc003575

Pape T., Geprägs P., Hammerschmidt S., Wintersteller P., Wei J., Fleischmann T., Bohrmann G. and Kopf A. (2014) Hydrocarbon seepge and its sources at mud volcanoes of the Kumano forarc basin, Nankai Trough subduction zone. *Geochemistry, Geophys. Geosystems*, 2180–2194. doi.org/10.1002/2013gc005057

Pape T., Kasten S., Zabel M., Bahr A., Abegg F., Hohnberg H. J. and Bohrmann G. (2010b) Gas hydrates in shallow deposits of the Amsterdam mud volcano, Anaximander Mountains, northeastern Mediterranean Sea. *Geo-Marine Lett.* **30**, 187–206. doi.org/10.1007/s00367-010-0197-8

Pape T., Ruffine L., Hong W. L., Sultan N., Riboulot V., Peters C. A., Kölling M., Zabel M., Garziglia S. and Bohrmann G. (2020b) Shallow gas hydrate accumulations at a Nigerian deepwater pockmark—quantities and dynamics. *J. Geophys. Res. Solid Earth* **125**. doi.org/10.1029/2019jb018283Paull C. K., Buelow W. J., Ussler III W. and Borowski W. S. (1996) Increased continental-margin slumping frequency during sea-level lowstands above gas hydrate--bearing sediments. *Geology* **24**, 143–146. doi.org/10.1130/0091-7613(1996)024<0143:icmsfd>2.3.co;2

Perry E. and Hower J. (1972) Late-stage dehydration in deeply buried pelitic sediments. *Am. Assoc. Pet. Geol. Bull.* **56**, 2013–2021. doi.org/10.1306/819A41A8-16C5-11D7-8645000102C1865D

Piñero E., Marquardt M., Hensen C., Haeckel M. and Wallmann K. (2013) Estimation of the global inventory of methane hydrates in marine sediments using transfer functions. *Biogeosciences* **10**, 959–975. doi.org/10.5194/bg-10-959-2013

Pohlman, J.W., Kaneko, M., Heuer, V.B., Coffin, R.B., Whiticar, M. (2009) Methane sources and production in the northern Cascadia margin gas hydrate system. *Earth Planet. Sci. Lett.* **287**, 504–512. doi.org/10.1016/j.epsl.2009.08.037

Prinzhofer A. and Pernaton É. (1997) Isotopically light methane in natural gas: Bacterial imprint or diffusive fractionation? *Chem. Geol.* **142**, 193–200. doi.org/10.1016/S0009-

2541(97)00082-X

Reeburgh W. S. (1976) Methane consumption in Cariaco Trench waters and sediments. *Earth Planet. Sci. Lett.* **28**, 337–344. doi.org/10.1016/0012-821X(76)90195-3

Reitz A., Pape T., Haeckel M., Schmidt M., Berner U., Scholz F., Liebetrau V., Aloisi G., Weise S. M. and Wallmann K. (2011) Sources of fluids and gases expelled at cold seeps offshore Georgia, eastern Black Sea. *Geochim. Cosmochim. Acta* **75**, 3250–3268. doi.org/10.1016/j.gca.2011.03.018

Riedel M., Wallmann K., Berndt C., Pape T., Freudenthal T., Bergenthal M., Bünz S. and Bohrmann G. (2018) In situ temperature measurements at the svalbard continental margin: Implications for gas hydrate dynamics. *Geochemistry, Geophys. Geosystems* **19**, 1165–1177. doi.org/10.1002/2017GC007288

Robinson A. G., Rudat J. H., Banks C. J. and Wiles R. L. F. (1996) Petroleum geology of the Black Sea. *Mar. Pet. Geol.* **13**, 195–223. doi.org/10.1016/0264-8172(95)00042-9

Römer M., Sahling H., Pape T., Bohrmann G. and Spieß V. (2012) Quantification of gas bubble emissions from submarine hydrocarbon seeps at the Makran continental margin (offshore Pakistan). *J. Geophys. Res. Ocean.* **117**, C10015. doi.org/10.1029/2011jc007424

Rothman D. H. and Forney D. C. (2007) Physical model for the decay and preservation of marine organic carbon. *Science.* **316**, 1325–1328. doi.org/10.1126/science.1138211

Rumble D., Ash J. L., Wang P. L., Lin L. H., Lin Y. T. and Tu T. H. (2018) Resolved measurements of $^{13}CDH_3$ and $^{12}CD_2H_2$ from a mud volcano in Taiwan. *J. Asian Earth Sci.* **167**, 218–221. doi.org/10.1016/j.jseaes.2018.03.007Sachsenhofer R. F., Popov S. V., Bechtel A., Coric S., Francu J., Gratzer R., Grunert P., Kotarba M., Mayer J., Pupp M., Rupprecht B. J. and Vincent S. J. (2018) Oligocene and Lower Miocene source rocks in the Paratethys: palaeogeographical and stratigraphic controls. *Geol. Soc. London Spec. Publ.* **464**, 267–306. doi.org/10.1144/sp464.1

Saffer D., McNeill L., Byrne T., Araki E., Toczko S., Eguchi N., Takahashi K. andthe Expedition 319 Scientists (2010) Expedition 319 summary. *Proc. IODP, 319*. doi.org/10.2204/iodp.proc.319.101.2010

Sahling H., Bohrmann G., Artemov Y. G., Bahr A., Brüning M., Klapp S. A., Klaucke I., Kozlova E., Nikolovska A., Pape T., Reitz A. and Wallmann K. (2009) Vodyanitskii mud volcano, Sorokin trough, Black Sea: Geological characterization and quantification of gas bubble streams. *Mar. Pet. Geol.* **26**, 1799–1811. doi.org/10.1016/j.marpetgeo.2009.01.010

Sahling H., Bohrmann G., Spiess V., Bialas J., Breitzke M., Ivanov M., Kasten S., Krastel S. and Schneider R. (2008) Pockmarks in the Northern Congo Fan area, SW Africa: Complex seafloor features shaped by fluid flow. *Mar. Geol.* **249**, 206–225. doi.org/10.1016/j.margeo.2007.11.010

Sahling H., Römer M., Pape T., Bergès B., dos Santos Fereirra C., Boelmann J., Geprägs P., Tomczyk M., Nowald N., Dimmler W., Schroedter L., Glockzin M. and Bohrmann G. (2014) Gas emissions at the continental margin west of Svalbard: Mapping, sampling, and quantification. *Biogeosciences* **11**, 6029–6046. doi.org10.5194/bg-11-6029-2014

Sassen R., Losh S. L., Cathles L., Roberts H. H., Whelan J. K., Milkov A. V, Sweet S. T. and DeFreitas D. A. (2001) Massive vein-filling gas hydrate: relation to ongoing gas migration from the deep subsurface in the Gulf of Mexico. *Mar. Pet. Geol.* **18**, 551–560. doi.org/10.1016/S0264-8172(01)00014-9

Saunois, M, Stavert, A.R., Poulter, B., Bousquet, P., Canadell, J.G., Jackson, R.B., Raymond, P.A., Dlugokencky, E.J., Houweling, S., Patra, P.K., Ciais, P., Arora, V.K., Bastviken, D., Bergamaschi, P., Blake, D.R., Brailsford, G., Bruhwiler, L., Carlson, K.M., Carrol, M., Castaldi, S., Chandra, N., Crevoisier, C., Crill, P.M., Covey, K., Curry, C.L., Etiope, G., Frankenberg, C., Gedney, N., Hegglin, M.I., Höglund-Isaksson, L., Hugelius, G., Ishizawa, M., Ito, A., Janssens-Maenhout, G., Jensen, K.M., Joos, F., Kleinen, T., Krummel, P.B., Langenfelds, R.L., Laruelle, G.G., Liu, L., Machida, T., Maksyutov, S., McDonald, K.C., McNorton, J., Miller, P.A., Melton, J.R., Morino, I., Müller, J., Murguia-Flores, F., Naik, V., Niwa, Y., Noce, S., O'Doherty, S., Parker, R.J., Peng, C., Peng, S., Peters, G.P., Prigent, C., Prinn, R., Ramonet, M., Regnier, P., Riley, W.J., Rosentreter, J.A., Segers, A., Simpson, I.J., Shi, H., Smith, S.J., Steele, L.P., Thornton, B.F., Tian, H., Tohjima, Y., Tubiello, F.N., Tsuruta, A., Viovy, N., Voulgarakis, A., Weber, T.S., van Weele, M., van der Werf, G.R., Weiss, R.F., Worthy, D., Wunch, D., Yin, Y., Yoshida, Y., Zhang, W., Zhang, Z., Zhao, Y., Zheng, B., Zhu, Q., Zhu, Q., and Zhuang, Q. (2020) The global methane budget 2000--2017. *Earth Syst. Sci. Data* **12**, 1561–1623. doi.org/10.5194/essd-12-1561-2020

Scheller, S., Goenrich, M., Boecher, R., Thauer, R.K., and Jaun, B. (2010) The key nickel enzyme of methanogenesis catalyses the anaerobic oxidation of methane. *Nature* **465**, 606–608. doi.org/10.1038/nature09015

Schink B. (1997) Energetics of syntrophic cooperation in methanogenic degradation. *Microbiol. Mol. Biol. Rev.* **61**, 262–280. doi.org/10.1128/mmbr.61.2.262-280.1997

Seewald J. S. (2003) Organic-inorganic interactions in petroleum-producing sedimentary basins. *Nature* **426**, 327–333. doi.org/10.1038/nature02132

Sheremet, Y., Sosson, M., Ratzov, G., Sydorenko, G., Voitsitskiy, Z., Yegorova, T., Gintov, O., Murovskaya, A., 2016. An offshore-onland transect across the north-eastern Black Sea basin (Crimean margin): Evidence of Paleocene to Pliocene two-stage compression. Tectonophys. 688, 84-100. doi.org/10.1016/j.tecto.2016.09.015

Shuai Y., Douglas P. M. J., Zhang S., Stolper D. A., Ellis G. S., Lawson M., Lewan M. D., Formolo M., Mi J., He K., Hu G. and Eiler J. M. (2018) Equilibrium and non-equilibrium controls on the abundances of clumped isotopologues of methane during thermogenic formation in laboratory experiments: Implications for the chemistry of pyrolysis and the origins of natural gases. *Geochim. Cosmochim. Acta* **223**, 159–174. doi.org/10.1016/j.gca.2017.11.024

Shuai, Y., Xie, H., Zhang, S., Zhang, Y., and Eiler, J.M. (2021) Recognizing the pathways of microbial methanogenesis through methane isotopologues in the subsurface biosphere. *Earth Planet. Sci. Lett*. **566**, 116960. doi.org/10.1016/j.epsl.2021.116960

Stadnitskaia A., Ivanov M. K., Poludetkina E. N., Kreulen R. and van Weering T. C. E. (2008) Sources of hydrocarbon gases in mud volcanoes from the Sorokin Trough, NE Black Sea, based on molecular and carbon isotopic compositions. *Mar. Pet. Geol.* **25**, 1040–1057.

doi.org/10.16/j.marpetgeo.2007.08.001

Stolper D. A., Lawson M., Davis C. L., Ferreira A. A., Santos Neto E. V., Ellis G. S., Lewan M. D., Martini A. M., Tang Y., Schoell M., Sessions A. L. and Eiler J. M. (2014) Formation temperatures of thermogenic and biogenic methane. *Science.* **344**, 1500–1503. doi.org/10.1126/science.1254509

Stolper D. A., Lawson M., Formolo M. J., Davis C. L., Douglas P. M. J. and Eiler J. M. (2017) The utility of methane clumped isotopes to constrain the origins of methane in natural gas accumulations. *Geol. Soc. London, Spec. Publ.* **468**, SP468.3. doi.org/10.1144/SP468.3

Stolper D. A., Martini A. M., Clog M., Douglas P. M., Shusta S. S., Valentine D. L., Sessions A. L. and Eiler J. M. (2015) Distinguishing and understanding thermogenic and biogenic sources of methane using multiply substituted isotopologues. *Geochim. Cosmochim. Acta* **161**, 219–247. doi.org/10.1016/j.gca.2015.04.015

Suess E. (2014) Marine cold seeps and their manifestations: geological control, biogeochemical criteria and environmental conditions. *Int. J. Earth Sci.* **103**, 1889–1916. doi.org/10.1007/s00531-014-1010-0

Suess E., Torres M. E., Bohrmann G., Collier R. W., Greinert J., Linke P., Rehder G., Trehu A., Wallmann K., Winckler G. and Zuleger E. (1999) Gas hydrate destabilization: enhanced dewatering, benthic material turnover and large methane plumes at the Cascadia convergent margin. *Earth Planet. Sci. Lett.* **170**, 1–15. doi.org/10.1016/S0012-821X(99)00092-8

Sultan N., Bohrmann G., Ruffine L., Pape T., Riboulot V., Colliat J. L., Prunele A. D., Dennielou B., Garziglia S., Himmler T., Marsset T., Peters C. A., Rabiu A. and Wei J. (2014) Pockmark formation and evolution in deep water Nigeria: Rapid hydrate growth versus slow hydrate dissolution. *J. Geophys. Res. Earth* **119**, 2679–2694. doi.org/10.1002/2013JB010546

Thauer, R.K. (2019) Methyl (alkyl)-coenzyme M reductases: Nickel F-430-containing enzymes involved in anaerobic methane formation and in anaerobic oxidation of methane or of short chain alkanes. *Biochemistry* **58**, 5198–5220. doi.org/10.1021/acs.biochem.9b00164

Thiagarajan N., Kitchen N., Xie H., Ponton C., Lawson M., Formolo M. and Eiler J. (2020) Identifying thermogenic and microbial methane in deep water Gulf of Mexico Reservoirs. *Geochim. Cosmochim. Acta* **275**, 188–208. doi.org/10.1016/j.gca.2020.02.016

Torres M. E., Teichert B. M. A., Tréhu A. M., Borowski W. and Tomaru H. (2004) Relationship of pore water freshening to accretionary processes in the Cascadia margin: Fluid sources and gas hydrate abundance. *Geophys. Res. Lett.* **31**, 1–4. doi.org/10.1029/2004GL021219

Treude T., Boetius A., Knittel K., Wallmann K. and Jørgensen B. B. (2003) Anaerobic oxidation of methane above gas hydrates at Hydrate Ridge , NE Pacific Ocean. *Mar. Ecol. Prog. Ser.* **264**, 1–14. doi.org/10.3354/meps264001

Turner, A.C., Korol, R., Eldridge, D.L., Bill, M., Conrad, M.E., Miller, T.F. III, and Stolper, D.A. (2021) Experimental and theoretical determinations of hydrogen isotopic equilibrium in the system CH_4 -H_2 -H_2O from 3 to 200 °C, *Geochim. Cosmochim. Acta.* **314**, 223-269. doi.org/10.1016/j.gca.2021.04.026

Urey H. C. (1947) The thermodynamic properties of isotopic substances. *J. Chem. Soc.* **0**, 562–581. doi.org/10.3354/meps264001

Valentine D. L., Chidthaisong A., Rice A., Reeburgh W. S. and Tyler S. C. (2004) Carbon and hydrogen isotope fractionation by moderately thermophilic methanogens. *Geochim. Cosmochim. Acta* **68**, 1571–1590. doi.org/10.1016/j.gca.2003.10.012

Vardaro M. F., MacDonald I. R., Bender L. C. and Guinasso N. L. (2006) Dynamic processes observed at a gas hydrate outcropping on the continental slope of the Gulf of Mexico. *Geo-Marine Lett.* **26**, 6–15. doi.org/1007/s00367-005-0010-2

ten Veen J. H., Woodside J. M., Zitter T. A. C., Dumont J. F., Mascle J. and Volkonskaia A. (2004) Neotectonic evolution of the Anaximander Mountains at the junction of the Hellenic and Cyprus arcs. *Tectonophysics* **391**, 35–65. doi.org/10.1016/j.tecto.2004.07.007

Vincent S. J. and Kaye M. N. D. (2018) Source rock evaluation of Middle Eocene-Early Miocene mudstones from the NE margin of the Black Sea. *Geol. Soc. Spec. Publ.* **464**, 329–363. doi.org/10.1144/sp464.7

Vogt P., Cherkashov G., Ginsburg G., Ivanov G., Milkov A., Crane K., Sundvor A., Pimenov N. and Egorov A. (1997) Haakon Mosby Mud Volcano provides unusual example of venting. *Eos, Trans. Am. Geophys. Union* **78**, 549. doi.org/10.1029/97EO00326

Wang D., Gruen D. S., Sherwood Lollar B., Hinrichs K.-U., Stewart L., Holden J., Hristov A., Pohlman J. W., Morrill P. L., Konneke M., Delwiche K. B., Reeves E. P., Seewald J. S., McIntosh J. C., Hemond H. F., Kubo M. D., Cardace D., Hoehler T. M. and Ono S. (2015) Nonequilibrium clumped isotope signals in microbial methane. *Science.* **348**, 428–431. doi.org/10.1126/science.aaa4326

Webb M. A. and Miller T. F. (2014) Position-specific and clumped stable isotope studies: Comparison of the urey and path-integral approaches for carbon dioxide, nitrous oxide, methane, and propane. *J. Phys. Chem. A* **118**, 467–474. doi.org/10.1021/jp41134v

Wei J., Pape T., Sultan N., Colliat J. L., Himmler T., Ruffine L., de Prunelé A., Dennielou B., Garziglia S., Marsset T., Peters C. A., Rabiu A. and Bohrmann G. (2015) Gas hydrate distributions in sediments of pockmarks from the Nigerian margin - Results and interpretation from shallow drilling. *Mar. Pet. Geol.* **59**, 359–370. doi.org/10.1016/j.marpetgeo.2014.09.013

Wenau S., Spieß V., Pape T. and Fekete N. (2017) Controlling mechanisms of giant deep water pockmarks in the Lower Congo Basin. *Mar. Pet. Geol.* **83**, 140–157. doi.org/10.1016/j.marpetgeo.2017.02.030

Weston N. B. and Joye S. B. (2005) Temperature-driven decoupling of key phases of organic matter degradation in marine sediments. *Proc. Natl. Acad. Sci. U. S. A.* **102**, 17036–17040. doi.org/10.1073/pnas.0508798102

White R. S. (1983) The Makran Accretionary Prism. In *Seismic Expression of Structural Styles: A Picture and Work Atlas. Volume 1–The Layered Earth, Volume 2–Tectonics Of Extensional Provinces, & Volume 3–Tectonics Of Compressional Provinces* (ed. A. W. Bally). American Association of Petroleum Geologists.

Whiteman G., Hope C. and Wadhams P. (2013) Vast costs of Arctic change. *Nature* **499**, 401–403. doi.org/10.1038/499401a

Whiticar M. J. (1999) Carbon and hydrogen isotope systematics of bacterial formation and oxidation of methane. *Chem. Geol.* **161**, 291–314. doi.org/10.1016/S0009-2541(99)00092-3

Wilhelms A., Larter S. R., Head I., Farrimond P., Di-Primio R. and Zwach C. (2001) Biodegradation of oil in uplifted basins prevented by deep-burial sterilization. *Adv. Pet. Geochemistry* **411**, 1034–1037. doi.org/ 10.1038/35082535

Xie, H., Dong, G., Formolo, M., Lawson, M., Liu, J., Cong, F., Mangenot, X., Shuai, Y., Ponton, and C., Eiler, J. (2021) The evolution of intra- and inter-molecular isotope equilibria in natural gases with thermal maturation. *Geochim. Cosmochim. Acta* **307**, 22–41. doi.org/10.1016/j.gca.2021.05.012

Xing, J., and Spiess, V. (2015) Shallow gas transport and reservoirs in the vicinity of deeply rooted mud volcanoes in the central Black Sea. *Mar. Geol*. **369**, 67–78. doi.org/10.1016/j.margeo.2015.08.005

Yoshinaga M. Y., Holler T., Goldhammer T., Wegener G., Pohlman J. W., Brunner B., Kuypers M. M. M., Hinrichs K. U. and Elvert M. (2014) Carbon isotope equilibration during sulphate-limited anaerobic oxidation of methane. *Nat. Geosci.* **7**, 190–194. doi.org/10.1038/ngeo2069

You K., Flemings P. B., Malinverno A., Collett T. S. and Darnell K. (2019) Mechanisms of methane hydrate formation in geological systems. *Rev. Geophys.* **57**, 1146–1196. doi.org/10.1029/2018RG000638

Young E. D., Kohl I. E., Lollar B. S., Etiope G., Rumble D., Li S., Haghnegahdar M. A., Schauble E. A., McCain K. A., Foustoukos D. I., Sutclife C., Warr O., Ballentine C. J., Onstott T. C., Hosgormez H., Neubeck A., Marques J. M., Pérez-Rodríguez I., Rowe A. R., LaRowe D. E., Magnabosco C., Yeung L. Y., Ash J. L. and Bryndzia L. T. (2017) The relative abundances of resolved $^{12}CH_2D_2$ and $^{13}CH_3D$ and mechanisms controlling isotopic bond ordering in abiotic and biotic methane gases. *Geochim. Cosmochim. Acta* **203**, 235–264.doi.org/10.1016/j.gca.2016.12.041

Young, E.D. (2019) A two-dimensional perspective on CH4 isotope clumping. Deep Carbon: Past to Present, 388–414.

Zhang N., Snyder G. T., Lin M., Nakagawa M., Gilbert A., Yoshida N., Matsumoto R. and Sekine Y. (2021) Doubly substituted isotopologues of methane hydrate ($^{13}CH_3D$ and $^{12}CH_2D_2$): Implications for methane clumped isotope effects, source apportionments and global hydrate reservoirs. *Geochim. Cosmochim. Acta* **315**, 127–151. doi.org/10.1016/j.gca.2021.08.027

Zhang T. and Krooss B. M. (2001) Experimental investigation on the carbon isotope fractionation of methane during gas migration by diffusion through sedimentary rocks at elevated temperature and pressure. *Geochim. Cosmochim. Acta* **65**, 2723–2742. doi.org/10.1016/S0016-7037(01)00601-9

Chapter 3

Kilometer-scale profiles of $\Delta^{13}CH_3D$ distinguish end-member mixing from methane production in deep marine sediments

ABSTRACT

Methane stored in marine sediments can form by microbial and thermal decomposition of organic matter. Identifying the source of methane allows us to assess the potential of natural gas reservoirs and the limits of subsurface microbial life. However, such assessments are complicated by the burial and transport of methane, which can produce mixtures from multiple sources. We measured the abundances of stable isotopes ($^{13}C/^{12}C$ and D/H), clumped isotopologue $^{13}CH_3D$, and *n*-alkanes (C_1/C_{2+3}, methane over ethane plus propane) for gas samples collected by mud-logging to test how $^{13}CH_3D$ additionally constrains the source(s) of methane. Two kilometer-scale depth profiles representing the transition between microbial and thermal methanogenic zones were analyzed from the northeastern Gulf of Mexico and the western Black Sea. We found that $\Delta^{13}CH_3D$ values of methane do not follow conservative two-component mixing between shallow microbial methane and deep thermogenic methane transported by advection. Rather, methane isotopologues indicate re-equilibration along geothermal gradients following burial, which continues up to apparent temperatures of 100^{+14}_{-15}°C. The re-equilibration is likely microbially catalyzed, although this apparent temperature is ~20° higher than the putative upper-temperature limit of microbial methanogenesis in marine sediments. Further, this signal may be preserved through 100s of meters of burial, and thus has the potential to trace the upper temperature limits of life in marine sedimentary environments. Above 150°C, methane isotopologues may equilibrate along geothermal gradients because the rate of temperature increase and abiotic D/H exchange becomes comparable. This study provides novel kilometer-scale profiles of clumped methane isotopes and the means to trace the upper-temperature limits of microbial activity in hydrocarbon-rich marine sedimentary environments.

A version of this chapter is being prepared for publication with the following authors:

Ellen Lalk, Jeffrey S. Seewald, L. Taras Bryndzia, and Shuhei Ono

3.1 INTRODUCTION

Methane is an energy resource, a reactant and product of microbial metabolisms, and a globally significant greenhouse gas. In marine sediments, methane can be found from the sediment-water interface to several kilometers deep, formed by microbial, thermogenic, and abiotic mechanisms. Identifying the source of methane can be used to determine the potential of natural gas reservoirs, assess processes of subsurface transport, and contribute to understanding the depths to which microbes are actively metabolizing organic matter and mediating biogeochemical cycles.

Mechanisms of methane production are broadly connected to sediment temperature (**Figure 3.2**), although the temperature limits of formation processes are debated. Methane can form via microbial metabolisms through organic matter decomposition (primary microbial methanogenesis), which occurs in relatively shallow sediments and low temperatures (typically < 60°C) (e.g., Rice and Claypool, 1981). Oil generation typically occurs at temperatures from 80 to 160°C. Biodegradation of oil may produce secondary microbial methane, which has been demonstrated to form up to temperatures of at least 80 to 90°C (e.g., Head et al., 2003; Wilhelms et al., 2001). Thermogenic methane is formed when organic-matter containing marine sediments are heated as burial progresses (peak generation ≈160°C) (Hunt, 1996). Thermogenic methane generation from kerogen is called primary thermogenic methanogenesis, and the cracking of long-chain hydrocarbons is called secondary thermogenic methanogenesis. Empirical observations and anhydrous experiments suggest that petroleum generation occurs at temperatures from 60 to 120°C (Lorant et al., 1998; Schoell, 1983), while refractory kerogen and bitumen produce gas at temperatures from ca. 160 to 220°C (Burnham, 1989; Seewald et al., 1998). Notably, the upper end of microbial methane generation overlaps with the lower end of thermal methane generation, herein referred to as the 'transition zone' (**Figure 3.2**).

The composition of low molecular weight n-alkanes (i.e., the abundance of methane, ethane, propane, etc.), and carbon and hydrogen isotope ratios, are often applied within interpretive frameworks to evaluate methane sources (e.g., Bernard et al., 1976; Milkov and Etiope, 2018; Whiticar, 1999). The use of these values to distinguish thermogenic from microbial end-members is relatively straightforward, but can be complicated by gases derived from multiple sources. Further, methane from sediment in the 'transition zone' between optimal

microbial (<60°C) and thermal (>150°C) methanogenic regions, is historically difficult to characterize using these frameworks. Methane from this zone may be from high-temperature microbial methanogenesis, low-temperature thermal methanogenesis, or mixtures of two or more sources of gas.

Methane isotopologues with more than one isotopic substitution (e.g., $^{13}CH_3D$ and $^{12}CH_2D_2$), known as 'clumped isotopologues,' can be used as a tool to estimate the temperature of methane generation or equilibration because the relative distribution of clumped isotopologues is a function of temperature under equilibrium (Stolper et al., 2014b, 2014a; Wang et al., 2015; Young et al., 2017). The distribution of isotopologues ($^{12}CH_4$, $^{13}CH_4$, $^{12}CH_3D$, $^{13}CH_3D$, and $^{12}CH_2D_2$) can also be applied to interpret methane origins by providing additional dimensions to well-established techniques (i.e., the relationships between C_1/C_{2+3}, $\delta^{13}C\text{-}CH_4$, and $\delta D\text{-}CH_4$). Measurement of doubly substituted isotopologues, $\Delta^{13}CH_3D$ and $\Delta^{12}CH_2D_2$ is analytically possible via laser spectroscopy and mass spectrometry (Gonzalez et al., 2019; Ono et al., 2014; Stolper et al., 2014b; Young et al., 2017).

Although clumped methane isotopologues can sometimes be linked to the temperature of methane generation, both microbial and thermogenic methane often indicate kinetic signals and disequilibrium isotopologue distributions. Microbial methane in sub-surface environments (e.g., marine sediment pore-water,) often yields environmentally reasonable temperatures, while methane from surface environments (e.g., freshwater, near-surface sediments) usually reflect kinetic fractionations (Ash et al., 2019; Douglas et al., 2020; Giunta et al., 2019; Stolper et al., 2014a; Wang et al., 2015; Young et al., 2017). Early maturity thermogenic gas tends to yield kinetic $\Delta^{13}CH_3D$ and $\Delta^{12}CH_2D_2$ signals, while late maturity thermogenic gas yields equilibrium signals, suggesting the production of methane with kinetic isotopologue signals and later re-equilibration during peak maturation (Xie et al., 2021). Experimental results show that clumped isotopologue disequilibrium in thermogenic methane may occur due to kinetic fractionation during cracking of organic matter associated with methane generation (Shuai et al., 2018), although these signals may be erased by isotope exchange as the methane equilibrates.

Clumped methane isotopologue compositions have been measured for several natural gas reservoirs in the Gulf of Mexico (Thiagarajan et al., 2020). While apparent temperatures of reservoir gas in this basin were in some cases consistent with *in situ* temperatures, apparent

temperatures lower than *in situ* temperatures were found, indicative of shallow production and burial of fossil methane, and apparent temperatures higher than *in situ* temperatures were found, indicative of production of methane at greater temperatures and depths or kinetic isotope effects.

Previously, isotopologue measurements have been applied to determine the provenance of hydrocarbon reservoirs, but detailed site measurements of $\Delta^{13}CH_3D$ through the sediment column have been lacking. Here we report relative hydrocarbon abundances (C_1/C_{2+3}), and isotopologue compositions of methane ($\delta^{13}C\text{-}CH_4$, $\delta D\text{-}CH_4$, $\Delta^{13}CH_3D$) from mud-gases from two sites, 1) in the northeastern Gulf of Mexico from 1619 to 3271 meters below seafloor (mbsf), where estimated sediment temperatures range from 52 to 96°C, and 2) in the western Black Sea from 2170 to 3990 mbsf, where estimated sediment temperatures range from 105 to 183°C. Although scientific drilling can provide well-characterized samples, the use of mud-gas to study methane geochemistry in deep sedimentary basins has several advantages, the most significant being that samples can be procured from much greater depths (mud-logging can reach depths >5 km, several km deeper than scientific drilling). To evaluate basin geochemistry and pressure, mud-logging became a standard technique used on drill rigs beginning in the 1930s and has repeatedly been employed for its scientific value over the last decades (Ablard et al., 2012, Hammerschmidt et al., 2014). Mud-gas has previously been used for scientific applications including monitoring the carbon and hydrogen isotope ratios of methane and C_1/C_{2+3} of gas (e.g., Hammerschmidt et al., 2014; Inagaki et al., 2015), as well as for clumped isotopes of methane ($\Delta^{13}CH_3D$) during IODP expedition 337 (Inagaki et al., 2015).

In this study, we use multi-kilometer depth profiles of $\Delta^{13}CH_3D$ to test whether $\Delta^{13}CH_3D$ values can differentiate closed-system production where isotoplogue abundances reflect *in situ* conditions from open-system advective transport and mixing of methane (e.g., Borowski et al., 2000). We further explore the relationship between isotope-based temperatures and sediment temperature by modeling $\Delta^{13}CH_3D$ values throughout the sediment columns to interpret methane history and equilibration timescales at these sites. The evaluation of $\Delta^{13}CH_3D$ values in the context of multi-kilometer depth profiles yields new insights into the depth/temperature limits of individual methane production mechanisms in deep sub-seafloor environments.

3.2 MATERIALS AND METHODS

3.2.1 Samples

Mug-gas samples were collected from the Gulf of Mexico (n=39), and the Black Sea (n=37). During drilling operations, drilling mud passes through an agitator and degasser along the mudflow line, and gas extracted from this process is monitored in real-time and collected as mud-gas samples. Samples from this study were stored in Isotubes until gas chromatographic and spectroscopic analyses. The drilling process disrupts *in situ* conditions, which causes temperature and pressure changes that lead to fluid loss and introduction (e.g., drilling fluids), as well as air introduction (Haworth et al., 1985). Thus, we report abundance ratios, not absolute gas concentrations.

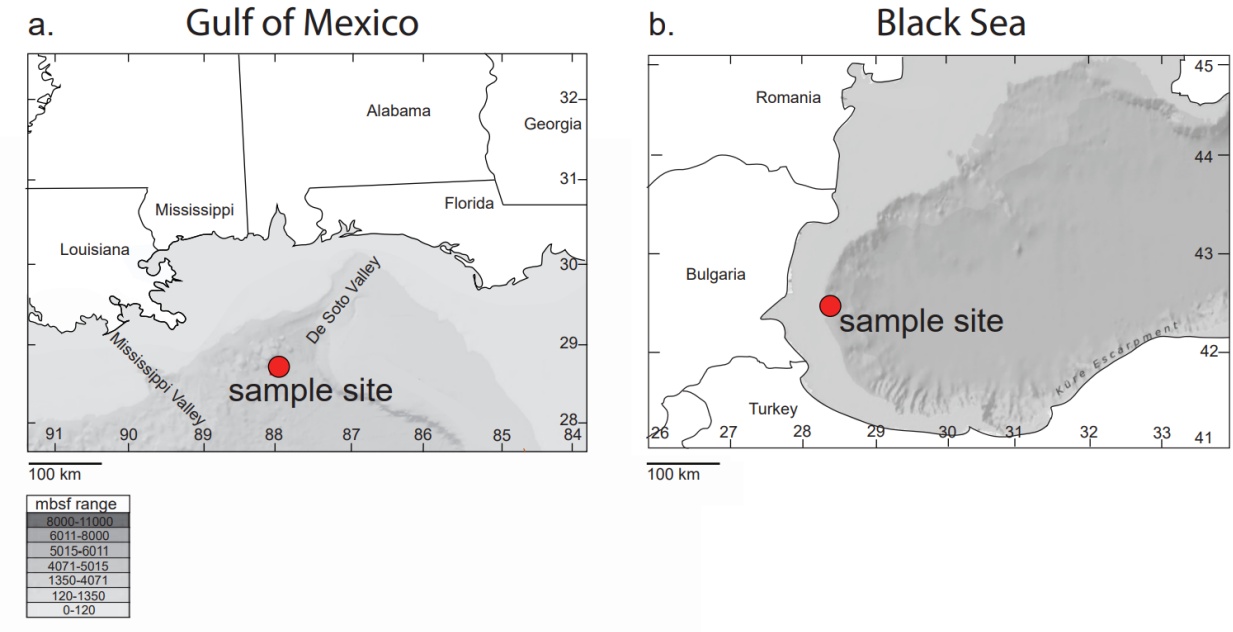

Figure 3.1: Sample locations **a** in the northeastern Gulf of Mexico, and **b** in the western Black Sea. Bathymetric shading is from the ESRI Ocean Base map.

3.2.1.1 Site Descriptions

Northeastern Gulf of Mexico: Drilling took place at the eastern boundary of the Gulf slope in the northeastern Gulf of Mexico, between the Mississippi and De Soto Canyon Areas (**Figure 3.1a**). This site is situated in the Appomattox deepwater field, which is part of a Jurassic-aged Norphlet-Smackover hydrocarbon system that extends onshore to gulf coast states including Florida, Alabama, Mississippi, and Louisiana (Godo, 2017). The Gulf slope sediment

column is mainly comprised of rapid Mesozoic-Cenozoic infill from the North American continent, underlain by middle Jurassic to late Cretaceous red beds, carbonates, and evaporites (Mcbride et al., 1998; Salvador, 1991). Samples in this study span from 1538 to 4881 mbsf, which encompasses sedimentation from the Miocene to the Upper Cretaceous; however, only samples that were hosted in Miocene sediments (ca. 1619 to 3271 mbsf) had enough methane for isotopologue measurement (**Figure 3.2a**). The sample depth profile spans a range of temperatures estimated from the geothermal gradient that increases from 52 to 132℃, suitable for investigating the transition from microbial to thermogenic methane production. The sediment in this region of the Gulf of Mexico is rich in marine and terrrigenous organic matter that can support microbial methane production. Within this sediment column there are also several well-known source rock intervals, including the Smackover formation, and the Haynesville and Eagleford shales (stratigraphic tops located at ca. 6.2, 6.1, and 4.0 kmbsf, respectively) (**Figure 3.2a**).

Western Black Sea: Drilling took place in the western Black Sea off the coast of Bulgaria, near the junction of the western Black Sea basin and Moesian Platform (**Figure 1b**). This site is part of the Khan Kubrat block. Samples span from 2170 to 4030 mbsf, which includes Miocene to Eocene-age sediments (**Figure 3.2b**). Sediment temperatures over this depth interval, estimated from the geothermal gradient, range from ca. 105 to 185℃. The lower end of this range is within the known temperature limits of microbial life and onset of early maturity thermogenic gas production, while the higher end of this range is conducive to late maturity thermal methane production. The Maykop and Kuma Formations are prolific source rocks in this region (Fallah et al., 2018). The Maykop group is found in Oligocene sediment (stratigraphic top located at 2.6 kmbsf), whereas the Kuma formation is located at greater depths (below 3.9 kmbsf) (**Figure 3.2b**).

3.2.2 Analyses

3.2.2.1 Methane, ethane, and propane (C_1/C_{2+3})

The relative abundance of C_1-C_3 hydrocarbon gases (C_1/C_{2+3}) in mud-gas was analyzed by gas chromatography (GC) with a flame ionization detector (FID). The GC is equipped with an 8-foot length column packed with HayeSep-Q (VICI), and helium carrier gas. Each gas sample was measured at least twice in comparison with calibration gas mixtures (SCOTTY®).

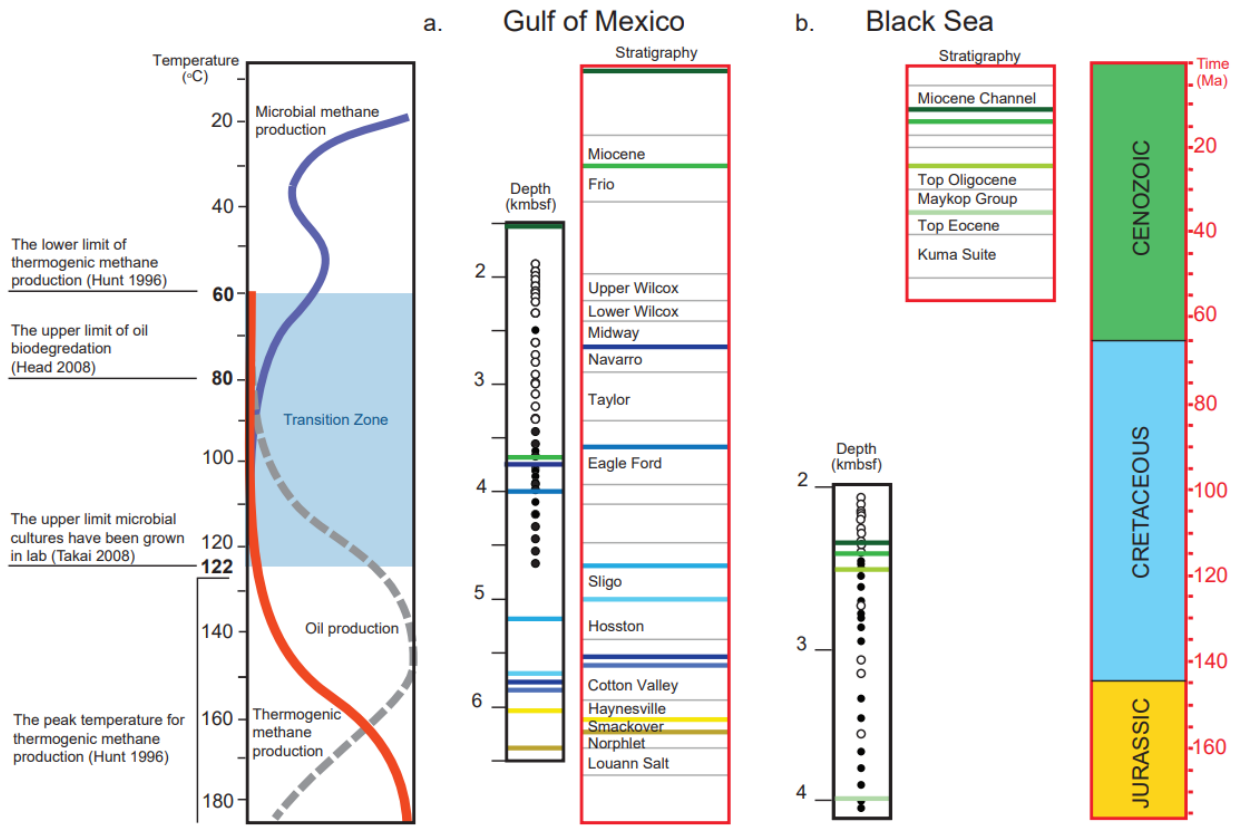

Figure 3.2: Context of the relative importance of microbial and thermogenic methanogenesis at increasing sediment temperatures and generalized depositional architecture associated with mud-gas samples. **a** Depths of mud-gas samples and generalized stratigraphy of sediments in the northeast Gulf of Mexico (Galloway, 2008). The nine colored lines between show depths of known stratigraphic boundaries within the profile, where green lines are Cenozoic strata, blue lines are Cretaceous strata, and yellow lines are Jurassic strata. **b** Depths of mud-gas samples and generalized stratigraphy of sediments in the western Black Sea (Simmons et al., 2018). The four green lines show depths of known stratigraphic boundaries within the profile. Open circles indicate samples measured via GC and TILDAS, and filled circles indicate samples measured via GC that contained insufficient methane for spectroscopic measurement.

3.2.2.2 $\delta^{13}C$-CH_4, δD-CH_4, $\Delta^{13}CH_3D$

From the Gulf of Mexico site, samples containing more than 1 mL methane at lab temperature and pressure were selected for methane isotopologue analysis (n = 18), while for the Black Sea site, samples containing more than 0.5 mL methane at lab temperature and pressure were selected (n = 15). Analysis of the small Black Sea samples was made possible by a low volume laser absorption cell, which lowered the minimum sample size by a factor of 2. The full contents of the Isotubes were extracted onto a cold trap filled with activated charcoal, submerged in liquid nitrogen (-196 °C), and then methane was purified from other gas components using gas

chromatography, as described by Wang et al., (2015). The relative abundances of methane isotopologues ($^{12}CH_4$, $^{13}CH_4$, $^{12}CH_3D$, and $^{13}CH_3D$) were measured using a Tunable Infrared Laser Direct Absorption Spectroscopy (TILDAS) instrument, as previously described (Ono et al., 2014; Wang et al., 2015). Samples were measured in recycling mode, during which methane is recovered from the absorption cell in a cold trap after measurement, and then re-introduced for ca. 9 comparisons of sample to reference gas.

For the Gulf of Mexico site, three additional samples containing ca. 0.15 mL methane were extracted to measure $\delta^{13}C\text{-}CH_4$. For the Black Sea site, eight additional samples containing ca. 0.25 mL methane were extracted to resolve $\delta^{13}C\text{-}CH_4$ and $\delta D\text{-}CH_4$. Standard methane gases with known $\delta^{13}C\text{-}CH_4$ and $\delta D\text{-}CH_4$ values have been run at these lower sample volumes to confirm that values could be determined accurately (within 0.12‰ and 0.40‰, respectively).

To calibrate the $\Delta^{13}CH_3D$ geothermometer, we use methane standards of known carbon and hydrogen isotopic compositions that were equilibrated at 250°C with a platinum catalyst. NGS-1 and NGS-3 were used for calibration of carbon and hydrogen isotope values, which are reported using standard delta notation against VPDB and VSMOW, respectively (Wang et al., 2015).

$\Delta^{13}CH_3D$ is defined as the abundance of $^{13}CH_3D$ relative to a stochastic distribution of isotopologues (Ono et al., 2014).

$$\Delta\ ^{13}CH_3D = \ln\left(\frac{[^{13}CH_3D][^{12}CH_4]}{[^{13}CH_4][^{12}CH_3D]}\right) \qquad (3.1)$$

Due to the temperature dependence of $\Delta^{13}CH_3D$ values at thermodynamic equilibrium, equilibration temperatures can be calculated from measured $\Delta^{13}CH_3D$ values. For this study, we used the temperature dependence of Eldridge et al. (2019), which is a polynomial fit to path-integrated Monte Carlo computations (PIMC). This temperature dependence for the value of $\Delta^{13}CH_3D$ yields slightly different results than those calculated as specified in Wang et al., 2015, although both approaches are consistent within a few degrees for the temperature range considered in this study (45 to 250°C). Calculated temperatures are herein referred to as 'apparent temperatures' ($T_{\Delta 13D}$) because equilibrium is assumed in the application of the geothermometer.

3.2.3 Estimates of *in situ* temperatures

Sediment temperature for the Gulf of Mexico and Black Sea sites was estimated from in-house basin models at Shell. Sediment temperature data in **Tables 3.1** and **3.2** represent a 1D extract from the best constraint scenario model run. Tie-point temperature measurements were not taken down-well at the Gulf of Mexico site, but the basin model was calibrated against other nearby wells using sediment thermal maturity records (**Figure 3.3d**). For the Black Sea, tie-point measurements were made at the site and used in addition to temperature data from nearby sites to calibrate the basin model estimate, and additional upper- and lower-bound model estimates are shown in **Figure 3.3h**.

3.3. RESULTS

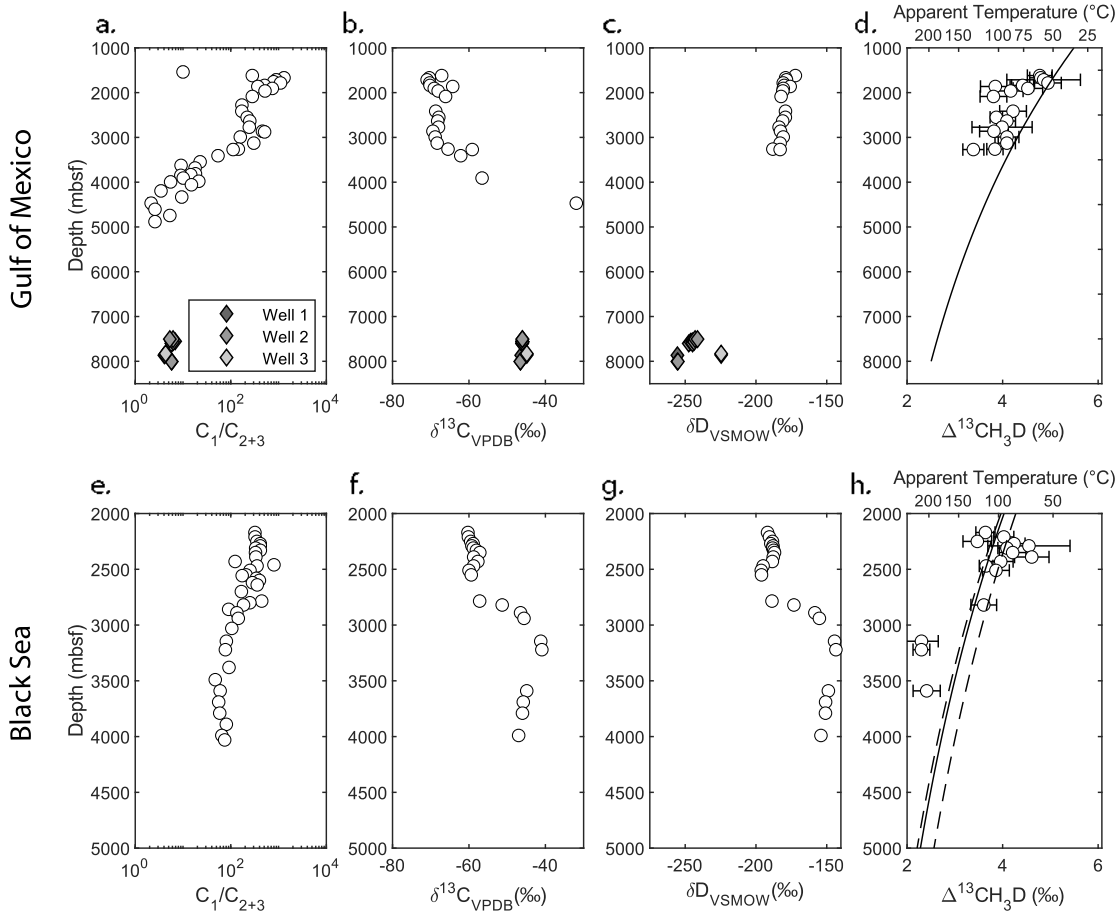

Figure 3.3: Depth profiles of relative hydrocarbon abundance, isotopic data, and temperature for the Gulf of Mexico (**a-d**) and Black Sea (**e-h**) sites. **a**, **e** Ratios of methane to ethane and propane (C_1/ C_{2+3}). **b**, **f** δ^{13}C-CH_4 in ‰ vs V-PDB. **c, g** δD-CH_4 in ‰ vs V-SMOW. **d**, **h** $\Delta^{13}CH_3D$ in ‰, in **d** dashed line reflects sediment temperature, in **h** the solid line reflects sediment temperature, and dashed lines reflect upper and lower bounds. Error bars for **a**-**c** and **e**-**g** are smaller than the marker width. Composition of nearby reservoir gas from Well 1, Well 2, and Well 3 are represented in **a**-**c** by grey diamonds.

Northeastern Gulf of Mexico											
Depth (mbsf)	**C_1/C_{2+3}**		**$\delta^{13}C$ (‰)**		**δD (‰)**		**$\Delta\ ^{13}CH_3D$ (‰)**		**Apparent T (°C)**		**Sediment T (°C)**
1538	10.0	±0.9	---	---	---	---	---	---	---	---	52
1619	282	±24	-67.14	±0.06	-172.17	±0.06	4.78	±0.26	64	+11/-11	54
1669	1300	±120	-70.38	±0.11	-179.05	±0.02	4.80	±0.23	63	+10/-9	56
1714	890	±80	-70.95	±0.10	-178.46	±0.23	4.86	±0.77	61	+34/-29	57
1757	790	±70	---	---	---	---	---	---	---	---	59
1784	1100	±100	-70.28	±0.15	-180.75	±0.19	4.95	±0.28	57	+12/-11	59
1839	510	±40	-70.20	±0.04	-180.06	±0.04	4.42	±0.23	80	+11/-11	61
1863	368	±32	-64.25	±0.05	-175.83	±0.09	3.85	±0.31	108	+18/-16	61
1906	740	±60	-69.08	±0.08	-180.69	±0.09	4.53	±0.31	75	+14/-13	63
1963	520	±50	-68.06	±0.06	-181.02	±0.09	4.17	±0.26	92	+13/-13	64
2086	282	±25	-66.12	±0.05	-182.26	±0.06	3.81	±0.28	110	+10/-9	68
2278	171	±15	---	---	---	---	---	---	---	---	73
2415	170	±15	-68.70	±0.03	-179.17	±0.05	4.22	±0.28	90	+14 /-14	77
2552	220	±19	-67.89	±0.06	-179.25	±0.09	3.87	±0.13	107	+7/-6	80
2634	250	±22	-68.18	±0.07	-181.13	±0.03	4.09	±0.18	95	+10/-9	82
2772	244	±21	-67.97	±0.05	-183.66	±0.09	3.99	±0.63	96	+35 /-30	84
2862	460	±40	-69.43	±0.06	-182.68	±0.04	3.82	±0.30	110	+16/-16	87
2877	510	±40	---	---	---	---	---	---	---	---	87
2991	158	±14	-68.84	±0.05	-180.74	±0.05	4.09	±0.25	96	+12 /-12	90
3128	303	±26	-68.31	±0.03	-182.93	±0.03	4.09	±0.18	96	+9/-9	94
3262	144	±12	-65.48	±0.02	-188.08	±0.06	3.84	±0.17	109	+9 /-10	96
3271	112	±10	-59.14	±0.07	-182.93	±0.06	3.39	±0.22	136	+14/-14	96
3409	54	±5	-62.15	±0.22	---	---	---	---	---	---	99
3546	22.8	±2.0	---	---	---	---	---	---	---	---	102
3625	9.1	±0.8	---	---	---	---	---	---	---	---	104
3683	17.9	±1.5	---	---	---	---	---	---	---	---	105
3812	18.2	±1.6	---	---	---	---	---	---	---	---	109
3832	14.5	±1.3	---	---	---	---	---	---	---	---	109
3847	9.0	±0.8	---	---	---	---	---	---	---	---	109
3908	10.1	±0.9	-56.57	±0.33	---	---	---	---	---	---	111
3979	21.4	±1.9	---	---	---	---	---	---	---	---	112
3994	5.5	±0.5	---	---	---	---	---	---	---	---	113
4058	15.0	±1.3	---	---	---	---	---	---	---	---	114
4195	3.46	±0.30	---	---	---	---	---	---	---	---	116
4332	9.4	±0.8	---	---	---	---	---	---	---	---	119
4469	2.15	±0.29	-31.92	±0.13	---	---	---	---	---	---	123
4606	2.59	±0.22	---	---	---	---	---	---	---	---	126
4744	5.3	±0.5	---	---	---	---	---	---	---	---	130
4881	2.59	±0.22	---	---	---	---	---	---	---	---	132

Table 3.1: Molecular ratios, stable isotope compositions, apparent and sediment temperatures of mud-gas samples from the Gulf of Mexico. The error of molecular composition represents sigma for an average signal consistency of 5% and the error of isotope ratios represents the 95% confidence interval.

Western Black Sea											
Depth (mbsf)	**C_1/C_{2+3}**		**$\delta^{13}C$ (‰)**		**δD (‰)**		**$\Delta^{13}CH_3D$**		**Apparent T (°C)**		**Sediment T (°C)**
2170	320	±27	-60.27	±0.18	-191.84	±0.57	3.64	±0.20	120	+12/-11	105
2210	322	±28	-60.15	±0.08	-190.48	±0.16	4.03	±0.21	98	+11/-10	107
2250	352	±30	-59.55	±0.27	-188.35	±0.30	3.47	±0.30	130	+20/-18	108
2270	414	±36	-58.90	±0.23	-189.52	±0.48	4.24	±0.23	88	+11/-11	109
2290	414	±36	-59.24	±0.16	-187.97	±0.19	4.55	±0.86	74	+43/-35	110
2310	331	±29	-58.87	±0.05	-188.21	±0.09	4.09	±0.19	95	+10/-9	111
2330	415	±36	-58.05	±0.17	-187.49	±0.29	---	---	---	---	112
2350	329	±28	-57.16	±0.05	-186.90	±0.10	4.21	±0.28	90	+14/-14	113
2390	335	±29	-58.77	±0.19	-187.81	±0.28	4.61	±0.36	71	+16/-15	114
2430	123	±11	-57.67	±0.25	-188.44	±0.28	3.96	±0.26	102	+14/-13	116
2460	801	±69	---	---	---	---	---	---	---	---	117
2470	354	±31	-58.80	±0.18	-194.97	±0.21	3.65	±0.14	119	+9/-7	118
2510	252	±22	-59.99	±0.04	-196.28	±0.12	3.86	±0.28	107	+16/14	119
2550	209	±18	-59.40	±0.21	-196.10	±0.56	---	---	---	---	121
2557	173	±15	---	---	---	---	---	---	---	---	121
2581	342	±30	---	---	---	---	---	---	---	---	122
2600	397	±34	---	---	---	---	---	---	---	---	123
2620	284	±25	---	---	---	---	---	---	---	---	124
2640	358	±31	---	---	---	---	---	---	---	---	125
2700	167	±14	---	---	---	---	---	---	---	---	128
2785	444	±38	-57.20	±0.18	-188.70	±0.43	---	---	---	---	131
2800	251	±22	---	---	---	---	---	---	---	---	132
2820	185	±16	-51.31	±0.17	-173.20	±0.32	3.61	±0.27	121	+17/-14	133
2859	90.2	±7.8	---	---	---	---	---	---	---	---	134
2890	134	±12	-46.50	±0.17	-158.40	±0.36	---	---	---	---	136
2940	143	± 12	-45.60	±0.18	-155.20	±0.29	---	---	---	---	138
3030	105	±9	---	---	---	---	---	---	---	---	142
3145	80.8	±6.9	-41.22	±0.13	-144.48	±0.34	2.30	±0.35	225	+41/-34	147
3221	77.1	±6.7	-40.93	±0.20	-143.52	±0.26	2.30	±0.18	225	+20/-18	150
3380	91.8	±7.9	---	---	---	---	---	---	---	---	157
3490	47.3	±4.1	---	---	---	---	---	---	---	---	162
3590	59.9	±5.2	-44.88	±0.17	-148.85	±0.19	2.41	±0.28	213	+32/-26	166
3690	55.8	±4.8	-45.79	±0.13	-150.81	±0.56	---	---	---	---	170
3790	58.7	±5.1	-46.00	±0.18	-150.90	±0.50	---	---	---	---	174
3890	80.7	±6.9	---	---	---	---	---	---	---	---	179
3990	64.9	±5.6	-47.00	±0.21	-154.1	±0.21	---	---	---	---	183
4030	74.5	±6.4	---	---	---	---	---	---	---	---	185

Table 3.2: Molecular ratios, stable isotope compositions, apparent and sediment temperatures of mud-gas samples from the Black Sea. The error of molecular composition represents sigma for an average signal consistency of 5% and the error of isotope ratios represents the 95% confidence interval

3.3.1 The northeastern Gulf of Mexico

Thirty-nine mud-gas samples from 1538 to 4881 mbsf in the northeastern Gulf of Mexico were measured to quantify the ratios of low molecular weight hydrocarbons (C_1/C_{2+3}). The C_1/C_{2+3} values range from 2 to 1300 and decrease with depth (**Table 3.1, Figure 3.3a**). From 1538 to 3271 mbsf (sediment temperatures from 52 to 96°C) C_1/C_{2+3} ratios are above 100, typical for microbial methane. Below 3271 mbsf, the C_1/C_{2+3} ratio values are less than ca. 25, typical of thermogenic methane.

Eighteen samples from ca. 1619 to 3271 mbsf yielded enough methane (> 1 mL at standard temperature and pressure, STP) for the measurement of $\delta^{13}C\text{-}CH_4$, $\delta D\text{-}CH_4$, and $\Delta^{13}CH_3D$ values (**Table 3.1**). The $\delta^{13}C\text{-}CH_4$ values of mud-gas samples fall between -71.0 to -59.1‰ relative to VPDB and generally increase with depth. Three additional samples were measured for $\delta^{13}C\text{-}CH_4$ only, due to a low abundance of methane (< 0.5%). The $\delta^{13}C\text{-}CH_4$ value of the deepest sample is -31.9‰ (**Table 3.1, Figure 3.3b**). The $\delta D\text{-}CH_4$ values of mud-gas samples fall between -172.2 to -188.1‰ relative to VSMOW, and generally decrease with depth (**Table 3.1**, **Figure 3.3c**).

The clumped isotopologue abundances of mud-gas samples range from $\Delta^{13}CH_3D$ = 3.4 to 5.0‰ (95% confidence interval ca. 0.30‰) (**Table 3.1**, **Figure 3.3d**). These values correspond to apparent temperatures (T_{13D}) of ca. 57°C at 1800 mbsf, and 136 °C at 3271 mbsf. The apparent temperatures of samples from this site are within error or greater than the estimated sediment temperatures. Samples from 1619 to 1784 mbsf (54 to 59°C) and 2772 to 3128 mbsf (84 to 94°C) are within error of sediment temperatures. Samples have apparent temperatures that are greater than estimated sediment temperatures by 2 to 47°C, and on average ca. 18°C.

3.3.2 The western Black Sea

Thirty-seven mud-gas samples from 2170 to 4030 mbsf in the western Black Sea were measured to quantify C_1/C_{2+3} (**Table 3.2**, **Figure 3.3e**). C_1/C_{2+3} ratios decrease with increasing depth. Values typical for microbial methane (from 200 to 400) are found above 2640 mbsf, while values typical for thermogenic methane (from 60 to 80) are found below 2640 mbsf.

Fifteen samples from 2170 to 3590 mbsf yielded enough methane (> 0.5 mL at STP) for the measurement of $\delta^{13}C\text{-}CH_4$, $\delta D\text{-}CH_4$, and $\Delta^{13}CH_3D$ (**Table 3.2**). Measurements of $\delta^{13}C\text{-}CH_4$

and δD-CH_4 were made for eight additional samples from this depth interval, which yielded >0.25 mL CH_4 at STP. The values of δ^{13}C-CH_4 and δD-CH_4 are positively correlated throughout the profile (**Table 3.2**, **Figure 3.3f, g**). The δ^{13}C-CH_4 values of mud-gas samples fall between -60.3 to -40.9‰ relative to VPDB, and the δD-CH_4 values of mud-gas samples fall between -196.3 to -143.5‰ relative to VSMOW. In sediments above 2630 mbsf, δ^{13}C-CH_4 and δD-CH_4 values are microbial-like and range from -60.3 to -57.2‰ and from -196.1 to -186.9‰, respectively. Below this depth interval, there is a transition to methane with δ^{13}C-CH_4 from -59.4 to -40.9‰ and δD-CH_4 from -196.1 to -143.5‰, which are thermogenic-like.

$\Delta^{13}CH_3D$ values (**Table 3.2**, **Figure 3.3h**) range from to 2.3 to 4.6‰ (95% confidence interval ca. 0.29‰), which corresponds to apparent temperature values ($T_{\Delta 13D}$) of 225 to 74 ℃. Generally, $\Delta^{13}CH_3D$ values decrease ($T_{\Delta 13D}$ increases) with depth as sediment temperature increases from 105 to 166℃. From 2170 to 2820 mbsf, apparent temperatures from $\Delta^{13}CH_3D$ values are similar to estimated sediment temperatures, or lower, by up to ca. 43 ℃. Below 2820 mbsf, the apparent temperatures are greater than 215 ℃ and higher than expected sediment temperature by ca. 75℃.

3.4 DISCUSSION

3.4.1 $\Delta^{13}CH_3D$ values do not support simple two end-member mixing

Information provided by the measurement of $\Delta^{13}CH_3D$ can be used assess the origin of methane that falls in the 'transition zone'. The methane in this zone is often interpreted as the mixing between microbial and thermogenic end-members from open-system advective transport of thermal methane to relatively cooler sediment. However, it is historically challenging to differentiate mixing from closed-system production of high-temperature microbial methane production and/or low-temperature thermogenic methane production that may reflect *in situ* conditions. The ability to decipher these processes has important implications. For example, microbial methane production at temperatures greater than previously recognized (i.e., 80 to 90℃) would challenge assumptions about metabolic rates, biomass turnover, and the activity of microbially-mediated biogeochemical cycles in the deep marine subsurface (e.g., D'Hondt et al., 2019; LaRowe and Amend, 2015; Onstott et al., 2014). Alternatively, if intermediate methane is produced by low-temperature thermal production, that may yield insights into potential source rock locations, which could be expanded to assess the possibility of similar accumulations in the

area. We define representative microbial (M_{GOM}, M_{BS}) and thermogenic (T_{GOM}, T_{BS}) end-member isotopologue and C_1/C_{2+3} ratios for both Gulf of Mexico and Black Sea sites, detailed below. Deviation from conservative two-end-member mixing from open-system advective transport can reveal the additional processes controlling the isotopologue signals in deep sediments, including the significance of closed-system methane production throughout sections of the marine sediment column.

We define microbial and thermogenic end-members in the northeastern Gulf of Mexico using the shallowest samples and nearby well gases, respectively (**Figure 3.4a**). At this site, methane samples collected from depths shallower than 1784 mbsf have apparent temperatures less than ca. 65°C, which aligns with the expected upper limits of primary microbial methane production. This is consistent with previous work on clumped methane isotopologues from reservoirs in the Gulf of Mexico, which found that primary microbial methane production occurs at apparent temperatures from 20 to 60°C (Thiagarajan et al., 2020). Thus, for the Gulf of Mexico site, we define the microbial end-member, $M_{GOM,}$ as $\delta^{13}C$ = -70‰, δD = -180‰, C_1/C_{2+3} =1500, and $\Delta^{13}CH_3D$ = 4.8‰ (T_{13D} = 64°C), reflecting the shallowest measured samples. Sample size was too small to measure the apparent temperature of the most thermogenic-like gases in this profile, with C_1/C_{2+3} values less than ca. 10 and one measurement of $\delta^{13}C$-CH_4 of -31.9‰, at 4469 mbsf. The depth of this sample aligns with the Eagle Ford shale source rock and has an estimated sediment temperature of 123°C. The other prominent source rocks at this site (the Haynesville shale and Smackover formation) are at depths of ca. 6 kmbsf, with an estimated sediment temperature of ca. 150°C. Accordingly, we define the thermogenic end-member, T_{GOM}, as $\delta^{13}C$ = -45‰, δD = -245‰, C_1/C_{2+3} = 5, and $\Delta^{13}CH_3D$ = 3 to 3.5‰ (120 to 150°C). $\delta^{13}C$ and C_1/C_{2+3} values are represent nearby reservoir gases (**Table 3.S2**), and $\Delta^{13}CH_3D$ is chosen from reasonable apparent temperature for thermogenic hydrocarbon formation from ca. 120 to 150°C based on the depths and approximate *in situ* temperatures of the Eagle Ford, Haynesville, and Smackover formations. We calculate the coefficient of determination (R^2) to assess how well mixing between M_{GOM} and T_{GOM} describe observed data. In C_1/C_{2+3} vs $\delta^{13}C$-CH_4 space (**Figure 3.4a**) the Gulf of Mexico mixing line has an R^2= 0.82, which implies a reasonable fit to the data.

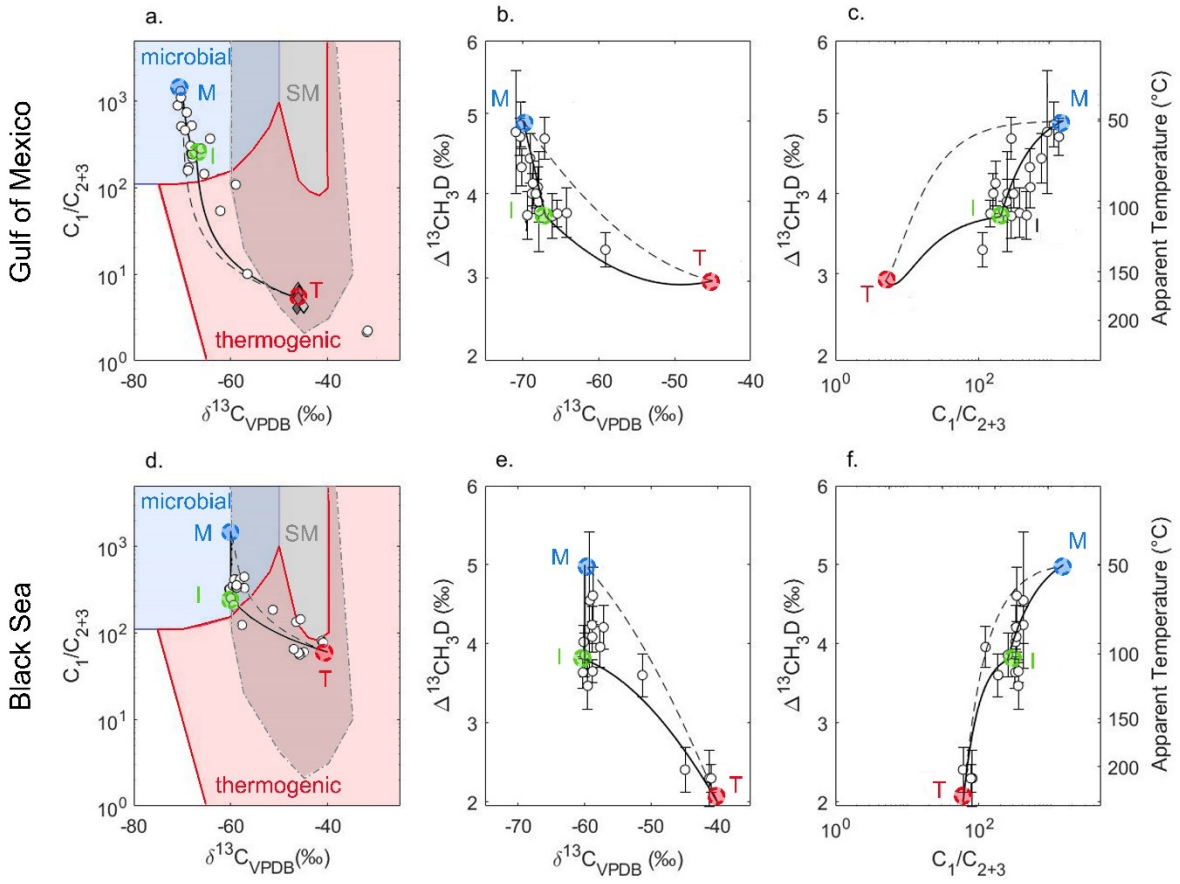

Figure 3.4: Clumped isotopologue data, along with other isotopic data and relative hydrocarbon abundance, do not support a two end-member mixing hypothesis in the eastern Gulf of Mexico (**a-c**) or the western Black Sea (**d-f**). **a**, **d** Mud-gas data is overlaid in $\delta^{13}C$ vs C_1/C_{2+3} space, in which boundaries for microbial (blue), thermogenic (red), and secondary microbial (grey) fields are adapted from Milkov and Etiope, 2018. The secondary microbial field overlaps partially with each microbial and thermogenic field. Grey diamonds in **a** are the compositions of nearby reservoir gases from 3 different wells. **b**, **e** Mud-gas data is plotted in $\delta^{13}C$ vs $\Delta^{13}CH_3D$ space. **c**, **f** Mud-gas data is plotted in $\delta^{13}C$ vs $\Delta^{13}CH_3D$ space. Isotope data is reported in per mille units. Mixing scenarios between microbial (M), intermediate (I) and thermogenic (T) end-members are depicted by dashed and bolded lines. Dashed lines represent end-member mixing scenarios between M_{GOM}-T_{GOM} and M_{BS}-T_{BS}, while solid lines represent M_{GOM}-I_{GOM}-T_{GOM} and M_{BS}-I_{BS}-T_{BS} whose values are tabulated in **Table** 3.**S1**.

We define microbial and thermogenic end-members in the western Black Sea using data from nearby Deep Sea Drilling Program (DSDP) sites 380 and 381, and the deepest samples measured in this study (**Figure 3.4d**). Methane samples from this site all have apparent temperature values (from 71 to 225°C) that are higher than what is expected for a primary

microbial source (i.e., >60°C), but may align with high-temperature oil biodegradation (~80 to 90°C) in the shallowest depth intervals. Samples from shallower depths (< 2550 mbsf) fall near the intersection of microbial, thermogenic, and secondary microbial (e.g., biodegradation) fields (Milkov and Etiope, 2018), and have the highest $\Delta^{13}CH_3D$ values (up to 4.6‰, T_{13D} = 71 °C). From 2170 to 2510 mbsf, apparent temperatures range from ca. 70 to 120 °C. These values fall within the known temperature limits of thermophilic microbial life (<122°C), and the lower end of this range is within the expected temperature limit for secondary microbial methane production (< 80-90°C). More deeply sourced samples (>2785 mbsf) have the lowest $\Delta^{13}CH_3D$ values (down to 2.3‰, T_{13D} = 225 °C), consistent with thermogenic methane generation, and have δD and $\delta^{13}C$ values characteristic of late maturity thermogenic gas. At this site, microbial end-member, M_{BS}, is defined as $\delta^{13}C$ = -60‰, δD = -200‰, C_1/C_{2+3} =1500, and $\Delta^{13}CH_3D$ = 5‰ (55°C), where $\delta^{13}C$, δD and C_1/C_{2+3} values were chosen from other observed primary microbial methane at nearby DSDP sites 380 and 381 (Faber et al., 1978; The Shipboard Scientific Staff et al., 1978), and the $\Delta^{13}CH_3D$ value was chosen to represent a reasonable temperature for high levels of microbial methanogenesis to occur. Thermogenic end-member, T_{BS}, is defined as $\delta^{13}C$ = -40‰, δD = -145‰, C_1/C_{2+3} = 60, and $\Delta^{13}CH_3D$ = 2‰, reflecting the composition of the deepest (3145-3590 mbsf) measured samples. In C_1/C_{2+3} vs $\delta^{13}C$-CH_4 space (**Figure 3.4d**) the Black Sea mixing line has an R^2 = 0.64, which implies a reasonable fit to the data.

While two-component mixing can reconcile trends in C_1/C_{2+3}, $\delta^{13}C$, and δD values, we find that mixing between end-member compositions does not adequately describe the $\Delta^{13}CH_3D$ values of methane samples in either the Gulf of Mexico or the Black Sea (**Figure 3.4a-f**, dashed lines M_{GOM}- T_{GOM}, M_{BS}-T_{BS}). Thus, the hypothesis that open-system mixing of thermogenic methane from advective transport with microbial methane cannot be sufficiently reconciled with our observations. In both C_1/C_{2+3} vs $\Delta^{13}CH_3D$ space (**Figure 3.4c, f**) and $\delta^{13}C$-CH_4 vs $\Delta^{13}CH_3D$ space (**Figure 3.4b, e**), coefficients of determination are negative (e.g., R^2 = -1.69 and -0.21, for two-component mixing in $\delta^{13}C$-CH_4 vs $\Delta^{13}CH_3D$ space for the Gulf of Mexico and Black Sea sites, respectively). These values mean that the mixing of microbial and thermogenic end-members is a worse statistical fit to the data than a horizontal line. Rather than following a mixing relationship, there is a steep negative slope from $\Delta^{13}CH_3D$ = 5‰ to $\Delta^{13}CH_3D$ ~ 3.8‰ ($T_{\Delta 13D}$ from ca. 50 to 110°C) over a < 5‰ increase in $\delta^{13}C$-CH_4 values, which could come from re-equilibration with burial or mixing with thermogenic methane carrying a kinetic signal. In the

deeper sections of the profiles we observe a more gradual slope from $\Delta^{13}CH_3D$ ~ 3.8‰ to $\Delta^{13}CH_3D$ = 2-3‰ over a ca. 20‰ increase in $\delta^{13}C\text{-}CH_4$ values (**Figure 3.4**).

Neither mixing of the microbial end-member with a kinetic signal (i.e., low $\Delta^{13}CH_3D$ values), nor non-linear clumped isotopologue effects associated with mixing explains the observed trends in $\Delta^{13}CH_3D$ values. Mixing between equilibrium microbial methane with a kinetic methane (e.g., $\delta^{13}C\text{-}CH_4 \cong$ -60 to -55‰; $\Delta^{13}CH_3D < 2.5$‰), could produce the observed decrease in $\Delta^{13}CH_3D$ values. However, thermogenic methane like this has not been characterized (**Figure 3.S1**). For example, in the Gulf of Mexico thermogenic methane with $\delta^{13}C\text{-}CH_4 \cong$ -60 to -55‰ has $\Delta^{13}CH_3D$ values between 3.8-6.1‰ (Thiagarajan et al., 2020). It is also important to note that mixing different methane sources can result in non-linearity of $\Delta^{13}CH_3D$ values. The abundance of $^{13}CH_3D$ varies non-linearly with δD and $\delta^{13}C$ such that end-members with the same $\Delta^{13}CH_3D$ value but different δD or $\delta^{13}C$ values can result in a mixture with a different $\Delta^{13}CH_3D$ value from either end-member (Douglas et. al., 2017; Young et al., 2017). Expected non-linearity in $\Delta^{13}CH_3D$ values between end-member mixtures are shown as mixing lines plotted in **Figure 3.4** and are unable to replicate the observed isotopologue abundances.

Our isotopologue data is best described by considering intermediate compositions "I_{GOM}, I_{BS}" to capture the range of microbial-like methane compositions. At the Gulf of Mexico site, the distribution of methane isotopologue values is 4.0±0.15‰, reflecting apparent temperatures of 100^{+7}_{-9} ºC (**Figure 3.5**). For the Gulf of Mexico, the intermediate node (I_{GOM}) is best fit as $\delta^{13}C$ = -68‰, δD = -180‰, C_1/C_{2+3} =250, and $\Delta^{13}CH_3D$ = 3.85-4.15‰. At the Black Sea site, the distribution of methane isotopologue values is 4.0±0.35‰, reflecting apparent temperatures of 100^{+18}_{-18} ºC (**Figure 3.5**). The intermediate composition at the Black Sea site (I_{BS}) is defined as $\delta^{13}C$ = -60‰, δD = -185‰, C_1/C_{2+3} =250, and $\Delta^{13}CH_3D$ = 3.75-4.35‰ (**Figure 3.4**). In $\delta^{13}C$ vs C_1/C_{2+3} space for the Gulf of Mexico and Black Sea profiles, the fit of mixing lines with the intermediate compositions are similar or better than mixing between end-members M and T (M_{GOM}-I_{GOM} R^2 = 0.41, I_{GOM}-T_{GOM} R^2 = 0.90, and I_{BS}-T_{BS} R^2 = 0.67).

At both sites, trends in data across all considered parameters (i.e., C_1/C_{2+3}, $\delta^{13}C\text{-}CH_4$, and $\Delta^{13}CH_3D$) are better represented by the production and/or equilibration of microbial-like methane up to apparent temperatures around 100°C ($\Delta^{13}CH_3D$ ~ 4.0‰), before mixing with a thermogenic source. Additionally, this hypothesis is consistent with the observation of microbial-

like C_1/C_{2+3}, $\delta^{13}C\text{-}CH_4$, and $\delta D\text{-}CH_4$ values found in association with $\Delta^{13}CH_3D \sim 4.0‰$ at depth. In both profiles, values from samples collected between thermogenic and intermediate compositions support conservative mixing between these pools.

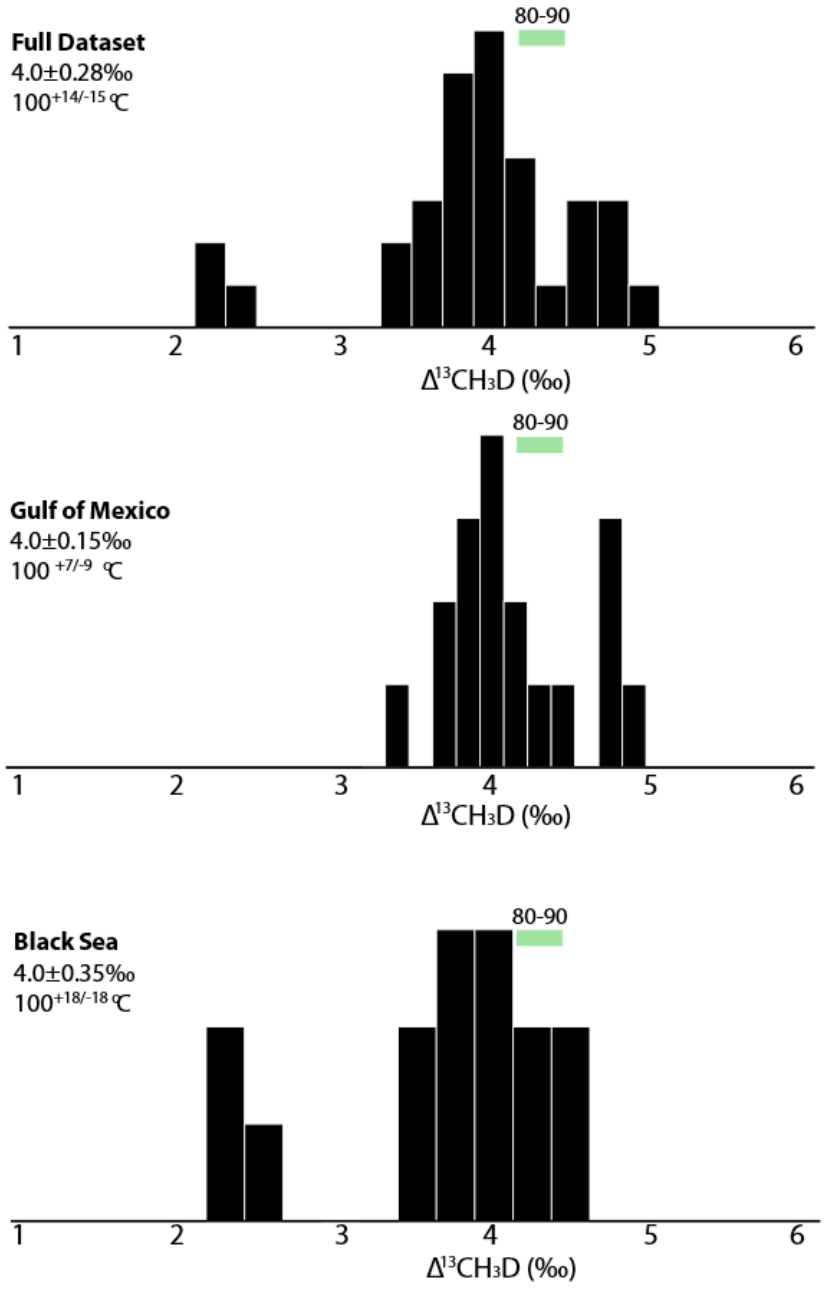

Figure 3.5: Histograms of $\Delta^{13}CH_3D$ values from the combined and individual datasets from the Gulf of Mexico and Black Sea. Distributions are defined from sections of the profile in which apparent temperature and sediment temperature do not match and methane has microbial-like $\delta^{13}C\text{-}CH_4$ values. Each plot indicates the range of $\Delta^{13}CH_3D$ values that correspond to temperatures from 80 to 90°C in green.

3.4.2 Insights to methane history from apparent-sediment temperature offsets

In both Gulf of Mexico and Black Sea profiles, we find that apparent temperature is not always equivalent to the estimated *in situ* sediment temperature (**Figure 3d, h**). This observation may yield insights into the transport and/or burial of methane within the sediment column. There are three general expected outcomes: 1) Apparent temperature and sediment temperature are equivalent within measurement error. This can occur if methane is both forming and equilibrating *in situ*, or transported methane is re-equilibrating faster than burial or advection. 2) Apparent temperature may be lower than sediment temperature. This may occur if methane produced at a cooler temperature is being buried faster than the rate of re-equilibration. 3) Apparent temperature may be higher than sediment temperature. This may occur if methane is transported upwards towards the sediment-water interface via diffusion or advection. We construct a model of expected $\Delta^{13}CH_3D$ values in these sediment columns and compare our observations to make interpretations about the mechanisms of equilibration and transport that are active at these sites.

In the Gulf of Mexico profile, the apparent temperatures of methane are typically higher than estimated sediment temperatures by 2 to 47 ℃ (**Figure 3.3d**), which may indicate that the rate of advection of methane from depth is greater than the burial rate and equilibration rate of methane. This is broadly consistent with the prior geologic understanding of the Mississippi Canyon region of the Gulf of Mexico, where upward advection of fluids may occur due to sediment loading and dewatering. During the past 5 to 10 million years, the high sedimentation rate in the eastern Gulf of Mexico (e.g., 250 cm/1000 yrs) compacts underlying sediment, causing water expulsion, and increasing burial rate and temperature of underlying sediment (Nunn and Sassen, 1986). As a result, many Norphlet reservoirs in the eastern Gulf of Mexico have burial temperatures around 160℃, which is favorable for thermogenic gas formation (Godo, 2017). Additionally, sediments that reach temperatures of 80 to 110℃ are subject to smectite illitization, which results in sediment dewatering, and may contribute to the upward advection of fluids from these strata (e.g., Osborne and Swarbrick, 1998).

In the Black Sea profile, we observe depth intervals where the apparent temperature is less than or within error of the sediment temperature (<2500 mbsf), and where the apparent temperature is greater than sediment temperature (>3000 mbsf) (**Figure 3.3h**). In sediment

<2500 mbsf, it is possible that methane formed at lower temperatures via microbial methanogenesis and is buried with sedimentation. From ~3100 to 3600 mbsf, apparent temperatures (ca. 220°C) are up to 100°C higher than sediment temperatures. Methane from this depth interval may have been generated at depths of ca. 5 kmbsf and transported.

To investigate the implications of apparent-sediment temperature offsets, we develop a model to predict $\Delta^{13}CH_3D$ values throughout the sediment column based on rates of microbial and abiotic equilibration (**Figure 3.6**). Methane is progressively buried, and sediment temperature increases according to the site's thermal gradient (Black Sea ca. 43°C/km and Gulf of Mexico ca. 24°C/km). For the Black Sea site, the sedimentation rate is assumed to be constant at 4 cm/1000yr (e.g., Degens et al., 2007), which corresponds to a rate of temperature change of 0.96 K/million years. For the Gulf of Mexico site, the sedimentation rate is assumed as a step function; sedimentation rate is 16.5 cm/1000 yrs above 3.75 kmbsf, and sedimentation rate is 3 cm/1000 yrs below 3.75 kmbsf. These sedimentation rates correlate to rates of temperature change of 3.96 and 0.73 K/million years, respectively.

The equilibration rate of methane is the sum of both abiotic and microbial equilibration rates. At sediment temperatures less than the temperature-limit for microbial life, a biotic equilibration rate is estimated using assumed methane activation rates and concentrations:

$$k_{biotic} \approx (\text{rate of methane activation}) * \frac{1}{\Phi} * \frac{1}{[CH_4]_{sat}} \qquad (3.2)$$

For this equation, k_{biotic} is the isotopologue exchange rate in yr^{-1}. We assume sediment porosity (Φ) at these depths is between 0.15 and 0.5 (e.g., Heuer et al., 2020; Godo, 2017; Tenzer and Gladkikh, 2014). Using sediment temperature and hydrostatic pressure, we estimate the saturation solubility of methane ($[CH_4]_{sat}$) at these depths using an equation of state (Duan, 1992), which represents a maximum exchangeable methane pool in porewater. Beulig and colleagues report a rate of methanogenesis of 0.3 pmol cm^{-3} day^{-1} from a ^{14}C incubation study of deep sediment from the Nankai Trough conducted at 95°C (Beulig et al., 2022). We assumed the rate of methane activation is the same as the rate of methanogenesis, implying reversibility (of 1) for the reaction catalyzed by methyl co-enzyme M reductase (i.e., the last step of methanogenesis). Equation (3.2) gives the methane turnover rate ($1/k_{bio}$) ~ 400 years.

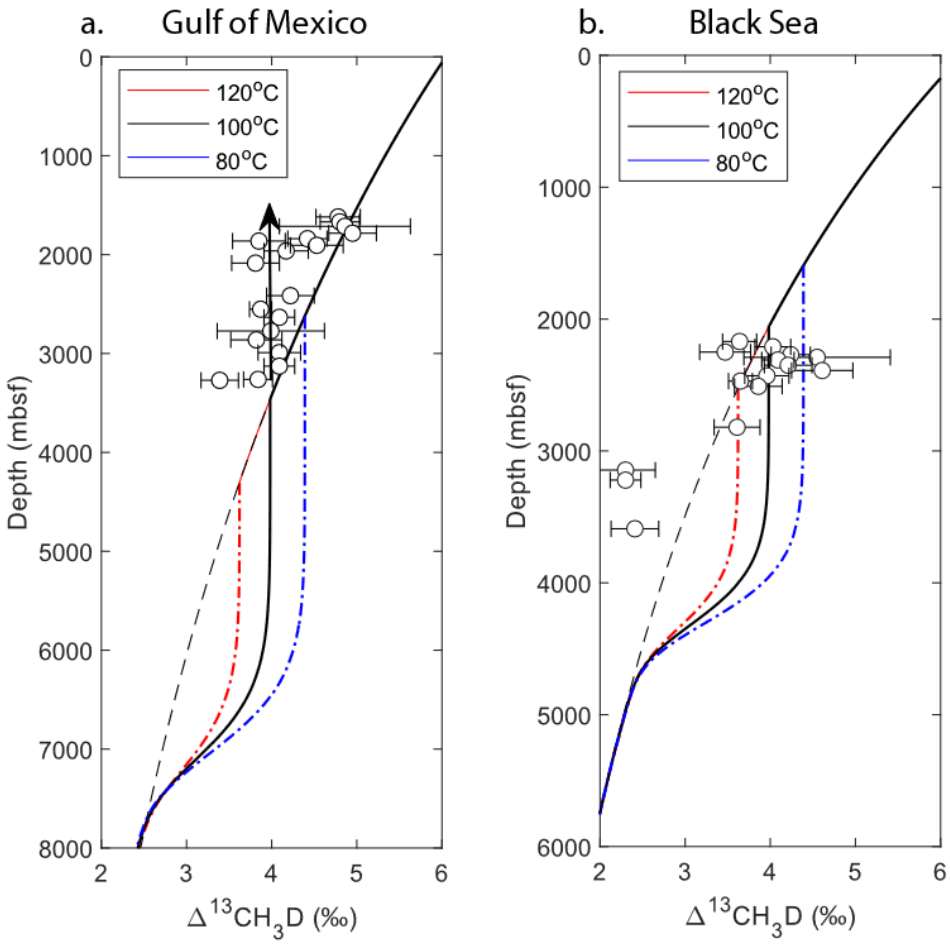

Figure 3.6: Model predicted $\Delta^{13}CH_3D$ values from microbe-catalyzed methane equilibration up to temperature limits of 80°C (blue), 100°C (black), and 120°C (red), followed by catalytic D-H exchange mediating methane equilibration at greater temperatures and depths in **a** the Gulf of Mexico and **b** the Black Sea. The dashed black line represents $\Delta^{13}CH_3D$ values in equilibrium with estimated sediment temperatures. The arrow indicates presumed advection.

At temperatures greater than the temperature-limit of microbial life, methane isotopologue equilibration likely proceeds by D/H exchange with water (e.g., Wang et al., 2015). Turner and colleagues (2022) experimentally determined the abiotic exchange rate at temperatures greater than 350°C (Turner et al., 2022). Extrapolating the temperature dependence to lower temperature yields:

$$k_{abiotic} = 55.6 * exp(3.19 - 17.32 * \frac{1000}{T}) \qquad (3.3)$$

Where $k_{abiotic}$ is in yr^{-1}, and T is the temperature in degrees K. $\Delta^{13}CH_3D$ equilibration is then modeled following Beaudry and colleagues (2021). We test three temperature-limits for microbial life: 80°C, which is the putative thermal limit of oil biodegradation, 100°C, which most closely aligns with observational data, and 120°C, which is the highest temperature provenance that microbes from marine sediments have demonstrated activity (e.g., Beulig et al., 2022).

This model predicts that in the absence of significant effects from advection and/or diffusion, sediment temperature and apparent temperature should be equal within measurement error for temperatures less than the temperature-limit of life, and greater than ca. 180°C. Between these temperatures, apparent temperatures are expected to be less than sediment temperatures, by as much as 1.5‰, due to slow expected equilibration rates. For both the Gulf of Mexico (**Figure 3.6a**) and Black Sea (**Figure 3.6b**) sites, a 100°C temperature-limit of microbial life best describes the data. Unlike the Black Sea, however, samples from the Gulf of Mexico appear to have significant influence from upward advection, broadly consistent with geologic understanding of both sites.

Abiotic exchange is too slow to explain methane equilibrated at temperatures below 150°C, but above ca. 80°C temperatures are expected to be too high for microbes to survive. Thus, we expect to see non-equilibrated methane at depth corresponding to temperatures between ca. 100-150°C. However, for both the Black Sea (**Figure 3.6b**) and Gulf of Mexico (**Figure 3.6a**) sites, we find that equilibration appears to cease at 100±10°C, between the putative temperature limit for oil biodegradation and the highest known temperature limit of microbial life. Methane found shallower than 2500 mbsf in the western Black Sea has an apparent temperature that is lower or within error of the current sediment temperatures, up to ca. 110 to 120°C sediment temperature, which supports the assumption that apparent temperature reflects equilibrium temperature. Methane isotopologue observations in the Gulf of Mexico are consistent with upward advection of methane equilibrated to a thermal boundary of ca. 100^{+14}_{-15}°C. Estimating the timescale of exchange using **Equation 3.3**, it would take 10^9 years for methane to equilibrate at 110°C sediment temperature via catalytic D/H exchange, about ¼ the age of the Earth. A change in $\Delta^{13}CH_3D$ from 4.4 to 4.2‰, which reflects a change in temperature from 80°C to 90°C, would take on the order of 10^8 years in sediments that are on the order of 10^7

years old. Thus, we propose that the microbial equilibration mechanisms may remain active at temperatures greater than the previously accepted 80 to 90°C thermal limit.

To further assess the potential of microbially-mediated methane equilibration at temperatures up to ca. 100^{+14}_{-15}°C we can estimate the timescale to fully exchange the methane pool at key depths in the study sites (**Table 3.S3**). For the Gulf of Mexico and Black Sea sites, we consider conditions at 100°C sediment temperature, which corresponds to 3700 mbsf and 2000 mbsf, respectively. Using our estimate for biotic exchange rate, 100°C sediment at the saturation limit of methane would exchange on a timescale of 10^6 years. For the Black Sea, a timescale of 10^6 years corresponds to ca. 40 m of sediment, assuming a sedimentation rate of 4cm/1000yr, and is within our sampling resolution of ca. 30-100m. For the Gulf of Mexico, a timescale of 10^6 years corresponds to ca. 165 m of sediment, assuming a sedimentation rate of 16.5cm/1000yr for the sediment strata that encompass this temperature zone. Given the existing uncertainty in methane concentration and microbial activity throughout these sites, microbially-mediated turnover of the methane pool at these depths and temperatures is possible.

An implication of this model is that we may expect the edge of the temperature limit of bond re-ordering (i.e., the intermediate compositions) may be preserved for up to hundreds of meters. Natural gas samples with isotope values similar to the intermediate gas compositions (e.g., δ^{13}C-CH_4 ≅ -60 to -50‰; δD-CH_4 ≅ -190 to -180‰; T_{13D} ≅ 85-114°C) have been reported previously (**Figure 3.S2**). For example, in the Gulf of Mexico, methane samples with similar isotope compositions (δ^{13}C-CH_4 ≅ -60‰; δD-CH_4 ≅ -190‰; T_{13D} ≅ 93-109°C) have been reported from the Pleistocene Genesis Field (well temperatures from 63 to 71 °C), as well as the Hoover Diana field (δ^{13}C-CH_4 ≅ -60 to -56‰; δD-CH_4 ≅ -202 to -192‰; T_{13D} ≅ 52-118°C), with well temperature ~60°C (Thiagarajan et al., 2020). Methane from the Pleistocene Genesis Field was hypothesized to be a mixture of microbial and thermogenic end-members with nearly identical δD values, where the thermogenic end-member is equilibrated at 120°C. At the Hoover Diana field, methane was hypothesized to be a mixture of secondary microbial methane with a thermogenic end-member, equilibrated at 120°C. Two samples from this site were measured for $\Delta^{12}CH_2D_2$ and found to be near intra-molecular equilibrium (Thiagarajan et al., 2020). Further, samples with similar isotope compositions have been reported in the Zonguldak basin in the western Black Sea (δ^{13}C-CH_4 ≅ -50‰; δD-CH_4 ≅ -190 to -177‰; C_1/C_{2+3} ≅ 80 to 750), and

attributed in part to secondary methane generation (Hoşgörmez et al., 2002). We postulate that the methane found at these sites may be consistent with the observation of intermediate methane described in this study.

We additionally consider whether equilibration is expected for the thermogenic methane found deeper than 3000 mbsf in the western Black Sea profile. If abiotic exchange can equilibrate thermogenic methane at current sediment temperatures on timescales that are less than the age of the sediments, the apparent temperature may add constraints to how long-ago methane was transported. The apparent temperature of methane may imply formation at ca. 220°C, and transport to sediments with *in situ* temperatures of ca. 150°C. Using **Equation 3.3,** the estimated timescale of abiotic D/H equilibration is ca. 4 million years at 150°C. Thus, methane stored in these sediments for longer than 4 million years should carry an apparent temperature signal of ca. 150°C. As this methane has an apparent temperature of 220°C, and the age of the sediment is ca. 20 to 40 million years, we can constrain the transport of methane from depth to have occurred within the past 4 million years (10 to 20% of the depositional age) (**Figure 3.2b**). Alternatively, the high apparent-sediment temperature offset of the samples from deeper than 3000 mbsf may occur from generation of methane that carries kinetic (low $\Delta^{13}CH_3D$) signals. Recent studies (e.g., Dong et al., 2021; Shuai et al., 2018; Xie et al., 2021) show that clumped isotopes of thermogenic methane are not always equilibrated. In particular, analysis of $\Delta^{13}CH_3D$ and $\Delta^{12}CH_2D_2$ for early through late-stage thermogenic gases supports early maturity thermogenic gas forming in isotopic disequilibrium, while late maturity thermogenic gas appears to be in intramolecular equilibrium (Xie et al., 2021). Methane from deeper than 3000 mbsf in the western Black Sea has the characteristics of a late maturity thermogenic origin. Isotopic evidence includes $\delta D\text{-}CH_4$ values around ca. -145‰, where $\delta D\text{-}CH_4$ values of late maturity thermogenic gas are greater than ca. -250‰, and $\delta^{13}C\text{-}CH_4$ values around ca. -40‰, while $\delta^{13}C\text{-}CH_4$ values of late maturity thermogenic gas are greater than ca. -50‰. Further, 220°C is a temperature that would support the generation of late maturity thermogenic gas, rather than early maturity thermogenic or oil-associated methane. This data supports the assumption that apparent temperature reflects equilibrium temperature for these methane samples.

3.4.3 Potential origins of 100^{+14}_{-15}°C apparent temperature

Putative upper limits of primary (e.g. fermentation of organic matter and CO_2 reduction) and secondary (e.g., oil biodegradation) methane production are ca. 60°C and 80-90°C, respectively (Head et al., 2003; Horsfield et al., 2006; Parkes et al., 2007; Wilhelms et al., 2001); however, the occurrence of microbial methanogenesis beyond 80-90°C has been proposed for several marine sedimentary environments. Empirical evidence for the temperature limit of primary microbial methanogenesis includes sediment incubation experiments where methane production is stimulated between 30-60°C, with microbial activity continuing through 90°C (Parkes et al., 2007). Microbial consortia including thermophilic methanogens were isolated from oil reservoirs with temperatures from 60 to 90°C (Orphan et al., 2000). Empirical evidence for the temperature limit of secondary microbial methanogenesis is largely based on putative sterilization temperatures (e.g., >80-90°C) that distinguish biodegraded from non-biodegraded oil reservoirs (Wilhelms et al., 2001). Additional biomarker evidence for life in deep sedimentary environments includes the observation of intact phospholipids, indicative of living cells, found in 85°C sediments of the Nankai Trough (Horsfield et al., 2006). More recent work revisiting this site presents geochemical (e.g., concentration and $\delta^{13}C$ values of methane and acetate) and microbiological (e.g., cell and endospore concentration) evidence for the persistence of microbial methanogenesis to at least ca. 85°C (Heuer et al., 2020). Work based on radiotracer experiments from the Nankai Trough subduction zone have suggested the habitability of sediments up to 120°C, beyond the proposed 80 to 90°C temperature-limit of life (Beulig et al., 2022). The Walker Ridge region of the northeastern Gulf of Mexico shows isotope and biomarker evidence of a significant contribution of methane produced by oil biodegradation, suggesting microbial methanogenesis at current reservoir temperatures of ca. 80 to 115°C(Milkov and Dzou, 2007).

In weighing the importance of the role of microbial processes in mediating isotopologue exchange in 100^{+14}_{-15}°C marine sediments, we must additionally consider the potential impact of measurement calibration, kinetic fractionation, and non-enzymatic bond re-ordering on $\Delta^{13}CH_3D$ values and their interpretations.

Differences in $\Delta^{13}CH_3D$ values on the scale of 0.5‰ have important implications for interpreting the temperature-limits of proposed bond re-ordering and the temperature-limit of microbial methanogenesis. For example, the difference between an apparent temperature of 80°C and 100°C is ca. 0.4‰. In calibrating the clumped isotopologue geothermometer, two different

theories predict slightly different temperature dependencies for the values of $\Delta^{13}CH_3D$ (e.g., Eldridge et al., 2019; Liu and Liu, 2016; Wang et al., 2015; Webb and Miller, 2014). Sample measurements from this study are calibrated against 250°C heated methane, and we define this value as 2.07‰, based on the calibration by Eldridge et al. (2019). This value is 0.09‰ higher than the value of 1.98‰ obtained by Wang et al. (2015), thus $\Delta^{13}CH_3D$ values reported in this study are approximately 0.1‰ higher than the alternative calibration. This difference is considered small relative to the 95% confidence intervals reported in **Tables 3.1** and **3.2** (ca. 0.3‰). The difference in derived apparent temperatures using two different calibrations are within 4° at temperatures < ca. 60°C and within 7° at temperatures < ca. 150°C.

Apparent temperatures 8 to 38°C higher than the putative upper-temperature limit of oil biodegradation (80°C) could reflect a contribution from kinetic isotope effects, such that apparent temperatures do not exactly reflect methane equilibration temperatures. Kinetic isotope effects may be imparted on methane by microbial metabolisms, physical processes like diffusion, or early maturity thermogenic methane production. While microbial methane from deep marine sediments have been found to have near equilibrium $\Delta^{13}CH_3D$ values, input from a kinetic microbial gas cannot be completely ruled out in this environment in the absence of concordant $\Delta^{12}CH_2D_2$ data to support the equilibrium assumption. Given the small sample sizes (e.g., ~0.5 mL CH_4 in the Black Sea) $\Delta^{12}CH_2D_2$ values are unable to be measured.

Kinetic fractionation could additionally come from early mature thermogenic methane production, although we evaluate this scenario to be unlikely. Temperatures around ca. 110°C and $\delta^{13}C$-CH_4 values ~-60‰ are reasonable for early maturity thermogenic methane; however, δD-CH_4 of samples (ca. -180‰ in the Gulf of Mexico and ca. -190‰ in the Black Sea) are typical of microbial gas, distinct from early maturity thermogenic which typically has δD-CH_4 values around -300‰. Further, expected molecular ratios (C_1/C_{2+3}) for intermediate methane are higher than what is typical for early maturity thermogenic gas (0.1 to 100, vs 250 expected in the Black Sea and the Gulf of Mexico) (Milkov and Etiope, 2018). A study of $\Delta^{13}CH_3D$ and $\Delta^{12}CH_2D_2$ of thermogenic gases have shown that methane generated at early thermal maturities is in intra-molecular disequilibrium, while methane generated at higher thermal maturities (peak temperatures from ca. 170 to 210°C) reaches equilibrium (Xie et al., 2021). Xie and colleagues observe apparent temperatures >150°C for all studied gas samples, and early mature thermogenic

gases have higher temperatures than equilibrated late maturity thermogenic gases. Thus, if the source of intermediate methane is from early-maturity thermogenic gas production, $\Delta^{13}CH_3D$ values would be expected to be much lower than equilibrium, and we could not assume that apparent temperatures are reflecting environmental temperatures. However, in this study, apparent temperatures of intermediate methane are comparably lower, and the near matches of apparent and sediment temperatures in the Black Sea support the equilibrium assumption.

Non-enzymatic bond re-ordering, catalyzed by clay/mineral interactions, has been hypothesized as a controlling mechanism for clumped methane isotopologue composition down to temperatures as low as 65°C (e.g., Labidi et al., 2020, Giunta et al., 2021), but this mechanism is not well substantiated by multi-km profile data. Giunta and colleagues observe a bimodal distribution of equilibrium apparent temperatures from cold seep methane around ca. 92 and 150°C, which matches closely with our prediction of biotic exchange up to ca. 100°C and abiotic exchange above 150°C (**Figure 3.5**). $\Delta^{13}CH_3D$ and $\Delta^{12}CH_2D_2$ data from these cold seeps are used to argue that abiotic isotopologue bond re-ordering rates of clumped species are faster than what is predicted from bulk D/H exchange (Giunta et al., 2021). Further, Abiotic bond re-ordering down to temperatures of 65°C in hydrothermal settings has been suggested to account for $\Delta^{12}CH_2D_2$ re-equilibration, but $\Delta^{13}CH_3D$ re-equilibration is suggested to be substantially slower (Labidi et al., 2020). It is difficult to reconcile the non-enzymatic exchange mechanism with our observation of a continuum of $\Delta^{13}CH_3D$ values from low temperatures to 100^{+14}_{-15}°C. Rather, we would expect that abiotic bond re-ordering would become more important at progressively higher temperatures. Abiotic bond re-ordering via D/H exchange is expected to be slow at temperatures of ca. 100^{+14}_{-15}°C; however, rates of re-equilibration $^{13}CH_3D/^{12}CH_4$ are uncharacterized at these temperatures.

Thus, multi-km depth profile data of $\Delta^{13}CH_3D$ may support the hypothesis, presented in Milkov and Dzou (2007) and Beulig and colleagues (2022), that microbial methanogenesis may be occurring in marine sediments at temperatures higher than 80°C. Further, there are continued opportunities for clumped methane isotopologue measurements to yield insight into the temperature limits of life and important fluid transport mechanisms in marine sedimentary environments.

3.5 SUMMARY

In this study, we applied clumped methane isotopologue geothermometry alongside isotope ratios of methane ($\delta^{13}C$, and δD) and hydrocarbon ratios (C_1/C_{2+3}) to investigate two kilometer-scale methane profiles in the northeastern Gulf of Mexico and the western Black Sea. The profiles of clumped isotopologues of methane yield new constraints in the investigation of methane provenance between optimal primary microbial and late maturity thermal methanogenic environments. New isotopic evidence suggests that conservative mixing between shallow microbial and deep thermogenic sources does not describe the composition of methane found between these sources. Rather, we observe microbial-like methane equilibrated to ca. 100^{+14}_{-15}°C before an apparent mixing with a deep thermogenic source. Further, the relationship between apparent and sediment temperatures can provide insight into the burial and transport history of methane. We estimate methane equilibration timescales based on rates of D/H exchange. We find that observed microbial-like methane with apparent temperatures of ca. 100^{+14}_{-15}°C cannot be explained by catalytic re-equilibration of methane formed at lower temperatures, on a geologically relevant timescale; however, microbial turnover of methane may occur on the order of 10^6 years at 100°C sediment temperature. Thus, we suggest that microbial methanogenesis may remain active at temperatures 5 to 34°C higher than what has been previously accepted. Alternatively, kinetic fractionation may cause the apparent temperature of methane to be slightly higher than the equilibration temperature.

3.6 ACKNOWLEDGEMENTS

We thank Esra Inan Villegas and Amr El-Azhary for helping to obtain samples. This work was supported by the Deep Carbon Observatory through a Deep Life Community Grant (to S.O.), and Neil R. Braunsdorf and Dirk J.H. Smit of Shell PTI/EG (to S.O). E.L. was supported by the Presidential Graduate Fellowship at MIT, and MIT-Shell Energy Initiative Graduate Fellowships.

3.7 SUPPLEMENTARY INFORMATION

3.7.1 $\Delta^{13}CH_3D$ as a tool to assess the two end-member mixing hypothesis

Gulf of Mexico				
	C_1/C_{2+3}	$\delta^{13}C$	δD	$\Delta^{13}CH_3D$
M_{GOM}	1500	-70	-180	5
I_{GOM}	200	-67	-180	3.85-4.15
T_{GOM}	5	-45	-245	3 to 3.5
Black Sea				
	C_1/C_{2+3}	$\delta^{13}C$	δD	$\Delta^{13}CH_3D$
M_{BS}	1500	-60	-200	5
I_{BS}	250	-60	-195	3.75-4.35
T_{BS}	60	-40	-145	2

Table 3.S1: Values used in mixing calculations

Well ID	Depth in m	C_1/C_{2+3}	$\delta^{13}C$	δD
1	7866	4.070	-46.33	-255.5
2	8005	5.811	-46.51	-255.5
2	8005	5.737	-46.55	-255.2
2	7601	5.781	-46.06	-247.5
2	7566	6.221	-45.95	-246.2
2	7554	5.672	-46.11	-245
2	7601	5.725	-46.13	-244.8
2	7554	6.838	-46.05	-243.9
2	7566	6.225	-46	-243.7
2	7505	6.189	-46.01	-243
2	7505	5.292	-46.03	-241.3
3	7857	4.195	-44.87	-224.6
3	7829	4.316	-44.86	-224.6

Table 3.S2: values of nearby GOM thermogenic well gases

3.7.2 No evidence for a kinetic intermediate-like end-member

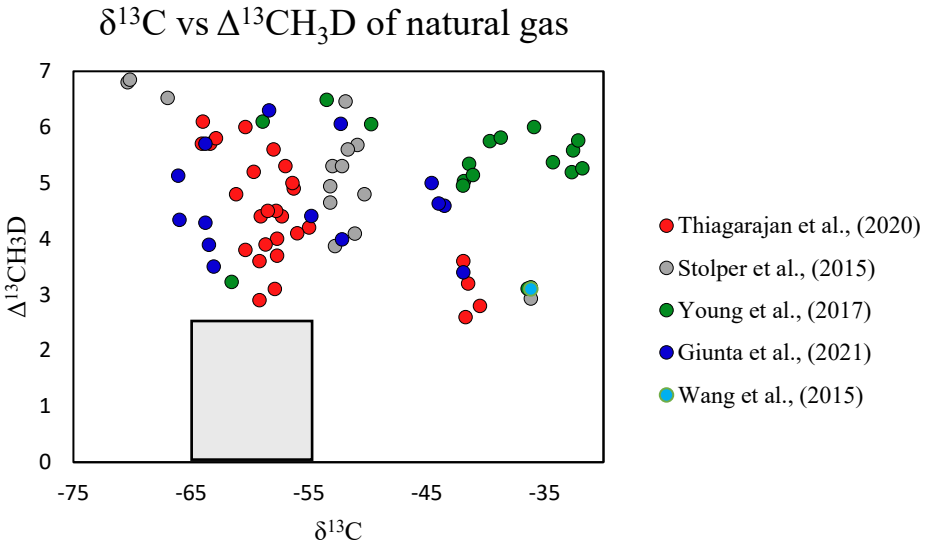

Figure 3.S1: $\delta^{13}C$ vs $\Delta^{13}CH_3D$ of natural gas. There is a lack of observational data for a kinetic microbial-like end-member (dark grey box). Isotopologue data is from: Giunta et al., 2021; Stolper et al., 2015; Thiagarajan et al., 2020; Wang et al., 2015; Young et al., 2017.

3.7.3 Data from other studies similar to intermediate end-members

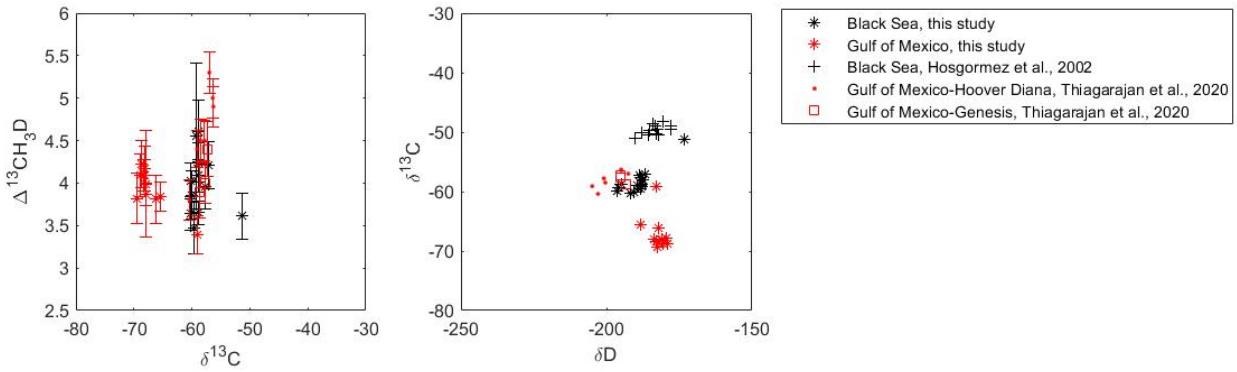

Figure 3.S2: Data from other studies (Hosgormez et al., 2002; Thiagarajan et al., 2020) with simiar isotope values to intermediate values. Values are in per mille units. Black symbols are for sites in the Black Sea, while red symbols are for sites in the Gulf of Mexico.

3.7.4 Abiotic D/H exchange

The isotopologue effect of abiotic D/H exchange is modeled similar to Beaudry et al. (2021), and based on the rate law (**Equation S1**) derived by Ohmoto and Lasaga (1982) and simplified (**Equation S2**) assuming a constant number density of exchangeable water in this environment. Based on experiments performed at temperatures from 376 to 420°C, an empirical rate law has been derived (**Equation S3**) to describe the exchange. The rate constant, k, is in units s^{-1}. The rate of exchange is calculated by multiplying the rate constant by 31,557,600 to convert the units to yr^{-1} and by 55.6 for exchange in water. Isotopic fractionation proceeds according to **Equation S4** and **Equation S5**, and clumped isotopologue distribution is defined as **Equation S6**. Temperature-dependent fractionation factors for H_2O-CH_4 ($^2\alpha$) and CO_2-CH_4 ($^{13}\alpha$) exchange are given by **Equation S7** and **Equation S8**, respectively. The calibration between $\Delta^{13}CH_3D$ and temperature in Kelvin is given by **Equation S1.** For **Equations S7**, **S8**, and **S9**, temperature (T) is in Kelvin.

Equation #	Equation	Reference
S1	$\ln\left(\frac{\alpha^e-\alpha}{\alpha^e-\alpha^0}\right)=-k([H_2O])t$	(Ohmoto and Lasaga, 1982)
S2	$\ln\left(\frac{\alpha^e-\alpha}{\alpha^e-\alpha^0}\right)=-k'*t$	(Pester et al., 2018)
S3	$k = \exp\left(-17.32*\frac{1000}{T}+3.19\right)$	Turner et al. (2022)
S4	$^{12}\alpha_{H_2O-CH_4}=\frac{[^{12}CH_4]*[HDO]}{[^{12}CH_3D]*[H_2O]}$	
S5	$^{13}\alpha_{H_2O-CH_4}=\frac{[^{13}CH_4]*[HDO]}{[^{13}CH_3D]*[H_2O]}$	
S6	$Q=\frac{[^{13}CH_3D]*[^{12}CH_4]}{[^{12}CH_3D]*[^{13}CH_4]}$	
S7	$^2\alpha = 1.0997+8.456*\frac{10^3}{T^2}+0.9611*\frac{10^9}{T^4}-27.82*\frac{10^{12}}{T^6}$	(Horibe and Craig, 1995; Whitehill et al., 2017)
S8	$1000\ln{}^{13}\alpha = 0.16+11.754*\frac{10^6}{T^2}-2.3655*\frac{10^9}{T^3}+0.2054*\frac{10^{12}}{T^4}$	(Horita, 2001; Richet et al., 1977)
S9	$\Delta\,^{13}CH_3D\,(T)=0.0147348*\frac{10^{21}}{T^7}-0.208648*\frac{10^{18}}{T^6}+1.19810*\frac{10^{15}}{T^5}-3.54757*\frac{10^{12}}{T^4}+5.54476*\frac{10^9}{T^3}-3.49394*\frac{10^6}{T^2}+8.8937*\frac{10^3}{T}$	(Eldridge et al., 2019)

Table 3.S3: Equations used to calculate isotopologue values and timescale of D/H exchange

We use the model to assess timescales of abiotic D/H equilibration for two scenarios in the Black Sea: 1) the equilibration of thermogenic methane formed at 220°C and transported to 150°C sediments, and 2) the equilibration of methane formed microbially at 80°C and buried in 110°C sediments. Timescales of isotopologue equilibration are shown in **Figure S3**.

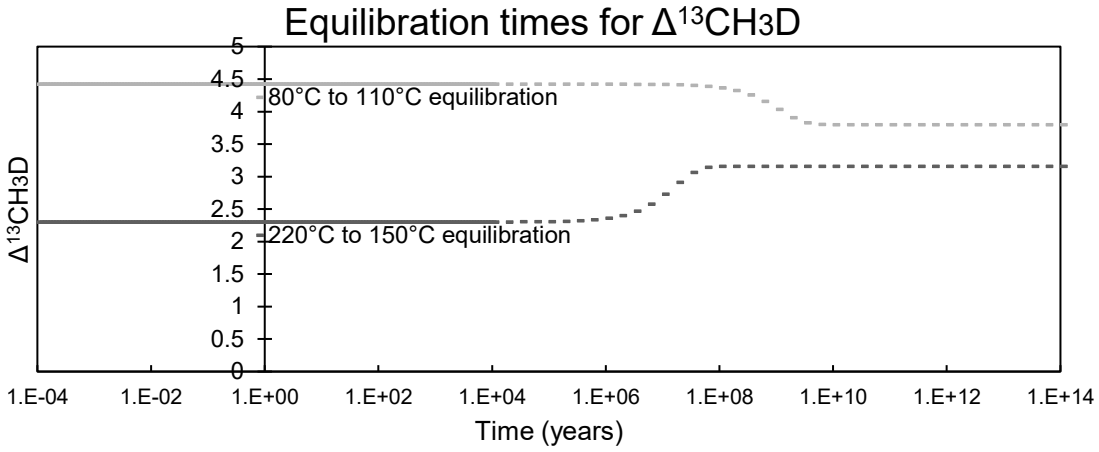

Figure 3.S3: Theoretical equilibration timescales of abiotic D/H exchange based on rate the described model for calculating D/H exchange

3.7.5 Timescale of microbial CH_4 turnover

					f_{sat}:	
					0.2	1
Site	**Depth m**	**Temperature °C**	**Pressure bar**	**[CH4]sat mol/kg**	**Time MYR**	**Time MYR**
Gulf of Mexico	3700	100	588.9	0.2328	0.213	0.106
Black Sea	2000	100	320	0.1642	0.105	0.750

Table 3.S4: Timescale of microbial methane turnover in 100°C sediments. MYR is million years.

The saturation concentration of methane is calculated using the equation of state by Duan et al., 1992. Timescale is calculated with the equation:

$$Time = \frac{f_{sat} * [CH_4]_{sat} * \Phi}{C\ cosumption\ rate}$$

Where porosity (Φ), is 0.35 (e.g., Heuer et al., 2020), and consumption rate (C) is 0.3 pmol cm_{ws}^{-3} day^{-1} (Beulig et al., 2022). f_{sat} is the concentration of methane over the saturation concentration of methane at relevant temperatures and depths.

3.8 REFERENCES

Ablard, P., Bell, C., Cook, D., Fornasier, I., Poyet, J.P., Sharma, S., Fielding, K., Lawtou, L., Haines, G., Herkonamer, M.A., McCarthy, K., Radakovic, M., Umar, L., 2012. The expanding role of mud logging. Oilf. Rev. 24, 24–41.

Ash, J.L., Egger, M., Treude, T., Kohl, I., Cragg, B., Parkes, R.J., Slomp, C.P., Lollar, B.S., Young, E.D., 2019. Exchange catalysis during anaerobic methanotrophy revealed by $^{12}CH_2D_2$ and $^{13}CH_3D$ in methane. Geochemical Perspect. Lett. 10, 26–30. https://doi.org/10.7185/geochemlet.1910

Bernard, B.B., Brooks, J.M., Sackett, W.M., 1976. Natural gas seepage in the Gulf of Mexico. Earth Planet. Sci. Lett. 31, 48–54. https://doi.org/10.1016/0012-821X(76)90095-9

Beulig, F., Schubert, F., Adhikari, R.R., Glombitza, C., Heuer, V.B., Hinrichs, K., Homola, K.L., Inagaki, F., Jørgensen, B.B., Kallmeyer, J., Krause, S.J.E., Morono, Y., Sauvage, J., Spivack, A.J., Treude, T., 2022. Rapid metabolism fosters microbial survival in the deep, hot subseafloor biosphere 1–9. https://doi.org/10.1038/s41467-021-27802-7

Borowski, W.S., Hoehler, T.M., Alperin, M.J., Rodriguez, N.M., Paull, C.K., 2000. Significance of anaerobic methane oxidation in methane-rich sediments overlying the Blake Ridge gas hydrates. Proc. Ocean Drill. Progr. Sci. Results 164, 87–99. https://doi.org/10.2973/odp.proc.sr.164.214.2000

Burnham, A.K., 1989. A simple kinetic model of petroleum formation and cracking.

D'Hondt, S., Pockalny, R., Fulfer, V.M., Spivack, A.J., 2019. Subseafloor life and its biogeochemical impacts. Nat. Commun. 10, 3519. https://doi.org/10.1038/s41467-019-11450-z

Degens, E.T., Stoffers, P., Golubic, S., Dickman, M., 2007. Varve Chronology: Esitmated rates of sedimentation in the Black Sea deep basin. Deep Sea Drill. Proj. Initial Reports 42, 499–508.

Dong, G., Xie, H., Formolo, M., Lawson, M., Sessions, A., Eiler, J., 2021. Clumped isotope effects of thermogenic methane formation: Insights from pyrolysis of hydrocarbons. Geochim. Cosmochim. Acta 303, 159–183. https://doi.org/10.1016/j.gca.2021.03.009

Douglas, P.M.J., Gonzalez Moguel, R., Walter Anthony, K.M., Wik, M., Crill, P.M., Dawson, K.S., Smith, D.A., Yanay, E., Lloyd, M.K., Stolper, D.A., Eiler, J.M., Sessions, A.L., 2020. Clumped Isotopes Link Older Carbon Substrates With Slower Rates of Methanogenesis in Northern Lakes. Geophys. Res. Lett. 47, 1–10. https://doi.org/10.1029/2019GL086756

Duan, Z., Moller, N., Greenberg, J., Weare, J.H., 1992. The prediction of methane solubility in natural waters to high ionic strength from 0 to 250 C and from 0 to 1600 bar. Geochim. Cosmochim. Acta 56, 4303. https://doi.org/10.1016/0016-7037(92)90271-J

Eldridge, D.L., Korol, R., Lloyd, M.K., Turner, A.C., Webb, M.A., Miller, T.F., Stolper, D.A., 2019. Comparison of experimental vs theoretical abundances of $^{13}CH_3D$ and $^{12}CH_2D_2$ for isotopically equilibrated systems from 1 to 500 °C. ACS Earth Sp. Chem. 3, 2747–2764. https://doi.org/10.1021/acsearthspacechem.9b00244

Faber, E., Schmitt, M., Stahl, W., 1978. Carbon Isotope Analyses of Head Space Methane From samples of leg 42B, Sites 379, 380, and 381. Deep Sea Drill. Proj. Initial Reports 42, 667–672.

Fallah, M., Mayer, J., Tari, G., Baur, J., 2018. Holocene source rock deposition in the Black Sea, insights from a dropcore study offshore Bulgaria. Geol. Soc. London, Spec. Publ. 464, 389 LP-401. https://doi.org/10.1144/SP464.11

Galloway, W.E., 2008. Chapter 15 Depositional Evolution of the Gulf of Mexico Sedimentary Basin, Sedimentary Basins of the World. Elsevier. https://doi.org/10.1016/S1874-5997(08)00015-4

Giunta, T., Young, E.D., Warr, O., Kohl, I., Ash, J.L., Martini, A., Mundle, S.O.C., Rumble, D., Pérez-Rodríguez, I., Wasley, M., LaRowe, D.E., Gilbert, A., Sherwood Lollar, B., 2019. Methane sources and sinks in continental sedimentary systems: New insights from paired clumped isotopologues $^{13}CH_3D$ and $^{12}CH_2D_2$. Geochim. Cosmochim. Acta 245, 327–351. https://doi.org/10.1016/j.gca.2018.10.030

Godo, T., 2017. The Appomattox Field: Norphlet aeolian sand dune reservoirs in the deep-water Gulf of Mexico. Giant fields Decad. 2000–2010 AAPG Mem. 113 29–54. https://doi.org/10.1306/13572000M1133680

Gonzalez, Y., Nelson, D.D., Shorter, J.H., Mcmanus, J.B., Formolo, M.J., Wang, D.T., Western, C.M., Ono, S., 2019. Precise measurements of $^{12}CH_2D_2$ by tunable infrared laser direct absorption spectroscopy. https://doi.org/10.1021/acs.analchem.9b03412

Hammerschmidt, S.B., Wiersberg, T., Heuer, V.B., Wendt, J., Erzinger, J., Kopf, A., 2014. Real-time drilling mud gas monitoring for qualitative evaluation of hydrocarbon gas composition during deep sea drilling in the Nankai Trough Kumano basin. Geochem. Trans. 15. https://doi.org/10.1186/s12932-014-0015-8

Haworth, J.H., Sellens, M., Whittaker, A., 1985. Interpretation of Hydrocarbon Shows Using Light (C_1-C_5) Hydrocarbon Gases From Mud-Log Data. Am. Assoc. Pet. Geol. Bull. 69, 1305–1310.

Head, I.M., Jones, D.M., Larter, S.R., 2003. Biological activity in the deep subsurface and the origin of heavy oil. Nature 426, 344–352. https://doi.org/10.1038/nature02134

Heuer, V.B., Inagaki, F., Morono, Y., Kubo, Y., Spivack, A.J., Viehweger, B., Treude, T., 2020. Temperature limits to deep subseafloor life in the Nankai Trough subduction zone. Science (80-.). 1234.

Horsfield, B., Schenk, H.J., Zink, K., Ondrak, R., Dieckmann, V., Kallmeyer, J., Mangelsdorf, K., di Primio, R., Wilkes, H., Parkes, R.J., Fry, J., Cragg, B., 2006. Living microbial ecosystems within the active zone of catagenesis: Implications for feeding the deep biosphere. Earth Planet. Sci. Lett. 246, 55–69. https://doi.org/10.1016/j.epsl.2006.03.040

Hoşgörmez, H., Yalçin, M.N., Cramer, B., Gerling, P., Faber, E., Schaefer, R.G., Mann, U., 2002. Isotopic and molecular composition of coal-bed gas in the Amasra region (Zonguldak basin - Western Black Sea). Org. Geochem. 33, 1429–1439.

Hunt, J., 1996. Petroleum Geochemistry and Geology, second. ed. New York.

Inagaki, F., Hinrichs, K.-U., Kubo, Y., Bowles, M.W., Heuer, V.B., Hong, W.-L., Hoshino, T., Ijiri, A., Imachi, H., Ito, M., Kaneko, M., Lever, M.A., Lin, Y.-S., Methe, B.A., Morita, S., Morono, Y., Tanikawa, W., Bihan, M., Bowden, S.A., Elvert, M., Glombitza, C., Gross, D., Harrington, G.J., Hori, T., Li, K., Limmer, D., Liu, C.-H., Murayama, M., Ohkouchi, N., Ono, S., Park, Y.-S., Phillips, S.C., Prieto-Mollar, X., Purkey, M., Riedinger, N., Sanada, Y., Sauvage, J., Snyder, G., Susilawati, R., Takano, Y., Tasumi, E., Terada, T., Tomaru, H., Trembath-Reichert, E., Wang, D.T., Yamada, Y., 2015. Exploring deep microbial life in coal-bearing sediment down to 2.5 km below the ocean floor. Science (80-.). 349, 420–424. https://doi.org/10.1126/science.aaa6882

LaRowe, D.E., Amend, J.P., 2015. Power limits for microbial life. Front. Microbiol. 6, 1–11. https://doi.org/10.3389/fmicb.2015.00718

Liu, Q., Liu, Y., 2016. Clumped-isotope signatures at equilibrium of CH_4, NH_3, H_2O, H_2S and SO_2. Geochim. Cosmochim. Acta 175, 252–270. https://doi.org/10.1016/j.gca.2015.11.040

Lorant, F., Prinzhofer, A., Behar, F., Huc, A.-Y., 1998. Carbon isotopic and molecular constraints on the formation and the expulsion of thermogenic hydrocarbon gases. Chem. Geol. 147, 249–264. https://doi.org/https://doi.org/10.1016/S0009-2541(98)00017-5

Mcbride, B.C., Weimer, P., Rowan, M.G., 1998. The Effct of Allochthonous Salt on the Petroleum Systems of Northern Green Canyon and Ewing Bank (Offshore Louisiana), Northern Gulf of Mexico. Am. Assoc. Pet. Geol. 1083–1112.

Milkov, A. V., Dzou, L., 2007. Geochemical evidence of secondary microbial methane from very slight biodegradation of undersaturated oils in a deep hot reservoir. Geology 35, 455–458. https://doi.org/10.1130/G23557A.1

Milkov, A. V., Etiope, G., 2018. Revised genetic diagrams for natural gases based on a global dataset of >20,000 samples. Org. Geochem. 125, 109–120. https://doi.org/10.1016/j.orggeochem.2018.09.002

Nunn, J.A., Sassen, R., 1986. Framework of Hydrocarbon Generation and Migration, Gulf of Mexico Continental Slope. Am. Assoc. Pet. Geol. Bull. 70, 257–262. https://doi.org/10.1306/94886b7d-1704-11d7-8645000102c1865d

Ono, S., Wang, D.T., Gruen, D.S., Sherwood Lollar, B., Zahniser, M.S., McManus, B.J., Nelson, D.D., 2014. Measurement of a doubly substituted methane isotopologue, $^{13}CH_3D$, by tunable infrared laser direct absorption spectroscopy. Anal. Chem. 86, 6487–6494. https://doi.org/10.1021/ac5010579

Onstott, T.C., Magnabosco, C., Aubrey, A.D., Burton, A.S., Dworkin, J.P., Elsila, J.E., Grunsfeld, S., Cao, B.H., Hein, J.E., Glavin, D.P., Kieft, T.L., Silver, B.J., Phelps, T.J., van Heerden, E., Opperman, D.J., Bada, J.L., 2014. Does aspartic acid racemization constrain the depth limit of the subsurface biosphere? Geobiology 12, 1–19. https://doi.org/10.1111/gbi.12069

Orphan, V.J., Taylor, L.T., Hafenbradl, D., Delong, E.F., 2000. Culture-dependent and culture-independent characterization of microbial assemblages associated with high-temperature petroleum reservoirs. Appl. Environ. Microbiol. 66, 700–711. https://doi.org/10.1128/AEM.66.2.700-711.2000

Osborne, M.J., Swarbrick, R.E., 1998. Mechanisms for generating overpressure in sedimentary basins: a reevaluation: reply. Am. Assoc. Pet. Geol. Bull. 82, 2270–2271. https://doi.org/10.1306/8626d379-173b-11d7-8645000102c1865d

Parkes, R.J., Wellsbury, P., Mather, I.D., Cobb, S.J., Cragg, B.A., Hornibrook, E.R.C., Horsfield, B., 2007. Temperature activation of organic matter and minerals during burial has the potential to sustain the deep biosphere over geological timescales. Org. Geochem. 38, 845–852. https://doi.org/10.1016/j.orggeochem.2006.12.011

Rice, D., Claypool, G., 1981. Generation, Accumulation, and Resource Potential of Biogenic Gas. Am. Assoc. Pet. Geol. Bull. 65. https://doi.org/10.1306/2F919765-16CE-11D7-8645000102C1865D

Salvador, A., 1991. Introduction, in: The Gulf of Mexico Basin, The Geology of North America. Geological Society of America, pp. 1–12.

Schoell, M., 1983. Genetic Characterization of Natural Gases. Am. Assoc. Pet. Geol. Bull. 67, 2225–2238. https://doi.org/10.1306/ad46094a-16f7-11d7-8645000102c1865d

Seewald, J.S., Benitez-Nelson, B.C., Whelan, J.K., 1998. Laboratory and theoretical constraints on the generation and composition of natural gas. Geochim. Cosmochim. Acta 62, 1599–1617. https://doi.org/10.1016/S0016-7037(98)00000-3

Shuai, Y., Douglas, P.M.J., Zhang, S., Stolper, D.A., Ellis, G.S., Lawson, M., Lewan, M.D., Formolo, M., Mi, J., He, K., Hu, G., Eiler, J.M., 2018. Equilibrium and non-equilibrium controls on the abundances of clumped isotopologues of methane during thermogenic formation in laboratory experiments: Implications for the chemistry of pyrolysis and the origins of natural gases. Geochim. Cosmochim. Acta 223, 159–174. https://doi.org/10.1016/j.gca.2017.11.024

Simmons, M.D., Tari, G.C., Okay, A.I., 2018. Petroleum geology of the Black Sea: Introduction. Geol. Soc. Spec. Publ. 464, 1–18. https://doi.org/10.1144/SP464.15

Stolper, D.A., Lawson, M., Davis, C.L., Ferreira, A.A., Santos Neto, E. V., Ellis, G.S., Lewan, M.D., Martini, A.M., Tang, Y., Schoell, M., Sessions, A.L., Eiler, J.M., 2014a. Formation temperatures of thermogenic and biogenic methane. Science (80-.). 344, 1500–1503. https://doi.org/10.1126/science.1254509

Stolper, D.A., Sessions, A.L., Ferreira, A.A., Santos Neto, E. V., Schimmelmann, A., Shusta, S.S., Valentine, D.L., Eiler, J.M., 2014b. Combined ^{13}C-D and D-D clumping in methane: Methods and preliminary results. Geochim. Cosmochim. Acta 126, 169–191. https://doi.org/10.1016/j.gca.2013.10.045

Tenzer, R., Gladkikh, V., 2014. Assessment of density variations of marine sediments with ocean and sediment depths. Sci. World J. 2014. https://doi.org/10.1155/2014/823296

The Shipboard Scientific Staff, ., Ross, D.A., Neprochnov, Y.P., Degens, E.T., Erickson, A.J., Hsu, K., Hunt, J.M., Manheim, F., Percival, S., Senalp, M., Stoffers, P., Supjo, P., Traverse, A., Trimonis, E.A., 1978. Site 381. Initial Reports Deep Sea Drill. Proj. 42 Pt. 2 42, 293–355. https://doi.org/10.2973/dsdp.proc.42-2.105.1978

Thiagarajan, N., Kitchen, N., Xie, H., Ponton, C., Lawson, M., Formolo, M., Eiler, J., 2020.

Identifying thermogenic and microbial methane in deep water Gulf of Mexico Reservoirs. Geochim. Cosmochim. Acta 275, 188–208. https://doi.org/10.1016/j.gca.2020.02.016

Turner, A.C., Pester, N.J., Bill, M., Conrad, M.E., Knauss, G., Stolper, D.A., 2022. Experimental determination of hydrogen isotope exchange rates between methane and water under hydrothermal conditions. Geochim. Cosmochim. Acta. https://doi.org/10.1016/j.gca.2022.04.029

Wang, D.T., Gruen, D.S., Sherwood Lollar, B., Hinrichs, K.U., Stewart, L.C., Holden, J.F., Hristov, A.N., Pohlman, J.W., Morrill, P.L., Könneke, M., Delwiche, K.B., Reeves, E.P., Sutcliffe, C.N., Ritter, D.J., Seewald, J.S., McIntosh, J.C., Hemond, H.F., Kubo, M.D., Cardace, D., Hoehler, T.M., Ono, S., 2015. Nonequilibrium clumped isotope signals in microbial methane. Science (80-.). 348, 428–431. https://doi.org/10.1126/science.aaa4326

Webb, M.A., Miller, T.F., 2014. Position-specific and clumped stable isotope studies: Comparison of the urey and path-integral approaches for carbon dioxide, nitrous oxide, methane, and propane. J. Phys. Chem. A 118, 467–474. https://doi.org/10.1021/jp411134v

Whiticar, M.J., 1999. Carbon and hydrogen isotope systematics of bacterial formation and oxidation of methane. Chem. Geol. 161, 291–314. https://doi.org/10.1016/S0009-2541(99)00092-3

Wilhelms, A., Larter, S.R., Head, I., Farrimond, P., Di-Primio, R., Zwach, C., 2001. Biodegradation of oil in uplifted basins prevented by deep-burial sterilization. Adv. Pet. Geochemistry 411, 1034–1037. https://doi.org/https://doi.org/10.1038/35082535

Xie, H., Dong, G., Formolo, M., Lawson, M., Liu, J., Cong, F., Mangenot, X., Shuai, Y., Ponton, C., Eiler, J., 2021. The evolution of intra- and inter-molecular isotope equilibria in natural gases with thermal maturation. Geochim. Cosmochim. Acta 307, 22–41. https://doi.org/10.1016/j.gca.2021.05.012

Yeager, K.M., Santschi, P.H., Rowe, G.T., 2004. Sediment accumulation and radionuclide inventories (239,240Pu, 210Pb and 234Th) in the northern Gulf of Mexico, as influenced by organic matter and macrofaunal density. Mar. Chem. 91, 1–14. https://doi.org/10.1016/j.marchem.2004.03.016

Young, E.D., Kohl, I.E., Lollar, B.S., Etiope, G., Rumble, D., Li, S., Haghnegahdar, M.A., Schauble, E.A., McCain, K.A., Foustoukos, D.I., Sutclife, C., Warr, O., Ballentine, C.J., Onstott, T.C., Hosgormez, H., Neubeck, A., Marques, J.M., Pérez-Rodríguez, I., Rowe, A.R., LaRowe, D.E., Magnabosco, C., Yeung, L.Y., Ash, J.L., Bryndzia, L.T., 2017. The relative abundances of resolved $^{12}CH_2D_2$ and $^{13}CH_3D$ and mechanisms controlling isotopic bond ordering in abiotic and biotic methane gases. Geochim. Cosmochim. Acta 203, 235–264. https://doi.org/10.1016/j.gca.2016.12.041

Chapter 4

Variability in $\Delta^{13}CH_3D$ values from ebullition in a mid-latitude lake: implications for lake biogeochemistry and source signature characterization

ABSTRACT

Methane is the second most important long-lived greenhouse gas in the atmosphere, and a significant component of carbon cycling in freshwater environments. Isotope ratios of methane ($^{13}C/^{12}C$ and D/H) are used as atmospheric tracers to identify sources of methane in the environment, but these tracers can be ambiguous when sources have overlapping values. Recently, the measurement of clumped isotopologues of methane ($^{13}CH_3D$ and $^{12}CH_2D_2$) has become analytically feasible, offering new opportunities to improve methane budgets. To leverage clumped isotopologues of methane to fingerprint local contributions to the atmospheric methane pool, accurate characterizations of the isotopologue source signatures and fluxes of major sources and sinks are required. Previous measurements of clumped isotopologues of methane from freshwater are limited. Here we characterize the abundance of methane isotopologues (n=40) and flux of methane (n=44) released via ebullition from a mid-latitude kettle lake, between May and November 2021. The measured values of $\Delta^{13}CH_3D$ range from 2.0 to 4.2‰, reflecting isotopologue fractionations during methanogenesis and post-generation processing (i.e., oxidation) in the lakebed. The variability of $\Delta^{13}CH_3D$ values is similar to that of ebullition from arctic lakes. This study presents the largest set of freshwater $\Delta^{13}CH_3D$ values in a single lake basin, which we use to recommend a sampling strategy to characterize lake source signatures. We find that sampling is likely to be biased if conducted at a single time point or within a narrow range of dates, but sampling from a limited number of locations over a longer timescale may yield representative data. We also estimate that at least 9 samples be measured to constrain the $\Delta^{13}CH_3D$ source signal within ca. 0.5‰. This work shows a relatively large variation in the $\Delta^{13}CH_3D$ values (2.2‰) from a single lake basin with a consistent bottom water temperature, pointing to the challenge of constraining the total source signal from freshwater lakes.

A version of this chapter is being prepared for publication with the following authors:

Ellen Lalk, Amber Velez, and Shuhei Ono

4.1 INTRODUCTION

Methane, a globally significant greenhouse gas, contributes approximately 25% radiative forcing in the atmosphere, and is emitted by both natural (e.g., inland waters, and smaller contributions from permafrost, oceans, and geologic sources) and anthropogenic (e.g., fossil fuels, agriculture, waste, and biomass burning) sources. Inland waters are the largest natural source of methane to the atmosphere, with emissions currently estimated as ca. 95 to 205 Tg CH_4 per year (Bastviken et al., 2011; Rosentreter et al., 2021; Saunois et al., 2020; Zheng et al., 2022). However, both relative source fluxes and causes of recent changes in the size of the atmospheric methane pool are poorly understood (Kai et al., 2011; Pison et al., 2013; Saunois et al., 2020; Schaefer et al., 2016; Schwietzke et al., 2016; Turner et al., 2019; Worden et al., 2017). For instance, bottom-up estimates of the atmospheric methane pool (i.e., point-measurement scaling and process-based modeling of isotope values and gas fluxes) do not currently match top-down (i.e., inverse modeling) estimates (Saunois et al., 2020). Better characterization of freshwater methane emissions is critical to constrain other atmospheric methane fluxes, as well as improve understanding of the impact of future climate scenarios on lake ecosystems (e.g., Yvon-Durocher et al., 2014).

Methane is produced in organic-rich lake sediments as a terminal end-product of microbially-mediated organic matter decomposition. Methane can be emitted from lakebeds to the atmosphere via two main mechanisms: 1) diffusion through the overlying water column, where it either reaches the atmosphere or gets oxidized by methanotrophic microbes, and 2) bubble formation and ebullition, when the total pressure of dissolved gases in the lakebed exceed hydrostatic pressure (Whiting and Chanton, 1996). The uncertainty in the contribution of freshwater bodies to the atmospheric methane budget is large (ca. 100 Tg CH_4 per year), due to unknowns in the spatial and temporal variability of emissions and limited measurements (Saunois et al., 2020). Many studies have demonstrated ebullition to be an important source of methane from lakes to the atmosphere, up to 50-90% of total emissions (e.g., Crill et al., 1988, Walter et al., 2006). However, ebullition fluxes are historically difficult to quantify due to their sporadic nature.

Isotopic ratios of methane (e.g., $^{13}C/^{12}C$ and D/H) have been used to ascribe sources of methane to the atmosphere. On a global scale, $^{13}C/^{12}C$ of methane ($\delta^{13}C$) can yield insights such

as distinguishing lower $\delta^{13}C$ values from microbial sources from generally higher $\delta^{13}C$ values from thermogenic sources. For example, atmospheric methane is becoming increasingly depleted in ^{13}C while the concentration of methane in the atmosphere has increased between 2007 and 2014 (e.g., Nisbet et al., 2016), suggesting increasing inputs from microbial sources or decreasing sink reactions. On a local scale, shifts in methane $\delta^{13}C$ can be used to estimate the fraction of methane that has undergone microbial oxidation (e.g., Börjesson et al., 2001). D/H of microbial methane (δD) may help distinguish geographic, as variation in δD-CH_4 values follows meteoric water, such that δD values are more depleted at high latitudes and altitudes (Chanton et al., 2006; Dansgaard, 1964; Stell et al., 2021; Waldron et al., 1999). Additionally, it is proposed that the biogeochemical pathways that mediate methanogenesis (e.g., via CO_2 reduction or acetogenesis) can in some cases be differentiated by δD values (Chanton et al., 2006; Whiticar and Schoell, 1986). Post formation processing like methane oxidation and gas transport also impart fractionation on δD, such that greater extents of oxidation increase values of δD and isotopically lighter gas diffuses more quickly (Prinzhofer and Pernaton, 1997; Waldron et al., 1999; Whiticar, 1999). Increasingly, efforts are being made to develop spatially and temporally resolved methane isotope source signatures, moving away from assumptions of globally uniform source signatures (Douglas et al., 2021; Ganesan et al., 2018; Sherwood et al., 2017).

In addition to bulk isotope ratios, the quantification of methane molecules with multiple isotope substitutions (clumped isotopologues) is now feasible by mass spectrometry and laser spectroscopy (Gonzalez et al., 2019; Ono et al., 2014; Stolper et al., 2014b; Young et al., 2017), and may offer additional information to constrain sources of methane to the atmosphere. Measurement of doubly substituted isotopologues $^{13}CH_3D$ and $^{12}CH_2D_2$ have been applied to understand methane formation and history in many environments including gas reservoirs, marine sediments, lakes, cow rumen, hydrothermal systems, and geothermal systems (Ash et al., 2019; Beaudry et al., 2021; Douglas et al., 2016, 2020a, Giunta et al., 2019, 2021; Jautzy et al., 2021; Labidi et al., 2020; Stolper et al., 2017; Wang et al., 2015). Precise measurement of isotopologues' abundances ($^{12}CH_4$, $^{13}CH_4$, $^{12}CH_3D$, $^{13}CH_3D$, and $^{12}CH_2D_2$) can in some cases yield an estimate of the temperature at which methane was last equilibrated. Methane samples from geologic environments demonstrate that this thermometer yields environmentally reasonable temperatures (Stolper et al., 2014a); while methane from lab and surface environments is characterized by kinetic isotope signals that arise during microbial methane

generation (Douglas et al., 2020b, 2016; Gruen et al., 2018; Stolper et al., 2015; Wang et al., 2015; Young et al., 2017). Both lab studies and natural samples of methane oxidized by aerobic and anaerobic methanotrophic metabolisms demonstrate that $\Delta^{13}CH_3D$ values can differentiate between these processes due to differences in their enzymatic reactions (Giunta et al., 2022; Ono et al., 2021; Wang et al., 2018).

Several studies have proposed that measurement of clumped methane isotopologues may improve understanding of contemporary changes in the atmospheric methane budget (e.g., Chung and Arnold, 2021; Ganesan et al., 2019; Haghnegahdar et al., 2017; Turner et al., 2019; Whitehill et al., 2017). These theoretical frameworks show that large changes in source emissions perturb $\Delta^{13}CH_3D$ values of tropospheric methane by less than 0.5‰ (approximately measurement error), and perturb $\Delta^{12}CH_2D_2$ values by up to 10‰, which can be used to constrain gradual changes in the balances of methane source and sink magnitudes (Chung and Arnold, 2021; Haghnegahdar et al., 2017). Thus, on a global scale, $^{13}CH_3D$ of air may yield further insight to local source, but not sink attributions, while $^{12}CH_2D_2$ may be useful to trace both source and sink fluxes. Both studies acknowledge the limited data used to define source and sink signatures, and more measurements of source signals with improved resolution are necessary to apply clumped methane isotopologues to interpreting atmospheric methane.

Presently, data for the $\Delta^{13}CH_3D$ source signature of methane from lakes is derived from geographically and temporally limited data. Cumulatively, measurements of $\Delta^{13}CH_3D$ and Δ_{18} (a value that includes both $^{13}CH_3D$ and $^{12}CH_2D_2$, but is approximately equal to $^{13}CH_3D$) have been made from 14 lakes, 3 of which are from the temperate Northern Hemisphere, and 11 of which are from the Arctic (Giunta et al., 2022; Douglas et al., 2020a, 2016; Wang et al., 2015). Within a single lake there is significant uncertainty (often >1‰) in the site-level mean $\Delta^{13}CH_3D$ value, as typically only 1-3 samples are analyzed. Douglas et al. (2020) have led the most focused application of the clumped methane isotopologue system to freshwater environments, and they have found that Δ_{18} values from lakes span over a 5‰ range.

In this study, we investigate the spatial and temporal variability of methane flux and $\delta^{13}C$, δD, and $\Delta^{13}CH_3D$ values of methane from ebullition in Upper Mystic Lake, MA. This work expands the existing dataset of clumped methane isotopologue measurements made for mid-latitude freshwater environments by about an order of magnitude, yielding improved source

signature characterizations, which are required to be able to use clumped methane isotopes to constrain global atmospheric methane budgets.

4.2 MATERIALS AND METHODS

4.2.1 Upper Mystic Lake, MA

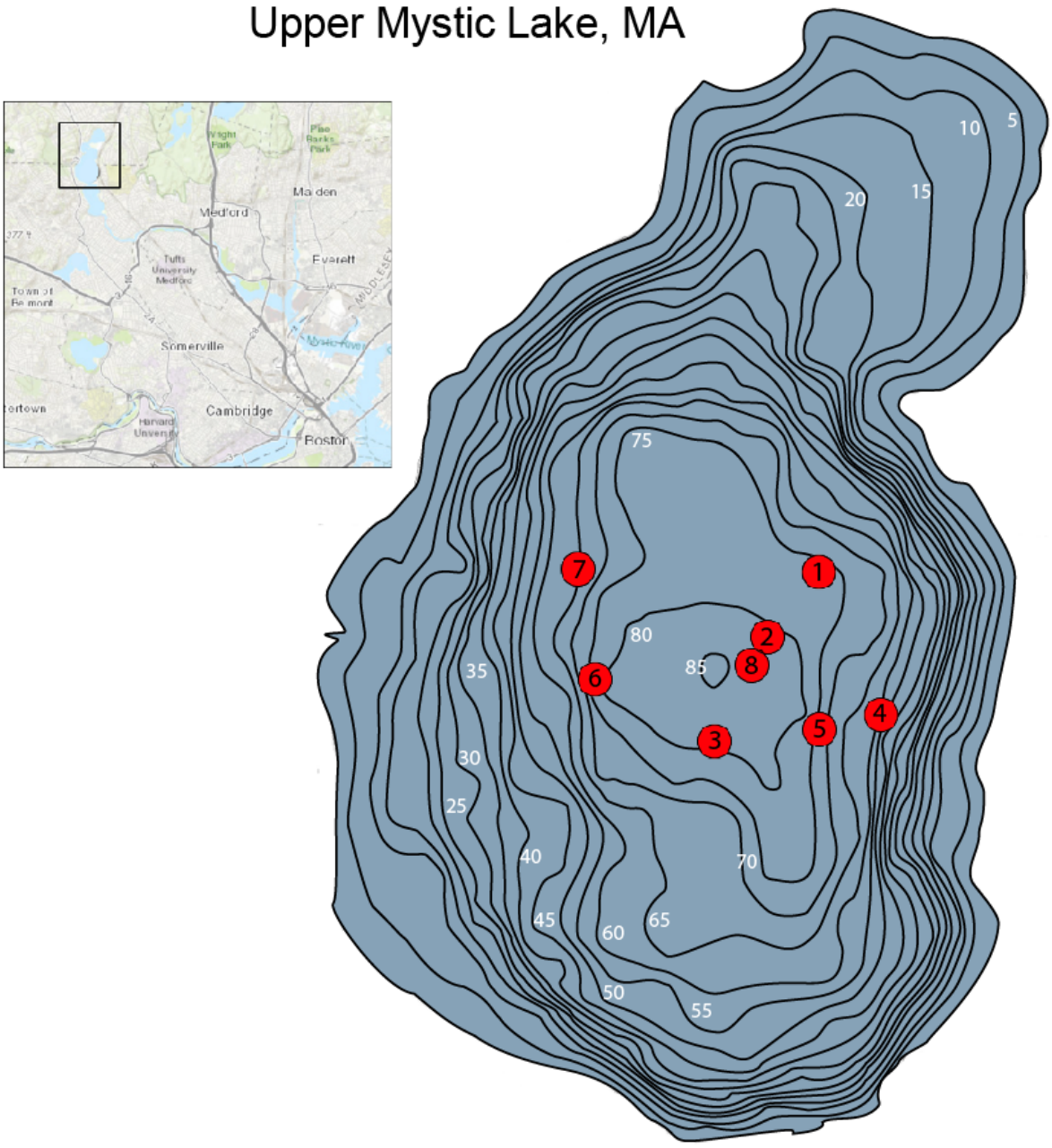

Figure 4.1: Locations of bubble traps stationed in Upper Mystic Lake, MA. Water depth is in ft.

Upper Mystic Lake is a eutrophic, dimictic, kettle hole lake in Medford, MA (**Figure 1**). It is fed by the Aberjona River and drains over a 2 m high stone dam into Lower Mystic Lake. The maximum depth of the lake is approximately 27 m, and average depth is ca. 6 m. The surrounding area is moderately developed, with homes and boating clubs along the western shores, while the eastern shores are protected parklands. It has a surface area of 0.58 km^2.

Typically, Upper Mystic Lake is thermally stratified from the late spring through fall, and by the early summer, the deepest 15 m of water column is anoxic. Observations of sediment temperature indicate that the deep lake basin is ca. 4°C between May and December (Peterson, 2005). Mixing occurs around late November or early December, and the lake often freezes over during the winter (Aurillo et al., 1994; Spliethoff, 1995).

4.2.2 Sample Collection

Eight bubble traps were deployed in Upper Mystic Lake between May and November 2021. Their placements can be found in **Table 4.S1** and **Figure 4.1**, and were at water depths from 20-26 m (65-85 ft). Bubble traps were custom-made following Varadharajan et al. (2010). A schematic of the trap design and parts can be found in the supplementary information (**Table 4.S2**, **Figure 4.S1**).

Traps were positioned such that the base of the trap was approximately 2.5 meters below the surface of the lake. Buoys 1, 2 and 3 were deployed on May 2, 2021. Buoys 4 and 5 were deployed on July 7, 2021. Buoys 6 7 and 8 were deployed on July 23, 2021. Buoy 8 was retrieved after ca. 1 month for repairs.

Once deployed, gas from bubble traps was collected from traps every 1 to 4 weeks until October 24, 2021. This sampling cadence was chosen to provide sufficient gas for isotopologue measurements (i.e., at least 10 mL gas desired for analyses). Sampling was conducted by lifting the bubble-trap to a depth just below the surface of the water, and measuring the volume of gas using the calibration markings made on the clear pvc pipe. Then, gas was removed ca. 20 mL at a time using a needle and syringe from the septum port. The gas volume was also quantified by complete removal of trapped gas via syringe. 20 mL aliquots of gas were stored via water displacement in borosilicate glass serum bottles that were pre-filled with water and sealed with blue butyl stoppers. Stoppers were pre-cleaned in a 1 M KOH bath, and rinsed overnight

(Oremland et al., 1987). Upon return to lab, samples were amended with 1 mL 1M NaOH to stop microbial activity, and then stored in the dark until measurement.

Since bubble traps were deployed for extended periods of time, there is some potential for the diffusive loss of methane from the trap headspace to the underlying water. Traps were designed to minimize the surface area between headspace and water, such that the maximum surface area is 5.07 cm^2 when sample volume is greater than ca. 20 mL (in 1" ID PVC tubing), and 1.77 cm^2 when sample volume is less than ca. 20 mL (in brass piping) (**Figure 4.S1**). The PVC funnel stem was designed to be sufficiently long to limit turbulence of water at the headspace-water interface, and thus minimize gas exchange rates. Further, several groups have addressed this concern and demonstrated no detectable loss of methane in long stemmed bubble funnels. For example, Walter et al. 2008 deployed control traps over the span of 55 days in which the surface area in contact with water was 3.98 cm^2. As this time scale is ca. double our maximum deployment timescale, diffusive loss is expected to be negligible.

4.2.3 Analytical Measurements

4.2.3.1 Methane Ebullition Flux

The concentrations of methane in bubble trap samples (n = 44) were determined using a gas chromatograph (GC) with a flame ionization detector. The GC is equipped with a 8-foot column packed with caroboxyn (Sigma-Aldrich), where helium serves as the carrier gas. Each gas sample was measured at least twice, and calibration was made using reference gas mixtures (70.5% methane, SCOTTY®).

The rate of methane emission via ebullition was calculated via the following equation.

$$\text{Ebullition } \left(\frac{\text{mL } CH_4}{m^2 \text{ day}}\right) = \frac{(MR_{CH_4})(V_{trap})}{(A_{funnel})(t)} \qquad (1)$$

MR_{CH_4} is the fraction of headspace that is methane

V_{trap} is the volume of gas in the bubble trap in mL

A_{funnel} is the area of the base of the funnel, which is equal to 0.254 m^2

t is the number of days for the sample interval

4.2.3.2 Methane Isotopologue Abundances

Measurement of $\delta^{13}C$, δD, and $\Delta^{13}CH_3D$ values were made using a Tunable Infrared Laser Direct Absorption Spectroscopy (TILDAS) instrument at MIT (Ono et al., 2014). Samples that yielded > 0.5 mL methane at lab pressure and temperature (n = 40) were selected for measurement. Bubble trap gas samples were first extracted onto a cold trap filled with activated charcoal and submerged in liquid nitrogen (-196°C). Then, methane was purified from other gas components (mainly N_2) using gas chromatography, as previously described (Wang et al., 2015).

Pure methane was introduced to the TILDAS absorption cell to quantify the abundances of methane isotopologues ($^{12}CH_4$, $^{13}CH_4$, $^{12}CH_3D$, and $^{13}CH_3D$). Approximately 7 to 12 comparisons of sample to reference gas were made for each sample. Measurements were calibrated using lab methane standard gases that were equilibrated at 250ºC with a platinum catalyst. Carbon ($\delta^{13}C$) and hydrogen (δD) isotope values are reported with respect to V-PDB and V-SMOW scales, calibrated against standards NGS-1 and NGS-3 (Wang et al., 2015).

$\Delta^{13}CH_3D$ is defined as the abundance of $^{13}CH_3D$ relative to a stochastic distribution (Ono et al., 2014), and reported in per mille units.

$$\Delta\ ^{13}CH_3D = \ln\left(\frac{[^{13}CH_3D][^{12}CH_4]}{[^{13}CH_4][^{12}CH_3D]}\right) \qquad (2)$$

4.2.4 Bubble Dissolution Model

The change in methane and nitrogen composition of bubbles between the lakebed and bubble traps was estimated using a single bubble dissolution model (Greinert and McGinnis, 2009; McGinnis et al., 2006). This model calculates gas transfer across the interface of rising bubbles with an initial composition of 100% methane, and tracks methane, nitrogen, and oxygen concentrations within the bubble. The gas composition of the bubble will change as methane dissolves out of the bubble into the surrounding water, and other gases exsolve into the bubble. The amount of gas transferred is most dependent on partial pressure, initial bubble size, and the amount of time the bubble travels through the water column (i.e. the height of the water column and rise velocity). Environmental parameters including water column temperature, and dissolved concentrations of oxygen, methane and carbon dioxide were used to inform the model, using measurements from the 2004 field season (Peterson, 2005) (**Table 4.S3**). For the Upper Mystic Lake sediment-water interface temperature was set as 4 °C, and water depth was set as 22 m,

which is the depth of water chemistry profiles (Peterson, 2005), and within the range of buoy placement (20-25 m).

4.3 RESULTS

Gas composition and isotope values of bubbles collected between May to November 2021 in Upper Mystic Lake are tabulated in **Table 4.1** and shown in **Figures 4.2** and **4.3**.

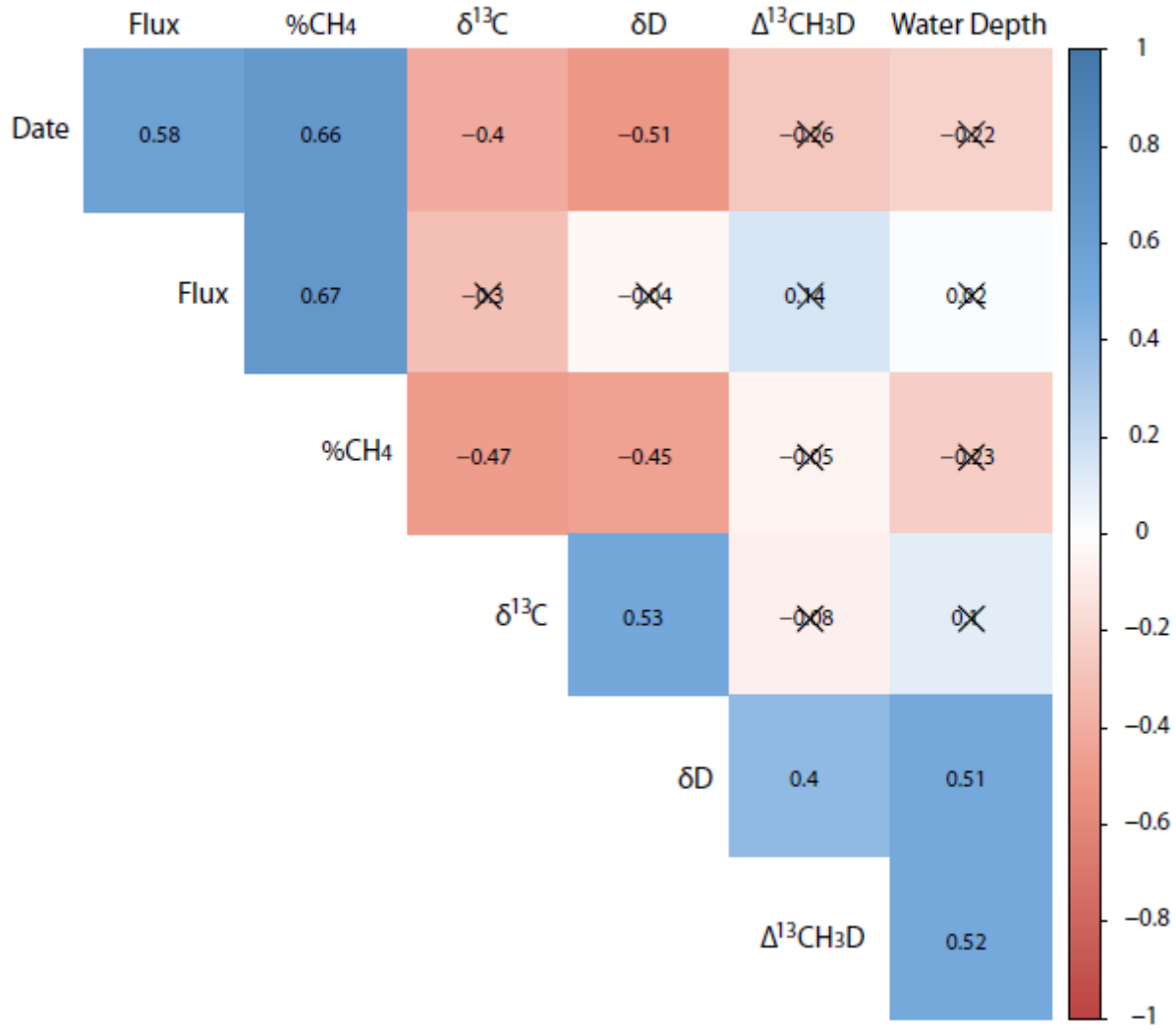

Figure 4.2: Correlation matrix between temporal (Date), spatial (Water Depth), and gas geochemical (CH_4 Flux, $\%CH_4$ in bubbles, $\delta^{13}C$, δD, $\Delta^{13}CH_3D$) data. Values represent the correlation coefficients between parameters, and Xs denote relationships that are not statistically significant ($p < 0.05$). Blue is used for positively correlated parameters and red is used for negatively correlated parameters. This figure was created using the corrplot R Package (Wei and Simko 2021).

Sampling Date	Buoy	CH_4 emission rate mL CH_4 m^{-2} day^{-1}	%CH_4	Gas volume (mL)	$\delta^{13}C$ ‰	95% CI	δD ‰	95% CI	$\Delta^{13}CH_3D$ ‰	95% CI
6/8/2021	2	0.27	2.10%	44						
6/8/2021	3	0.38	8.60%	15.5	-63.25	±0.04	-228.27	±0.07	3.45	±0.33
6/29/2021	1	2.14	34.50%	33	-67.01	±0.04	-255.68	±0.08	4.18	±0.09
6/29/2021	2	9.19	58.90%	83	-69.21	±0.03	-254.31	±0.06	4.15	±0.12
6/29/2021	3	7.03	59.30%	63	-68.35	±0.02	-258.51	±0.08	4.08	±0.39
7/7/2021	2	3.77	31.80%	24	-66.69	±0.42	-252.03	±0.46	3.74	±0.36
7/7/2021	3	2.73	22.20%	25	-68.01	±0.29	-257.75	±0.38	3.96	±0.25
7/23/2021	2	2.12	37.40%	23	-67.46	±0.11	-255.97	±0.15	4.16	±0.22
7/23/2021	3	1.01	24.10%	17	-58.36	±0.07	-261.09	±0.14	2.54	±0.35
7/23/2021	4	1.24	45.70%	11	-69.61	±0.05	-276.91	±0.15	2.77	±0.37
7/23/2021	5	0.27	36.89%	3						
8/2/2021	1	1.19	37.70%	8	-68.99	±0.05	-271.83	±0.19	2.83	±0.39
8/2/2021	2	3.39	34.30%	25	-68.29	±0.05	-262.85	±0.11	2.82	±0.22
8/2/2021	3	0.89	32.10 %	7						
8/2/2021	4	6.00	66.10%	23	-69.14	±0.02	-276.92	±0.12	1.97	±0.32
8/2/2021	5	1.72	41.60%	10.5						
8/2/2021	6	3.20	32.40%	25	-68.16	±0.06	-265.36	±0.18	3.73	±0.49
8/2/2021	7	1.10	27.90%	10						
8/2/2021	8	3.47	31.40%	28	-67.96	±0.02	-264.82	±0.09	3.86	±0.27
8/17/2021	1	0.38	0.90%	155						
8/17/2021	3	0.69	26.10%	10	-68.59	±0.05	-265.39	±0.15	2.94	±0.28
8/17/2021	4	3.75	56.90%	25	-69.42	±0.03	-277.67	±0.09	2.89	±0.19
8/17/2021	5	3.95	53.60%	28	-70.10	±0.02	-274.71	±0.06	3.10	±0.23
8/17/2021	6	1.70	41.60%	10	-68.03	±0.06	-268.75	±0.17	2.94	±0.28
8/17/2021	7	1.45	27.50%	28	-61.08	±0.07	-265.79	±0.07	2.28	±0.22
8/17/2021	8	4.76	51.60%	15.5	-68.39	±0.05	-267.64	±0.10	3.56	±0.21
9/11/2021	1	1.00	45.30%	20	-69.00	±0.32	-270.96	±0.48	3.00	±0.16
9/11/2021	2	5.29	58.00%	35	-68.04	±0.02	-265.69	±0.11	2.50	±0.19
9/11/2021	3	3.82	57.60%	14	-66.95	±0.07	-257.61	±0.14	3.05	±0.23
9/11/2021	4	3.97	51.30%	58	-72.66	±0.06	-279.16	±0.06	2.11	±0.43
9/11/2021	5	2.58	51.10%	42	-71.59	±0.44	-276.74	±0.14	3.50	±0.31
9/11/2021	6	4.86	55.90%	49	-68.08	±0.03	-265.07	±0.14	3.54	±0.21
9/11/2021	7	8.78	63.10%	32	-64.76	±0.03	-258.7	±0.12	3.18	±0.19
9/25/2021	1	1.10	39.10%	10						
9/25/2021	2	7.68	61.00%	45	-66.89	±0.36	-272.09	±0.51	3.84	±0.18
9/25/2021	3	1.08	42.40%	9	-72.09	±0.33	-268.76	±0.29	3.40	±0.28
9/25/2021	4	4.76	56.30%	30	-72.45	±0.32	-285.26	±0.26	3.27	±0.31
9/25/2021	5	2.79	49.50%	20	-70.76	±0.31	-277.68	±0.06	2.88	±0.33
9/25/2021	6	2.45	51.10%	17	-70.40	±0.31	-272.32	±0.12	3.07	±0.38
9/25/2021	7	2.85	50.50%	20	-63.01	±0.44	-271.28	±0.47	2.21	±0.31
10/24/2021	1	10.81	60.20%	132	-67.49	±0.06	-258.20	±0.07	3.29	±0.37
10/24/2021	2	16.47	67.00%	180	-70.01	±0.27	-261.53	±0.26	3.09	±0.32
10/24/2021	3	13.67	57.40%	175	-70.14	±0.32	-256.52	±0.21	2.73	±0.24
10/24/2021	4	5.60	58.80%	70	-71.08	±0.04	-280.82	±0.26	2.26	±0.36
10/24/2021	5	19.02	57.00%	245	-72.32	±0.29	-276.04	±0.24	2.84	±0.38
10/24/2021	6	13.70	67.10%	150	-69.74	±0.36	-268.55	±0.52	4.19	±0.26
10/24/2021	7	14.61	65.10%	165	-69.71	±0.33	-270.77	±0.28	4.05	±0.28

Table 4.1: Methane ebullition emission rate, gas composition, and isotope data

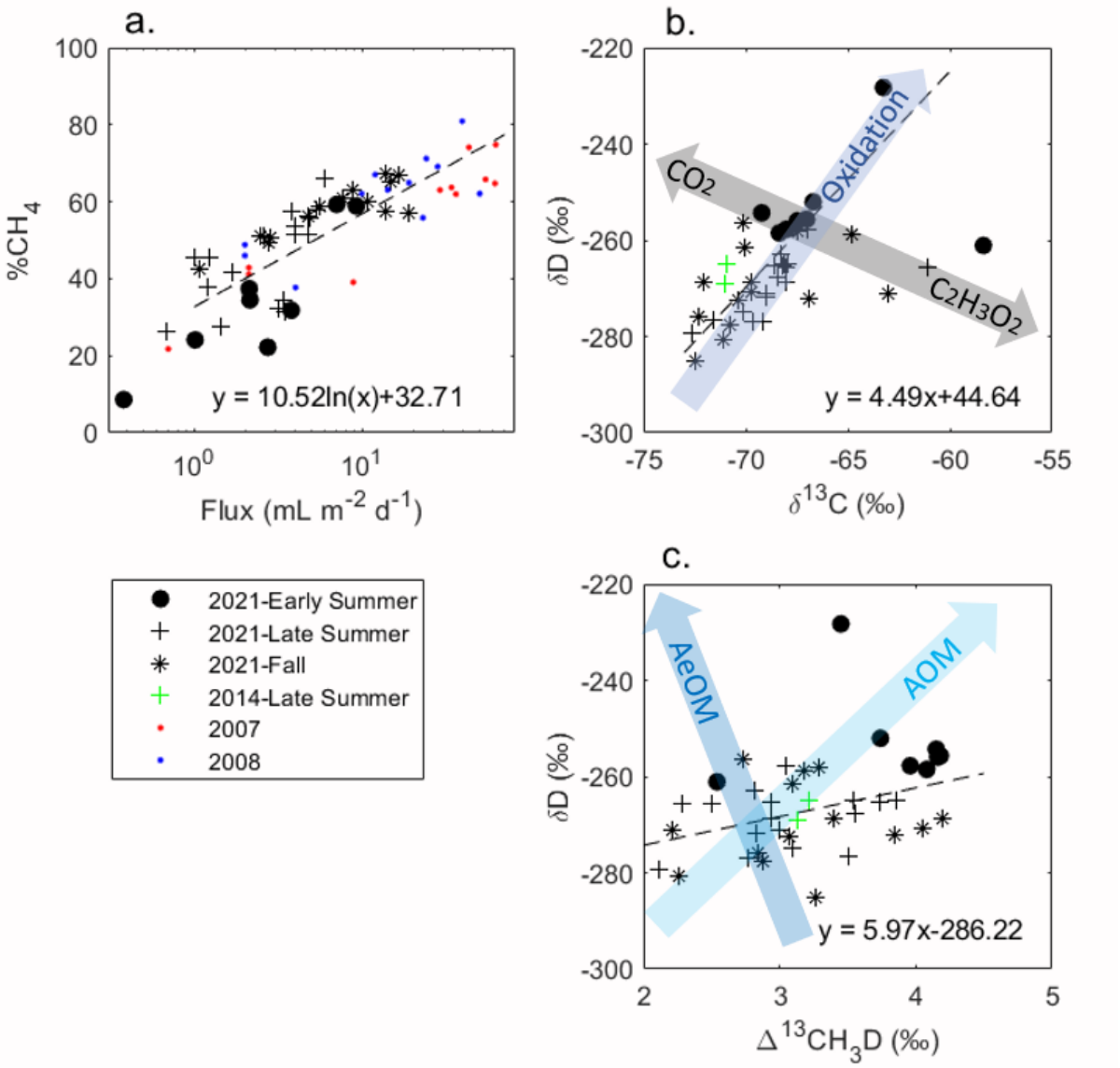

Figure 4.3: Scatter plots of **a** CH_4 flux vs $\%CH_4$ in bubbles, **b** $\delta^{13}C$ vs δD, and **c** $\Delta^{13}CH_3D$ vs δD. Regression models are shown with dashed lines and equations in the bottom right corner of each plot. For 2021 data, marker shape is used to distinguish time, where filled circles are used for samples collected in early summer (May 25-July 23), plus signs are used for samples collected in late summer (July 23-September 11), and asterixis are used for samples collected in fall (September 11-October 24). **a** includes data from 2007 and 2008 (Varadharajan 2009). **b** and **c** include data from 2014 (Wang et al., 2015). In **b** we show that oxidation typically enriches the $\delta^{13}C$ and δD values of remaining methane. Additionally, the arrows show the effects of methane produced via the CO_2-reduction pathway has relatively enriched δD values and depleted $\delta^{13}C$ values with respect to methane produced via the acetogenesis pathway. In **c** the arrows show that while both aerobic (AeOM) and anaerobic oxidation methane (AOM) enrich δD values, $\Delta^{13}CH_3D$ values increase with AOM and decrease with AeOM (Ono et al., 2021; Wang et al., 2018).

Ebullitive methane flux ranges between 0 to 20 mL/m^2/day and is positively correlated with time and methane concentration (%CH_4) in bubbles (**Figure 4.2, 4.S2**). The largest gas flux was observed during October 2021. Differences in fluxes across buoy locations are observed for each sampling interval and vary between sites within ca. 5 mL/m^2/day (**Table 4.1, Figure 4.S2**).

The concentration of methane in bubbles (%CH_4) is strongly correlated with time and methane flux (**Figure 4.2**). The concentration of CH_4 generally increased from ca. 9-60% in May and early June to ca. 50-67% in late October. The relationship between ebullition flux and the concentration of methane in bubbles is best fit by log relationship, such that fluxes less than ca. 5 mL CH_4/m^2/day are less than 50% CH_4 by volume, while larger fluxes are composed of 50 to 67% methane by volume (**Figure 4.3a**). No samples were composed of more than 67% methane. During the early summer, variability between concentrations of methane is large, even on short timescales. For example, between the June 29 and July 7 collections, there is a difference in methane concentration of 40% by volume at buoy 3.

Values of $\delta^{13}C$ and δD are inversely correlated to time and %CH_4, and positively correlated to each other (**Figure 4.2, 4.3b**). Throughout the season, values of $\delta^{13}C$ range from -73 to -58‰ and values of δD range from ca. -281 to -228‰. Values are highest in the early summer ($\delta^{13}C$ ca. -68‰ and δD ca. -255‰) and are lower in late fall ($\delta^{13}C$ ca. -73‰ and δD ca. -270‰). A linear fit to $\delta^{13}C$ and δD data yields a slope of 4.49 (**Figure 4.3b**).

Values of $\Delta^{13}CH_3D$ range from 1.9 to 4.3‰ and have positive correlations with δD data and water depth (**Figure 4.2**, 4.**3c**). A linear fit to $\Delta^{13}CH_3D$ and δD data yields a slope of 6.0. Samples collected in the early summer have relatively higher $\Delta^{13}CH_3D$ values (>4‰), compared to samples collected during late summer and fall (**Figure 4.3c**). While buoys located over deeper sections of the lake have methane with relatively higher $\Delta^{13}CH_3D$ values, the range in water depths captured by buoy placement is limited from ca. 65-84 ft, as all buoys were positioned in the deep basin of Upper Mystic Lake. Statistically significant ($p>0.05$) correlations between $\Delta^{13}CH_3D$ values and time, ebullition flux, concentration of CH_4, or $\delta^{13}C$ values are not observed (**Figure 4.2**).

4.4 DISCUSSION

4.4.1 Controls on molecular and isotopologue variations in Upper Mystic Lake

Within Upper Mystic Lake, we investigate the impact of methane transport and consumption mechanisms on both the concentration of methane in bubbles (%CH_4) and isotopologue abundances ($\delta^{13}C$, δD, and $\Delta^{13}CH_3D$). In lake environments, ebullition is the most direct mechanism for methane to reach the atmosphere. While ebullition is expected to have a negligible isotope effect, the volume and transit time of bubbles have significant impacts on the amount of methane that reaches the lake surface. Additionally, storage of methane in the lake sediment, water column, and bubble traps can impact the relative significance of anaerobic and aerobic oxidation on gas bubbles.

During the 2021 field season, one of the strongest correlations was observed between the concentration of methane in gas bubbles, ebullition flux, and time (**Figure 4.2**, 4.**3a**). This phenomenon has been previously documented, both in Upper Mystic Lake (e.g., Varadharajan, 2009) and other freshwater lakes (e.g., Walter et al., 2008; Chanton et al., 1989). Data from Upper Mystic Lake during the 2007 and 2008 field seasons fall on the same trajectory as those from the 2021 field season; however, methane fluxes were typically 10 to 20 times greater in 2007 and 2008 than 2021, at comparable water depths and locations (**Figure 4.3a**) (Varadharajan, 2009).

Gas bubbles are mainly composed of methane, nitrogen, and oxygen, and variability in bubble composition is due to both 1) differences in dissolved gases in sediment porewater, and 2) bubble dissolution and gas exchange in the water column. The relationship between methane concentration and methane ebullition flux has often been attributed to the stripping of N_2 from porewaters during bubble formation (Chanton et al., 1989). At higher methane fluxes, a higher proportion of porewater N_2 has been stripped from sediments, thus the initial composition of bubbles is expected to be proportionally higher in methane. The pressure and temperature conditions at the lakebed underlying buoys is ca. 3 to 3.5 bar and 4°C, and methane can reach concentrations up to 4.5 to 5.3 mM in porewater. Lake bottom water equilibrated with the atmosphere has a N_2 concentration of ca. 0.54 mM. Thus, the initial concentration of methane in bubbles can be as low as ca. 88-90% and is expected to increase with higher methane fluxes. Once methane is stripped from porewaters, it can be replenished via diffusive exchange with atmosphere-equilibrated lake water, although diffusion through 20 cm of sediments (i.e., the estimated sediment-depth origin of bubble gas) takes on the order of 7-8 months (Langenegger et

al., 2019; Varadharajan, 2009). Similarly, denitrification can increase porewater N_2, but complete and instantaneous denitrification of nitrate in Upper Mystic Lake porewaters (ca. 150μM) (Peterson, 2005), can only cause a ca. 0.1 bar change in N_2 partial pressure (Varadharajan, 2009). Porewater N_2 may also be replenished by atmosphere-equilibrated groundwater, the role of which is presently uncharacterized.

Additionally, methane concentration is a function of bubble size. When bubbles ascend through the water column, gas exchanges across the gas-water interface according to solubility and concentration gradient. As a result, methane typically dissolves into the water column from bubbles, while nitrogen and oxygen are added from the water column into the bubble. The extent of gas exchange is determined by the timescale of bubble ascent and the surface area of the bubble (e.g., McGinnis et al., 2006; references therein). The Single Bubble Dissolution Model (Greinert and McGinnis, 2009) estimates the exchange of gas (including CH_4, N_2, and O_2) across the gas-water interface. This model predicts that larger bubbles retain higher methane concentrations than smaller bubbles because of the lower surface area/volume ratios and faster rise velocity of larger bubbles. For example, the model predicts that a bubble with a 5 mm diameter that contains 100% methane at a 22 m deep lakebed would take 1.5 min to reach the surface, and only contain ca. 68% methane. In comparison, a 3 mm diameter bubble would contain ca. 38% methane when it reaches the surface. This model was previously validated for conditions at Upper Mystic Lake (Delwiche and Hemond, 2017), and input parameters are detailed in **section 4.2.4**.

The variation in isotopologue composition of bubble methane is either due to 1) oxidation, or 2) methanogenic pathway (i.e., CO_2 reduction or acetoclastic methanogenesis). While N_2 stripping of porewaters would affect the molecular composition of bubbles, it should not cause significant variation in methane isotopologue abundances (Chanton, 2005). Dissolution is known to impart a relatively small isotopic fractionation. The carbon isotope effect of methane dissolution ($\alpha_{dissolution}$) is 0.99938 (Harting et al., 1976; Leonte et al., 2018). Thus, if all the variations in methane composition of bubbles were due to dissolution upon ascent, we would expect initial carbon isotope values of methane to be 0.25 to 1.42‰ heavier than the measured values, which is relatively minor compared to the range of isotope variation observed. Variation due to methanogenic or oxidative pathway can be differentiated by the correlation between $\delta^{13}C$

and δD (**Figure 4.3b**). If variation in methanogenic pathway (hydrogenotrophic or acetoclastic) is the main cause of correlation, one would expect a negative association between $\delta^{13}C$ and δD values, while methane oxidation produces a positive association (**Figure 4.3**). The observed positive correlation (slope = 6) between $\delta^{13}C$ and δD values is consistent with oxidation as a controlling mechanism. Previous work characterizing the presence of methane oxidation in freshwater environments has documented δD/ $\delta^{13}C$ slopes between 2.5 and 15 (e.g., Walter et al., 2008). The carbon isotope effect of aerobic oxidation ($\alpha_{oxidation}$) is between 0.979 to 0.995 (Barker and Fritz, 1981; Grant and Whiticar, 2002; Leonte et al., 2017; Whiticar and Faber, 1986), such that oxidation would increase the $\delta^{13}C$ of methane remaining in the bubble. This isotope effect is several times larger than that associated with dissolution for the same amount of methane loss, and thus able to reconcile a much greater range in observed $\delta^{13}C$ values.

Oxidation could occur by aerobic methanotrophs in the oxic upper 15 m of the water column, or by the anaerobic oxidation of methane (AOM) in the lake sediments. While aerobic methanotrophs can oxidize methane in the water column, they can only metabolize methane in the dissolved form. Further, the transit time of a methane bubble through the water column is short (e.g., the velocity of a 5 mm bubble is ca. 24.8 cm/s) (McGinnis et al., 2006). Therefore, it is unlikely that methane in bubbles is directly oxidized. Methane diffused from the water column into gas bubbles could be relatively oxidized; however, the concentration gradient of methane between gas bubbles and lake water would favor methane loss from bubbles over methane gain. Microbial activity and diffusive exchange can also occur across the headspace-water interface in bubble traps, but expectations about concentration gradients are the same. AOM is possible in freshwater sediments, and can oxidize dissolved methane before bubbles form. Previously, sulfate-coupled AOM has been reported in eutrophic lakes (Eller et al., 2005), shallow thermokarst lakes (Wik et al., 2020; Winkel et al., 2019), rice paddies (Murase and Kimura, 1994), and peatlands (Smemo and Yavitt, 2007). This process is viable at Upper Mystic Lake, as bottom waters are sulfidic. AOM in eutrophic lakes can also be coupled to processes other than sulfate reduction, including denitrification (e.g., Deutzmann and Schink, 2011). If AOM is proceeding in lake sediments, longer residence time of methane, associated with lower gas flux, may result in a relatively more oxidized methane pool. Thus, AOM is more likely to be significant compared to aerobic oxidation in Upper Mystic Lake.

Aerobic and anaerobic oxidation of methane impart indistinguishable $\delta^{13}C$ and δD isotope fractionations, but may be differentiated using $\Delta^{13}CH_3D$ values. Work characterizing the aerobic oxidation of methane by methanotrophs found that as oxidation proceeds, the $\delta^{13}C$ and δD values of the remaining methane pool become higher and $\Delta^{13}CH_3D$ values become slightly lower (Wang et al., 2018). Alternatively, work characterizing the anaerobic oxidation of methane found that as oxidation proceeds and the $\delta^{13}C$ and δD values of the remaining methane pool become higher, $\Delta^{13}CH_3D$ values also increase (Ono et al., 2021). The differences in kinetic isotope effects between these two processes was then demonstrated in natural methanotrophic waters (Giunta et al., 2022). The slopes of δD vs $\Delta^{13}CH_3D$ in these studies are shown alongside our data in **Figure 4.3c**. Methane collected in early summer may have undergone a greater extent of oxidation than methane collected later in the season. The positive correlation we observe between δD and $\Delta^{13}CH_3D$ values is broadly consistent with the isotope effect imparted by anaerobic oxidation of methane, although the slope is shallower than observed under experimental conditions.

Further, we can estimate the extent of methane oxidation that has occurred to determine whether there is a relationship with either sampling date (expected for an anerobic mechanism) or storage time (expected for an aerobic mechanism). The extent of oxidation ($f_{oxidation}$) is estimated using Rayleigh fractionation, assuming that initial $\delta^{13}C$ values of methane are approximately equal across space and time before oxidation occurs. We use an initial $\delta^{13}C$ value of -72‰, representing the lowest observed values, and a fractionation factor ($\alpha_{oxidation}$) of 0.98863 (Leonte et al., 2017), which is in the middle of the range of experimentally determined values. We estimate $f_{oxidation}$ to be between ca. 0.05 and 0.5. Generally, $f_{oxidation}$ decreases with time (**Figure 4.4a**), but is uncorrelated to the length of time that methane is stored in gas traps **(Figure 4.4b**). Consequently, we would expect oxidation in the anoxic lake sediment to be the most likely scenario.

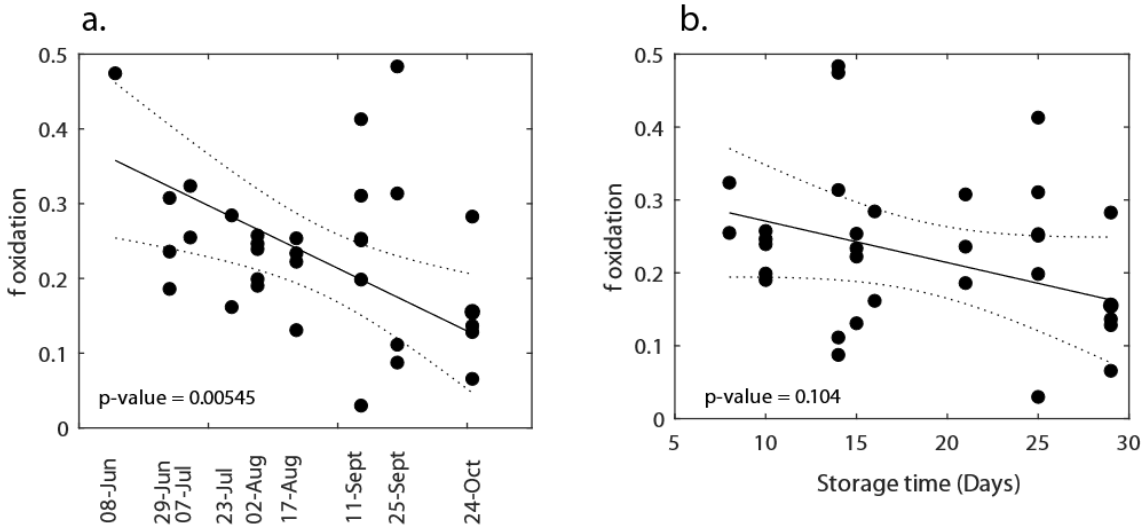

Figure 4.4: **a** The relationship between the proportion of methane that has undergone oxidation ($f_{oxidation}$) vs time **b** The relationship between the proportion of methane that has undergone oxidation ($f_{oxidation}$) vs storage time in bubble traps.

Given the trends in isotopologue values and variation of $f_{oxidation}$ with time, we hypothesize that the range in non-equilibrium $\Delta^{13}CH_3D$ values originate primarily from isotopologue effects during methanogenesis and post-generation processing (oxidation) in the lakebed. Our methane concentration observations are broadly consistent with higher fluxes of methane during late summer and fall, which may yield larger bubbles and strip N_2 from sediments so that as the season progresses, bubbles have higher concentrations of methane. We can explain the observed range in $\Delta^{13}CH_3D$, $\delta^{13}C$, and δD values by anaerobic oxidation of methane in lake sediments, where an increase in methane flux decreases the amount of time methane is stored in sediments, producing less significant fractionations from oxidation. This observed seasonal difference is likely associated with the onset of thermal stratification, and thus increasing anoxia in the deep lake basin through the early summer.

4.4.2 Similar isotopologue variability in ebullition across lake sites

Establishing a representative $\Delta^{13}CH_3D$ source value is needed to compare ebullition from Upper Mystic Lake with ebullition from other freshwater lakes and assess the extent that $\Delta^{13}CH_3D$ values from different lake systems have different distributions. Data from Upper

Mystic Lake follows a normal distribution (**Figure 4.S2**); therefore, a mean value is appropriate to characterize the lake source signature. To account for both $\Delta^{13}CH_3D$ values and the volume of methane emitted, we first calculate a flux-weighted mean and standard deviation of 3.3±0.6‰. We then use the number of observations (n = 40) and the student t-score to estimate a 95% confidence interval of 0.19‰ for the Upper Mystic Lake site-level mean (**Figure 4.5b**).

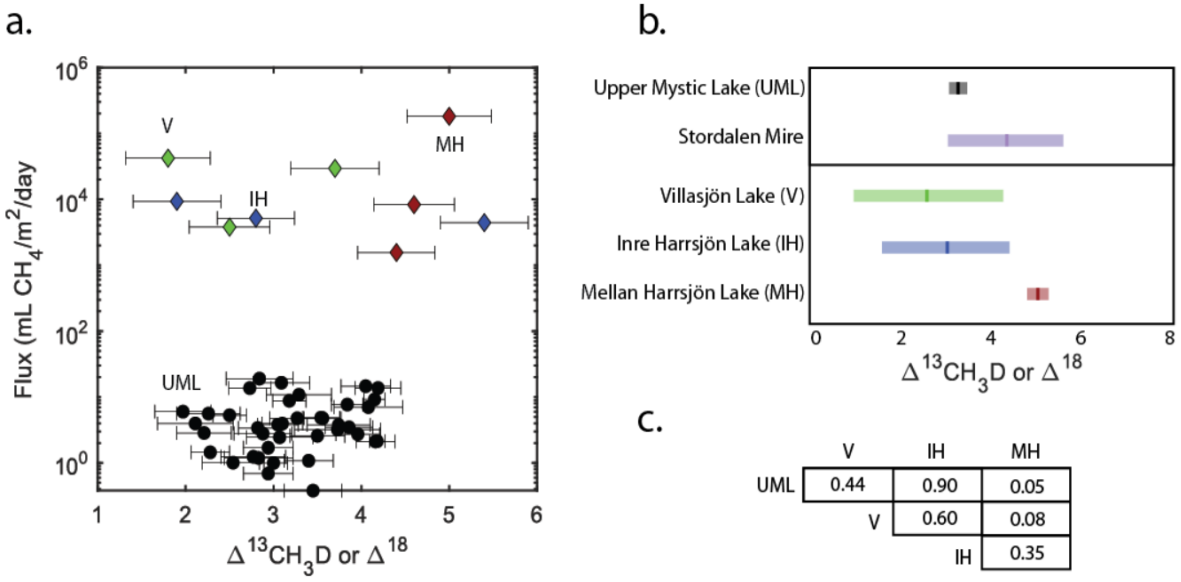

Figure 4.5: $\Delta^{13}CH_3D$ value variability and lake source signatures for methane emitted by ebullition **a** Scatter plot of $\Delta^{13}CH_3D$ and Δ^{18} values (‰) vs methane flux (mL/m^2/day) for bubbles collected from Upper Mystic Lake in 2021 (black circles, this study) and from Stordalen Mire, Sweden in 2014 (diamonds, Douglas et al., 2016). Three Stordalen Mire lakes are distinguished by color, where Villasjön (V) is in green, Inre Harrsjön (IH) is in blue, and Mellersta Harrsjön (MH) is in red. **b** Mean $\Delta^{13}CH_3D$ source signatures and 95% confidence interval calculated using the student t-score and standard deviation of site measurements. **c** Matrix of p-values for student-t tests to determine whether a pair of two lakes can be confidently distinguished from each other. Typically p-scores less than 0.05 are considered statistically significant.

The Upper Mystic Lake site-level mean can then be compared to other freshwater bodies for which sampling was conducted for background ebullition (i.e., by distributing bubble traps throughout the lake without identifying bubbling hotspots). We chose to exclude lakes with only one $\Delta^{13}CH_3D$ measurement as being insufficient to define a site-level mean (e.g., Lower Mystic Lake), as well as hot spot samples, which have been documented as having different isotopic trends from other ebullition (Douglas et al., 2016). Thus, we limit our scope to additionally look

at data from the three lakes of Stordalen Mire, Sweden (Villasjön, Inre Harrsjön, and Mellersta Harrsjön) (Douglas et al., 2016). Upper Mystic Lake and Stordalen Mire lakes share morphologic similarities; for example, they are all post-glacial kettle lakes. Unlike Upper Mystic Lake, however, the Stordalen Mire lakes are intertwined with areas of thawing permafrost. Seasonality of sampling these sites overlaps, as sampling Stolderen Mire for Δ^{18} analysis was conducted during the months of June and July, while sampling of Upper Mystic Lake was conducted from May through October.

One key observation in both Upper Mystic Lake and Stordalen Mire is the high variability of $\Delta^{13}CH_3D$ and Δ^{18} values from ebullition across space and time (spanning 2.0 to 4.2‰ in Upper Mystic Lake and 1.8 to 5.4‰ in Stordalen Mire). Further, while ebullition flux is approximately three orders of magnitude higher in Stordalen Mire than Upper Mystic Lake during summer months (**Figure 4.5a**), in both flux regimes, no correlation between $\Delta^{13}CH_3D$ or Δ^{18} values and ebullition flux is observed. Previously, positive correlation between methane flux and Δ_{18} has been documented for lacustrine seeps in Alaska (Douglas et al., 2016), due to methane input from hot spots. Our observation is an important negative result, which suggests that $\Delta^{13}CH_3D$ measurements from ebullition are not sensitive as a proxy for ebullition emissions across both temperate and arctic environments. Rather, methane isotopologue distributions may be controlled by kinetic fractionations associated with methanogenesis and/or methane oxidation.

We use the same methodology applied to the Upper Mystic Lake dataset to define flux-weighted means with 95% confidence intervals for Stordalen Mire as a whole, as well as the three Stordalen Mire lakes individually. For the whole Stordalen Mire dataset, the mean $\Delta^{13}CH_3D$ value is 4.2±1.3‰ (**Figure 4.5b**). Notably, this value is heavily influenced by one measurement made from Mellersta Harrsjön, for which flux was ca. an order of magnitude greater than other flux measurements; excluding this measurement yields a value of 2.8±1.2‰. Regardless, neither estimate is distinguishable from that of Upper Mystic Lake. The observation of similar isotopologue variability observed for ebullition across both presently characterized sites supports an assumption that similar variability may exist for all freshwater ebullition.

We estimate the site-level $\Delta^{13}CH_3D$ means of the individual lakes within Stordalen Mire to assess if ebullition characterization from any individual lake is statistically distinguishable from another. Flux-weighted means and 95% confidence intervals are as follows: Villasjön

2.6±1.7‰, Inre Harrsjön 3.0±1.4‰, and Mellersta Harrsjön 5.0±0.2‰ (**Figure 4.5b**). We probe whether $\Delta^{13}CH_3D$ values from lakes are statistically distinguishable by running a series of Welch's unequal variances two-tailed t-tests for lake pairs. This analysis tests a null hypothesis that two populations, with potentially unequal variances and unequal sample sizes, have equal means. p-values less than 0.05 are considered statistically significant, meaning measurements from lakes are from different distributions; resultant p-values from this analysis are reported in **Figure 5c**. We find that Upper Mystic Lake and Mellersta Harrsjön are the only statistically distinguishable lakes (p = 0.05) (**Figure 4.5c**). Notably, these are also the two lakes that are most tightly constrained. An implication of this is that if other lakes were similarly constrained (e.g., 95% confidence interval <0.5‰), more lakes source signatures may be differentiable. However, given the observation of high $\Delta^{13}CH_3D$ variability in Upper Mystic Lake, Villasjön, and Inre Harrsjön, it is possible that more measurements from Mellersta Harrsjön may yield higher variability than the current characterization. Thus, it is uncertain that the measurements used to define the site-level mean $\Delta^{13}CH_3D$ value at Mellersta Harrsjön capture the true range of $\Delta^{13}CH_3D$ values from ebullition at this site.

The observation of a tightly constrained site-level mean $\Delta^{13}CH_3D$ estimate from a small (≤ 3 samples) dataset, as seen in Mellersta Harrsjön, was also made for the 2014 characterization of Upper Mystic Lake (Wang et al., 2015). The mean $\Delta^{13}CH_3D$ estimate from the 2014 field season is 3.17±0.4‰, and the two measured $\Delta^{13}CH_3D$ values were equal within 0.1‰. Given the variability in $\Delta^{13}CH_3D$ values observed during the 2021 field season, we know that the 2014 sampling campaign does not capture the $\Delta^{13}CH_3D$ variability of background, and thus exists the potential to severely mischaracterize the source signature. Remarkably, the mean source signature from the 2 measurements made in 2014 is nearly identical to that from the 40 measurements made in 2021 (3.17±0.4‰ vs 3.21±0.19‰). The overlap between the 2 measurements in 2014 with the 40 in 2021 provides some tentative evidence that $\Delta^{13}CH_3D$ values from lake ebullition do not vary significantly between years.

The uncertainty in $\Delta^{13}CH_3D$ estimates using a 3-sample characterization indicates that this level of characterization is insufficient to constrain mean $\Delta^{13}CH_3D$ source signatures. Regardless of whether variability is over- or under- estimated, we cannot predict the effect (i.e.,

under- or over- estimation) on mean $\Delta^{13}CH_3D$ values. Thus, without more measurements per site, ebullition between lake sources cannot be conclusively distinguished.

4.4.3 Recommendations for constraining $\Delta^{13}CH_3D$ source signatures of freshwater lakes

The dichotomy between 1) the high uncertainty in site-level $\Delta^{13}CH_3D$ means based on three or fewer measurements, versus 2) the diminishing returns in precision based on the 40 measurements used to characterize Upper Mystic Lake (e.g., **Figure 4.6a,b**), yields the question of what an appropriate number of samples is to define lake $\Delta^{13}CH_3D$ source signatures. Making $\Delta^{13}CH_3D$ measurements is time consuming and expensive, thus it is important to consider a minimum number of samples to address environmentally important questions. Given the similar isotopologue variability observed for ebullition samples across sites, we exploit the uniquely large Upper Mystic Lake dataset to recommend a best practice sampling strategy to constrain $\Delta^{13}CH_3D$ source estimates for freshwater lakes.

While different scientific endeavors may require different levels of precision, we herein consider a 95% confidence interval of 0.5‰ as a reasonable threshold to define site-level $\Delta^{13}CH_3D$ means. We choose this threshold as it is precise enough to differentiate some freshwater lake sources (e.g., if mean $\Delta^{13}CH_3D$ values from the Stordalen Mire lakes are accurate). Additionally, this threshold is more constrained than the expected standard deviation of values from freshwater lakes (assumed ca. 0.63‰). In sampling, ideally there is high enough sample coverage to be representative of the lake basin, and precision is improved upon as a function of the number of samples. By calculating the 95% confidence interval using t-scores and the standard deviation of the entire population (0.63‰), we can predict that constraining a population within 0.5‰, requires ca. 9 samples (**Figure 4.6a**). This number of samples is reasonable to attain within a field campaign. Alternatively, measurement error is typically about 0.3‰, so to constrain a site-level mean on par with measurement error, 15-20 measurements are needed. This is an effort commensurate with the sampling conducted in this study.

We then simulate different sampling strategies to probe their impact on constraining an accurate and precise site-level $\Delta^{13}CH_3D$ mean for Upper Mystic Lake. We first simulate sampling strategies where we vary 'n', the number of samples that are collected, by randomly pulling values from our dataset. In any single simulation, a measurement can only be sampled

once (i.e., values are not replaced). Then, the site-level mean $\Delta^{13}CH_3D$ value is calculated from the resultant sample set. We simulate each sampling strategy 1000 times and plot the distribution of site-level means (**Figure 4.6b,c**). For these calculations we assume that methane flux is approximately equal for each sample, as flux data may be unknown.

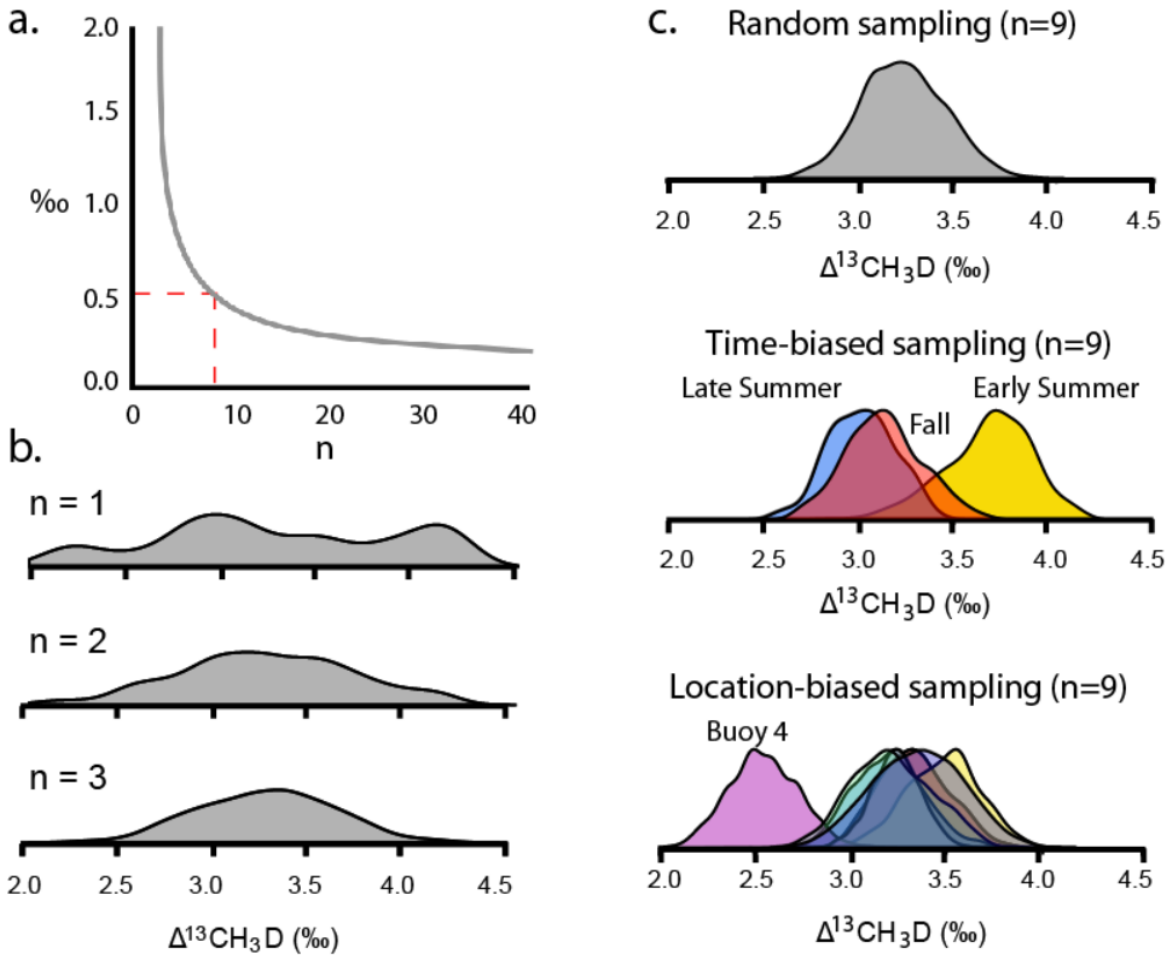

Figure 4.6: **a** The 95% confidence interval for the sample mean if the lake was sampled n times. Dashed red lines indicate that 8-9 samples are necessary to constrain the sample mean within 0.5‰. **b** The probability distribution of mean $\Delta^{13}CH_3D$ values if Upper Mystic Lake was sampled n times. n is from 1 to 3, reflecting previous sample coverage **c** The probability distribution of mean $\Delta^{13}CH_3D$ values if Upper Mystic Lake was sampled the recommended 9 times 1) randomly across space and time, 2) restricted by season (early summer, late summer, or fall), and 2) restricted by location by buoy.

The probability densities of site-level $\Delta^{13}CH_3D$ means estimated by sampling three or fewer times are shown in **Figure 4.6b**, and by sampling the recommended nine times is shown in **Figure 4.6c**. When three or fewer measurements are used to constrain the Upper Mystic Lake source signal, there is a relatively high chance of mischaracterizing the mean. For example, when only two measurements are available, which is what was previously available from Upper Mystic Lake, there is a 48% chance of mischaracterization by more than 0.5‰. Using the sampling strategy of randomly selecting measurements across space and time, the chance of a site-level $\Delta^{13}CH_3D$ mean to be over- or under- estimated is similarly likely; however, field campaigns are not representative of true random sampling.

We simulate time- and location- biased sampling to show that sampling at a single timepoint will yield biased results, but sampling at a limited number of locations over longer timescales may yield sufficiently representative samples (**Figure 4.6c**). To assess the impact of time-bias on probability distributions, we simulate 1000 sampling campaigns for each of three seasonal categories for which data is subdivided into: early summer (May 25-July 23), late summer (July 23- September 11), and fall (September 11-October 24). 9 measurements are sampled for each simulation to define a site-level $\Delta^{13}CH_3D$ mean within ca. 0.5‰. For these simulations, re-sampling is allowed. Sampling conducted in the early summer would result in a distinguishably higher $\Delta^{13}CH_3D$ source value than sampling conducted during the late summer and fall. If temporal variation in isotopologue composition is a widespread phenomenon, then sampling on a single sampling date or narrow range of sampling days (<2 month) may yield biased results. The need for temporally diverse sampling is also relevant for characterizing ebullition flux (Wik et al., 2016). Work analyzing large datasets of background ebullition flux measurements shows that there is a higher (up to 72%) risk of mischaracterization when sampling is limited to 1-3 days (Wik et al., 2016).

Location-bias within the Upper Mystic Lake dataset is expected to have a small effect, as the deep basin of the lake was specifically targeted for characterization. To assess the impact of location-bias on probability distributions, we simulate 1000 sampling campaigns in which 9 measurements are sampled (allowing resampling) for each buoy location. We find that over the course of the field season, sampling at each buoy yielded similar probability distributions, except for buoy 4 which had anomalously low $\Delta^{13}CH_3D$ values (**Figure 4.6c**). This buoy was also

located at the shallowest location along the slope of the deep basin, and thus perhaps not representative of the deep basin of Upper Mystic Lake. Additionally, randomly selecting 9 data points from the entire data set or randomly selecting 1 measurement per sampling day (total 9) yield undifferentiable probability distributions and confidence intervals (3.21±0.50 and 3.33±0.32, respectively). An implication of these findings is that technology like moored automated samplers (e.g., Thanh Duc et al., 2019) may offer promising sample coverage for this endeavor. However, given that we sampled to specifically target the deep basin of Upper Mystic Lake, greater location-based variability may be observed in shallower sediments with more disparate organic matter inputs.

4.5 SUMMARY

Abundances of clumped methane isotopologue ($\Delta^{13}CH_3D$) were characterized from background ebullition in Upper Mystic Lake, MA over the course of 5 months. In doing so, this study yields unprecedented constraints on the spatial and temporal variability of $\Delta^{13}CH_3D$ values from a freshwater lake. Interpretations of isotopologue values, along with $\delta^{13}C$, δD, CH_4 flux, and $\%CH_4$ in bubbles, show that measurements of $\Delta^{13}CH_3D$ values may yield insight to the biogeochemical processing of methane in the lakebed versus the water column. We find that the extent of anaerobic oxidation of methane in the lakebed decreases as methane flux increases, and as methane storage time in sediments decreases. The seasonal differences in methane flux and extent of oxidation between the early summer and the late summer and fall are likely connected to the timing of thermal stratification and development of deep water anoxia. We compare data from this study to previous work in Upper Mystic Lake and Stordalen Mire Sweden to show that background ebullition may have similar isotopologue variability, across sites. However, the previous sample sizes (≤ 3) are insufficient to differentiate lake source signatures. Finally, we recommend at least 9 samples be collected to characterize site-level $\Delta^{13}CH_3D$ means to within ca. 0.5‰. Sampling is likely to be biased if collected within a narrow range of dates, but sampling from a limited number of locations may be representative. This study demonstrates that even within a single lake basin with a consistent bottom water temperature, a large variation in $\Delta^{13}CH_3D$ values (2.0 to 4.2‰) is observed, making it unlikely to yield additional constraints to the atmospheric methane budget.

4.6 ACKNOWLEDGMENTS

We would like to thank Harry Hemond and Kyle Delwiche for helpful conversations regarding sampling Upper Mystic Lake. Funding for this study was provided by the MIT Earth, Atmosphere and Planetary Sciences Montrym Fund for student climate research (awarded to E.L.), the MIT m-Terra Catalyst Fund (to S.O and E.L), and the MIT Undergraduate Research Opportunities Program (to support A.V.).

4.7 SUPPLEMENTARY INFORMATION

Buoy #	Latitude	Longitude	Water Depth (ft)
1	42.435470	-71.148300	75
2	42.434010	-71.149500	84
3	42.434910	-71.148900	80
4	42.434240	-71.147600	60
5	42.434130	-71.148300	75
6	42.434550	-71.150900	80
7	42.435490	-71.151000	65
8	42.434010	-71.149500	84

Table 4.S1: Coordinates and water depths of bubble traps stationed in Upper Mystic Lake, MA. Water Depths are determined from bathymetric map.

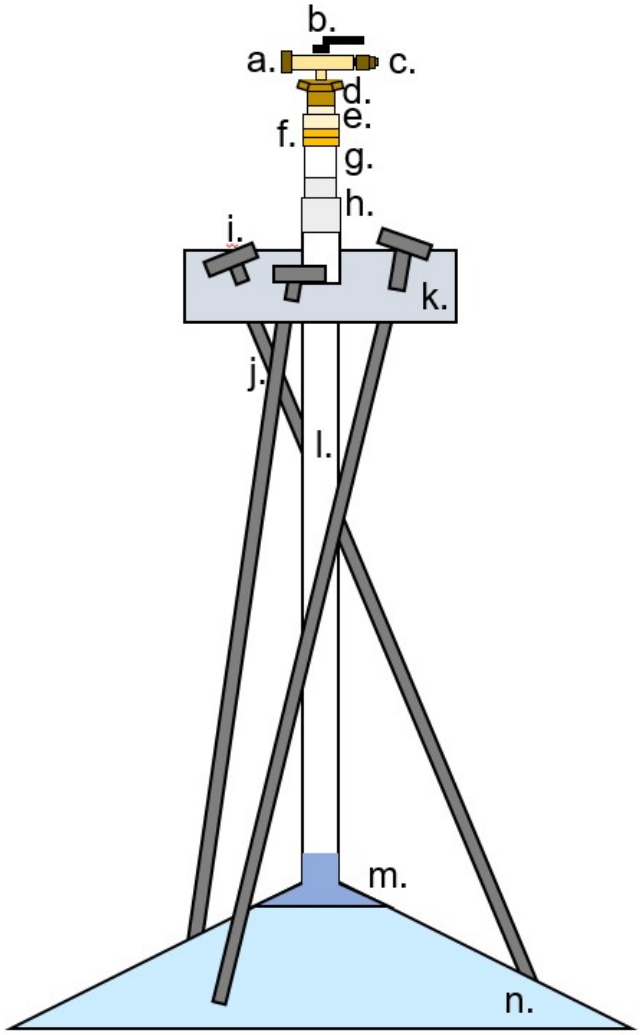

Figure 4.S1: Annotated bubble trap design and picture of bubble trap at the lake shore

Diagram ID	Part Name	#/Trap	Vendor	Part #	Cost
a	Septum Port	1			
b	1/4" Brass Ball Valve	1	McMaster	46095K51	$22.95
c	1/4" NPT Brass Hex Nipple	1	Grainger	6AZD1	$1.74
d	1/2" NPT Male x 1/4" NPT female reducer	1	Toolegin	N/A	$4.25
e	Reducing Coupling 3/4" x 1/2"	1	Grainger	22FK22	$4.24
f	Transition Adaptor: 3/4" PVC to NPT	1	Grainger	23NY85	$13.98
g	1/2" PVC	1	McMaster		
h	PVC 3/4" to 1/2" reducing coupling	1	Grainger	22FK22	$0.54
i	1/4" tee connector	6	McMaster	4881K47	$3.55
j	1/4" PVC pipe - 10 ft	1	McMaster	48925K41	$14.18
k	12"x12"x1/4" semi-clear polypropylene sheet	1	McMaster	8742k135	$13.29
l	3/4" clear PVC pipe - 3 ft	1	McMaster	49035K24	$14.35
m	PETG custom fitting	1		N/A	N/A
n	55-gallon Deer Funnel	1	Boss Buck	N/A	$33
	Buoy	1			
	Cement Block Anchor	1			
	Parachute Rope	1			
	PVC Cement	N/A	McMaster	74605A14	$9.10
	Epoxy Adhesive, 3 min work life	N/A	Grainger	3KYZ1	$23.62
	Rust Prevention Spray	N/A	Grainger	4TH62	$9.26

Table 4.S2: Bubble trap parts and cost as of March 2021.

Depth [m]	Temperature[^{o}C]	Salinity	O_2[mM]	CO_2[mM]	CH_4[mM]
0	25	0	0.29	0.69	0
1	24.5	0	0.283	0.68	0
2	23.5	0	0.27	0.71	0
3	21.5	0	0.256	0.73	0
4	18.3	0	0.239	0.75	0
5	13.6	0	0.145	0.8	0
6	10	0	0.059	0.83	0
7	8.1	0	0.021	0.87	0
8	7	0	0.016	0.88	0
9	6.3	0	0.014	0.88	0
10	5.8	0	0.013	0.88	0
11	5.2	0	0.012	0.87	0.02268
12	4.6	0	0.011	0.87	0.047422
13	4.2	0	0.011	0.87	0.064948
14	4.1	0	0.011	0.87	0.075257
15	3.8	0	0.01	0.86	0.107216
16	3.7	0	0.01	0.9	0.119587
17	3.6	0	0.008	0.92	0.131958
18	3.6	0	0.008	1.06	0.168041
19	3.6	0	0.008	1.21	0.208247
20	3.6	0	0.008	1.32	0.246392
21	3.6	0	0.008	1.35	0.288659
22	3.6	0	0.008	1.4	0.314433

Table 4.S3: Upper Mystic Lake water column physical and chemical properties used in the bubble dissolution model, from (Peterson, 2005).

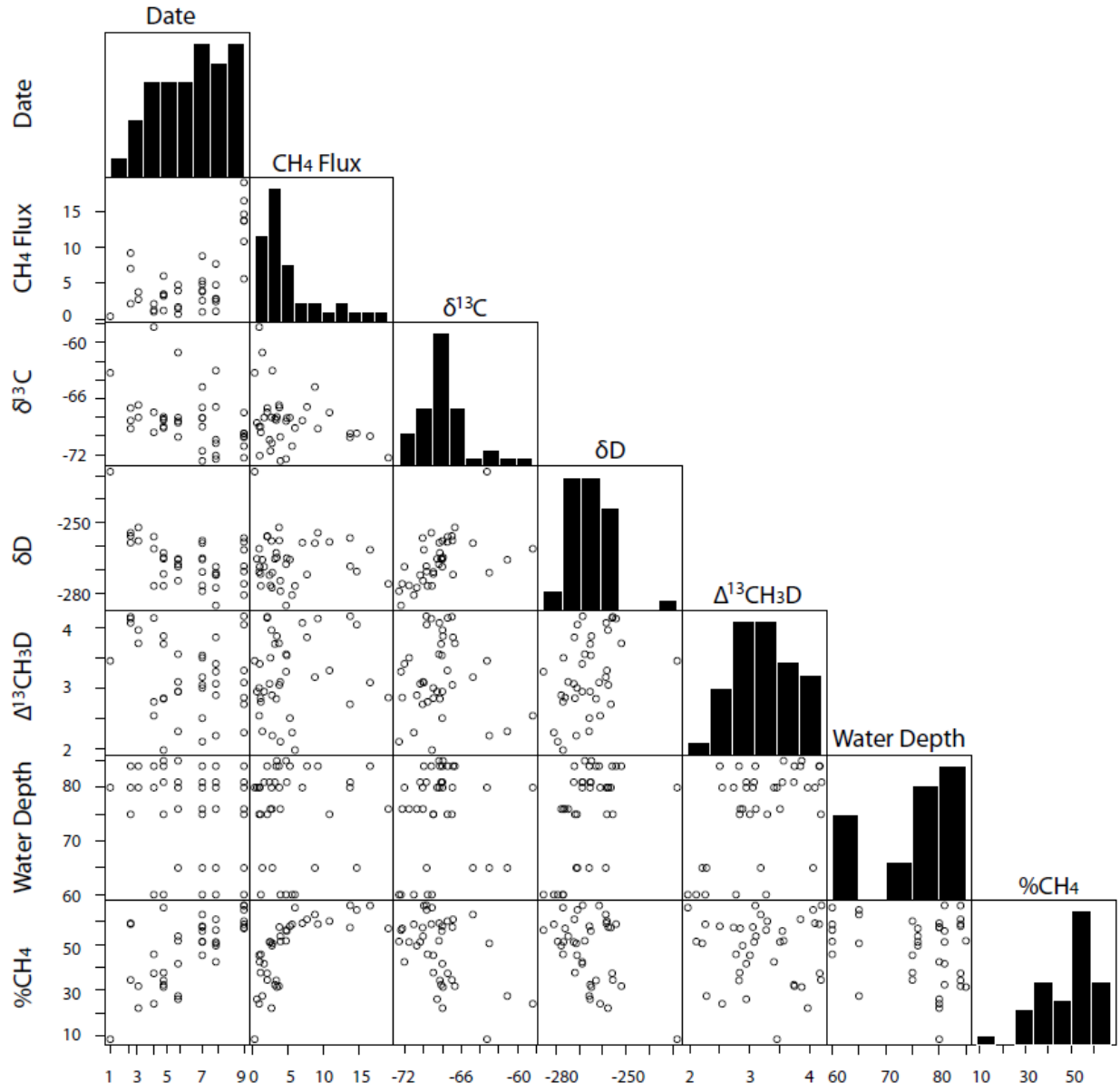

Figure 4.S2: Matrix of histograms and correlation of data. Date is plotted by sampling day where 1 is 6/8/21, 2 is 6/23/21, etc. CH_4 flux is plotted in units mL/m^{2}day. Values of $\delta^{13}C$, δD, and $\Delta^{13}CH_3D$ are plotted in per mille (‰) units. Water depth is in feet and also indicates different buoy locations.

4.8 REFERENCES

Ash, J.L., Egger, M., Treude, T., Kohl, I., Cragg, B., Parkes, R.J., Slomp, C.P., Lollar, B.S., Young, E.D., 2019. Exchange catalysis during anaerobic methanotrophy revealed by $^{12}CH_2D_2$ and $^{13}CH_3D$ in methane. Geochemical Perspect. Lett. 10, 26–30. https://doi.org/10.7185/geochemlet.1910

Aurillo, A.C., Mason, R.P., Hemond, H.F., 1994. Speciation and Fate of Arsenic in Three Lakes of the Aberjona Watershed. Environ. Sci. Technol. 28, 577–585. https://doi.org/10.1021/es00053a008

Barker, J.F., Fritz, P., 1981. Carbon isotope fractionation during microbial methane oxidation. Nature 293, 289–291.

Bastviken, D., Tranvik, L.J., Downing, J.A., Crill, P.M., Enrich-Prast, A., 2011. Freshwater methane emissions offset the continental carbon sink. Science (80-.). 331, 50. https://doi.org/10.1126/science.1196808

Beaudry, P., Stefánsson, A., Fiebig, J., Rhim, J.H., Ono, S., 2021. High temperature generation and equilibration of methane in terrestrial geothermal systems: Evidence from clumped isotopologues. Geochim. Cosmochim. Acta 309, 209–234. https://doi.org/10.1016/j.gca.2021.06.034

Börjesson, G., Chanton, J., Svensson, B.H., 2001. Methane Oxidation in Two Swedish Landfill Covers Measured with Carbon-13 to Carbon-12 Isotope Ratios. J. Environ. Qual. 30, 369–376. https://doi.org/10.2134/jeq2001.302369x

Chanton, J.P., 2005. The effect of gas transport on the isotope signature of methane in wetlands. Org. Geochem. 36, 753–768. https://doi.org/10.1016/j.orggeochem.2004.10.007

Chanton, J.P., Fields, D., Hines, M.E., 2006. Controls on the hydrogen isotopic composition of biogenic methane from high-latitude terrestrial wetlands. J. Geophys. Res. Biogeosciences 111, 1–9. https://doi.org/10.1029/2005JG000134

Chung, E., Arnold, T., 2021. Potential of Clumped Isotopes in Constraining the Global Atmospheric Methane Budget. Global Biogeochem. Cycles 35, 1–14. https://doi.org/10.1029/2020GB006883

Dansgaard, W., 1964. Stable isotopes in precipitation. Tellus 16, 436–468. https://doi.org/10.3402/tellusa.v16i4.8993

Delwiche, K.B., Hemond, H.F., 2017. Methane Bubble Size Distributions, Flux, and Dissolution in a Freshwater Lake. Environ. Sci. Technol. 51, 13733–13739. https://doi.org/10.1021/acs.est.7b04243

Deutzmann, J.S., Schink, B., 2011. Anaerobic oxidation of methane in sediments of Lake Constance, an oligotrophic freshwater lake. Appl. Environ. Microbiol. 77, 4429–4436. https://doi.org/10.1128/AEM.00340-11

Douglas, P.M.J., Gonzalez Moguel, R., Walter Anthony, K.M., Wik, M., Crill, P.M., Dawson, K.S., Smith, D.A., Yanay, E., Lloyd, M.K., Stolper, D.A., Eiler, J.M., Sessions, A.L.,

2020a. Clumped isotopes link older carbon substrates with slower rates of methanogenesis in northern lakes. Geophys. Res. Lett. 47, e2019GL086756. https://doi.org/10.1029/2019GL086756

Douglas, P.M.J., Gonzalez Moguel, R., Walter Anthony, K.M., Wik, M., Crill, P.M., Dawson, K.S., Smith, D.A., Yanay, E., Lloyd, M.K., Stolper, D.A., Eiler, J.M., Sessions, A.L., 2020b. Clumped Isotopes Link Older Carbon Substrates With Slower Rates of Methanogenesis in Northern Lakes. Geophys. Res. Lett. 47, 1–10. https://doi.org/10.1029/2019GL086756

Douglas, P.M.J., Stolper, D.A., Smith, D.A., Walter Anthony, K.M., Paull, C.K., Dallimore, S., Wik, M., Crill, P.M., Winterdahl, M., Eiler, J.M., Sessions, A.L., 2016. Diverse origins of Arctic and Subarctic methane point source emissions identified with multiply-substituted isotopologues. Geochim. Cosmochim. Acta 188, 163–188. https://doi.org/10.1016/j.gca.2016.05.031

Douglas, P.M.J., Stratigopoulos, E., Park, S., Phan, D., 2021. Geographic variability in freshwater methane hydrogen isotope ratios and its implications for global isotopic source signatures. Biogeosciences 18, 3505–3527. https://doi.org/10.5194/bg-18-3505-2021

Eller, G., Känel, L., Krüger, M., 2005. Cooccurrence of aerobic and anaerobic methane oxidation in the water column of Lake Plußsee. Appl. Environ. Microbiol. 71, 8925–8928. https://doi.org/10.1128/AEM.71.12.8925-8928.2005

Ganesan, A.L., Schwietzke, S., Poulter, B., Arnold, T., Lan, X., Rigby, M., Vogel, F.R., van der Werf, G.R., Janssens-Maenhout, G., Boesch, H., Pandey, S., Manning, A.J., Jackson, R.B., Nisbet, E.G., Manning, M.R., 2019. Advancing Scientific Understanding of the Global Methane Budget in Support of the Paris Agreement. Global Biogeochem. Cycles 33, 1475–1512. https://doi.org/10.1029/2018GB006065

Ganesan, A.L., Stell, A.C., Gedney, N., Comyn-Platt, E., Hayman, G., Rigby, M., Poulter, B., Hornibrook, E.R.C., 2018. Spatially Resolved Isotopic Source Signatures of Wetland Methane Emissions. Geophys. Res. Lett. 45, 3737–3745. https://doi.org/10.1002/2018GL077536

Giunta, T., Young, E.D., Labidi, J., Sansjofre, P., Jézéquel, D., Donval, J.P., Brandily, C., Ruffine, L., 2022. Extreme methane clumped isotopologue bio-signatures of aerobic and anaerobic methanotrophy: Insights from the Lake Pavin and the Black Sea sediments. Geochim. Cosmochim. Acta 338, 34–53. https://doi.org/10.1016/j.gca.2022.09.034

Giunta, T., Labidi, J., Kohl, I.E., Ruffine, L., Donval, J.P., Géli, L., Çağatay, M.N., Lu, H., Young, E.D., 2021. Evidence for methane isotopic bond re-ordering in gas reservoirs sourcing cold seeps from the Sea of Marmara. Earth Planet. Sci. Lett. 553, 116619. https://doi.org/10.1016/j.epsl.2020.116619

Giunta, T., Young, E.D., Warr, O., Kohl, I., Ash, J.L., Martini, A., Mundle, S.O.C., Rumble, D., Pérez-Rodríguez, I., Wasley, M., LaRowe, D.E., Gilbert, A., Sherwood Lollar, B., 2019. Methane sources and sinks in continental sedimentary systems: New insights from paired clumped isotopologues $^{13}CH_3D$ and $^{12}CH_2D_2$. Geochim. Cosmochim. Acta 245, 327–351. https://doi.org/10.1016/j.gca.2018.10.030

Gonzalez, Y., Nelson, D.D., Shorter, J.H., Mcmanus, J.B., Formolo, M.J., Wang, D.T., Western, C.M., Ono, S., 2019. Precise measurements of $^{12}CH_2D_2$ by tunable infrared laser direct absorption spectroscopy. https://doi.org/10.1021/acs.analchem.9b03412

Grant, N.J., Whiticar, M.J., 2002. Stable carbon isotopic evidence for methane oxidation in plumes above Hydrate Ridge, Cascadia Oregon Margin. Global Biogeochem. Cycles 16, 71-1-71–13. https://doi.org/10.1029/2001gb001851

Greinert, J., McGinnis, D.F., 2009. Single bubble dissolution model – The graphical user interface SiBu-GUI. Environ. Model. Softw. 24, 1012–1013. https://doi.org/https://doi.org/10.1016/j.envsoft.2008.12.011

Gruen, D.S., Wang, D.T., Könneke, M., Topçuoğlu, B.D., Stewart, L.C., Goldhammer, T., Hinrichs, K.U., Ono, S., 2018. Experimental investigation on the controls of clumped isotopologue and hydrogen isotope ratios in microbial methane. Geochim. Cosmochim. Acta 237, 339–356. https://doi.org/10.1016/j.gca.2018.06.029

Haghnegahdar, M.A., Schauble, E.A., Young, E.D., 2017. A model for $^{12}CH_2D_2$ and $^{13}CH_3D$ as completmentay tracers for the budget of atmospheric CH_4. Global Biogeochem. Cycles 1387–1407. https://doi.org/10.1111/1462-2920.13280

Harting, P., Schütze, H., Christoph, G., 1976. Der thermodynamische Kohlenstoffisotopieeffekt im System CH_4–H_2O. Isot. Isot. Environ. Heal. Stud. 12, 232–234. https://doi.org/10.1080/10256017608543923

Jautzy, J.J., Douglas, P.M.J., Xie, H., Eiler, J.M., Clark, I.D., 2021. CH_4 isotopic ordering records ultra-slow hydrocarbon biodegradation in the deep subsurface. Earth Planet. Sci. Lett. 562, 116841. https://doi.org/10.1016/j.epsl.2021.116841

Joelsson, L.M.T., Forecast, R., Schmidt, J.A., Meusinger, C., Nilsson, E.J.K., Ono, S., Johnson, M.S., 2014. Relative rate study of the kinetic isotope effect in the $^{13}CH_3D$ + Cl reaction. Chem. Phys. Lett. 605–606, 152–157. https://doi.org/10.1016/j.cplett.2014.05.022

Joelsson, L.M.T., Schmidt, J.A., Nilsson, E.J.K., Blunier, T., Griffith, D.W.T., Ono, S., Johnson, M.S., 2016. Kinetic isotope effects of $^{12}CH_3D$+OH and $^{13}CH_3D$+OH from 278 to 313K. Atmos. Chem. Phys. 16, 4439–4449. https://doi.org/10.5194/acp-16-4439-2016

Kai, F.M., Tyler, S.C., Randerson, J.T., Blake, D.R., 2011. Reduced methane growth rate explained by decreased Northern Hemisphere microbial sources. Nature 476, 194–197. https://doi.org/10.1038/nature10259

Labidi, J., Young, E.D., Giunta, T., Kohl, I.E., Seewald, J., Tang, H., Lilley, M.D., Früh-Green, G.L., 2020. Methane thermometry in deep-sea hydrothermal systems: Evidence for re-ordering of doubly-substituted isotopologues during fluid cooling. Geochim. Cosmochim. Acta 288, 248–261. https://doi.org/10.1016/j.gca.2020.08.013

Lalk, E., Pape, T., Gruen, D.S., Kaul, N., Karolewski, J.S., 2021. Clumped methane isotopologue-based temperature estimates for sources of methane in marine gas hydrates and associated vent gases 1–46.

Langenegger, T., Vachon, D., Donis, D., Mcginnis, D.F., 2019. What the bubble knows : Lake methane dynamics revealed by sediment gas bubble composition 1526–1544.

https://doi.org/10.1002/lno.11133

Leonte, M., Kessler, J.D., Kellermann, M.Y., Arrington, E.C., Valentine, D.L., Sylva, S.P., 2017. Rapid rates of aerobic methane oxidation at the feather edge of gas hydrate stability in the waters of Hudson Canyon, US Atlantic Margin. Geochim. Cosmochim. Acta 204, 375–387. https://doi.org/10.1016/j.gca.2017.01.009

Leonte, M., Wang, B., Socolofsky, S.A., Mau, S., Breier, J.A., Kessler, J.D., 2018. Using Carbon Isotope Fractionation to Constrain the Extent of Methane Dissolution Into the Water Column Surrounding a Natural Hydrocarbon Gas Seep in the Northern Gulf of Mexico. Geochemistry, Geophys. Geosystems 19, 4459–4475. https://doi.org/10.1029/2018GC007705

McGinnis, D.F., Greinert, J., Artemov, Y., Beaubien, S.E., Wüest, A., 2006. Fate of rising methane bubbles in stratified waters: How much methane reaches the atmosphere? J. Geophys. Res. Ocean. 111, 1–15. https://doi.org/10.1029/2005JC003183

Murase, J., Kimura, M., 1994. Methane production and its fate in paddy fields: Vi. Anaerobic oxidation of methane in plow layer soil. Soil Sci. Plant Nutr. 40, 505–514. https://doi.org/10.1080/00380768.1994.10413328

Nisbet, E.G., Dlugokencky, E.J., Manning, M.R., Lowry, D., Fisher, R.E., France, J.L., Michel, S.E., Miller, J.B., White, J.W.C., Vaughn, B., Bousequet, P., Pyle, J.A., Warwick, N.J., Cain, M., Brownlow, R., Zazzeri, G., Lanoiselle, M., Manning, A.C., Gloor, E., Worthy, D.E.J., Brunke, E.-G., Labuschagne, C., Wolff, E.W., Ganesan, A.L., 2016. Rising atmospheric methane: 2007-2014 growth and isotopic shift. Global Biogeochem. Cycles 5, 1–17. https://doi.org/10.1002/2015GB005204.Received

Ono, S., Wang, D.T., Gruen, D.S., Sherwood Lollar, B., Zahniser, M.S., McManus, B.J., Nelson, D.D., 2014. Measurement of a doubly substituted methane isotopologue, $^{13}CH_3D$, by tunable infrared laser direct absorption spectroscopy. Anal. Chem. 86, 6487–6494. https://doi.org/10.1021/ac5010579

Oremland, R.S., Miller, L.G., Whiticar, M.J., 1987. Sources and flux of natural gases from Mono Lake, California. Geochim. Cosmochim. Acta 51, 2915–2929. https://doi.org/10.1016/0016-7037(87)90367-X

Ostrovsky, I., D. F. McGinnis, L. Lapidus and W. Eckert. 2008. Quantifying gas ebullition with echosounder: The role of methane transport by bubbles in a medium-sized lake. Limnol. Oceanogr. - Methods. **6:** 105-118.

Peterson, E.J.R., 2005. Carbon and electron flow via methanogenesis, SO_4^{2-}, NO_3^-, and Fe^{3+} reduction in the anoxic hypolimnia of Upper Mystic Lake. Massachusetts Institute of Technology.

Pison, I., Ringeval, B., Bousquet, P., Prigent, C., Papa, F., 2013. Stable atmospheric methane in the 2000s: Key-role of emissions from natural wetlands. Atmos. Chem. Phys. 13, 11609–11623. https://doi.org/10.5194/acp-13-11609-2013

Prinzhofer, A., Pernaton, É., 1997. Isotopically light methane in natural gas: Bacterial imprint or diffusive fractionation? Chem. Geol. 142, 193–200. https://doi.org/10.1016/S0009-

2541(97)00082-X

R Core Team (2021). R: A language and environment for statistical computing. R Foundation for Statistical Computing, Vienna, Austria. URL http://www.R-project.org/.

Rehder, G., P. W. Brewer, E. T. Peltzer and G. Friederich. 2002. Enhanced lifetime of methane bubble streams within the deep ocean. Geophys. Res. Lett. **29:** 1731.

Rosentreter, J.A., Borges, A. V., Deemer, B.R., Holgerson, M.A., Liu, S., Song, C., Melack, J., Raymond, P.A., Duarte, C.M., Allen, G.H., Olefeldt, D., Poulter, B., Battin, T.I., Eyre, B.D., 2021. Half of global methane emissions come from highly variable aquatic ecosystem sources. Nat. Geosci. 14, 225–230. https://doi.org/10.1038/s41561-021-00715-2

Saunois, M., Stavert, A.R., Poulter, B., Bousquet, P., Canadell, J.G., Jackson, R.B., Raymond, P.A., Dlugokencky, E.J., Houweling, S., Patra, P.K., Ciais, P., Arora, V.K., Bastviken, D., Bergamaschi, P., Blake, D.R., Brailsford, G., Bruhwiler, L., Carlson, K.M., Carrol, M., Castaldi, S., Chandra, N., Crevoisier, C., Crill, P.M., Covey, K., Curry, C.L., Etiope, G., Frankenberg, C., Gedney, N., Hegglin, M.I., Höglund-Isaksson, L., Hugelius, G., Ishizawa, M., Ito, A., Janssens-Maenhout, G., Jensen, K.M., Joos, F., Kleinen, T., Krummel, P.B., Langenfelds, R.L., Laruelle, G.G., Liu, L., Machida, T., Maksyutov, S., McDonald, K.C., McNorton, J., Miller, P.A., Melton, J.R., Morino, I., Müller, J., Murguia-Flores, F., Naik, V., Niwa, Y., Noce, S., O'Doherty, S., Parker, R.J., Peng, C., Peng, S., Peters, G.P., Prigent, C., Prinn, R., Ramonet, M., Regnier, P., Riley, W.J., Rosentreter, J.A., Segers, A., Simpson, I.J., Shi, H., Smith, S.J., Steele, L.P., Thornton, B.F., Tian, H., Tohjima, Y., Tubiello, F.N., Tsuruta, A., Viovy, N., Voulgarakis, A., Weber, T.S., van Weele, M., van der Werf, G.R., Weiss, R.F., Worthy, D., Wunch, D., Yin, Y., Yoshida, Y., Zhang, W., Zhang, Z., Zhao, Y., Zheng, B., Zhu, Q., Zhu, Q., Zhuang, Q., 2020. The Global Methane Budget 2000--2017. Earth Syst. Sci. Data 12, 1561–1623. https://doi.org/10.5194/essd-12-1561-2020

Schaefer, H., Fletcher, S.E.M., Veidt, C., Lassey, K.R., Brailsford, G.W., Bromley, T.M., Dlugokencky, E.J., Michel, S.E., Miller, J.B., Levin, I., Lowe, D.C., Martin, R.J., Vaughn, B.H., White, J.W.C., 2016. A 21st-century shift from fossil-fuel to biogenic methane emissions indicated by 13CH4. Science (80-.). 352, 80–84. https://doi.org/10.1126/science.aad2705

Schwietzke, S., Sherwood, O.A., Bruhwiler, L.M.P., Miller, J.B., Etiope, G., Dlugokencky, E.J., Michel, S.E., Arling, V.A., Vaughn, B.H., White, J.W.C., Tans, P.P., 2016. Upward revision of global fossil fuel methane emissions based on isotope database. Nature 538, 88–91. https://doi.org/10.1038/nature19797

Sherwood, O.A., Schwietzke, S., Arling, V.A., Etiope, G., 2017. Global inventory of gas geochemistry data from fossil fuel, microbial and burning sources, version 2017. Earth Syst. Sci. Data 9, 639–656. https://doi.org/10.5194/essd-9-639-2017

Smemo, K.A., Yavitt, J.B., 2007. Evidence for anaerobic CH_4 oxidation in freshwater peatlands. Geomicrobiol. J. 24, 583–597. https://doi.org/10.1080/01490450701672083

Spliethoff, H.M., 1995. Biotic and abiotic transformations of arsenic in the Upper Mystic Lake. Massachusetts Institute of Technology.

Stell, A.C., Douglas, P.M.J., Rigby, M., Ganesan, A.L., 2021. The impact of spatially varying

wetland source signatures on the atmospheric variability of δD-CH_4. Philos. Trans. R. Soc. A Math. Phys. Eng. Sci. 379. https://doi.org/10.1098/rsta.2020.0442

Stolper, D.A., Lawson, M., Davis, C.L., Ferreira, A.A., Santos Neto, E. V., Ellis, G.S., Lewan, M.D., Martini, A.M., Tang, Y., Schoell, M., Sessions, A.L., Eiler, J.M., 2014a. Formation temperatures of thermogenic and biogenic methane. Science (80-.). 344, 1500–1503. https://doi.org/10.1126/science.1254509

Stolper, D.A., Lawson, M., Formolo, M.J., Davis, C.L., Douglas, P.M.J., Eiler, J.M., 2017. The utility of methane clumped isotopes to constrain the origins of methane in natural gas accumulations. Geol. Soc. London, Spec. Publ. 468, SP468.3. https://doi.org/10.1144/SP468.3

Stolper, D.A., Martini, A.M., Clog, M., Douglas, P.M., Shusta, S.S., Valentine, D.L., Sessions, A.L., Eiler, J.M., 2015. Distinguishing and understanding thermogenic and biogenic sources of methane using multiply substituted isotopologues. Geochim. Cosmochim. Acta 161, 219–247. https://doi.org/10.1016/j.gca.2015.04.015

Stolper, D.A., Sessions, A.L., Ferreira, A.A., Santos Neto, E. V., Schimmelmann, A., Shusta, S.S., Valentine, D.L., Eiler, J.M., 2014b. Combined ^{13}C-D and D-D clumping in methane: Methods and preliminary results. Geochim. Cosmochim. Acta 126, 169–191. https://doi.org/10.1016/j.gca.2013.10.045

Thanh Duc, N., Silverstein, S., Wik, M., Crill, P., Bastviken, D., Varner, R.K., 2019. Greenhouse gas flux studies: An automated online system for gas emission measurements in aquatic environments. Hydrol. Earth Syst. Sci. Discuss. 1–18. https://doi.org/10.5194/hess-2019-83

Turner, A.J., Frankenberg, C., Kort, E.A., 2019. Interpreting contemporary trends in atmospheric methane. Proc. Natl. Acad. Sci. U. S. A. 116, 2805–2813. https://doi.org/10.1073/pnas.1814297116

Varadharajan, C., 2009. Magnitude and spatio-temporal variability of methane emissions from a eutrophic freshwater lake 1–243.

Waldron, S., Lansdown, J.M., Scott, E.M., Fallick, A.E., Hall, A.J., 1999. The global influence of the hydrogen isotope composition of water on that of bacteriogenic methane from shallow freshwater environments. Geochim. Cosmochim. Acta 63, 2237–2245. https://doi.org/10.1016/S0016-7037(99)00192-1

Wang, D.T., Gruen, D.S., Sherwood Lollar, B., Hinrichs, K.U., Stewart, L.C., Holden, J.F., Hristov, A.N., Pohlman, J.W., Morrill, P.L., Könneke, M., Delwiche, K.B., Reeves, E.P., Sutcliffe, C.N., Ritter, D.J., Seewald, J.S., McIntosh, J.C., Hemond, H.F., Kubo, M.D., Cardace, D., Hoehler, T.M., Ono, S., 2015. Nonequilibrium clumped isotope signals in microbial methane. Science (80-.). 348, 428–431. https://doi.org/10.1126/science.aaa4326

Wei T, Simko V (2021). R package 'corrplot': Visualization of a Correlation Matrix. (Version 0.92), https://github.com/taiyun/corrplot.

Whitehill, A.R., Joelsson, L.M.T., Schmidt, J.A., Wang, D.T., Johnson, M.S., Ono, S., 2017. Clumped isotope effects during OH and Cl oxidation of methane. Geochim. Cosmochim. Acta 196, 307–325. https://doi.org/10.1016/j.gca.2016.09.012

Whiticar, M., Faber, E., 1986. Methane oxidation in sediment and water column environments -- Isotopic evidence. Org. Geochem. 10, 759–768.

Whiticar, M.J., 1999. Carbon and hydrogen isotope systematics of bacterial formation and oxidation of methane. Chem. Geol. 161, 291–314. https://doi.org/10.1016/S0009-2541(99)00092-3

Whiticar, M.J., Schoell, M., 1986. Biogenic methane formation in marine and freshwater environments: CO_2 reduction vs. acetate fermentation--Isotopic evidence. Geochim. Cosmochim. Acta 50, 693–709.

Whiting, G.J., Chanton, J.P., 1996. Control of the diurnal pattern of methane emission from emergent aquatic macrophytes by gas transport mechanisms. Aquat. Bot. 54, 237–253. https://doi.org/https://doi.org/10.1016/0304-3770(96)01048-0

Wik, M., Thornton, B.F., Bastviken, D., Uhlbäck, J., Crill, P.M., 2016. Biased sampling of methane release from northern lakes : A problem for extrapolation. AGU Publ. 1256–1262. https://doi.org/10.1002/2015GL066501.Received

Wik, M., Thornton, B.F., Varner, R.K., McCalley, C., Crill, P.M., 2020. Stable Methane Isotopologues From Northern Lakes Suggest That Ebullition Is Dominated by Sub-Lake Scale Processes. J. Geophys. Res. Biogeosciences 125. https://doi.org/10.1029/2019JG005601

Winkel, M., Sepulveda-Jauregui, A., Martinez-Cruz, K., Heslop, J.K., Rijkers, R., Horn, F., Liebner, S., Walter Anthony, K.M., 2019. First evidence for cold-adapted anaerobic oxidation of methane in deep sediments of thermokarst lakes. Environ. Res. Commun. 1. https://doi.org/10.1088/2515-7620/ab1042

Worden, J.R., Bloom, A.A., Pandey, S., Jiang, Z., Worden, H.M., Walker, T.W., Houweling, S., Röckmann, T., 2017. Reduced biomass burning emissions reconcile conflicting estimates of the post-2006 atmospheric methane budget. Nat. Commun. 8, 1–11. https://doi.org/10.1038/s41467-017-02246-0

Young, E.D., Kohl, I.E., Lollar, B.S., Etiope, G., Rumble, D., Li, S., Haghnegahdar, M.A., Schauble, E.A., McCain, K.A., Foustoukos, D.I., Sutclife, C., Warr, O., Ballentine, C.J., Onstott, T.C., Hosgormez, H., Neubeck, A., Marques, J.M., Pérez-Rodríguez, I., Rowe, A.R., LaRowe, D.E., Magnabosco, C., Yeung, L.Y., Ash, J.L., Bryndzia, L.T., 2017. The relative abundances of resolved $^{12}CH_2D_2$ and $^{13}CH_3D$ and mechanisms controlling isotopic bond ordering in abiotic and biotic methane gases. Geochim. Cosmochim. Acta 203, 235–264. https://doi.org/10.1016/j.gca.2016.12.041

Yvon-Durocher, G., Allen, A.P., Bastviken, D., Conrad, R., Gudasz, C., St-Pierre, A., Thanh-Duc, N., Del Giorgio, P.A., 2014. Methane fluxes show consistent temperature dependence across microbial to ecosystem scales. Nature 507, 488–491. https://doi.org/10.1038/nature13164

Zheng, Y., Wu, S., Xiao, S., Yu, K., Fang, X., Xia, L., Wang, J., Liu, S., Freeman, C., Zou, J., 2022. Global methane and nitrous oxide emissions from inland waters and estuaries. Glob. Chang. Biol. 4713–4725. https://doi.org/10.1111/gcb.16233

Chapter 5

Development of a method to quantify in situ methane concentration based on dissolved gas ratios: A case study from the Scotian Slope

ABSTRACT

The concentration of methane in gas-rich sediments is historically difficult to quantify due to depressurization and free gas formation ("void gas") during sample retrieval. We test whether the accurate measurement of the ratios of dissolved gases (CH_4, N_2, and Ar) can be used to estimate the extent of core degassing, and, further, to constrain the *in situ* methane concentration. The method relies on the relative differences in the solubilities of molecules to control the fractionation between dissolved and gas phases. The quantification of resultant gas ratios may thus yield information about the extent of degassing. We test this method using gas-rich sediment from seep sites on the Scotian Slope, and results are compared to those of four other methods used to estimate methane concentration, including: standard headspace analysis, the volume of the void gas, ratios of N_2, Ar, and CH_4 in void gas, and the upper-limit of methane concentration from the saturation solubility of methane at *in situ* conditions using an equation of state. Methane concentrations estimated from both void gas-based measurements agreed, which is significant because the volume dissolution method has not been previously validated. These methods also indicate core degassing as much as ca. 70-80%. We were unable to determine *in situ* methane concentration by quantifying the composition of dissolved gas in porewaters. Comparison between CH_4/Ar of the void gas and dissolved gas in porewaters shows that these gas pools are not maintained in chemical equilibrium, and significant methane degassing occurs between void formation and sample processing. Additionally measured N_2/Ar values deviate significantly from values predicted by fractionation according to the molecules relative solubilities, and thus cannot be used to constrain the extent of degassing. This observation is further supported by the volumes of N_2 and Ar extracted from porewaters, which match predicted yields for air-equilibrated seawater, while degassed core is expected to have relatively lower yields. Additionally, O_2 reacts quickly in reduced sediments, limiting the ability to remove air contamination artifacts and thus precisely constrain the volumes and ratios of N_2 and Ar. System modifications and further testing are required to employ this method to quantify *in situ* methane concentrations, but currently, it can validate methane concentration data from standard headspace analysis.

Collaborators on this work include:

Ellen Lalk, Arthur Spivack, David T. Wang, and Shuhei Ono

5.1 INTRODUCTION

Methane (CH_4) is a potent greenhouse gas and product of subseafloor microbial metabolisms and thermal cracking of large organics. Quantification of methane abundance in the seafloor is important to understand the energetic environment in which subsurface biology and biochemistry functions. However, standard methods (i.e., headspace analysis) of extracting and determining concentrations of dissolved methane fail in gas-rich and poorly competent sediments. The decrease of hydrostatic pressure and increase of temperature associated with transporting gas-bearing sediment from the seafloor to the surface both reduce methane solubility in water, causing free gas formation. As a result, gas pockets form in core liners ("void gas"). Thus, methane concentration measurements from headspace analysis have the potential to significantly underestimate *in situ* values.

Several methods have been developed to improve the accuracy of methane concentration measurements, including technological innovation to avoid depressurization during core retrieval, and leveraging proxies based on porewater and gas chemistry. For example, the pressure core sampler was developed to recover and maintain sediments under *in situ* pressure, particularly to recover hydrate-rich sediments (Abegg and Anderson, 1997; Dickens et al., 2000; Heeschen et al., 2007; Paull et al., 2000). The earliest versions of this device were deployed in shallow sediments with the assistance of divers (Abegg and Anderson, 1997). Versions of this tool have since been developed to interface with the operations of the Deep Sea Drilling Project and the International Ocean Drilling Program, and can be deployed as deep as 6500 m below the water surface (Li et al., 2016). However, this device can collect only ca. 39 inches of core at a time, meaning that pressurized sampling is possible as spot coring only. Additionally, this method requires a specialty platform and expertise to operate, limiting its use as a standard technique.

For shallow sediments, freeze coring techniques have also been developed avoid sudden degassing (e.g., Pachur et al., 1984), however not without core disturbance (Dück et al., 2019). This technique requires a coring device that can be filled with a coolant such as dry ice or liquid nitrogen (Pachur et al., 1984). A limitation of this method is that it can be applied only to surface sediments at shallow water depths, and is better suited for freshwater systems than deep marine environments.

Chemical indicators have also been used to infer the presence and volume of hydrate and free gas in sediments. Porewater chlorinity is one proxy used to infer the presence of hydrate in marine sediments (Hesse and Harrison, 1981). The dissociation of gas hydrate releases water and methane into interstitial pores, thus diluting the concentration of chloride ions in porewaters (i.e., "freshening"). The relative amplitude of chloride concentration anomalies is proportional to the amount of gas hydrate that dissociated during core recovery. However, the process of hydrate formation concentrates chloride ions in porewater, as they are selectively excluded from the hydrate lattice. This method requires that enough time passed since hydrate formation for elevated porewater chlorinity to diffuse to background seawater concentrations. Additionally, this method cannot yield quantitative porewater methane concentrations.

An additional method was presented by Spivack et al. (2006) to quantify *in situ* methane concentrations in gas-rich sediments using the relative abundance of CH_4, N_2, and Ar in void gas. This method assumes that Ar and N_2 are inert in the deep subsurface and relies on the deviation of N_2/Ar from *in situ* values to estimate the extent of core degassing, which then allows for the estimation of pre-degassing CH_4 concentrations. Due to the differences in solubility between N_2 and Ar, these molecules are expected to fractionate differently between dissolved and gas phases, according to Henry's Law. Thus, by measuring the ratio of N_2/Ar in pore water and void gas, one could estimate the extent of degassing. End-member constraints on expected values for N_2/Ar and CH_4/Ar can be calculated via two degassing models: 1) equilibrium degassing, in which the void gas is created in equilibrium with the entire pool of degassing fluid, and 2) fractional degassing, in which void gas is removed from the pool of degassing fluid immediately upon formation (**Figure 5.5**). A limitation of this method is that it requires sampling of void gas, which may be lost during core retrieval, inaccessible to the outside of the core liner, or too small to reasonably sample.

In this study we test whether the quantification of remaining gases (CH_4, N_2, and Ar) dissolved in porewaters could serve as a high-fidelity indicator for *in situ* methane concentration. The goal of the method is to measure *in situ* methane concentration without specialty sampling equipment or additional ship time. We develop a sediment degasser interfaced with a quadrupole mass spectrometer (QMS) to quantify gas volumes and ratios (N_2, Ar, CH_4, and O_2) from sediment porewater concentrations. We compare five estimates of methane concentration for

marine sediments collected from three seep sites on the Scotian Slope, including: 1) standard headspace concentration quantification (e.g., Morono et al., 2017), 2) volumes of void gas and porewater, 3) ratios of N_2, Ar, and CH_4 in void gas (Spivack et al., 2006), 4) maximum concentration from gas phase saturation and *in situ* conditions (Duan et al., 1992), and 5) the ratios of N_2, Ar, and CH_4 in remaining porewater. In addition to improving constraints on *in situ* methane concentration, the ability to extract and quantify ratios of dissolved gases in sediment porewaters has broader implications as a means to access proxy records of past CO_2 equilibration between the ocean and atmosphere. For example, ratios of noble gases in deeply buried porewaters may preserve information about past fluctuations in air-sea gas exchange (e.g., Stanley et al., 2009).

5.2 DEVELOPMENT OF A QUADRAPOLE MASS SPECTROMETER INLET SYSTEM AND SEDIMENT DEGASSER

5.2.1 Quadrapole mass spectrometer inlet system

A quadrapole mass spectrometer (QMS) was interfaced with a vacuum line and sediment degasser (**Figure 5.1**) to analyze ratios of dissolved gases from porewaters. The QMS is a Stanford Research Systems Closed Ion Source Gas Analyzer (SRS CIS 200) with an electron multiplier detector. The QMS is set to measure masses 15 (methane), 18 (water), 28 (N_2), 32 (O_2), and 40 (Ar). The system is designed so that the signal size of the sample measurement is 100-1000 times greater than the background.

The inlet system has three sample introduction ports for: 1) a reference gas mixture (35.7% methane in air), 2) an interface with the sediment degasser, and 3) a septum port for samples (e.g., void gas) introduced via syringe. The sample volumes associated with each of these ports can be adjusted to accommodate sample gas concentration. Gas introduced through all ports passes through a U-trap, which is submerged in liquid nitrogen to remove H_2S, CO_2 and water. The reference gas gets loaded into a bellow volume, where volume is programed to adjust to match the pressure of the sample gas throughout the measurement cycles. Sample gas from either the sediment degasser or septum port gets loaded into a cold finger with a silica gel active phase and submerged in liquid nitrogen to concentrate the gas volume. Before a measurement cycle, the cold-finger is heated to 60°C. The measurement sequence consists of 8 cycles of sample-standard bracketing, for which gas is introduced to the QMS for 100 seconds. The QMS

is backed by a turbopump, which additionally vacuums the introduction volume between measurements.

The inlet system can additionally be used to concentrate the headspace of the degasser for applications like methane purification and isotopologue characterization. A U-trap filled with silica gel can be submerged in liquid nitrogen and backed by a vacuum pump so that the contents of the sediment degasser get slowly pulled through (**Figure 5.1**). Gas can then be extracted from the system by cryogenically concentrating the contents of the U-trap into an exterior vial through the exit port.

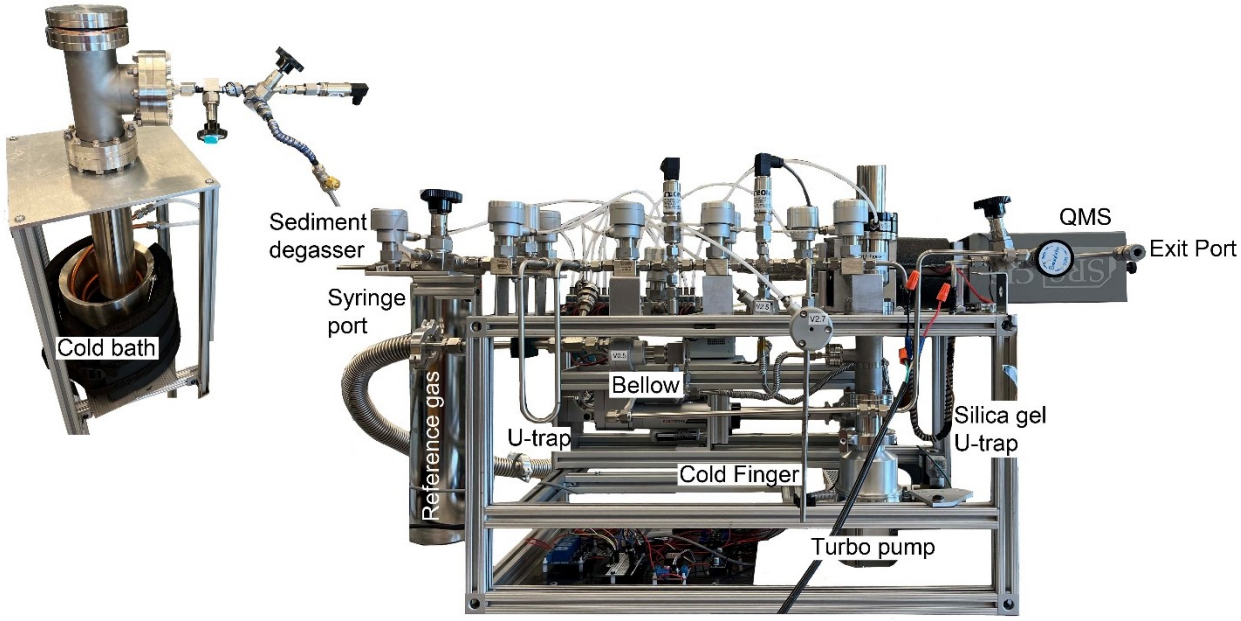

Figure 5.1: Sediment extractor interfaced with an inlet system and quadrapole mass spectrometer (QMS).

5.2.2 Sediment degasser

A logistical challenge of using N_2 and Ar abundances is the potentially significant contamination from air. A 2.8 L stainless-steel vessel with a ConFlat® lid was developed to provide an air-tight environment to degas sediment samples (**Figure 5.1**). This vessel yielded no detectable air leak over the course of a month, making it sufficient to hold a vacuum environment for 1-3 days of sediment degassing. Before extraction, the degasser is placed under vacuum overnight and then filled with research grade CO_2 (ca. 1.1 bar), which is meant to limit

the amount of air in the system when the sample is introduced. The bottom of the sediment degasser is then submerged in a cold bath (60% ethanol in water) and chilled to ca. -20℃ for one hour. The sample is placed in the chilled degasser, sealed with a copper O-ring and ConFlat® flange, and placed under vacuum for 15 minutes. A subsample of the degasser headspace is then analyzed to serve as a background measurement. The degasser is isolated from the rest of the inlet system, and heated to 60℃ to extract the dissolved gases. The pressure in the reactor is continuously monitored with a pressure gauge to detect leaks and degassing progress.

We also tested the use of Calibrated Instruments 5-Layer Cali-Bond bags and a glass degasser with an O-ring seal (**Figure 5.S1**); however, these systems had comparably high leakage rates, and gas ratio artifacts. Additionally, some modifications to the current system were tested to increase signal size. For example, use of a shorter vessel can decrease the headspace volume from 2.8 L to 1.2 L.

5.2.3 Signal processing

The raw QMS data is processed by calculating the signal and background mean from each measurement, after removing the first and last 0.3 minutes of signal to remove artifacts associated with gas introduction and removal from the QMS. The background mean was subtracted from each signal. We then used reference gas measurements to correct the signal magnitudes of the sample gases. The signal size of each gas component in the reference gas was normalized to its concentration in the reference gas, and the sample gas signal was then divided by this correction factor. Next, the reference-corrected oxygen signal size was used to account for air contamination. The ratio of N_2 or Ar to O_2 in the atmosphere is used to proportionally subtract air-derived N_2 and Ar from their signal sizes. This correction is summarized by the following equation, using N_2 as an example:

$$S_{N2-corrected} = \frac{(S_{N2-sample} - S_{N2-background})}{(S_{N2-reference} - S_{N2-background})/0.507} - \frac{0.78}{0.21}\frac{(S_{O2-sample} - S_{O2-background})}{(S_{O2-reference} - S_{O2-background})/0.137}$$

Where: $S_{N2\text{-}corrected}$ – the reference and oxygen corrected signal size of N_2 in the sample

$S_{N2\text{-}sample}$– the raw QMS signal size of N_2 in the sample gas

$S_{N2\text{-}reference}$– the raw QMS signal size of N_2 in the reference gas

$S_{N2\text{-}background}$– the raw QMS signal size of N_2 in the background

$S_{O2\text{-}sample}$– the raw QMS signal size of O_2 in the sample gas

$S_{O2\text{-}reference}$– the raw QMS signal size of O_2 in the reference gas

$S_{O2\text{-}background}$– the raw QMS signal size of O_2 in the background

The fractional abundance of N_2, CH_4, and Ar in gas samples is calculated by taking the signal size of each component over the sum of all signal sizes for each sample. The average fractional abundance for all sample measurements in a run is taken and used to estimate methane concentration. Typically, the measurement noise is ca. 4-5% of the signal size for CH_4, 3-4% of the signal size for N_2, and 2-4% of the signal size for Ar.

5.2.4 Ice cube validation

The use of the sediment degasser interfaced with the QMS inlet system was validated by measuring the ratio of N_2/Ar in an ice cube (**Table 5.S1**). At near freezing temperatures, air-equilibrated freshwater has a dissolved N_2 concentration of 830.5 μM/kg and a dissolved Ar concentration of 22.3 μM/kg. Thus, the N_2/Ar in an ice cube is expected to be 37.2.

The ice cube was melted in the sediment degasser, following the protocol described in **section 5.2.2**, and signal processing following **section 5.2.3** except for the O_2-correction step. Notably, as the ice cube is expected to contain dissolved oxygen, small amounts of air contamination or trapped bubbles cannot be accounted for using O_2 abundance. We measured N_2/Ar after complete melting of the ice cube as 39.4. This is considered to reasonably match the theoretical prediction of 37.2.

5.3 MATERIALS AND SAMPLING PROTOCOLS

5.3.1 Scotian Slope Seeps

The Scotian Slope is a passive margin located in the northwest Atlantic, off-shore Nova Scotia in eastern Canada. This area shows evidence of potential hydrocarbon seepage with the occurrence of pockmarks, diapirs, and polygonal faults, observed from seafloor bathymetry and seismic reflection data (Campbell, 2019). Recent efforts to characterize the source of hydrocarbon seepage show isotope and biomarker evidence for thermogenic hydrocarbons in some locations, in addition to many sites fueled by microbial methanogenesis (Fowler et al., 2018).

Sediment and void gas samples were collected from the Scotian Slope on the *Atlantic Condor* during August 2021 (**Figure 5.2a**). Sample sites were chosen based on seafloor bathymetry as having features characteristic of active and paleo cold seeps. Push core samples were collected using a Remotely Operated Vehicle (ROV). Three push core samples (core 3, core 65, and core 66) were selected for this study due to the presence of large (>10 mL) void gas pockets.

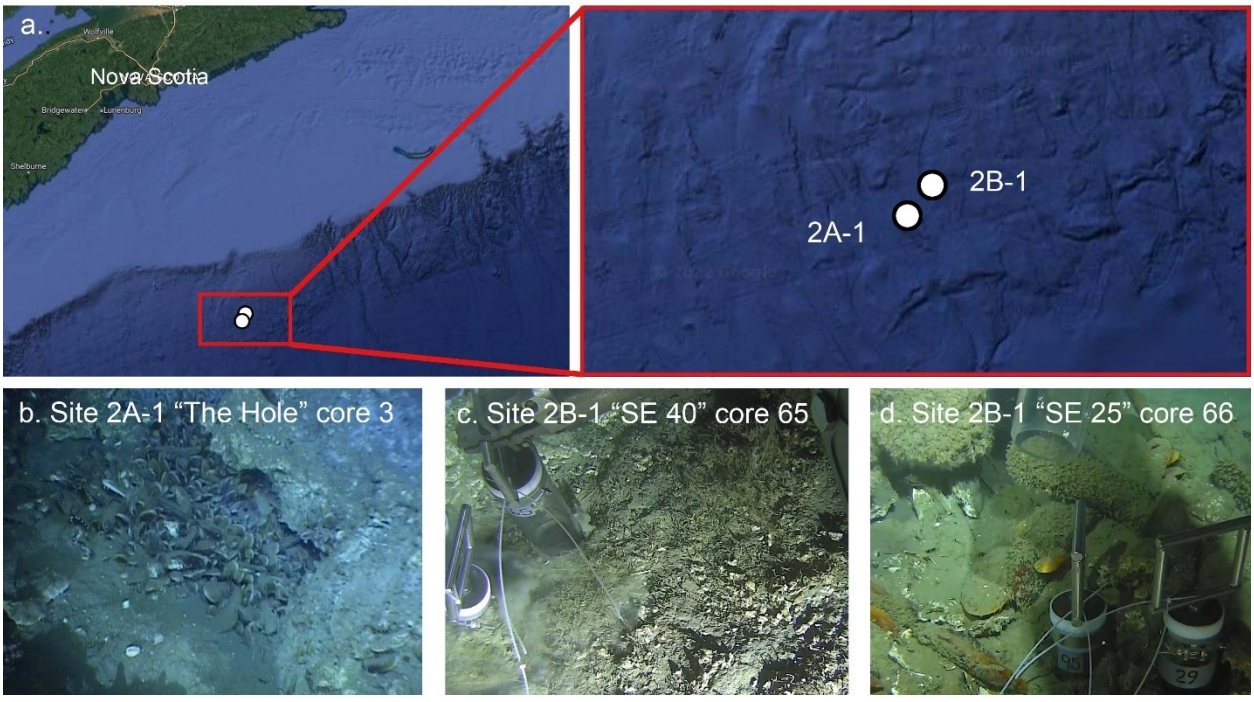

Figure 5.2: **a** Map of site location along the Nova Scotian slope. The seafloor at the sampling location of **b** core 3, **c** core 65., and **d** core 66.

Core 3 was sampled from 'The Hole' at site 2A-1 (lat: 42.162689, long: -62.372356), which is at 2687 m water depth. This site is characterized by abundant clam beds and nearby bubble streams (**Figure 5.2b**). The top 6 cm of this core consists of light brown, fine-textured sediment. Sediment from 6-14 cm is a medium/dark grey, and from 14-18 cm is a light grey, cracked sediment. From 18-32 cm there is a large central void pocket, followed by more light grey, cracked sediment from 32-42 cm (**Figure 5.3a**).

Cores 65 and 66 were sampled from a transect at site 2B-1. Core 65 was sampled from 'SE 40m' (lat: 42.207639, long: -62.323819), which is at 2782 m water depth. This site is characterized by thin coverage by filamentous growth (**Figure 5.2c**). The top 3 cm of the core are light brown and bulbous from gas bubbles pushing up on the sediment, and covered by a filamentous microbial mat. Degassing from the top of this core was observed on deck. From 4-12 cm, sediment is grey-brown and fine-textured, from 12-16 cm the sediment is medium grey and fine-textured, and from 16-40 cm the sediment is light grey with a bubbly-cracked texture (**Figure 5.3b**).

Core 66 was sampled from 'SE 25m' (lat: 42.204979, long: -62.326410), which is at 2784 m water depth. This site had dead clam shells and debris, but no active clam beds (**Figure 5.2d**). The top 4 cm of this core are a light brown, fine texture sediment, followed by a fine-textured, medium-grey interval from 4-8 cm. From 10-13 cm sediment is light grey and clay-like, with evidence of gas cracking. There is a void pocket from ca. 13-18cm, and then from 18-40 cm, sediment is light grey, cracked, and clay-like (**Figure 5.3c**).

5.3.2 Shipboard sampling methods

5.3.2.1 Sediment for headspace analysis

Sampling for methane concentration quantification by headspace analysis was conducted based on the protocol from the IODP 370 methods (Morono et al., 2017). A 10 mL syringe was modified by removing the tip with a saw, and used to subsample ca. 5 mL of sediment. The sediment plug was then extruded into a 20 mL serum vial, which was pre-filled with 2 glass beads and 5 mL 1M NaOH (bactericide). Vials were sealed with pre-treated (cleaned in a 1M KOH bath, and rinsed overnight) blue butyl septa (Oremland et al., 1987), and then manually shaken and stored at 4^{o}C.

5.3.2.2 Void gas

Void gas collection was the first sampling procedure conducted after core description. Cores were secured on the lab bench and the lowest point of the gas pocket was marked. A handheld drill with a 1/16” drill bit and drill bit stop collar was pierced through a rubber septum to secure the hole in case the piercing was made completely. The stop collar was positioned so that the drill would go through all but 1 mm of core-liner. While holding the septum to the core liner, the drill bit was removed, and a needle attached to a 50 mL syringe was used to pierce through the remaining core liner and sample the void pocket. Samples were transferred from the syringes to long-term storage in pre-evacuated 50 mL serum bottles, which were sealed with pre-treated (cleaned in a 1M KOH bath, and rinsed overnight) blue butyl septa (Oremland et al., 1987).

5.2.2.3 Sediment for gas ratio analysis

Sediments for gas ratio analysis were also sampled based on the protocol from the IODP 370 methods (Morono et al., 2017). The sediment section immediately above and below the void pocket were targeted. The core was manually extruded from the core-liner, and sectioned into 1-2 cm whole round core subsamples. Samples were placed in petri dishes, heat sealed into gas barrier film, and then immediately stored at -80^{o}C.

5.4 METHODS FOR ESTIMATING METHANE CONCENTRATION

5.4.1 Standard headspace analysis

Samples were sonicated for 15 minutes prior to extracting headspace gas. For each sample, 0.3 mL of gas was quantified at least twice using a Shimadzu GC-2014 gas chromatograph. The GC was equipped with a packed column (Carboxen—1000, 5’ x 1/8”), and operated at a temperature of 90^{o}C, where helium served as the carrier gas. Measurements were calibrated using reference gas mixtures (SCOTTY®).

Sampling exact volumes of sediment into vials was challenging due to the different competencies of sediments. In order to verify the volume of sediment and porewater collected, we back calculate sediment volume with measurements of headspace volume and the known volume of liquid added to vials. To estimate headspace volume, vials were sonicated for 15 minutes, so that sediment settled to the bottoms of the vials. The height of headspace in the vial

was measured and compared to a standard curve (**Figure 5.S2**) to estimate headspace volumes in mL. The volume of sediment and porewater collected was then estimated by subtracting the headspace volume and 5 mL (from known addition of 5mL 1M NaOH) from the total vial volume of 19.6 mL. The volume of pore-water in each vial is calculated assuming a range of porosity between 0.6(low porosity of surface sediments) and 1(upper limit).

The concentration of methane was calculated using the following equation:

$$[CH_4]_0\ (mM) = 1000 * \frac{X_{CH4} * P_{atm} * V_H}{R * T * V_{PW}}$$

Where: X_{CH4} – Concentration of CH_4 in headspace

P_{atm} – Pressure of sample (1 atm for all sediment samples)

V_H – Volume of headspace in vial

R – Gas constant (0.082057 L*atm/K*mol)

T- Temperature in K

V_{PW} – Volume of pore-water in vial

5.4.2 Dissolution of void gas in porewater

This concentration quantification method uses the results from the standard headspace analysis (**section 5.4.1**), the volume of the void gas, and the volume of porewater to estimate the concentration of methane if the gas void was re-dissolved into the porewater. For this method, only volumes of methanogenic sediment and porewater are considered, as this is the most likely source of dissolved methane. Thus, the light brown sections of cores above the putative sulfur-methane transition zone (SMTZ) are excluded from the volume of porewater (**Figure 5.3**).

The volume of void pockets was estimated before sampling, by measuring the height of the void pocket. We later estimate void gas volume more precisely by digitally analyzing photos of the sediment cores. Displaced sediment from void gas formation had clean boundaries, such that the void pocket cut across the core liner. We use WebPlotDigitizer to trace the boundaries of sediment along the void spaces and estimate an average height of the void pocket (Rohatgi, 2022). The core liners have an inner diameter 3.5 inches, and 1 cm length of core is 62.1 mL gas

at standard temperature and pressure. It is possible that these cores are somewhat overpressure, thus this volume of gas is considered a minimum estimate.

Initial methane concentration is calculated:

$$[CH_4]_0\ (mM) = [CH_4]_{headspace} + 1000 * \frac{\frac{V_{void\ gas}}{22.4}}{V_{pore\ water}}$$

Where $[CH_4]_{headspace}$ is the concentration estimate from standard headspace analysis, $V_{void\ gas}$ is the volume of the void pocket, and $V_{porewater}$ is the volume of methanogenic porewater in the core. 22.4 is the liters of ideal gas for 1 mon at 25ºC.

Figure 5.3: Push cores images used for image analysis to estimate void gas volume for **a** core 3, **b** core 65, and **c** core 66. The red points are used to define the upper and lower boundaries of the void pockets.

5.4.3 Void gas composition

Subsamples (0.3-0.5 mL) of void gas samples were measured using the QMS to assess the abundance of CH_4, N_2, Ar and O_2. Samples were syringe-injected into the QMS inlet septum

port, and frozen into the cold finger. The cold finger was then heated to 60°C before starting the analysis method for sample-standard bracketing. Data processing was conducted as described in **section 5.2.3**.

Methane concentration is then calculated using the equation reproduced from Spivack et al., 2006:

$$[CH4]_0 = (\frac{[N_2]_0 X_{CH4}}{X_{N2}})(\{K_H^{CH4} + [([N_2]_0 X_{Ar} K_H^{Ar} - [Ar]_0 X_{N2} K_H^{N2})/([Ar]_0 X_{N2} - ([N_2]_0 X_{Ar})]\}/\{K_H^{N2} + [([N_2]_0 X_{Ar} K_H^{Ar} - [Ar]_0 X_{N2} K_H^{N2})/([Ar]_0 X_{Ar} - [N_2]_0 X_{Ar})]\})$$

Where: K_H^{CH4} is Henrys constant for methane and set as 0.000893

K_H^{N2} is Henrys constant for N_2 and set as 0.000416

K_H^{Ar} is Henrys constant for Ar and set as 0.000918

$[N_2]_0$ is the initial *in situ* concentration of N_2 and set as 0.000432 M

$[Ar]_0$ is the initial *in situ* concentration of Ar and set as 0.0000126 M

X is the fraction of each component in the sample gas.

The theoretically predicted N_2/Ar ratios associated with different extents of core degassing are shown in **Figure 5.5a**. Void gas formed from < 20% core degassing is expected to have N_2/Ar > 70, while void gas formed from > 60% core degassing is expected to have N_2/Ar < 50. CH_4/Ar is expected to increase with greater extents of degassing, and change by < 10%.

5.4.4 Porewater dissolved gas composition

Following the protocol described in **section 5.2.2**, the sediment degasser was prepared, and the frozen sediment sample was placed on a pre-chilled stainless-steel platform and lowered into the vessel. The degasser was then vacuumed for 15 minutes, and a background measurement was made. The cold bath was removed from the degasser and after 1 hour another subsample was measured. Then, a heat gun was used to expedite degassing of the core, until pressure in the vessel plateaued. Another timepoint was measured at 2 hours, and then again at the 24 hour mark.

The theoretically predicted N_2/Ar ratios of dissolved gas in porewater associated with different extents of core degassing are shown in **Figure 5.5a**. Dissolved gas left after < 20% core degassing is expected to have N_2/Ar > 30, while dissolved gas left after > 80% core degassing is expected to have N_2/Ar < 20. CH_4/Ar values of void gas and dissolved gas are expected to differ by less than ca. 10% (**Figure 5.5b**), although the value of this ratio will vary between sites as a function of the methane concentration. Code used to produce the evolution of gas ratios with different extents of degassing is provided in **section 5.9.1.4**.

5.4.5 Methane solubility from the equation of state

The maximum concentration of dissolved methane in porewater is calculated using the gas phase saturation for *in situ* pressure and temperature conditions (Duan et al., 1992). For all cores, we assume a bottom water temperature of 4°C. The hydrostatic pressure is 270 bar for site 2A-1 core 3, 278.3 bar for site 2B-1 core 65, and 278.2 bar for site 2B-1 core 66. We use the following concentrations of salt for this calculation: 0.5405 mol/kg Cl, 0.4645 mol/kg Na, 0.01011 mol/kg Ca (Duan et al., 1992).

5.5 RESULTS

Methane concentrations from headspace analysis, dissolution of void gas in porewater, void gas composition, and the *in situ* methane saturation limit are summarized in **Table 5.1**. The results from the porewater dissolved gas composition are excluded from this table, as they did not yield an *in situ* methane concentration estimate; gas ratios from this analysis are reported in **Table 5.3**.

5.5.1 Standard headspace analysis

Methane concentrations based on headspace analysis are between ca. 0-4.5 mM (**Table 5.1**, **Figure 5.4**). The lowest methane concentrations are found in the shallowest sediment (typically < 8 cm), while the highest methane concentrations are found within the bottom 4 cm of core and near the void gas. All three cores yield similar methane concentrations by this measurement. Additional headspace methane concentration data for other sites on the Nova Scotian Slope can be found in **Table 5.S2**.

Sample	[CH_4] (mM)				
	Headspace (Φ=1)	Headspace (Φ=0.6)	Void Gas Dissolution	Void Gas Composition	Saturation solubility
Core 3					
8	0.20	0.33			
13	1.22	2.03			
Void			30±5 (49±5)	41 ±1.5	230
42	0.71	1.19			
Core 65					
4	0	0			
8	0	0			
12	0.91	1.51			
Void			9±2	11 ±2	234
28	0.60	1.00			
32	0.71	1.19			
36	0.82	1.37			
39	2.05	3.42			
Core 66					
4	0.31	0.52			
8	0.48	0.79			
Void			12±3	15 ±1	234
24	2.71	4.52			
28	0.89	1.49			
32	0.90	1.51			
36	1.00	1.66			
40	0.80	1.34			

Table 5.1: Summary of methane concentrations in mM, using four quantification methods. Values from standard headspace analysis are calculated using porosities of 1 and 0.6 (**section 5.5.1**). Void gas dissolution shows results from **section 5.5.2**. Void gas composition shows results from **section 5.5.3**. Saturation solubility represents the maximum amount of methane that can be dissolved in porewaters at the seafloor (**section 5.5.5**).

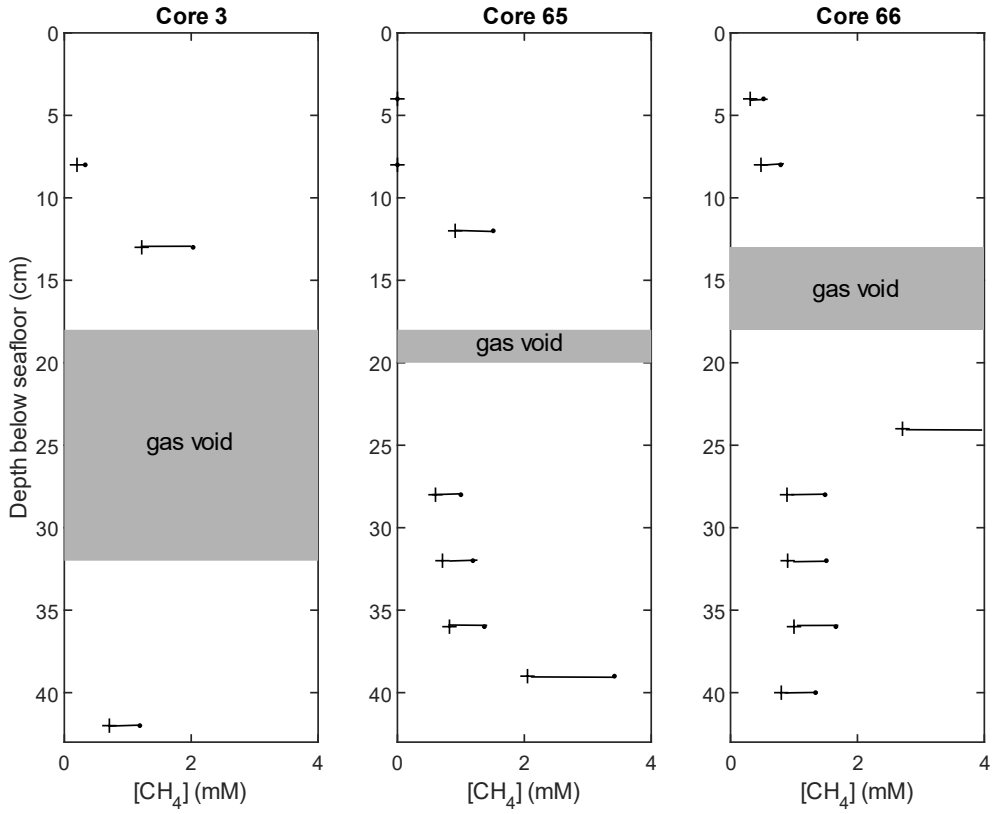

Figure 5.4: Depth profiles from the headspace analysis method of methane quantification for cores 3, 65, and 66. Plus symbols are for a porosity of 1 (an upper bound), and circles are for a porosity of 0.6 (a lower bound for surface sediments).

5.5.2 Dissolution of void gas in porewater

Methane concentrations estimated from dissolution of the void gas in porewaters are between ca. 9 and 50 mM (**Table 5.1**). Core 3 is estimated to have an *in situ* methane concentration that is 3-4 times greater than that of cores 65 and 66. The volume of pore-water is estimated using measurements of the wet weight (123.5 g) and dry weight (75.3 g) of a 1.3 cm length whole round core from site 2A-1 core 3, which corresponds to ca. 47 mL of porewater. Assuming a sediment density of 3 g/cm^3, the porosity of this sediment is about 0.68.

For site 2A-1 core 3, *in situ* methane concentration is estimated to be between 30.8 and 49.4 mM. An average length of 13.9 cm of void space (863 mL gas) is measured by image analysis (**Figure 5.3a**), which closely matches the estimated 14 cm measured upon core retrieval.

We estimate 22.1 cm of methanogenic sediment corresponding to 799 mL porewater; however, some core was expelled into the basket from the bottom of this core due to the large void space created during degassing. If we assume the void gas displaced methanogenic sediment from the bottom of the core, the void gas may have derived from up to 36 cm of core and 1300 mL porewater.

For site 2B-1 core 65, *in situ* methane concentration is estimated to be 9.2 mM. An average length of 2.42 cm of void space (150 mL gas) is measured by image analysis (**Figure 5.3b**), which is within the range of 2-3 cm observed upon core retrieval. The length of methanogenic sediment is 24.58 cm, corresponding to ca. 889 mL porewater.

For site 2B-1 core 66, *in situ* methane concentration is estimated to be 12.0 mM. An average length of 4.21 cm of void space (261 mL gas) is measured by image analysis (**Figure 5.3c**), which is within the range of 4-5 cm observed upon core retrieval. 31.79 cm of vertical sediment (1149 mL porewater) is estimated to be in the methanogenic zone.

Uncertainties in concentrations are estimated to have a lower bound based on a sediment porosity of 0.85, which is more typical of surface sediments than our measurement of 0.68. Upper bounds of estimated uncertainty are based on the void gas being slightly over pressure (ca. 1.25 bar).

5.5.3 Void gas composition

	X_{CH4}	X_{N2}	X_{Ar}	N_2/Ar	CH_4/Ar	$f_{N2,\ remaining}$	$[CH_4]_0$ (mM)
Core 3	0.985	0.0145	0.00030	48.5 ± 4	3290 ± 120	0.319	40.8 ± 1.5
Core 65	0.950	0.0490	0.00104	46.9 ± 2	935 ± 150	0.286	11.3 ± 2.0
Core 66	0.966	0.0333	0.00080	42.0 ± 4	1220± 78	0.182	15.1 ± 1.0

Table 5.2: Gas ratios of void gases collected from cores 3, 65, and 66. $f_{N2,\ remaining}$ is a proxy for the extent of core degassing estimated from the deviation of N_2/Ar from that of bottom water. Values of *in situ* methane concentration ($[CH_4]_0$) are calculated as described in **section 5.4.3**.

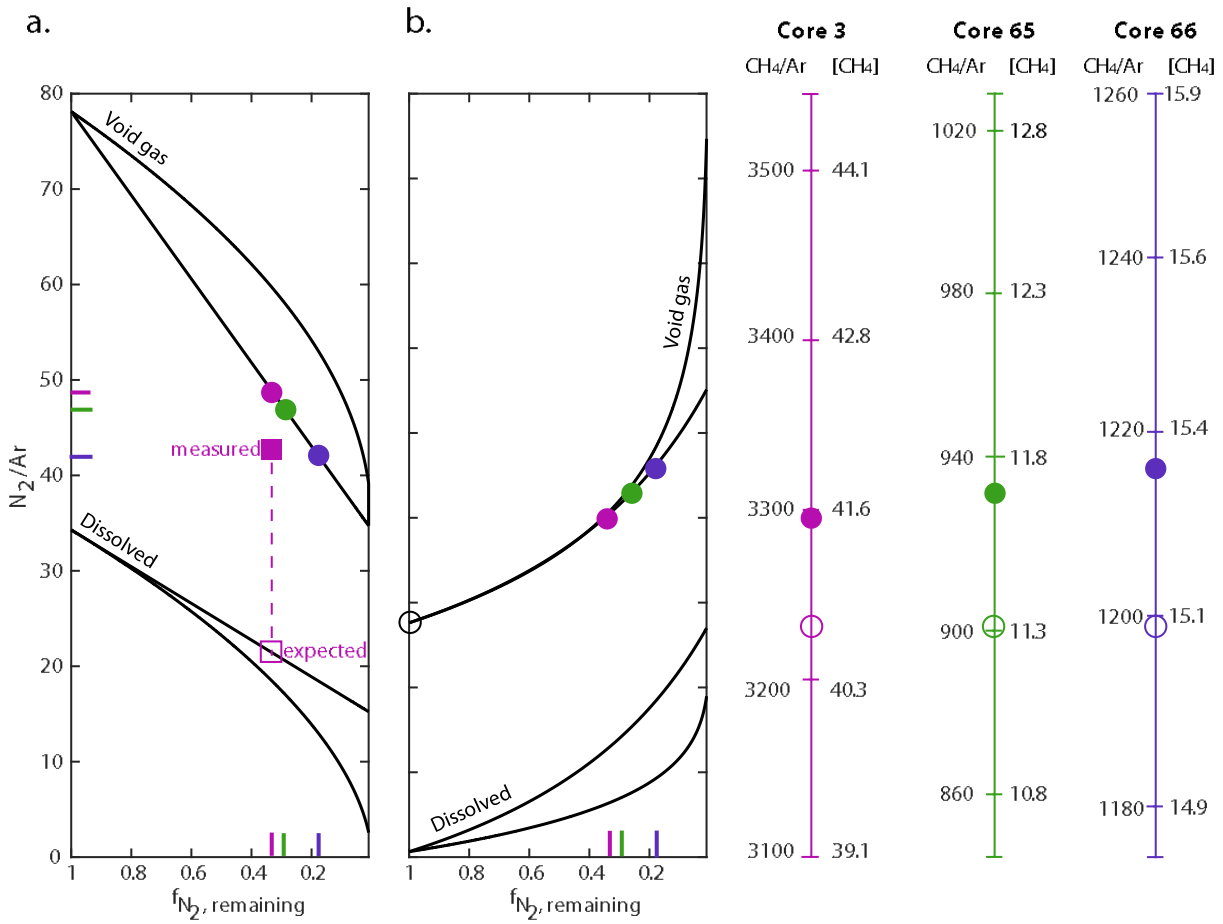

Figure 5.5: Predicted and measured values of **a** N_2/Ar and **b** CH_4/Ar for different extents of core degassing ($f_{N2,\ remaining}$). The top two black lines represent the expected ranges in gas ratios for void gas. The top void gas lines in each plot are calculated from the fractional degassing model, while the bottom void gas lines are calculated from the equilibrium degassing model (Spivack et al., 2006). The bottom two black lines represent the expected ranges in gas ratios for remaining dissolved gas. The top dissolved gas lines in each plot are calculated from the equilibrium degassing model, while the bottom dissolved gas lines are calculated from the fractional degassing model (Spivack et al., 2006). **a** Shows the measured and expected values of N_2/Ar from porewater with closed and open squares, respectively. The y axis for **b** is normalized as different sites have different initial methane concentrations (reported in mM). Closed circles indicate measured gas ratios, and open circles indicate initial methane concentrations.

Estimates of *in situ* methane concentrations based on the ratios of N_2, Ar, and CH_4 in void gas are ca. 40.8, 11.3, and 15.1 mM for cores 3, 65, and 66, respectively (**Tables 5.1** & **5.2**, **Figure 5.5**). Similar to the estimates based on dissolution of the void gas in porewater, core 3 is estimated to have an *in situ* methane concentration that is 3-4 times greater than that of cores 65 and 66.

Ratios of N_2/Ar are used to estimate the extent of degassing, which we indicate as the fraction of N_2 remaining in porewaters '$f_{N2,\ remaining}$' (**Table 5.2**). Given the measured N_2/Ar ratios between 40 and 50, it is estimated that 65% to 85% of N_2 was degassed between coring at the seafloor and sample storage. Core 66 exhibits the greatest extent of degassing. Notably, cores 3 and 65 were processed immediately upon core retrieval; however, cores 65 and 66 were retrieved from the seafloor simultaneously, so core 66 was processed after ca. 1 additional hour.

5.5.4 Porewater dissolved gas composition

Sediment from site 2A-1 core 3 was degassed, and volumes of gases and dissolved gas ratios in the degasser headspace are reported in **Table 5.3**. Results both with (**Table 5.3b**) and without (**Table 5.3a**) oxygen-correction for air contamination are reported because oxygen abundance decreases from 2.0 mL to 0 mL between 2 and 24 hours of degassing, making it an unreliable contamination indicator. Results reported in **Table 5.3b** additionally have the initial volumes of gas quantified during the background measurement removed, so gas volumes reflect change due to degassing.

Gas volumes and ratios from 0 hr reflect the headspace composition before core material was heated. There was ca. 14 mL air (11.9 mL N_2 and 2.5 mL O_2) in the sediment degasser upon set-up. The measurements taken after 1 and 2 hours yield consistent gas volumes and ratios, and were measured after pressure in the sediment degasser plateaued. The abundances of N_2, O_2, and Ar are similar to the first measurement, and ca. 1.56 mL CH_4 degassed from the core. These timepoints are expected to be most representative of the dissolved gas composition. There was a timepoint taken after 24 hours, but results are not considered to be representative of the dissolved gas composition, as all the oxygen in the headspace was removed within this timeframe, so artifacts associated with air contamination cannot be removed. The volumes of N_2 and Ar are similar to previous measurements (**Table 5.3a**), indicating that the system has not experienced any significant leaks. For timepoints 0 to 2, the air-contamination corrected signal size is 17-33% of the raw signal.

The value of N_2/Ar is ca. 43.4 from timepoints 1 and 2 with oxygen-correction and subtraction of gas volumes from the 0 hr measurements (**Table 5.3b**). This value is greater than the theoretically predicted upper limit of 34.3 (**Figure 5.5a**). The value of CH_4/Ar from these timepoints is ca. 136, about 24 times less than the CH_4/Ar value of the corresponding void gas,

while the two values are not expected to differ by more than ca. 10% (**Figure 5.5b**). Thus, we are unable to estimate an *in situ* methane concentration from this data.

After sample degassing, the remaining headspace of the sediment degasser was concentrated in the silica gel U-trap and extracted from the inlet system. Methane was purified from the headspace gas using a gas chromatography cryogenic preparatory system (described in Wang et al., 2015). This extraction yielded 1.66 mL methane at lab temperature and pressure. This corresponds to a porewater methane concentration of 1.57 mM.

a.	Volume of gas (mL)					
Time (hr)	**CH_4**	**N_2**	**O_2**	**Ar**	**N_2/Ar**	**CH_4/Ar**
0	0.047	11.891	2.467	0.154	77.3	0.3
1	1.487	10.663	2.026	0.143	74.3	10.4
2	1.624	10.466	1.916	0.148	70.7	11.0
24	1.710	11.036	0.000	0.147	74.9	11.6
b.	Oxygen-corrected and T-0 substracted volume of gas (mL)					
Time (hr)	**CH_4**	**N_2**	**O_2**	**Ar**	**N_2/Ar**	**CH_4/Ar**
0	(0.047)	(2.729)	(0.000)	(0.045)	(61.2)	(1.1)
1	1.439	0.408	0.000	0.009	44.6	157.5
2	1.577	0.584	0.000	0.014	42.1	113.8
24	1.663	7.315	0.000	0.080	91.8	20.9

Table 5.3: Volume of gases (CH_4, N_2, O_2, and Ar) and gas ratios in headspace as core 3 degasses. **a** shows results that are not O_2-corrected. **b** shows results that are O_2-corrected and volumes present at 0 hours are subtracted.

5.5.5 Methane solubility from the equation of state

Saturation solubilities for each core are reported in **Table 5.1**. Site 2A-1 core 3 could have and upper limit of 230 mM CH_4 dissolved in the porewaters of near-seafloor sediments, while Site 2B-1 cores 65 and 66 could have an upper limit of 234 mM CH_4 dissolved in the porewaters of near-seafloor sediments.

5.6 DISCUSSION

5.6.1 Challenges in constraining dissolved gas ratios

In situ methane concentration could not be independently determined using the composition of dissolved gas in porewaters because 1) the values of CH_4/Ar and N_2/Ar deviate from values predicted by the theoretical framework (**Figure 5.5**), and 2) the decrease in oxygen signal limits the use of oxygen as an air contamination indicator (**Table 5.3**).

The discrepancy between the methane concentrations calculated using the standard headspace method and predicted by the void gas composition (0.71 to 2.03 mM and 20 mM, respectively), implies that additional methane loss from porewater occurred between void gas formation and sediment sampling. The theory of the gas composition methods relies on fractionation of dissolved gas between the vapor and aqueous phase occurring during decompression, and that partitioning of gas components is dominantly controlled by differences in their solubilities (Spivack et al., 2006). Thus, it is expected that the value of CH_4/Ar should be preserved between void gas and dissolved methane pools within ca. 10%, (e.g., CH_4/Ar of porewater is expected to be ca. 3160), given the similar solubilities of these gases; however, observed dissolved gas CH_4/Ar is lower that void gas CH_4/Ar by a factor of ca. 24.

Additionally, the deviation of N_2/Ar from a reasonable range of values (i.e., 0 to 34.3) expected for degassed porewater means that it cannot be used to estimate the extent of degassing, and rather, this value more closely reflects equilibration with the atmosphere. In addition to comparing ratios of dissolved gases to predicted values, the yield of dissolved gases in the degasser headspace can also be compared to predicted volumes (**Table 5.4**). Predicted initial concentrations of N_2 and Ar are from air saturation with seawater, and the predicted initial concentration of CH_4 is from void gas-based *in situ* methane concentration quantification methods. The predicted degassed concentrations are based on the extent of core degassing ($f_{N2,\ remaining} = 0.31$) from void gas composition. Given the value of CH_4/Ar in void gas, porewaters are expected to have a methane concentration of ~20 mM. The methane concentration estimate from standard headspace analysis is also included, as this value should directly reflect the amount of methane in degassed porewaters. As core 3 contained ca. 47 mL porewater, expected yields of dissolved gases at lab temperature and pressure are: 1.2 to 43 mL CH_4, 0.14 to 0.46 mL N_2, 0 mL O_2, and 0.0065 to 0.013 mL Ar.

The volumes of dissolved gas released from porewaters all fall within a reasonable range of the predicted values (**Table 5.3b**). The volume of methane (1.66 mL) is close to the volume predicted by standard headspace analysis and corresponds to a comparable concentration estimate (1.37 to 1.57 mM vs 0.71 to 2.03 mM, respectively). The volumes of N_2 and Ar align with the values expected for air-equilibrated water at surface conditions (0.49 vs 0.46 mL N_2 and 0.011 vs 0.013 mL Ar, respectively), rather than those expected for degassed core (**Table 5.4**).

	CH_4	**N_2**	**O_2**	**Ar**
Predicted Initial Concentration (mM)	*40.8	0.432	0	0.0126
mL gas	43.0	0.455	0	0.0133
Predicted Degassed Concentration (mM)	1.2-*19.0	*0.134	0	*0.00614
mL gas	1.26-*20.0	*0.141	0	*0.00647

Table 5.4: expected volumes of dissolved gases from core 3. Concentration predictions are based on extent of degassing ($f_{N2,\ remaining} = 0.31$) estimated from *void gas measurements, and initial concentrations of air-saturated water. The 1.2 mM degassed concentration for methane is taken from the headspace analysis.

Some of these observations are also replicated during degassing of core material form IODP expedition 370 (**section 5.9.3**); however, a void gas was not collected from this depth so there is no prediction for the extent of degassing. The volume of methane (2.0 mL) similarly corresponds to concentration estimates from standard headspace analysis (3.5 mM vs 3.2 mM) (Heuer et al., 2020). The volume of degassed N_2 is in line with expectations, being similar to, but slightly lower than the expected volume from air-saturated porewater (ca. 0.20 mL vs 0.30 mL). The volume of degassed Ar is within the same order of magnitude, but lower than the expected yield from air saturated water (ca. 0.0033 mL vs 0.0087 mL), which is expected for a degassed core. While all of these volumes are within expected ranges, decreases in the oxygen signal throughout degassing and higher than expected N_2/Ar of 59 precludes an estimation of an *in situ* methane concentration.

Volumes and gas ratios of N_2 and Ar from sediment porewaters from core 3 align with air-saturated porewater, rather than values based on the extent of degassing estimated from void gas composition (e.g., an expected value of ca. 22 for N_2/Ar of dissolved gases). We consider the diffusion timescale of air in water, as cores bottoms were exposed to air for up to 4 hours before sample processing, which may result in some diffusion. However, this is thought to have a negligible impact on the non-exposed core, as the timescale of N_2 diffusion into even 10 cm is approximately 8 weeks. On the other hand, once cores are sectioned into ca. 1 cm patties and exposed to air on all sides, the timescale of diffusion through the entire section is less than 3.5 hours. This may result in non-negligible artifacts between sectioning and complete freezing. Diffusion timescale is estimated for N_2 using a dimensionless approximation of diffusion:

$$t = \frac{L^2}{D}$$

Where t is time in seconds, L is the diffusion pathlength in cm, and D is the diffusion coefficient in cm^2/s. D_{N2} is $2*10^{-5}$ cm^2/s. If there is significant gas exchange, for example by diffusion of gases into and out of sediment porewaters, additional artifacts may be imparted onto the composition of dissolved gases in porewaters. Diffusion is a function of concentration gradient and diffusivity (D). While $D_{Ar} > D_{N2} > D_{CH4}$, concentration gradient between stripped porewater and the atmosphere would favor diffusion of air components into porewaters, while the concentration gradient between methane in porewater and the atmosphere is large and would favor diffusion of methane out of porewaters. Thus, while gas partitioning between void gas and dissolved gas in porewater may set the composition of void gases, additional loss of methane from porewaters would indicate that sediment porewaters are not maintained in a closed system and experience additional methane degassing before sample processing.

Aside from air contamination, deviations of N_2/Ar greater than theoretically predicted values may be due in part to denitrification. The theory of the gas composition methods assumes N_2 is an inert gas in sediment porewaters, which is known to be false in shallow sediments. On the Scotian Slope, sediment-surface porewater has a nitrate concentration between 20 and 50 μM (Lakhanpal, 2022). Complete denitrification of this pool could only elevate the value of N_2/Ar in non-degassed sediment from 34.3 to 36. This effect is minor relative to the observed deviation of

N_2/Ar from predicted values. Ultimately, without a reliable way to precisely quantify air contamination, interpreting volumes and ratios of N_2 and Ar will remain challenging.

6.2 Oxygen as an unreliable contamination indicator for reduced sediments

The decrease in oxygen signal to the analytical baseline over the course of < 24 hours limits the use of oxygen as a contamination indicator (**Figure 5.6, 5.S3**). While initial air contamination before sediment degassing can still be quantified, no additional artifacts or air leakage in the system can be monitored.

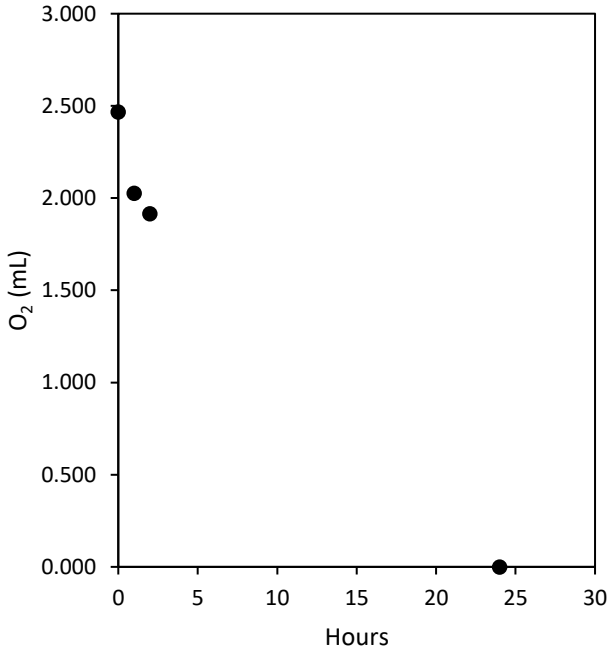

Figure 5.6: Oxygen signal decrease (mL) observed during degassing of core 3

We hypothesize that the loss of oxygen from the degasser headspace is due to oxidation of sulfide and/or reduced metals. In sulfidic sediments, manganese and iron can be oxidized kinetically fast, either abiotically or microbially (Clement et al., 2009; Trouwborst et al., 2006). Assuming that sulfide oxidation is thermodynamically favored relative to metal oxidation, these oxidized metals can then help to overcome the kinetic barrier of sulfide oxidation, and in doing so return to their reduced forms (Ma et al., 2006; Yakushev et al., 2009). Additionally, direct abiotic oxidation of sulfide by O_2 has been demonstrated (Millero et al., 1987), but is relatively

slow compared to the reaction in the presence of trace metals (reaction half-life on the order of 1-2 days, vs minutes) (Vazquez et al., 1989). Both reaction timescales are significant with respect to the timescale of sediment degassing (reaction half-life on the order of hours).

Options to improve air contamination monitoring include better constraint on O_2 or reliance on an alternative contamination indicator. For example, in order to minimize O_2 loss during degassing, gas could be circulated from the degasser headspace and passed through a cryogen to scrub H_2S. This option would require significant modifications to the inlet design. Alternatively, chemical traps like silver phosphate may be used to limit the effect of sulfide reactions on oxygen abundance. Moreover, if porewaters may be equilibrating with air before sample processing, air contamination may have to be accounted for based on ratios of dissolved oxygen in air-saturated waters instead of atmospheric composition.

6.3 Reasonable $[CH_4]_o$ estimates from void-gas based methods

Both void gas-based *in situ* methane concentration estimates yield similar results, within ca. 2 mM. These values are about an order of magnitude greater than those from headspace analysis of degassed core and about an order of magnitude less than saturation solubility, which are expected to serve as lower and upper concentration limits. Concentration estimated from these methods are much closer to the hydrate saturation concentration (ca. 40-50 mM). Methane concentration estimates from headspace analysis (**Table 5.1, 5.S2**, **Figure 5.4**) are comparable to the 1.195 mM saturation limit of methane in seawater at surface temperature and pressure conditions. Thus, we can infer that significant degassing has occurred for all cores. While this measurement does not yield accurate *in situ* methane concentrations for near-surface sediments, it can indicate sediments with little to no methane, as well as horizons of sediment that have relatively higher concentrations of methane. On the other hand, the maximum *in situ* methane concentration is set by the saturation solubility at seafloor pressure and temperature conditions. All core material would be expected to have an *in situ* methane concentration below saturation, as bubbling was not observed at the locations on the seafloor where coring occurred. Given the observation of bubbling at the seafloor near site 2A-1 core 3, this core is expected to have the highest *in situ* methane concentration, which is supported by the void gas-based estimates. Using the void gas dissolution method, for porewater from core 3 to reflect the *in situ* saturation

concentration, the void would have had to derive from only ca. 17% of the methanogenic core volume, or significant volumes of gas escaped the core liner during ascent.

The ability to replicate *in situ* methane concentration estimates with two void gas-based methods is useful because this would provide 1) a means to validate concentration estimates while only relying on one sample type, and 2) security against information loss. A major benefit of the void gas dissolution method is that imaging to estimate void gas volume is quick, non-intrusive, and poses little risk for sample loss. Sampling void gas pockets can be challenging, as the sample can easily be lost or compromised from needle clogs, core positioning, and over-drilling. Additionally, this method may be used to quantify void spaces that are smaller in size than what can be sampled for chemical analysis. Unlike other concentration quantification methods, this does not require specialty equipment; however, quantifying void space may be challenging in the absence of a large central void. This method, as it is accomplished in this study, requires several assumptions about void pressure and the neglects the volumes of gas cracks and other smaller void spaces. Some of these concerns could be addressed by intentional efforts to accurately constrain these volumes during future sampling.

The cross validation between void gas-based methods, one using gas and water volumes and the other using the chemical composition of that gas, is significant because these methods have not previously been compared. The method of *in situ* methane concentration quantification based on gas ratios has been validated with measurements of samples collected with a pressure core sampler (Spivack et al., 2006). However, quantification of *in situ* methane concentration based on void gas and water volumes is not well-documented. Thus, the similar results from these two methods demonstrates the potential value of the void gas dissolution method.

5.7 SUMMARY

In this study we present the development of a sediment degasser and QMS inlet system to extract and quantify dissolved gases in porewater for a new method to estimate *in situ* methane concentration in gas-rich sediments. We test this method using sediments from hydrocarbon seeps on the Scotian Slope and compare methane concentration estimates using four other quantification methods, including standard headspace analysis, dissolution of the void gas volume into the porewater, ratios of N_2, Ar, and CH_4 in void gas, and the saturation solubility of methane at *in situ* conditions using an equation of state.

We find that the volume of CH_4 extracted from porewaters follows predictions from standard headspace analysis, reflecting methane concentration after significant degassing and often saturation at surface pressure. Additionally, sediment porewaters appear to exchange with air quickly, as evidenced by volumes of N_2 and Ar extracted from porewaters similar to predicted yields from air-saturated water. Additionally, values of N_2/Ar are high, the interpretation of which is complicated by the lack of a reliable air-contamination indicator, as O_2 reacts quickly in reduced sediments. Thus, *in situ* methane concentration could not be determined using the composition of dissolved gas in porewaters. System modifications and further testing are required to employ this method to quantify *in situ* methane concentrations, but currently, it can validate concentration data from standard headspace analysis

We also find that void gas-based methane concentration quantification methods yield reasonable *in situ* methane concentrations that are 10 to 40 times greater than those from standard headspace analysis (i.e., 2 to 10% of methane remains after degassing). This is a significant level of degassing, which has currently unconstrained impact of isotopologue signals of the dissolved methane pool. The agreement between these two methods is promising for use of the void gas dissolution method, which has not previously been corroborated.

5.8 ACKNOWLEDGEMENTS

We would like to acknowledge the efforts and expertise of the shipboard scientists and crew of the Atlantic Condor 2021 cruise and the IODP Expedition 370 in obtaining sediment and void gas samples. Funding for this study was provided by the U.S. Science Support Program Office associated with the International Ocean Discovery Program (OCE-14-50528 to D.T.W., and S.O.), MISTI Japan, and the Woods Hole Oceanographic Institution Ocean Venture Fund (awarded to E.L.). E.L. was additionally funded by the National Science Foundation (EAR-1852946 to S.O.).

5.9 SUPPLEMENTARY INFORMATION

5.9.1 Additional details on methodology

5.9.1.1 Alternative sediment degassing vessels

Calibrated Instruments Cali-Bond bags and glass vessels with O-ring seals were tested as sediment extraction vessels. For use of the Cali-Bond bags, we placed frozen core material inside the bag, heat sealed it shut, and flushed the volume three times with helium to remove air. We found that over 24 hours, leakage of air resulted in the addition of 4.4 mL of O_2 to the 0.5 mL O_2 initially present. However, it is expected that this volume of O_2 should be accompanied by ca. 16 mL N_2 for an air source, but only 6.4 mL N_2 was observed. These results may reflect gas absorption or diffusion rates across the bag lining.

For the use of the glass degasser, frozen core material was placed inside the degasser, which was then sealed and placed on dry ice to keep the sample cold. The degasser was then placed under vacuum for 20 minutes and filled with helium gas. Glass degassers were found to have leakage through the O-ring (ca. 0.2 mL O_2 detected after 24 hours). While N_2/Ar of the air leak is similar to typical air ratios (85 vs 83.95), the N_2/O_2 ratio deviates from air ratios (25 vs 3.7). Thus, this source of contamination is challenging to account for in addition to air contamination associated with sampling.

Figure 5.S1: Degassers tested to extract gas from marine sediments: **a** Calibrated Instruments Cali-Bond bag, and **b** glass degasser with O-ring seal

5.9.1.2 Ice cube validation

	CH_4 (15)	N_2 (28)	O_2 (32)	Ar (40)	N_2/Ar
T-0 hr	182	12560	3156	520	24.1
T-4 hr	3211	2433565	817139	61764	39.4

Table 5.S1: Background-corrected signals and N_2/Ar for a melted ice cube

5.9.1.3 20 mL vial volume calibration

The vertical height of headspace in 20 mL serum vials was calibrated to volume by displacing known volumes of water.

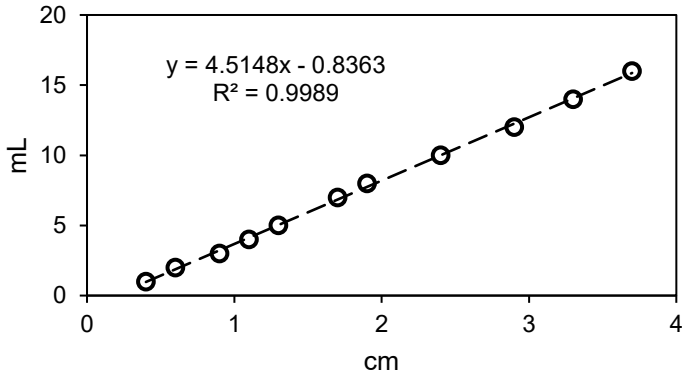

Figure 5.S2: Standard curve of headspace volume (mL) versus headspace height (cm) in 20 mL serum vials.

5.9.1.4 N_2/Ar and CH_4/Ar in void gas and dissolved gas

The following code is used to produce the evolution of N_2/Ar and CH_4/Ar vs different extents of degassing in **Figure 5**. The derivation of these equations can be found in Spivack et al., 2006.

```
%Volume of vapor phase over Mass of interstitial water in m^3/kg
V_M = [0:0.01:150];
% initial concentrations from air saturation at S=35, T = 20 in mM
N20 = 0.432; Ar0 = 0.0126;
% this is set to the estimated methane concentration
CH40 = 40.8;
% gas solubilities
N2sol = 0.747747; Arsol = 1.703826; CH4sol = 1.777888;
%concentration of N2 dissolved in porewater
N2_conc_eq_sed = N20.*N2sol.*((1./(0.08314.*(283.15-6))).*V_M.*1000+N2sol).^-1;
%concentration of Ar dissolved in porewater
Ar_conc_eq_sed = Ar0*Arsol*(1/(0.08314*(283.15-6)).*V_M*1000+Arsol).^-1;
%concentration of CH4 dissolved in porewater
CH4_conc_eq_sed = CH40*CH4sol*(1/(0.08314*(283.15-6)).*V_M*1000+CH4sol).^-1;
%concentration of N2 in void gas
```

```
N2_conc_eq_void = N20-N2_conc_eq_sed;
%concentration of Ar in void gas
Ar_conc_eq_void = Ar0- Ar_conc_eq_sed;
%concentration of CH4 in void gas
CH4_conc_eq_void = CH40 -CH4_conc_eq_sed;
% Calculation of N2/Ar ratios dissolved in porewater (sed) and in void gas (void)
N2Ar_eq_sed = N2_conc_eq_sed./Ar_conc_eq_sed;
N2Ar_eq_void = N2_conc_eq_void./Ar_conc_eq_void;
% Calculation of CH4/Ar ratios dissolved in porewater (sed) and in void gas (void)
CH4Ar_eq_sed = CH4_conc_eq_sed./Ar_conc_eq_sed;
CH4Ar_eq_void = CH4_conc_eq_void./Ar_conc_eq_void;
% Fraction of N2 remaining in porewater
N2_remaining_eq = 1-(N20-N2_conc_eq_sed)/N20;
```

5.9.2 Additional details on results

5.9.2.1 Headspace analysis concentrations for more sites on the Nova Scotian slope

Site	Site Name	Lat	Long	Water Depth (m)	Core	Depth (cm)	MR CH_4	$[CH_4]_{\Phi=1}$ mM	$[CH_4]_{\Phi=0.7}$ mM
1-1	SpongeBob	43.009463	-60.212290	2348	24	10	0%	0.00	0.00
2B-1	Clam Shell	42.207654	-62.324409	2743	53	4	1.18%	1.74	2.18
2B-1	Clam Shell	42.207654	-62.324409	2743	53	8	1.25%	1.14	1.43
2B-1	Clam Shell	42.207654	-62.324409	2743	53	12	0.87%	0.92	1.15
2B-1	Clam Shell	42.207654	-62.324409	2743	53	16	0.64%	0.94	1.18
2B-1	Clam Shell	42.207654	-62.324409	2743	53	20	0.79%	1.17	1.46
2B-1	Clam Shell	42.207654	-62.324409	2743	53	28	2.74%	4.04	5.05
2B-1	Clam Shell	42.207654	-62.324409	2743	53	40	0.98%	1.04	1.30
2B-1	Transect NW 75	42.208265	-62.324424	2781	104	40	0	0.00	0.00
2B-2	Dark Sea Bed	42.205502	-62.327032	2747	63	30	0.76%	0.94	1.18
2B-2	Big Purple	42.205502	-62.327292	2746	38	30	2.88%	1.75	2.19
2A-1	Holey Ground	42.162353	-62.372062	2688	27	3	0.20%	0.25	0.31
2A-1	Holey Ground	42.162353	-62.372062	2688	27	6	0.71%	0.75	0.94
2A-1	Holey Ground	42.162353	-62.372062	2688	27	9	1.00%	0.79	0.99
2A-1	Holey Ground	42.162353	-62.372062	2688	27	12	0.61%	0.56	0.70
2A-1	Holey Ground	42.162353	-62.372062	2688	27	21	1.66%	2.06	2.58
2A-1	Crusty White Clams	42.162198	-62.371378	2684	101	32	0.49%	1.40	1.76
2A-2	Purple Haze	42.159817	-62.360243	2734	63	36	1.27%	1.16	1.45
2A-transect	NW 525m	42.161334	-62.366394	2693	5	40	0%	0.00	0.00
6-1	Smithers	42.229798	-62.442895	2563	104	30	0%	0.00	0.00
6-2	Arm & Hammer	42.228632	-62.432911	2542	9	7	0%	0.00	0.00
6-2	Arm & Hammer	42.228632	-62.432911	2542	9	30	0%	0.00	0.00

Table 5.S2: Additional headspace analysis methane concentration measurements made for sites along the Nova Scotian slope. MR CH_4 is the percent CH_4 in the vial headspace, measured by gas chromatography.

5.9.3 Degassing experiment for IODP 370 core sample

One sample was degassed from IODP 370 hole C0023A, in the Nankai Trough, off Cape Muroto, Japan. Samples from the upper ca. 500 m of the sediment column are suspected to have experienced some degassing, as evidenced from the large range in head space methane concentration data (**Figure S3**) (Heuer et al., 2017). The upper limit of methane concentration at this site is the the saturation concentration, calculated using the equation of state (Duan et al., 1992) (**Figure S3**).

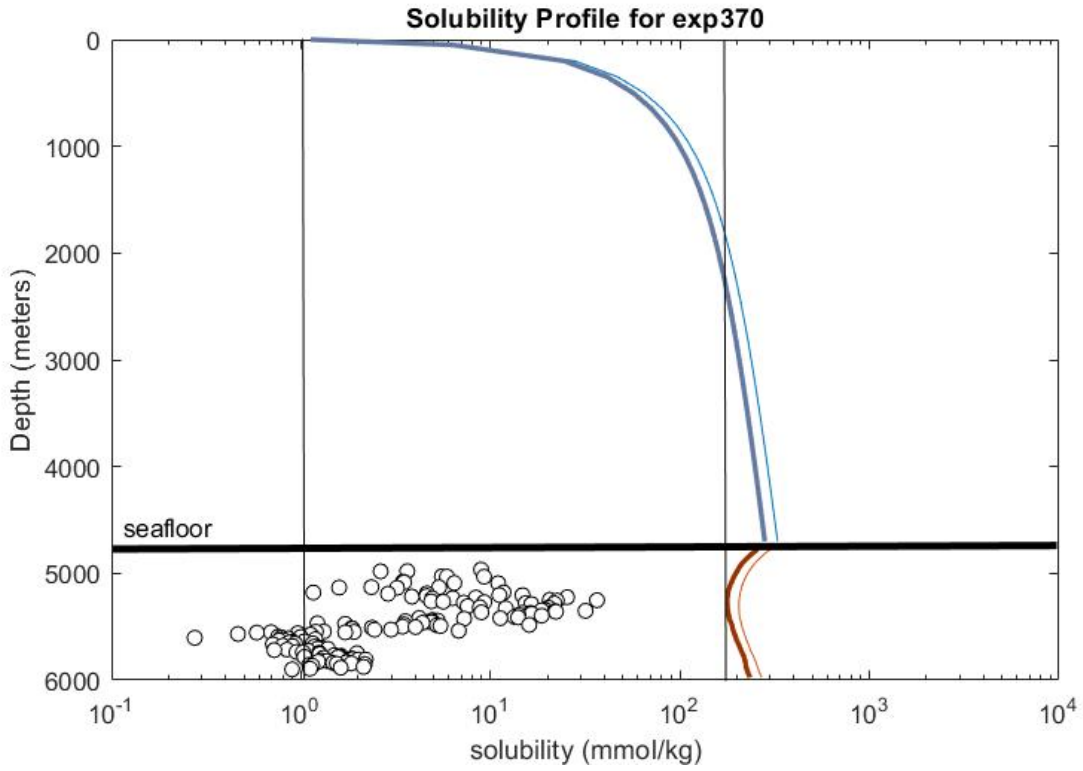

Figure 5.S3: Solubility of methane in porewater and the water column. Open circles are methane concentration data reproduced from Heuer et al., 2017. The orange lines represent the saturation concentration of methane in the porewater, and the blue lines represent the saturation concentration of methane through the water column.

The sample (CKY000000000006946500) is from 506.8 mbsf. Results are shown in **Table S3**. Sample volume is 68 cm^3 with a porosity of ~45%. Thus, approximately 30.8 mL porewater is expected. 30.5 mL of air-equilibrated porewater is expected to yield 0.30 mL N_2 and 0.0087 mL Ar.

a.	Gas volumes (mL)					
Time (hr)	**CH_4**	**N_2**	**O_2**	**Ar**	**N_2/Ar**	**CH_4/Ar**
0	0.00034	0.066	0.015	0.00083	60.3	2.14
0.5	0.015	0.071	0.015	0.0010	44.7	39.6
2	1.53	0.20	0.00282	0.00316	62.5	502.4
4	2.03	0.23	0.00122	0.00392	58.3	524.3
6	2.39	0.31	0.00075	0.00466	67.4	516.3
24	2.16	0.27	0.00025	0.00411	65.3	526.6
b.	Oxygen-corrected gas volumes (mL)					
Time (hr)	**CH_4**	**N_2**	**O_2**	**Ar**	**N_2/Ar**	**CH_4/Ar**
0	0.00034	0.0094	0.0000	0.00015	61.9	2.2
0.5	0.015	0.015	0.0000	0.00035	41.5	41.9
2	1.53	0.14	0.0000	0.0025	57.8	614.4
4	2.03	0.17	0.0000	0.0032	53.4	625.0
6	2.39	0.26	0.0000	0.0040	64.8	600.0
24	2.16	0.21	0.0000	0.0034	61.7	629.3

Table 5.S3: Results of gas extraction from IODP 370 sample CKY000000000006946500. Values for CH_4, N_2, O_2, and Ar are in mL of gas in the degasser at lab temperature and pressure. **a** shows results that are not O_2-corrected. **b** shows results that are O_2-corrected.

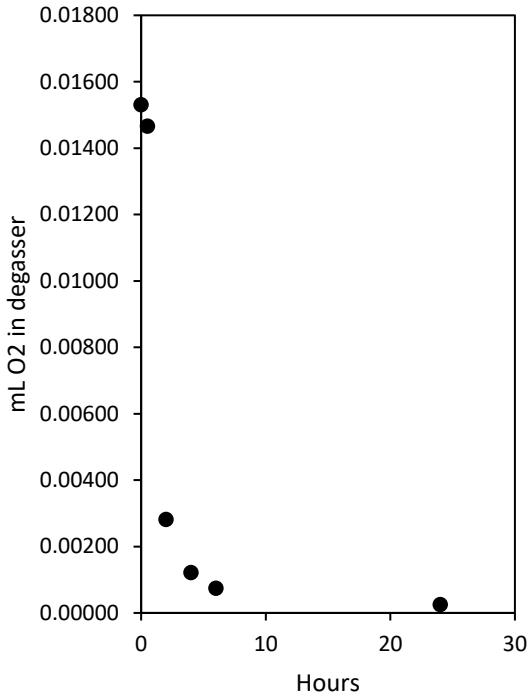

Figure 5.S4: Oxygen signal decrease observed during degassing of sample CKY000000000006946500

5.10 REFERENCES

Abegg, F., Anderson, A.L., 1997. The acoustic turbid layer in muddy sediments of Eckernfoerde Bay, Western Baltic: Methane concentration, saturation and bubble characteristics. Mar. Geol. 137, 137–147. https://doi.org/10.1016/S0025-3227(96)00084-9

Campbell, D.C., 2019. CCGS Hudson Expedition 2016-011 , phase 2 . Cold seep investigations on the Scotian Slope , offshore Nova Scotia , June 15 – July 6 , 2016. Geol. Surv. Canada, Open File 8525 88.

Clement, B.G., Luther, G.W., Tebo, B.M., 2009. Rapid, oxygen-dependent microbial Mn(II) oxidation kinetics at sub-micromolar oxygen concentrations in the Black Sea suboxic zone. Geochim. Cosmochim. Acta 73, 1878–1889. https://doi.org/10.1016/j.gca.2008.12.023

Dickens, G.R., Wallace, P.J., Paull, C.K., Borowski, W.S., 2000. Detection of methane gas hydrate in the pressure core sampler (PCS): Volume-pressure-time relations during controlled degassing experiments. Proc. Ocean Drill. Progr. Sci. Results 164, 113–126. https://doi.org/10.2973/odp.proc.sr.164.210.2000

Duan, Z., Moller, N., Greenberg, J., Weare, J.H., 1992. The prediction of methane solubility in natural waters to high ionic strength from 0 to 250 C and from 0 to 1600 bar. Geochim. Cosmochim. Acta 56, 4303. https://doi.org/10.1016/0016-7037(92)90271-J

Dück, Y., Lorke, A., Jokiel, C., Gierse, J., 2019. Laboratory and field investigations on freeze and gravity core sampling and assessment of coring disturbances with implications on gas bubble characterization. Limnol. Oceanogr. Methods 17, 585–606. https://doi.org/10.1002/lom3.10335

Fowler, M., Webb, J., Hubert, C., Li, C., Macdonald, A., 2018. Implications for Petroleum Systems on the deep water Scotian Slope, offshore Nova Scotia based on geochemical and microbiological analyses of piston core samples, in: Geoconvention. pp. 1–3.

Heeschen, K.U., Hohnberg, H.J., Haeckel, M., Abegg, F., Drews, M., Bohrmann, G., 2007. In situ hydrocarbon concentrations from pressurized cores in surface sediments, Northern Gulf of Mexico. Mar. Chem. 107, 498–515. https://doi.org/10.1016/j.marchem.2007.08.008

Hesse, R., Harrison, W.E., 1981. Gas hydrates (clathrates) causing pore-water freshening and oxygen isotope fractionation in deep-water sedimentary sections of terrigenous continental margins. Earth Planet. Sci. Lett. 55, 453–462. https://doi.org/10.1016/0012-821X(81)90172-2

Heuer, V.B., Inagaki, F., Morono, Y., Kubo, Y., Spivack, A.J., Viehweger, B., Treude, T., 2020. Temperature limits to deep subseafloor life in the Nankai Trough subduction zone. Science (80-.). 1234.

Lakhanpal, N., 2022. Honors thesis: Survey of porewater geochemistry within deep marine hydrocarbon seep sediments of the Scotian Slope, Canada. Saint Mary's Univeristy. https://doi.org/10.46883/onc.2022.3605

Li, L., Peng, J., Gao, Q., Sun, M., Liu, Y., Li, M., Chen, B., Bo, K., 2016. Pressure retaining method based on phase change for coring of gas hydrate-bearing sediments in offshore drilling. Appl. Therm. Eng. 107, 633–641.

https://doi.org/10.1016/j.applthermaleng.2016.06.174

Ma, S., Noble, A., Butcher, D., Trouwborst, R.E., Luther, G.W., 2006. Removal of H_2S via an iron catalytic cycle and iron sulfide precipitation in the water column of dead end tributaries. Estuar. Coast. Shelf Sci. 70, 461–472. https://doi.org/10.1016/j.ecss.2006.06.033

Millero, F.J., Hubinger, S., Fernandez, M., Garnett, S., 1987. Oxidation of H_2S in Seawater as a Function of Temperature, pH, and Ionic Strength. Environ. Sci. Technol. 21, 439–443. https://doi.org/10.1021/es00159a003

Oremland, R.S., Miller, L.G., Whiticar, M.J., 1987. Sources and flux of natural gases from Mono Lake, California. Geochim. Cosmochim. Acta 51, 2915–2929. https://doi.org/10.1016/0016-7037(87)90367-X

Pachur, H.-J., Denner, H.-D., Walter, H., 1984. A freezing device for sampling the sediment-water interface of lakes. Catena 11, 65–70.

Paull, C.K., Lorenson, T.D., Dickens, G., Borowski, W.S., Ussler, W., Kvenvolden, K., 2000. Comparisons of in situ and core gas measurements in ODP Leg 164 bore holes. Ann. N. Y. Acad. Sci. 912, 23–31. https://doi.org/10.1111/j.1749-6632.2000.tb06756.x

Rohatgi A. (2022). WebPlotDigitizer (Version 4.6) [Computer software]. Retrieved from http://arohatgi.info/WebPlotDigitizer

Spivack, A.J., Mcneil, C., Holm, N.G., Hinrichs, K.-U., 2006. Determination of In Situ Methane Based on Analysis of Void Gas. Proc. Ocean Drill. Program, Sci. Results 201. https://doi.org/10.2973/odp.proc.sr.201.119.2006

Stanley, R.H.R., Jenkins, W.J., Lott, D.E., Doney, S.C., 2009. Noble gas constraints on air-sea gas exchange and bubble fluxes. J. Geophys. Res. Ocean. 114, 1–14. https://doi.org/10.1029/2009JC005396

Trouwborst, R.E., Clement, B.G., Tebo, B.M., Glazer, B.T., Luther, G.W., 2006. Soluble Mn(III) in suboxic zones. Science (80-.). 313, 1955–1957. https://doi.org/10.1126/science.1132876

Vazquez, F.G., Zhang, J., Millero, F.J., 1989. Effect of metals on the rate of the oxidation of H2S in seawater. Geophys. Res. Lett. 16, 1363–1366.

Wang, D.T., Gruen, D.S., Sherwood Lollar, B., Hinrichs, K.U., Stewart, L.C., Holden, J.F., Hristov, A.N., Pohlman, J.W., Morrill, P.L., Könneke, M., Delwiche, K.B., Reeves, E.P., Sutcliffe, C.N., Ritter, D.J., Seewald, J.S., McIntosh, J.C., Hemond, H.F., Kubo, M.D., Cardace, D., Hoehler, T.M., Ono, S., 2015. Nonequilibrium clumped isotope signals in microbial methane. Science (80-.). 348, 428–431. https://doi.org/10.1126/science.aaa4326

Yakushev, E., Pakhomova, S., Sørenson, K., Skei, J., 2009. Importance of the different manganese species in the formation of water column redox zones: Observations and modeling. Mar. Chem. 117, 59–70. https://doi.org/10.1016/j.marchem.2009.09.007

Chapter 6

Outlook

This thesis was centered around the quantification of the natural abundance of methane isotopologues from marine and lacustrine sediments to test assumptions about prevailing mechanisms of methane formation and consumption. In this pursuit, the contents of this thesis fill several large information gaps in the use of clumped methane isotopologues as a biogeochemical tracer across different scales and environments.

Chapter 2 presents a global survey of the abundance of $^{13}CH_3D$ in marine gas hydrate specimen from 11 of the world's most prominent hydrate-bearing regions. We document the link between methane isotopologue-based temperature estimates and key submarine gas hydrate seepage features for the first time. The results from gas hydrates associated with cold seeps, pockmarks, and oil-seeps validate previous models about their geologic driving forces, while methane from mud volcanoes comes from at least two different sources, depending on the tectonic environment.

Chapter 3 reports two novel kilometer-scale profiles of methane isotopologues from marine sediments, representing the transition between microbial and thermal methanogenic zones. Methane isotopologues do not follow two-component mixing between microbial and thermal sources, but rather indicate microbially catalyzed re-equilibration along geothermal gradients up to temperature of 100^{+14}_{-15}°C. This signal may be preserved up until the rate of abiotic exchange becomes comparable to the rate of temperature increase, around 150°C. These results suggest that methane isotopologue characterization represents a means to trace the upper-temperature limits of microbial activity in hydrocarbon-rich marine sedimentary environments.

Chapter 4 applies the characterization of $^{13}CH_3D$ abundance to ebullition from the sediments of a mid-latitude lake. We produce the largest set of freshwater $\Delta^{13}CH_3D$ values in a single lake basin, which is used to develop a sampling strategy to constrain lake source signatures. The results show that clumped methane isotopologues may yield a means to isotopically differentiate aerobic and anerobic methane oxidation in freshwater environments, but the large variation in $\Delta^{13}CH_3D$ values from a single lake basin points to the challenge of constraining the total source signal from freshwater lakes.

Chapter 5 documents the development of a method to extract and quantify dissolved gases in sediment porewaters to determine *in situ* methane concentration from gas-rich

sediments. This method is tested using surface sediments from hydrocarbon seeps, and results are compared to those from four other methods of methane quantification. The results show that volumes of gas components match predictions from air-equilibrated water (N_2 and Ar) and standard headspace analysis (CH_4), but dissolved gases in porewater experience additional alteration between void gas formation and sample processing. The functionality of this method is additionally limited by unreliable accounting of air-contamination, as O_2 reacts quickly in reduced sediment.

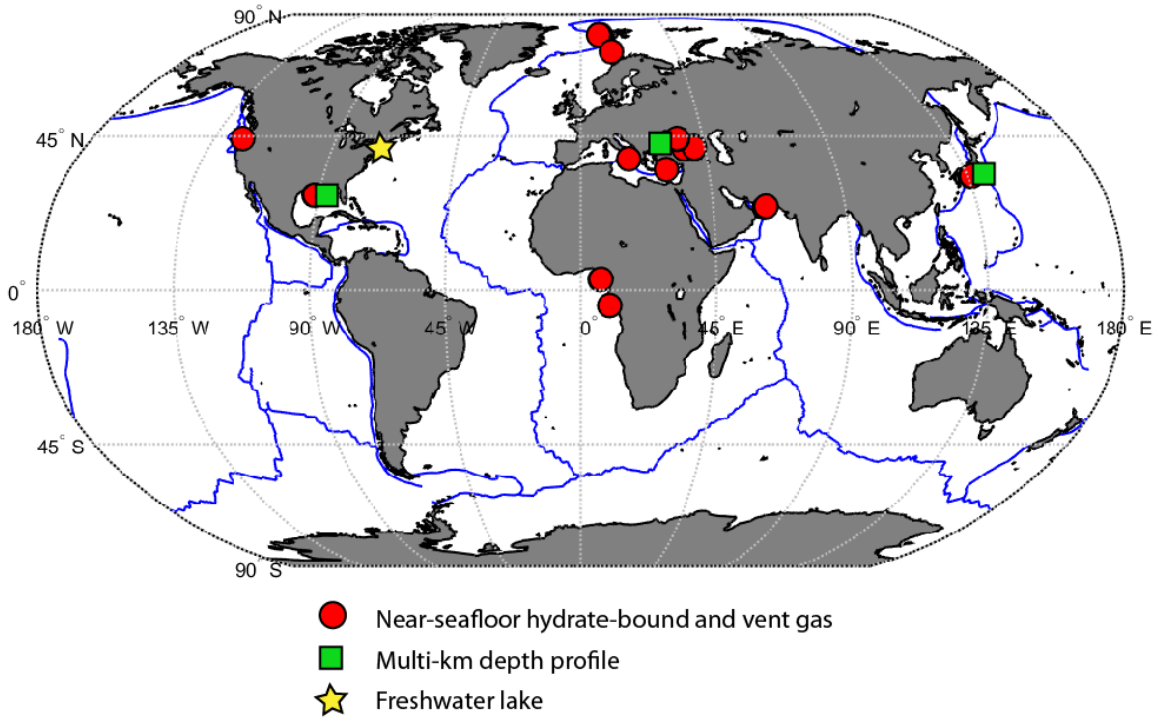

Figure 6.1: Map of site locations for clumped isotopologue data presented in this thesis.

The data presented in the preceding chapters of this dissertation (summarized in **Figure 6.1**) demonstrate the insights on methane origin and fate attainable by the focused application of clumped methane isotopologue measurements. These datasets span different spatial and temporal scales including, 1) the high surface spatial coverage of the global gas hydrate survey, 2) the high depth resolution, but low surface spatial coverage of the multi-kilometer depth profiles, and 3) the high temporal and spatial coverage of a single deep lake basin. In synthesizing these varying

perspectives, we acknowledge how the scopes of each of these studies and ensuing conclusions shape and are shaped by the spatial and temporal scales at which samples are collected. For example, global-scale surveys are useful to compare many similar environments; however, each of these localities is also expected to have its own complexity, which may be revealed by observing underlying vertical profiles of methane. Additionally, in the context of this thesis, the data from Chapter 4 serves as a reminder of some of the limitations in extrapolating small sample sizes to global processes.

Several opportunities remain to advance the use clumped methane isotopologues to understand methane origin. This includes expanding the interpretations of kinetic methane for differentiating enzymatic reactions by using experiments to better constrain the kinetics associated with breaking and reforming C-H bonds. Further, there is a persisting need to reconcile hypotheses of microbial and abiotic methane equilibration mechanisms between lab studies, numerical models, and natural environment observations. I suspect that many of the exciting steps forward in the world of clumped methane isotopologues will involve the pairing of this analysis with other isotope systems (e.g., noble gases), as well as well-documented hydro-geology and microbiology.

Appendix A

Methane clumped isotopologue ($^{13}CH_3D$) measurements from the Nankai Trough, off Cape Muroto

---

Collaborators on this work include:

Ellen Lalk, David T. Wang, Verena Heuer, Arthur Spivack, and Shuhei Ono

A.1 SUMMARY

International Ocean Discovery Program (IODP) Expedition 370: The Deep Biosphere off Muroto set out with an objective to identify unique combinations of geochemical and microbial signatures in order to discern biotic and abiotic sediments and their transitions. Hole C0023 is located in the Nankai Trough off Cape Muroto at a water depth of 4776 m (**Figure A.1**). Unlike the kilometer-scale profiles presented in **chapter 3**, this site is an active margin in the subduction boundary between the Eurasian plate and the Philippine Sea plate. Near surface sediments are pelagic muds and mudstones, with basin-style deposition found from 494-635 mbsf. The site is characterized by a decollement zone at 800 m (Heuer et al., 2017). Coring at this site was achieved down to 1.2 kmbsf, and samples collected from this expedition span the full range of temperatures at which life is known to exist from 2°C at the seafloor to 120°C at 1.2 kmbsf. These temperatures include conditions that are favorable both for microbial and thermogenic methane production.

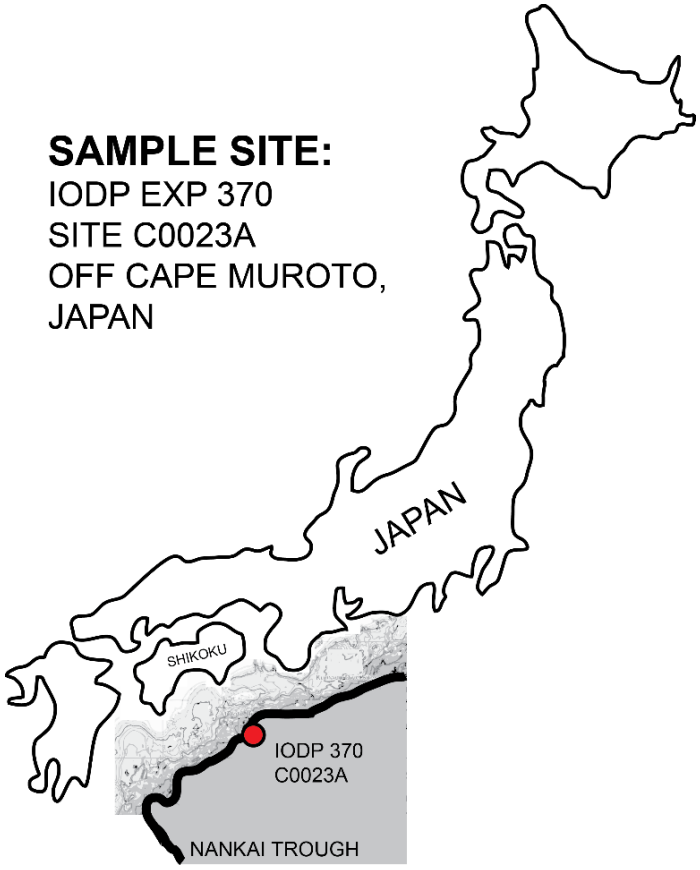

Figure A.1: Site location for IODP 370 hole C0023A

Three samples were extracted from frozen core samples using the degasser and inlet system described in **chapter 5**. There is a replicate of sample CKY000000000006769600 that was partitioned during sample recovery from the inlet system. Three additional samples are gas sub-sampled from void pockets. Gas samples were purified using an automated preparative gas chromatography system (Wang et al., 2015), and analyzed using the Tunable Infrared Laster Direct Absorption Spectroscopy instrument at MIT (Ono et al., 2014). Results from this analysis are reported in **Table A.1** and **Figure A.2**.

The values of $\delta^{13}C$ range from -66.4 to -62.9 ‰ and are consistent with previous measurements from -65.0 to -62.8 ‰ (**Figure A.2a**) (Heuer et al., 2021). The values of δD range from -191.4 to -178.8 ‰ (**Figure A.2b**). $\Delta^{13}CH_3D$ range from 2.6 to 4.1 ‰ (**Figure A.2c**), corresponding to apparent temperatures from 91 to 189℃. Apparent temperatures of methane are ca. 40 to 140℃ higher than the sediments they are sampled from (**Figure A.2d**).

Sample	**Depth**	**Sediment T**	**$\delta^{13}C$**		**δD**		**$\Delta^{13}CH_3D$**		**T_{13D}**	
	mbsf	**℃**	**‰**		**‰**		**‰**		**℃**	
CKY000000000006769600-1	319	44	-64.22	0.16	-183.3	0.07	2.6	0.32	189	+31/-26
CKY000000000006769600-2	319	44	-65.13	0.18	-183.2	0.07	2.8	0.23	168	+19/-17
1597_X370-13F-01(75cm)-Void	360	48	-65.06	0.05	-179.1	0.07	3.7	0.45	110	+27/-23
1601_X370-13F-02(121cm)-Void	361	48	-64.54	0.13	-178.8	0.40	2.9	1.26	159	+134/-75
1639_X370_13F-02(121cm)-Void	361	48	-64.53	0.03	-178.9	0.06	4.1	0.41	91	+22/-19
CKY000000000006845400	415	54	-62.92	0.15	-184.0	0.40	4.0	0.38	96	+21/-18
CKY000000000006946500	507	63	-66.40	0.13	-191.4	0.35	2.6	0.26	184	+24/-21

Table A.1: Isotopologue values and apparent temperature of methane from hole C0023A.

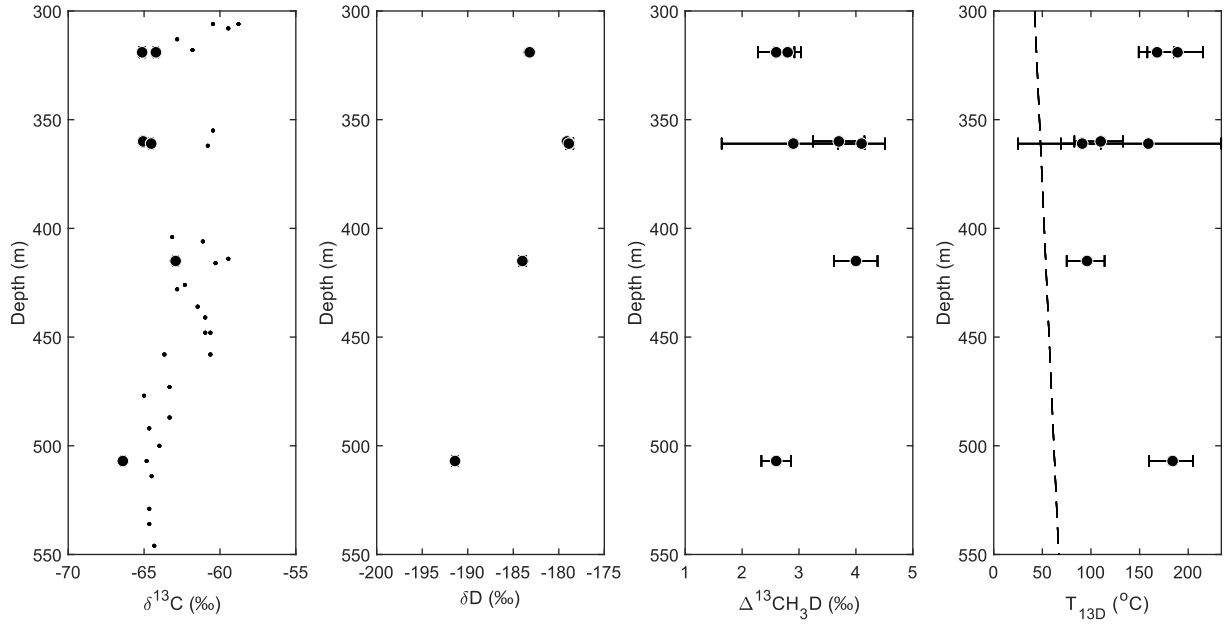

Figure A.2: Depth profiles of isotopologue ratios of methane from hole C0023A, including **a** $\delta^{13}C$, **b** δD, **c** $\Delta^{13}CH_3D$, and **d** apparent temperature (T_{13D}). Dots in **a** are data from Heuer et al., 2020. The dashed line in **d** is the estimated sediment temperature.

The observation of apparent temperatures ca. 40 to 140°C greater than the estimated sediment temperature could be due to either thermogenic contribution or kinetic fractionations. Between 300 and 550 mbsf, relatively low $\delta^{13}C$ values, relatively high δD values, and high C_1/C_2 values support methane formation by a microbial source via the hydrogenotrophic metabolism (**Figure A.3a, b**). Calculated Gibbs free energy yields of methanogenesis from hydrogen and acetate are negative for this sediment zone, and methane production rates from radiotracer experiments are from 0.11 to 2.48 pmol $d^{-1}cm^{-3}$ (Heuer et al., 2020). Thus, isotopologue values may be due to kinetic fractionations during microbial methanogenesis. Notably, methane samples with similar isotopologue values were observed from mud volcanoes in the Black Sea (e.g., **Figure 2.3**).

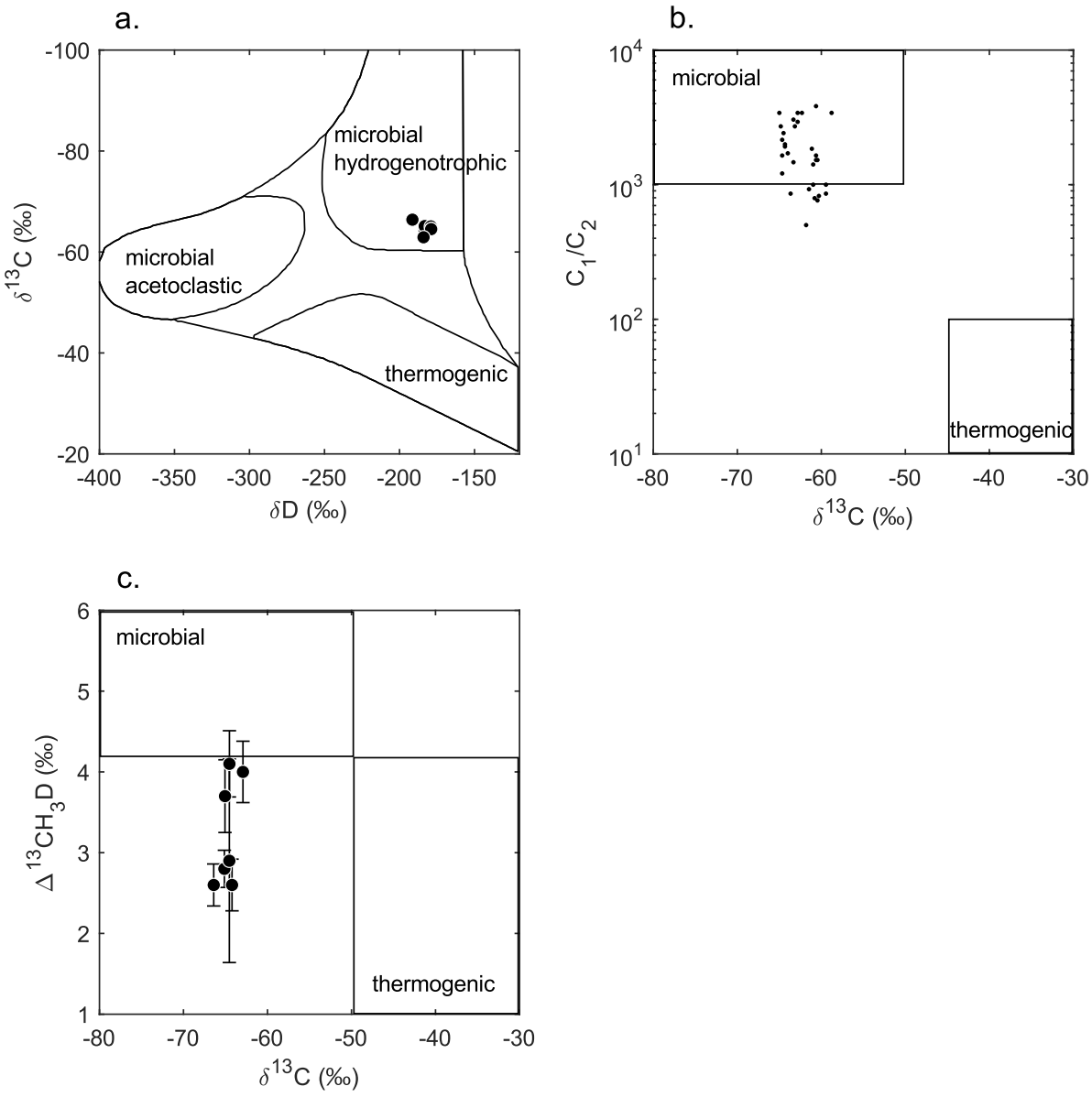

Figure A.3: Diagrams for methane source. **a** $\delta^{13}C$ vs δD of methane, **b** $\delta^{13}C$ of methane vs methane to ethane ratio (C_1/C_2), and **c** $\delta^{13}C$ vs $\Delta^{13}CH_3D$ of methane. Data in **b** is reproduced from Heuer et al., 2020.

Additional samples may be extracted and measured to supplement the results in **Table A.1**. The data presented in **section 5.9.3** support a good agreement between published methane concentration data (Heuer et al., 2020) and gas yields from extraction using the sediment degasser. A summary of the most likely (i.e., based on the minimum range of methane concentration) of samples stored at MIT to yield at least 1 mL CH_4 at STP is shown in **Table A.2**. All 68 cm^3 sediment samples from less than 600 mbsf have a chance of yielding 1 mL CH_4 based on the maximum range of methane concentration.

Sample ID	Depth (mbsf)	Porewater Volume (mL)	Expected Yield (mL)
CKY000000000006887100	452	33	1.9
CKY000000000006905200	473	50	2.3
CKY000000000007033600	579	29	1.4
CKY000000000007042600	585	29	1.4

Table A.2: Samples from the IODP 370 expedition stored at MIT that are most likely to yield enough methane for additional isotopologue data

A.2 ACKNOWLEDGEMENTS

We would like to acknowledge the efforts and expertise of the shipboard scientists and crew of the IODP Expedition 370 in obtaining sediment and void gas samples. Funding for this work was provided by the U.S. Science Support Program Office associated with the International Ocean Discovery Program (OCE-14-50528 to D.T.W., and S.O.).

A.3 REFERENCES

Heuer, V.B., Inagaki, F., Morono, Y., Kubo, Y., Maeda, L., Bowden, S., Cramm, M., Henkel, S., Hirose, T., Homola, K., Hoshino, T., Ijiri, A., Imachi, H., Kamiya, N., Kaneko, M., Lagostina, L., Manners, H., McClelland.H.-L., Metcalfe, K., Okutsu, N., Pan, D., Raudsepp, M.J., Sauvage, J., Schubotz, F., Spivack, A., Tonai, S., Treude, T., Tsang, M.-Y., Viehweger, B., Wang, D.T., Whitaker, E., Yamamoto, Y., Yang, K., 2017. Expedition 370 Summary.

Heuer, V.B., Inagaki, F., Morono, Y., Kubo, Y., Spivack, A.J., Viehweger, B., Treude, T., Beulig, F., Schubotz, F., Tonai, S., Bowden, S.A., Cramm, M., Henkel, S., Hirose, T., Homola, K., Hoshino, T., Ijiri, A., Imachi, H., Kamiya, N., Kaneko, M., Lagostina, L., Manners, H., McClelland, H.-L., Metcalfe, K., Okutsu, N., Pan, D., Raudsepp, M.J., Sauvage, J., Tsang, M.-Y., Wang, D.T., Whitaker, E., Yamamoto, Y., Yang, K., Maeda, L., Adhikari, R.R., Glombitza, C., Hamada, Y., Kallmeyer, J., Wendt, J., Wormer, L., Yamada, Y., Kinoshita, M., Hinrichs, K.-U., 2020. Temperature limits to deep subseafloor life in the Nankai Trough subduction zone. Science (80-.). 1234.

Ono, S., Wang, D.T., Gruen, D.S., Sherwood Lollar, B., Zahniser, M.S., McManus, B.J., Nelson, D.D., 2014. Measurement of a doubly substituted methane isotopologue, $^{13}CH_3D$, by tunable infrared laser direct absorption spectroscopy. Anal. Chem. 86, 6487–6494. https://doi.org/10.1021/ac5010579

Wang, D.T., Gruen, D.S., Sherwood Lollar, B., Hinrichs, K.U., Stewart, L.C., Holden, J.F., Hristov, A.N., Pohlman, J.W., Morrill, P.L., Könneke, M., Delwiche, K.B., Reeves, E.P., Sutcliffe, C.N., Ritter, D.J., Seewald, J.S., McIntosh, J.C., Hemond, H.F., Kubo, M.D., Cardace, D., Hoehler, T.M., Ono, S., 2015. Nonequilibrium clumped isotope signals in microbial methane. Science (80-.). 348, 428–431. https://doi.org/10.1126/science.aaa4326